STABILITY BEHAVIOR OF PULTRUDED GLASS-FIBER REINFORCED POLYMER I-SECTIONS SUBJECT TO FLEXURE

by

Tianqiao Liu

Bachelor of Science, Chang'an University, 2012

Master of Science, Carnegie Mellon University, 2013

Submitted to the Graduate Faculty of

Swanson School of Engineering in partial fulfillment

of the requirements for the degree of

Doctor of Philosophy in Civil Engineering

University of Pittsburgh

2017

UNIVERSITY OF PITTSBURGH

SWANSON SCHOOL OF ENGINEERING

This dissertation was presented

by

Tianqiao Liu

It was defended on

February 1, 2017

and approved by

Kent A. Harries, PhD, Associate Professor, Department of Civil and Environmental Engineering, Bicentennial Board of Visitors Faculty Fellow

Qiang Yu, PhD, Assistant Professor, Department of Civil and Environmental Engineering

Janine D. Vieira, PhD, Assistant Professor, Federal Fluminense University, Niterói, Brazil

John C. Brigham, PhD, Associate Professor, Durham University, Durham, UK

Dissertation Director: Kent A. Harries, PhD, Associate Professor, Department of Civil and Environmental Engineering, Bicentennial Board of Visitors Faculty Fellow

Copyright © by Tianqiao Liu

2017

STABILITY BEHAVIOR OF PULTRUDED GLASS-FIBER REINFORCED POLYMER I-SECTIONS SUBJECT TO FLEXURE

Tianqiao Liu, PhD

University of Pittsburgh, 2017

Pultruded glass fiber reinforced polymer (pGFRP) composite profiles, having the advantages of high strength-to-weight ratio and light weight, have seen significant developmental progress and numerous practical applications in the field of civil engineering. However, the low modulus of elasticity and high anisotropy, in addition to the relative slenderness of the thin-walled profiles, result in complex local and global buckling behavior for pGFRP members and significant interaction between local and global buckling modes. In this work, the stability behavior of pGFRP I-sections subject to flexure was addressed. An extensive review of stability behaviors of pGFRP members, including: flange local buckling (FLB), global lateral torsional buckling (LTB) and interaction between local and global buckling (interactive buckling) behaviors, was carried out. Two experimental programs were conducted: 62 four-point bending tests to investigate FLB behavior and 86 three-point bending tests to investigate LTB behavior. Interactive buckling behavior was observed in both series of tests and was shown to be quite prevalent in results from the LTB tests. Experimental results were compared with existing design guides and analytical solutions. Uniform under-predictions were found for FLB behavior of the I-sections considered and over-predictions were generally found for LTB behavior, exhibiting the need of new design formulas with improved accuracy. Analytical studies were presented and non-empirical design

formulas derived using energy methods were proposed with respect to the buckling behaviors observed in the experimental program. Supporting the experimental work, a series of material characterization tests were carried out to evaluate the mechanical properties of the pGFRP materials used. Both standard and nonstandard test methods that can be readily conducted using typically available test equipment as well as those requiring simple material preparations are recommended.

Keywords: pultruded GFRP, flexural stability, material characterization test, flange local buckling, lateral torsional buckling, interactive buckling.

TABLE OF CONTENTS

1.0 INTRODUCTION 1

1.1 BACKGROUND 1

1.2 MOTIVATION 5

1.3 OBJECTIVES AND ORGANIZATION OF DISSERTATION 6

1.4 NOTATION AND DEFINITIONS 7

1.4.1 Notation 7

1.4.2 Definitions 11

2.0 LITERATURE REVIEW 12

2.1 FLANGE LOCAL BUCKLING 14

2.1.1 FLB of pGFRP 14

2.1.2 Approach to rational analysis of pGFRP FLB 19

2.2 LATERAL TORSIONAL BUCKLING 21

2.2.1 LTB of pGFRP 21

2.3 INTERACTIVE BUCKLING 25

2.3.1 Interactive Buckling of pGFRP 26

2.4 DETERMINATIONS OF BUCKLING LOADS FOR PGFRP I-SECTIONS 27

2.4.1 Determinations of FLB 28

2.4.1.1 ASCE (1984) 28

2.4.1.2 ASCE (2010) 29
2.4.1.3 EUR 27666 (2016) 29
2.4.1.4 Other Predictions of FLB 31
2.4.2 Determinations of LTB 32
2.4.2.1 ASCE (1984) 32
2.4.2.2 ASCE (2010) 33
2.4.2.3 EUR 27666 (2016) 34
2.4.2.4 Other Predictions of LTB 35
3.0 MATERIAL AND GEOMETRIC CHARACTERIZATIONS 37
3.1 INTRODUCTION TO PULTRUDED GFRP MATERIALS 37
3.2 THEORETICAL MATERIAL CHARACTERIZATION 41
3.3 EXPERIMENTAL MATERIAL CHARACTERIZATION 44
3.3.1 Longitudinal and Transverse Tensile Strength and Modulus of Elasticity 44
3.3.2 Transverse Flexural Strength and Modulus of Elasticity 48
3.3.3 Longitudinal Compressive Strength and Modulus of Elasticity 51
3.3.4 In-Plane Shear Modulus of Elasticity 56
3.3.5 Summary 60
3.4 GEOMETRIC CHARACTERIZATION 61
4.0 FINITE STRIP METHOD 63
4.1 INTRODUCTION 63
4.2 MODELING USING CUFSM 66
4.3 SUMMARY OF MODELING 70
5.0 FLANGE LOCAL BUCKLING BEHAVIOR 73

5.1 EXPERIMENTAL PROGRAM 73
5.2 EXPERIMENTAL RESULTS 76
5.3 COMPARISONS WITH STANDARDS, NUMERICAL AND FSM MODELING 80
5.4 ANALYTICAL STUDY OF FLANGE LOCAL BUCKLING 82
5.4.1 Formulations 82
5.4.2 Validation of Eq. 5.16 87
5.4.3 Determination of Elastic Spring Constant 88
5.4.4 Corrections to Predictions Accounting for Test Geometry 90
6.0 LATERAL TORSIONAL BUCKLING BEHAVIOR 93
6.1 EXPERIMENTAL PROGRAM 93
6.2 EXPERIMENTAL RESULTS 97
6.3 COMPARISONS WITH STANDARDS, NUMERICAL AND FSM MODELING 101
6.4 ANALYTICAL STUDY OF LATERAL TORSIONAL BUCKLING 105
6.4.1 Formulations 105
6.4.2 Validation of Eq. 6.16 110
7.0 INTERACTIVE BUCKLING BEHAVIOR 112
7.1 EXPERIMENTAL RESULTS 112
7.1.1 Summary of Experimental Behaviors 113
7.2 ANALYTICAL STUDY OF INTERACTIVE BUCKLING 115
7.2.1 Formulations 115
7.2.1.1 Web 117
7.2.1.2 Top Flange 119
7.2.1.3 Bottom Flange 119

7.2.2 Validations 121

8.0 CONCLUSIONS 127

8.1 EXPERIMENTAL FINDINGS 128

8.1.1 Material Characterizations 128

8.1.2 FLB Tests 129

8.1.3 LTB Tests 129

8.2 ANALYTICAL PREDICTIONS 130

8.2.1 FLB 130

8.2.1.1 Revision to Kollár Assumptions 131

8.2.2 LTB 131

8.2.3 Interactive Buckling 132

8.3 FUTURE RESEARCH 132

APPENDIX A: EXPERIMENTAL RESULTS 135

A.1 FOUR-POINT BENDING TESTS 135

A.2 THREE-POINT BENDING TESTS 167

APPENDIX B: FLEXURAL STIFFNESS PARAMETERS 254

APPENDIX C: KOLLÁR'S EQUATIONS 255

APPENDIX D: FLB FORMULA SIMPLIFICATIONS 257

BIBLIOGRAPHY 261

LIST OF TABLES

Table 2.1 pGFRP profiles tested for studying the flange local buckling 18

Table 2.2 Summary of Cardoso et al. (2015) equations for local flange buckling capacity of pGFRP members subject to concentric axial load 20

Table 2.3 pGFRP profiles tested for studying the lateral torsional buckling 25

Table 3.1 Typical properties of glass, carbon, and aramid fibers (Barbero 2011) 38

Table 3.2 Typical properties of polyester, vinyl ester, and epoxy resins (Barbero 2011) 39

Table 3.3 Mechanical properties of pGFRP profiles 61

Table 3.4 Section dimensions of all pGFRP I-beams 62

Table 4.1 FSM predictions of critical moments for FLB for test specimens described in Chapter 5 71

Table 4.2 FSM predictions of critical moments for LTB for test specimens described in Chapter 6 72

Table 5.1 Experimental results and predictions of flange local buckling specimens 79

Table 5.2 Average critical FLB moments of each specimen geometry 81

Table 5.3 Comparisons with additional experimental results 87

Table 5.4 Comparisons between experimental and analytical $M_{cr\,FLB}$ 92

Table 6.1 Longitudinal slenderness ratios of LTB specimens 94

Table 6.2 Experimental results and predictions of lateral torsional buckling specimens 99

Table 6.3 Summary of ratios of predicted to experimental capacity for LTB tests 102

Table 6.4 Comparisons with additional experimental results 111

Table 7.1 Comparisons between experimental and analytical buckling moments 123

LISTS OF APPENDIX TABLES

Table C.1 Kollár's Equations for uniaxially compressed orthotropic plates with various boundary conditions (Kollár 2003) 256

LIST OF FIGURES

Figure 1.1 Pultrusion process (Creative 2015a) 2
Figure 1.2 Examples of pGFRP shapes including complex interlocking elements 3
Figure 1.3 Cooling tower with pGFRP structure (Midwest Cooling Towers 2015) 4
Figure 1.4 Pedestrian bridge fabricated of pGFRP members (Composite Advantage 2015) 4
Figure 1.5 pGFRP farm buildings (Bedford 2015) 4
Figure 1.6 Sign conventions and primary dimensions for pGFRP I-sections 11
Figure 2.1 Buckling modes of beams subject to flexure (after Kabir and Sherbourne 1998) 13
Figure 2.2 Double-webbed I-shape (Strongwell) 19
Figure 2.3 Local and global coordinate systems for LTB of an I-section 35
Figure 3.1 Constitution of pultruded profiles showing a two-layer architecture 41
Figure 3.2 Tensile test set-up 48
Figure 3.3 Non-standard test for transverse flexural modulus of flange 49
Figure 3.4 Non-standard test for transverse flexural modulus of web 50
Figure 3.5 Loading mechanisms 51
Figure 3.6 Shear loading test fixture 53
Figure 3.7 Combined loading test fixture (ASTM D6641) 54
Figure 3.8 Compressive test set-up 56
Figure 3.9 Shear test set-ups 58
Figure 3.10 ±45° tensile test specimen (Adam et al. 2003) 59

Figure 3.11 Shear test set-up (Image at right: after Cardoso et al. 2014) 60
Figure 3.12 Section geometries of FLB and LTB test specimens 62
Figure 4.1 Applications of FSM (after Cheung 1976) 64
Figure 4.2 Displacement function constructed using B-3 spline 65
Figure 4.3 FSM model 67
Figure 4.4 Example of critical buckling modes for 152.4 x 152.4 x 6.35 (6 x 6 x ¼) I-section... 69
Figure 4.5 Example of modal participation for 152.4 x 152.4 x 6.35 (6 x 6 x ¼) I-section 69
Figure 5.1 Four-point bending tests span arrangements for FLB tests 74
Figure 5.2 Test set-up of FLB tests 74
Figure 5.3 Flange local buckling (FLB5 over 2600 mm span) 76
Figure 5.4 Experimentally determined critical FLB moments versus flange slenderness ratios .. 78
Figure 5.5 Average critical FLB moments versus flange slenderness ratios 82
Figure 5.6 Coordinate system and boundary conditions for flange outstand plate 83
Figure 5.7 Modelling of the elastic rotational restraint at flange-web interface 90
Figure 6.1 Three-point bending tests span arrangements for LTB tests 94
Figure 6.2 Test set-up of three-point bending tests 95
Figure 6.3 Lateral torsional buckling (LTB3 over spans of 2896 mm) 97
Figure 6.4 Critical LTB moments versus longitudinal slenderness ratios 101
Figure 6.5 Critical LTB moments versus longitudinal slenderness ratios for LTB6 103
Figure 6.6 Critical LTB moments versus longitudinal slenderness ratios for LTB5 103
Figure 6.7 Critical LTB moments versus longitudinal slenderness ratios for LTB4 104
Figure 6.8 Critical LTB moments versus longitudinal slenderness ratios for LTB3 104
Figure 6.9 Critical LTB moments versus longitudinal slenderness ratios for LTB2 105
Figure 6.10 Global (x, y, z) and local (x, y', z') coordinate systems in LTB of I-beam 106
Figure 6.11 Vertical load positions 108

Figure 7.1 Interaction between local and global buckling (LTB6 under span of 2896 mm)..... 113

Figure 7.2 Nature of observed buckling failures 114

Figure 7.3 Experimentally determined critical buckling moments versus longitudinal and flange slenderness ratios..... 114

Figure 7.4 Axis and displacement notations..... 116

Figure 7.5 Rotational angles of top and bottom flanges 117

Figure 7.6 Critical buckling moments versus longitudinal slenderness ratios for LTB6 124

Figure 7.7 Critical buckling moments versus longitudinal slenderness ratios for LTB5 124

Figure 7.8 Critical buckling moments versus longitudinal slenderness ratios for LTB4 125

Figure 7.9 Critical buckling moments versus longitudinal slenderness ratios for LTB3 125

Figure 7.10 Critical buckling moments versus longitudinal slenderness ratios for LTB2 126

LISTS OF APPENDIX FIGURES

Figure A.1 Strain gage layout on the compression flange for four-point bending tests 135

Figure A.2 Strain gage layout on the compression flange for three-point bending tests 167

Figure D.1 Simplified- versus nonsimplified-critical FLB moments 260

ACKNOWLEDGMENTS

I would like to express my sincere gratitude to my advisor Prof. Kent Harries. You have been a tremendous mentor for me. I would like to thank you for your continuous support of my Ph.D study and research, for your patience and knowledge. You have been encouraging me to grow as a researcher. I would also like to express my special thanks Prof. Janine Vieira for your help with my research. We spent eight months working in the lab and I indeed learned a lot from you. I would also like to thank my committee members, Prof. Qiang Yu and Prof. John Brigham for serving as my committee members as well as providing me insightful comments and advises. I would especially thank my good friends, Shawn Platt, Charles “Scooter” Hager, and Qi Guo for your help not only for my research, but also for my life.

At the end, a special thanks to my beloved wife, Qing Wang, my mother, Qiong Zhang, my father, Guangyi Liu, and all my family members for your constant love and support through these years. I can never be what I am without the sacrifices that you have made on my behalf.

1.0 INTRODUCTION

1.1 BACKGROUND

Composite materials, manufactured by combining at least two distinct constituent materials into an element with certain proportions, are among the most basic structural materials in the world (Herakovich 1998; Gibson 2011). In a typical composite material, a strong constituent is embedded into, and typically reinforces, a second constituent, referred to as the matrix, (Hull and Clyne 1996). In fiber reinforced polymer (FRP) composites, lineal fibers reinforce a polymer matrix. From the standpoint of mechanical properties of FRP materials, the fibers contribute to the strength parallel to the direction(s) in which they are aligned. The matrix transmits loads between fibers and provides stability and both mechanical and environmental protection to the fibers (Hyer 2009). Commonly used fibers include glass (GFRP), carbon (CFRP), aramid (AFRP), basalt (BFRP) and steel (SFRP) or other metallic fibers. The most common matrices are polyester, vinylester and epoxy resins. In this work, the flexural behavior of pultruded glass fiber reinforced polymer (GFRP) members comprised of E-glass fiber reinforcement embedded in a polyester matrix is studied.

Due to the high cost of FRP materials, the earliest applications were limited to the aerospace and military industries. After World War II, glass based fiber reinforced polymers (GFRP) became available (Bakis et al. 2002). To date, GFRP composite materials have seen significant developmental progress and numerous practical applications in the field of civil

engineering. The motivation of implementing GFRP into civil structures lies in a number of advantages GFRP has over other materials, including: high strength-to-weight ratio, light weight, superior corrosion resistance and fatigue performance, and electromagnetic transparency. Moreover, the lighter weight of GFRP sections as compared to conventional construction materials, such as steel or timber, makes them a superior choice for long-distance transportation and rapid on-site installation (Maji et al. 1997; Nagaraj and GangaRao 1997; Hai et al. 2010).

Although initial high cost has been an obstacle to the widespread application of GFRP materials, the invention and continuous improvement of the pultrusion process has played an important role in decreasing manufacturing cost over the last few decades. Pultrusion (Figure 1.1) is a manufacturing process of continuously pulling resin-impregnated reinforcement materials, including unidirectional glass roving, multidirectional mat, and a surface veil, through a heated die to form, cure and harden the desired profiles (Bedford 2012). Additionally, using the pultrusion process, GFRP materials can be tailored to virtually any cross section geometry (Figure 1.2).

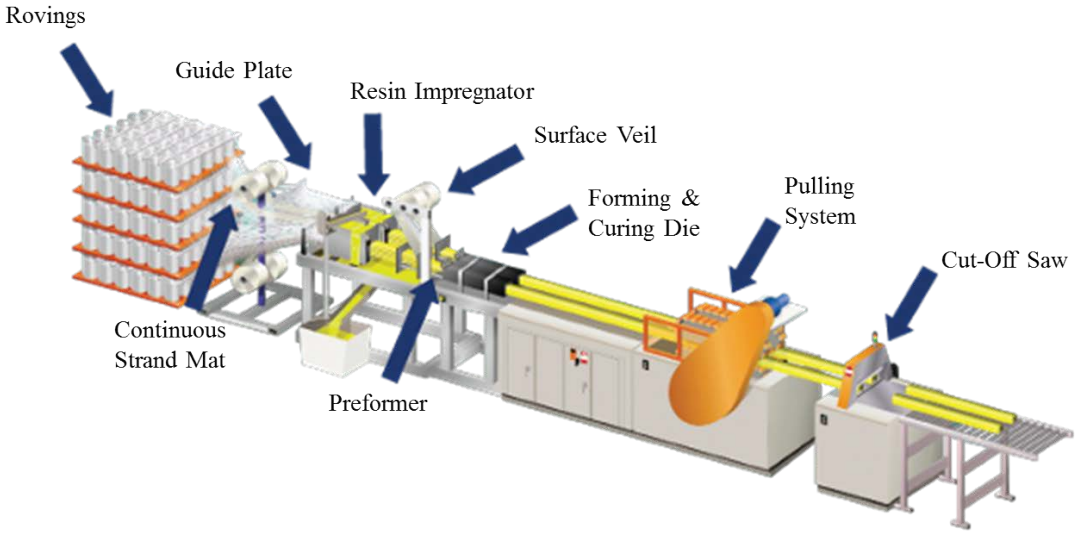

Figure 1.1 Pultrusion process (Creative 2015a)

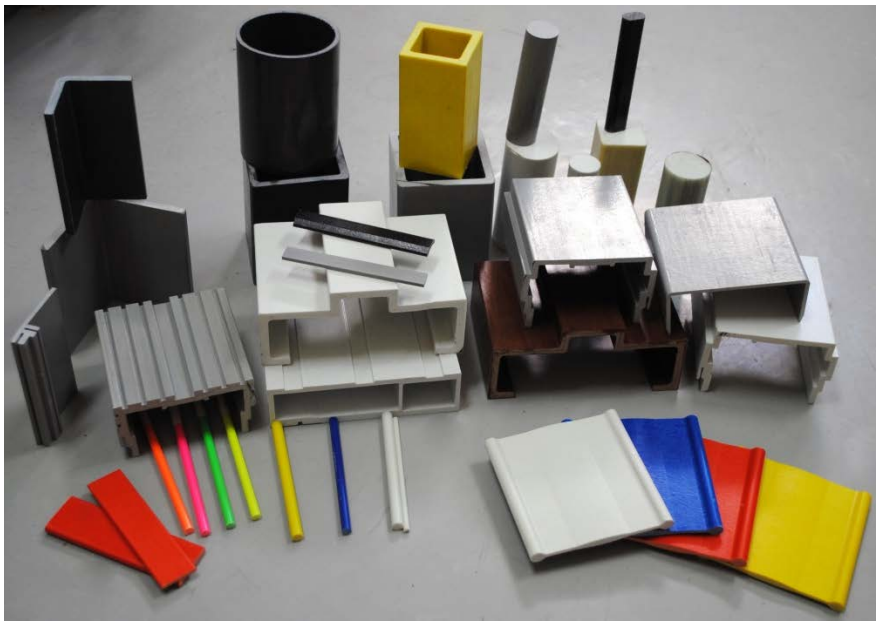

Figure 1.2 Examples of pGFRP shapes including complex interlocking elements (Fastec 2015)

With the adoption of the pultrusion process, the manufacturing speed and efficiency of GFRP materials has increased, which has led to a reduction in their cost. At present, many structure types take advantage of the properties of pultruded GFRP (pGFRP) materials. Water cooling towers (Figure 1.3) are presently the largest single market for pGFRP sections. Their light weight and corrosion resistance make GFRP the preferred materials for these structures (Mockry 2001). Indeed, it is the cooling tower industry that is driving efforts to develop design standards for pGFRP structures (ASCE 2010). GFRP bridge elements (Figure 1.4) are also gaining acceptance because of their light weight, high durability, ease of transportation (particularly to remote sites) and construction (Bank 2006). Low-rise modular buildings, particularly for agricultural use (Figure 1.5), walkway and secondary structures in many corrosive industrial environments and pipeline elements are also common industry applications (Van Den Einde et al. 2003).

Figure 1.3 Cooling tower with pGFRP structure (Midwest Cooling Towers 2015)

Figure 1.4 Pedestrian bridge fabricated of pGFRP members (Composite Advantage 2015)

Figure 1.5 pGFRP farm buildings (Bedford 2015)

1.2 MOTIVATION

The tensile strength in the fiber-direction of pGFRP materials, F_{Lt}, may exceed 200 MPa (Bedford 2012), which is comparable to that of mild structural steel (F_y = 245 – 350 MPa). However, the longitudinal modulus of elasticity, E_L, ranges from 20 to 30 GPa (Nguyen et al. 2013), only about one-tenth that of steel (E_s = 200 GPa). Furthermore, pGFRP materials are highly anisotropic. The ratios of longitudinal to transverse tensile strength and modulus are on the order of F_{Lt}/F_{Tt} = 4 and E_L/E_T = 3, respectively (Cunningham and Harries 2015). Such low modulus of elasticity and high anisotropy, in addition to the relative slenderness of the thin-walled profiles, result in complex local and global buckling behaviour for pGFRP members and significant interaction between local and global buckling modes (Cardoso 2014). Therefore, unlike the behavior of hot-rolled steel members (whose shapes pGFRP often mimic), pGFRP members will usually buckle before the material strength limit state is reached. Thus, deflection and stability criteria typically control the design of pGFRP members and structures (Barbero and Tomblin 1994; Godoy et al. 1995).

The lack of design code guidance continues to impede the wide application of pGFRP materials (Barbero and DeVivo 1999). Although design guides are available from pultruders, such guides are not consensus standards and are often conservative in their calculation of capacities, which may lead to an increase in the total cost of the project. Most of these *ad hoc* design guides (and indeed, the ASCE *Prestandard* (2010)) are based on the design of hot-rolled steel shapes (AISC 2011). As discussed in Chapter 2, many formulations of pGFRP design values have been proposed although these are often too complicated for practical design-office implementation. Thus, a suite of design formulas that are easy to understand and implement is needed (Johnson and Shield 1998). In 2007, the American Composites Manufacturers

Association (ACMA) began to prepare a design prestandard on the basis of Load and Resistance Factor Design (LRFD) for pultruded fiber-reinforced plastic structures. The *Prestandard* was completed in 2010 (ASCE 2010) and forms the basis for ongoing development of an ASCE *Design Standard for Load & Resistance Factor Design (LRFD) of Pultruded Fiber Reinforced Polymer (FRP) Structures* (ASCE 2017). The work presented in this dissertation directly supports the development of this *Standard* and is informed by ongoing changes within the draft and balloted documents provided by the thesis advisor, Prof. Harries. It must be noted that this dissertation does not report the final version of the *Standard* as this document remains in the balloting process at the time of publication (Spring 2017).

1.3 OBJECTIVES AND ORGANIZATION OF DISSERTATION

Although a number of researchers have studied the buckling behavior of pGFRP beams subject to flexure, resulting proposed formulas are either based on a series of empirical coefficients or too complicated for practical implementation by designers. The primary objective of this work is therefore to develop a set of credible and applicable design formulas suitable for adoption in design standards.

To accomplish this objective, an extensive literature review (Chapter 2) is conducted focusing on the local and global buckling behaviors of orthotropic materials, focusing on pGFRP sections. To augment the limited data available (particularly in the sense of section geometry), two experimental programs are conducted addressing: 1) flange local buckling (FLB) of pGFRP sections in flexure (Chapter 5) and 2) lateral torsional buckling (LTB) of these members

(Chapter 6). Both programs are designed to capture a range of buckling behaviors and especially the interaction of, and transition between, FLB and LTB (Chapter 7).

Extensive material characterization tests are also conducted (Chapter 3). This requires adapting innovative experimental means of establishing in-plane properties. While not a specific objective of this work, the materials testing component – together with earlier work conducted by Cardoso (2014) – forms the basis of the development of proposed new test standards suitable for obtaining these otherwise difficult-to-obtain material properties from pGFRP sections.

Following the approach described by Cardoso (2014) for concentrically loaded axial compression carrying (column) members, plate theory and energy methods are used to derive explicit equations for flange local buckling of pGFRP members subject to flexure. These equations are validated through the experimental results obtained in the present study and those available in the literature (Chapters 5 – 7). Results are compared with finite strip method (FSM) analyses (Chapter 4), shown to be quite accurate by Cardoso, and the 'exact' analytical solutions of Kollár (2003).

1.4 NOTATION AND DEFINITIONS

1.4.1 Notation

Super- and sub-indices *f* and *w* refer to flange and web, respectively.

Sub-indices *L* and *T* refer to longitudinal and transverse directions of anisotropic plate, respectively.

Sub-indices *t, c* and *b* refer to material properties derived from tension, compression and bending tests, respectively.

Sub-index i = 1, 2, 3, etc. are used for a variety of coefficients; these are defined in the text.

A	cross-sectional area of the specimen; $A = wt$ (Chapter 3)
a	distance from application of load to strain gage (Chapter 3)
a	distance from application of load to the shear center (Chapters 6 and 7)
b	flange width
C_b	moment modification factor accounting for varying moment
C_i	restraint coefficient in EUR 27666 (2016)
C_w	torsional warping constant; $C_w = t_f d^2 b^3/24$ for an I-section
c	constant coefficient
D_{ij}	plate flexural stiffness parameters, D_{ij} (i, j = 1,2 and 6) are given in Appendix B. superscripts indicate flange (f) or web (w).
d	section height
E	modulus of elasticity of an isotropic material
E_f	longitudinal modulus of fiber
E_L	longitudinal modulus of elasticity
E_m	longitudinal modulus of matrix
E_s	modulus of elasticity of steel
E_T	transverse modulus of elasticity
E_{Tb}	transverse flexural modulus of elasticity
F_{Lc}	longitudinal compressive strength
F_{Lt}	longitudinal tensile strength
F_{Tb}	transverse flexural strength
F_{Tt}	transverse tensile strength
F_y	yielding strength of steel
f_{cr}	critical buckling strength
f_x	uniform compressive stress in the longitudinal direction of the plate
G	shear modulus of an isotropic material
G_f	in-plane shear modulus fiber
G_{LT}	shear modulus of elasticity
G_m	in-plane shear modulus matrix

G_s	shear modulus of steel
I	moment of inertia about principle axis; $I = [bd^3 - (b - t_w)(d - 2t_f)^3]/12$ for an I-section
I_2	weak-axis moment of inertia
$I_{y'}$	moment of inertia about the local weak-axis y'
I_η	moment of inertia about η-axis
I_ξ	moment of inertia about ξ-axis
J	section torsional constant; $J = 0.33\Sigma b_i t_i^3$ for and open section in which there are i elements each having $b > t$
K	effective length factor for column buckling (Chapter 2)
K_G	geometric matrix
K_S	stiffness matrix
k	load coefficient in EUR 27666 (2016) (chapter 2)
k	spring constant, simulating rotational restraint at flange-web interface
k_{cr}	critical plate buckling coefficient
L	half wave length of the buckled flange plate in the longitudinal direction
L_b	length between points that are either braced against lateral displacement of the compression flange or braced against twist of the cross-section
L_{cr}	critical half wave length of FLB
$L_{provided}$	experimentally observed half wave length of FLB
M	applied moment
M_{cr}	critical buckling flexural strength
M_n	nominal flexural strength
$M_{y'}$	bending moment about the local weak-axis y'
M_η	bending moment about η-axis
M_ξ	bending moment about ξ-axis
M_ζ	twisting moment about ζ-axis
$N(x)$	conventional beam shape functions along x-axis
n	observed number of half waves of FLB
P	applied point load
P_{cr}	critical buckling load

P_{e2}	weak-axis Euler buckling load
P_{max}	maximum applied force
r_y	radius of gyration of cross section about *y*-axis
S	elastic section modulus about principle axis; $S = [bd^3 – (b – t_w)(d – 2t_f)^3]/6d$ for an I-section
t	flange or web thickness, for pGFRP it is typical that $t_f = t_w$
t_f	flange thickness
t_w	web thickness
U	strain energy
u	displacement along *x* axis
v	displacement along *y* axis
W	potential energy
w	displacement function
w	length of test specimen (Chapter 3)
α	parameter, accounting for the restraining effect at the flange-web connection
β	empirical parameter, accounting for the orthotropic nature of the flange material
γ_{12}	shear strain
γ_M	partial factor in EUR 27666 (2016), together with η_c accounting for the uncertainties in the behaviors of the material
Δ	vertical displacement
ζ	coefficient of restraint
η	ratio of flange-to-web widths; coefficient
η_c	conversion factor in EUR 27666 (2016)
λ	eigenvalue
ν_f	major Poisson’s ratio of fiber
ν_{LT}	major Poisson’s ratio of anisotropic plate
ν_m	major Poisson’s ratio of matrix
ν_{TL}	minor Poisson’s ratio of anisotropic plate
ξ	coefficient of restraint
Π	total potential energy
σ	stress

σ_i	principal stresses, i = 1 and 2
τ_{12}	shear stress
ϕ	rotational angle of the cross section
ϕ_{bf}	rotational angle of bottom flange
ϕ_{tf}	rotational angle of top flange
φ	material resistance factor
$\varphi_i(y)$	B-3 spline function along y axis
χ	load reduction factor in EUR 27666 (2016)

1.4.2 Definitions

Figure 1.6 shows the dimension notation and orientation conventions for longitudinal and transverse directions for flanges and web of pGFRP I-sections.

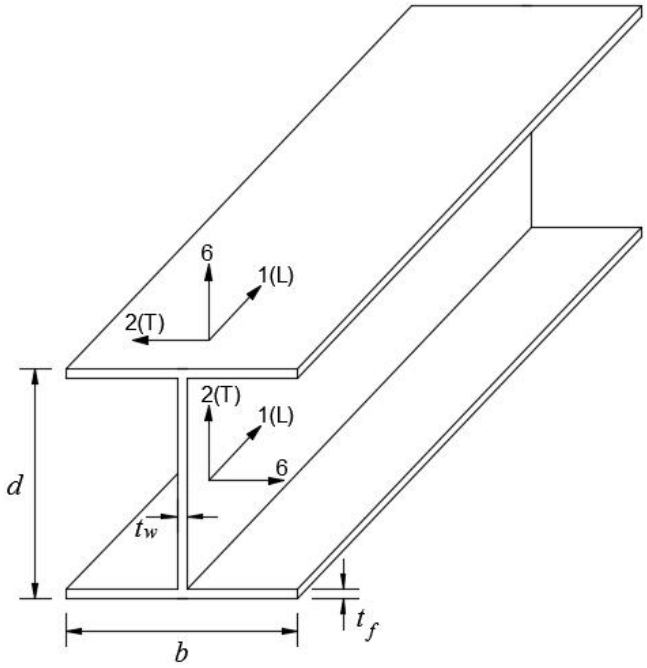

Figure 1.6 Sign conventions and primary dimensions for pGFRP I-sections
Note that typically $t_f = t_w = t$

2.0 LITERATURE REVIEW

There are three buckling modes that may occur in beams subject to flexure: local buckling of the flange and/or web (FLB and WLB), global lateral torsional buckling (LTB), and interaction between local buckling and LTB (Figure 2.1).

A number of researchers have studied FLB and LTB. Some representative studies are reviewed and summarized in the following sections. Interaction between local and global buckling, however, has only been emphasized in a few studies, which are also presented in this Chapter.

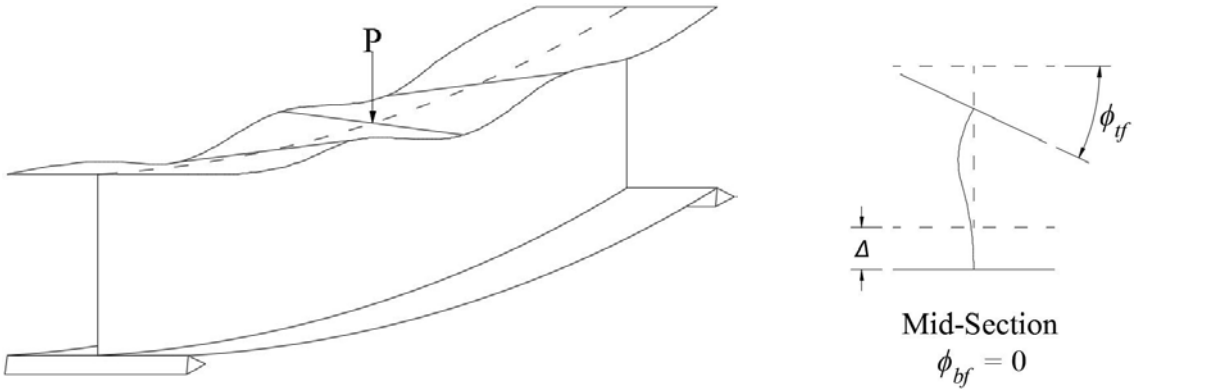

a) Local buckling (FLB and WLB)

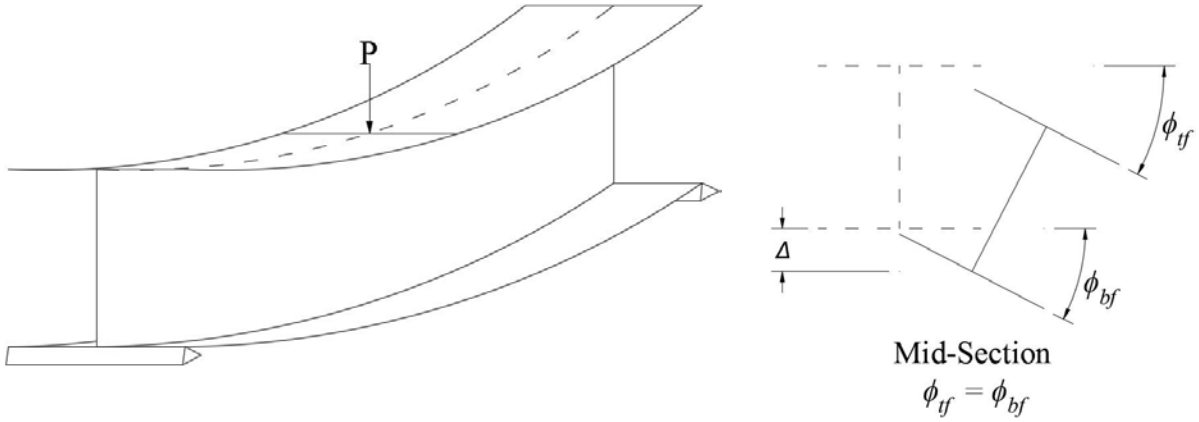

b) Lateral torsional buckling (LTB)

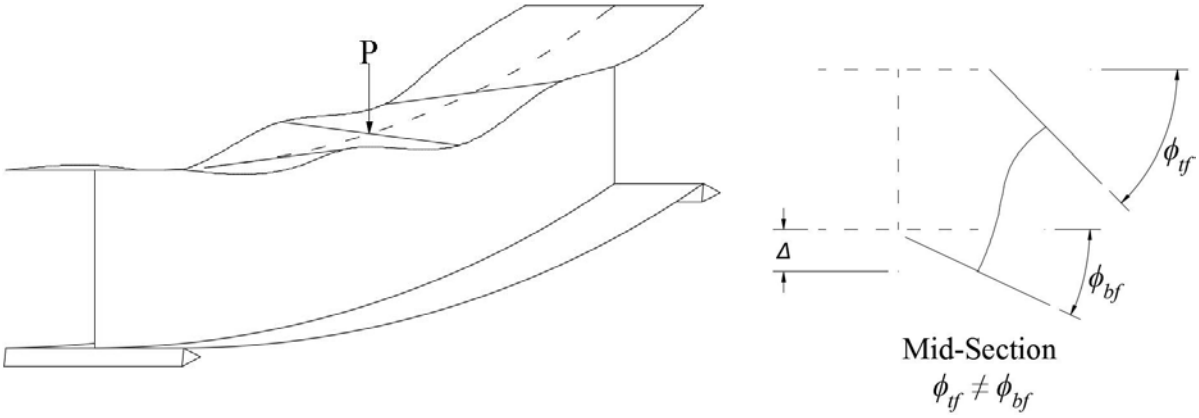

c) Interaction between local buckling and LTB

Figure 2.1 Buckling modes of beams subject to flexure (after Kabir and Sherbourne 1998)

2.1 FLANGE LOCAL BUCKLING

When a thin-walled pGFRP I-beam is subject to strong-axis bending, the compression flange and a part of web are placed in compression and tend to buckle before the material strength limit is reached; this is flange (FLB) and/or web (WLB) local buckling (Geschwindner 2008) (Figure 2.1a). FLB and WLB essentially occur together since, in order for the flange to deform, the web must also buckle as seen in Figure 2.1a. Due to practical beam geometries and lengths used in practice, it is typically FLB that "initiates" this process; therefore, FLB initiation is the focus of this study.

2.1.1 FLB of pGFRP

To study the flange local buckling behavior of pGFRP composites, Barbero et al. (1991) conducted 38 three-point bending tests and 18 four-point bending tests on wide flange pGFRP I-beams, as well as 8 three-point bending tests on box beams. Through the results of these 64 tests, local buckling was observed in the compression flanges and it was found that the pGFRP beams behaved in an essentially linear manner to failure. To simulate the beam behavior obtained from the tests, an analytical model was created using plate theory to model the sections. Half of the beam flange was modeled as a simply-supported plate with one long edge free and the other connected to the web. In their analysis, three types of flange-web connections were modeled: an elastic connection (rigid flange-web junction with elastic web); a hinged connection (hinged flange-web junction); and a clamped connection (rigid flange-web junction with rigid web). The experimental behavior was shown to be best modelled by the clamped connection because of the thickened 'fillet' region at the intersection of flange and web. Barbero and Raftoyiannis (1993) continued developing the analytical solutions for the local buckling modes taking the flange-web

connections into account. The solutions presented were also extended to be capable of predicting the local buckling behavior for other pGFRP section shapes.

Bank et al. (1995) also emphasized the importance of including the properties of edge restraints and flange-web connections in analyses predicting the buckling loads of pGFRP beams. Subsequently, Bank et al. (1996) conducted a series of four-point bending tests on pGFRP wide flange I-beams, from which it was demonstrated that the local buckling of the compression flanges could lead to failure of the entire beam. Additionally, in this study, a group of beams were retrofit by adding wet layed-up GFRP to the fillet region in order to increase the stiffness of flange-web connection. From the test results, a change of failure mode from local buckling of the compression flange to longitudinal shear failure of flange-web connection was observed (the beams were supported laterally in this study thereby mitigating lateral torsional buckling). This result clearly demonstrated that flange buckling can be mitigated and the ultimate strength of the FLB-susceptible pGFRP beams can be enhanced by increasing the stiffness of flange-web connection.

Pecce and Cosenza (2000) carried out a series of four-point bending tests on pGFRP I-beams. Additionally, an analytical study was conducted in which the elastic flange-web connection was considered. Consequently, a buckling curve and design formula were proposed to predict the critical stress for flange local buckling:

$$f_{cr} = \alpha\beta \left[\frac{\pi^2 D_{11}^f}{(b/2)^2 t_f} \right] \tag{2.1}$$

The term in brackets is the classical formulation for critical flange buckling stress for an isotropic material [1]. The empirically-derived parameter $\beta = (E_L/E_T)^{0.85}$ accounts for the

[1] Plate flexural stiffness parameters, D_{ij} $(i, j = 1,2 \text{ and } 6)$ are given in Appendix B. Superscripts indicate flange (f) or web (w).

orthotropic nature of the flange material. The parameter α accounts for the restraining effect at the flange-web connection. For a pinned flange, $\alpha = 0.425$ and for a clamped flange, $\alpha = 1.277$; both well-known limits established in plate theory. Pecce and Cosenza proposed a variation of the parameter α to account for the restraining effect of the flange-web connection:

$$0.425 < \alpha = \frac{(b/2)}{t_f}\frac{t_w}{d}\left(\frac{E_T^w}{E_T^f}\right)^{0.5} + 0.125 \leq 1.277 \tag{2.2}$$

Additionally, Pecce and Cosenza demonstrated the utility of the Finite Element Method (FEM) for predicting the flange local buckling load.

Qiao et al. (2001) also derived a formula to calculate the critical flange local buckling load by employing plate theory. In their study, it was once again demonstrated that the stiffness of the flange-web connection fell between that of hinged and clamped connections. Expressions describing the appropriate restraint coefficients were proposed for both I-beams and box beams. For an I-beam, using the same formulation as Eq. 2.1:

$$\alpha\beta = \frac{1.277 - 0.425}{0.83\zeta^{0.75} + 1} + 0.425 \tag{2.3}$$

Where the coefficients 0.83 and 0.75 in the denominator are empirically derived from curve fitting to experimental results. The restraint coefficient, ζ, is given as:

$$\zeta = \frac{2\left(d - t_f\right)}{(b/2)}\frac{D_{22}^f}{D_{22}^w}\Bigg/\left(1 - \frac{\frac{0.425\pi^2 D_{11}^f}{(b/2)^2}}{\frac{2\pi}{\left(d - t_f\right)^2}\left(\sqrt{D_{11}^w D_{22}^w} + D_{12}^w + 2D_{66}^w\right)}\right) \tag{2.4}$$

Qiao and Zou (2003) proposed an explicit expression for calculating the critical local buckling load for pGFRP wide flange I-beams. Similarly, plate theory and an elastic connection between flange and web were assumed.

$$f_{cr} = \frac{-20(2+3\xi)D_{12}^{f}+15.49\sqrt{2+\xi}\sqrt{6+15\xi+10\xi^2}\sqrt{D_{11}^{f}D_{22}^{f}}+40(4+6\xi+3\xi^2)D_{66}^{f}}{t_f(b/2)^2(6+15\xi+10\xi^2)} \quad (2.5)$$

Where the restraint coefficient, ξ, is given as:

$$\xi = \frac{2(d-t_f)}{(b/2)}\frac{D_{22}^{f}}{D_{22}^{w}}/(1-0.106\frac{(d-t_f)^2}{(b/2)^2}\frac{\sqrt{D_{11}^{f}D_{22}^{f}}+D_{12}^{f}+2D_{66}^{f}}{\sqrt{D_{11}^{w}D_{22}^{w}}+D_{12}^{w}+2D_{66}^{w}}) \quad (2.6)$$

Eqs 2.2, 2.3 and 2.5 are shown by their respective authors to represent the limited experimental data on which they are based quite well. No known study extends the results to other sections or materials. Additionally, it may be argued that the resulting empirical equations (with the exception of Eq. 2.2, perhaps) are not “design office friendly”.

Mottram (2002) collected and assessed nine equations for predicting the local buckling loads from different researchers and pultrusion manufacturers, concluding that the equation promulgated in ASCE (1984), given in Eq. 2.11, was the most accurate.

In a critical paper for the field, Kollár (2003) proposed a set of explicit solutions based on plate theory addressing the full suite of possible boundary conditions and flange-web connection types. The expressions in this study were validated by numerical models. Later, Kollár et al. (2010) made some corrections to the previously published explicit solutions. While generally considered accurate, the so-called ‘Kollár equations’ are too cumbersome for designers to use although they are acknowledged to provide benchmark solutions (Cardoso 2014). The Kollár equations—presented in Appendix C—will be used as benchmark solutions in this study.

Correia et al. (2011) conducted a series of three-point bending tests on pGFRP I-beams, once again, concluding that the performance of the pGFRP members were practically governed by deformation criteria instead of material strength criteria. More recently, Ascione et al. (2013)

developed a mechanical model, also using plate theory, to predict the critical local buckling load of pGFRP columns and beams.

Table 2.1 summarizes the experimental programs described in this section. It is important to note that, with the exception of Correia et al. (2011), all sections reported are wide flange sections (having the flange width, *b*, equal to the beam depth, *d*) and that only a relatively small range of beam sizes have been considered. More critically, effectively only two flange slenderness ratios are included: $b/2t \approx 8$ and 12.

Table 2.1 pGFRP profiles tested for studying the flange local buckling

Authors	Four-Point Bending Test	Three-Point Bending Test
Barbero et al. (1991)	100 x 100 x 4.3 mm Box	-
	100 x 100 x 6.4 mm I-beam	100 x 100 x 6.4 mm I-beam
	150 x 150 x 6.4 mm I-beam	150 x 150 x 6.4 mm I-beam
	200 x 200 x 9.5 mm I-beam	200 x 200 x 9.5 mm I-beam
Bank et al. (1996)	203 x 203 x 9.5 mm I-beam	-
	203 x 203 x 12.7 mm I-beam	-
	203 x 203 x 9.5 mm I-beam (retrofit)	-
Pecce and Cosenz (2000)	102 x 102 x 6.4 mm I-beam	-
Correia et al. (2011)	-	200 x 100 x 10 mm I-beam

Dimensions shown are *d* x *b* x *t*; for pGFRP it is typical that $t_f = t_w$.

In considering the previous work on pGFRP flexural members, it becomes clear that FLB is a dominate limit state effected by a) the relatively slender flanges of I-shapes and the b) the relatively poor restraint provided by the web. This suggests that despite their availability, I-sections do not represent an optimal use of GFRP materials. Indeed, efficient pGFRP flexural members have been fabricated as “double webbed” I-shapes (sometimes referred to as flanged box sections) (Schniepp 2002; Strongwell 2003). These shapes (an example is shown in Figure 2.2) simultaneously reduce the flange slenderness and provide effectively stiffer web restraint.

While such sections are not the subject of the present work, and are uncommon outside of proprietary bridge elements, the discussion and investigation of FLB presented in this work remains fundamentally valid for the flange outstands of such sections.

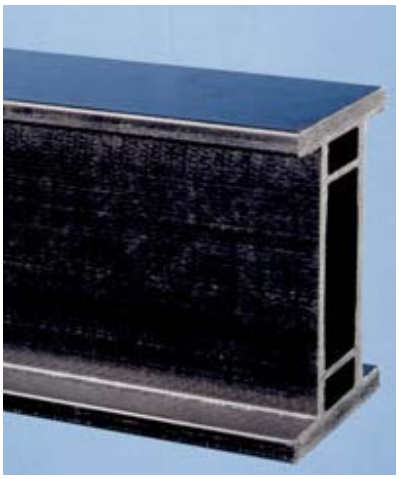

a) Pultruded shape

b) Use as bridge girder (VA Route 601 over Dickey Creek)

Figure 2.2 Double-webbed I-shape (Strongwell)

2.1.2 Approach to rational analysis of pGFRP FLB

Relevant to the present study, Cardoso et al. (2015) employed plate theory (Bleich 1952) and the Rayleigh Quotient energy method (Bažant and Cedolin 2010) to derive explicit equations for flange local buckling of pGFRP members subject to axial compression. The equations were validated through a series of tests of I-sections with different pGFRP materials (vinylester and polyester) and different sectional dimensions ($\eta = b/d$ ranged from 0.44 to 1.00; $b/2t$ ranged from 2.6 to 8; and d/t ranged from 10.8 to 15.4). Additionally, analyses using the Kollár equations and the finite strip method (FSM) of analysis were presented to validate and extend the parameters to

which the equations could be applied. By limiting section geometry to "realistic" values, Cardoso et al. succeeded in developing equations, based on the well-established form of Eq. 2.1:

$$f_{cr} = k_{cr}\left[\frac{\pi^2 D_{11}^f}{(b/2t_f)^2}\right] \tag{2.7}$$

Where k_{cr} is given in Table 2.2. for the range of $\eta = b/2d$ given, the proposed explicit equations differed from finite strip method (FSM) derived solutions by less than 6% for I-shapes and 10% for all shapes considered (Table 2.2). Eq. 2.7 is therefore proposed as being suitable for use in a design office while accurately capturing the local buckling behavior of a variety of I-shapes, angles, boxes and channels. The approach used by Cardoso will be extended to flexural buckling in the present study. It is noted that Cardoso did not differentiate material properties of the flange and web, assuming them to be the same. In the present study, an attempt is made to address this shortcoming.

Table 2.2 Summary of Cardoso et al. (2015) equations for local flange buckling capacity of pGFRP members subject to concentric axial load

Section	k_{cr}	Range of applicable $\eta = b/2d$	Greatest relative difference from FSM solution
Angles	$k_{cr} = \frac{12(\eta+1)}{\pi^2(\eta^3+1)}(1-\nu_{LT}\nu_{TL})\frac{G_{LT}}{E_L}$	0.33 – 1.00	0.01
I-shapes	$k_{cr} = \frac{2}{\sqrt{\pi^2\eta^3/3+1}}\sqrt{E_T/E_L} + \frac{2\nu_{LT}E_T/E_L + 4(1-\nu_{LT}\nu_{TL})G_{LT}/E_L(1+4\eta)}{(\pi^2\eta^3/3+1)}$	0.45 – 1.05	0.06
Channels	$k_{cr} = \frac{2}{\sqrt{4\pi^2\eta^3/3+1}}\sqrt{E_T/E_L} + \frac{2\nu_{LT}E_T/E_L + 4(1+4\eta)(1-\nu_{LT}\nu_{TL})G_{LT}/E_L}{(4\pi^2\eta^3/3+1)}$	0.15 – 0.53	0.10
Boxes	$k_{cr} = 2\sqrt{3.4-2.4\eta}\sqrt{\frac{E_T}{E_L}} + (0.81+1.32\eta-1.13\eta^2)\left[2\nu_{LT}\frac{E_T}{E_L}/+4(1-\nu_{LT}\nu_{TL})\frac{G_{LT}}{E_L}\right]$	0.25 – 1.00	0.03

2.2 LATERAL TORSIONAL BUCKLING

When a laterally unbraced pGFRP I-beam is subject to flexure, the compression flange may buckle laterally prior to the material strength limit being reached, while the tension flange restrains such lateral movement, causing the entire beam to twist. This phenomenon, exhibiting combined lateral and torsional displacements, shown in Figure 2.1b, is called lateral torsional buckling (LTB) (Geschwindner 2008; Bažant and Cedolin 2010).

2.2.1 LTB of pGFRP

In structures with pGFRP members, lateral torsional buckling is of great importance, particularly since in many typical pGFRP structures, full support of the compression flange is not provided (in cooling towers and truss bridges, for instance); in many cases, lateral support is intermittent and often minimal. A number of researchers have studied LTB of pGFRP composites.

Mottram (1992) conducted a series of three-point bending tests on pGFRP I-beams. Both lateral and torsional behaviors were simultaneously observed and the corresponding critical LTB loads were obtained. It was also identified that such tests are very sensitive to imperfections in the test set-up, including those induced by the specimen itself as well as those inherent in the boundary conditions of the test set-up. Experimental results were compared with those calculated based on the extant equation for nominal moment capacity, M_n (ASCE 1984), given in Eq. 2.30, which proved to be conservative.

Experimental tests as well as finite element analysis of pGFRP cantilever I-beams were conducted by Brooks and Turvey (1995). The experimental and analytical results in terms of the critical LTB loads were compared with approximate formulations proposed by Timoshenko and Gere (1961), and Nethercot and Rockey (1973). Both finite element analyses and approximations

were found to be conservative in predicting the critical lateral buckling loads. Pandey et al. (1995) conducted a series of analytical studies predicting the critical lateral buckling loads for pGFRP I-beams under varying loading conditions, including simply-supported beams with uniformly distributed or discrete transverse loads or end moments, and cantilever beams with a tip load. The load pattern-dependent expressions derived in this work were further used in a parametric study intended to optimize fiber architecture.

Another analytical study based on the Finite Element Method was conducted by Lin et al. (1996), in which they calculate the critical buckling loads for both symmetric and nonsymmetrical pGFRP sections. In particular, shear strain was found to have a significant influence on the lateral torsional buckling mode. That is to say the G_{LT} term can be more critical for anisotropic pGFRP than it is for isotropic materials. For example, for steel, $E_s/G_s \approx 2.6$ whereas for pGFRP, E_L/G_{LT} may vary from 4 to 12 (Liu et al. 2017).

Turvey (1996a) carried out a set of experiments on square box-shaped pGFRP cantilever beams. The results of the critical moments from the tests were compared with those calculated using a modified formula for isotropic material (Nethercot and Rockey 1971). It was found that this formula provided a reasonable correlation with the experimental data only at higher span-depth ratios. Later, another set of tests (Turvey 1996b) on pGFRP cantilever I-beams, ranging from $L_b/d = 5$ to 15, having three different load positions (just below the top flange, at the section centroid, and just above the bottom flange) were conducted. The modified formula from Nethercot and Rockey (1971) was, once again, employed to estimate the critical LTB loads. Additionally, an FEM analysis was conducted using ABAQUS. Finally, Turvey compared the results from all three predictions. The numerical approximation was found to not be able to provide good correlation with the experimental data. Correct definition of the prebuckling

deformation, nonlinear geometry, and a more accurate assessment of in-plane shear modulus were suggested to be included to accurately evaluate the LTB loads.

Davalos et al. (1997) conducted a series of tests on simply-supported pGFRP wide flange beams under midspan point-load. Additionally, a numerical solution based on the principle of minimum potential energy was developed (Eq. 2.8) and a FEM model was created to calculate the LTB loads. Good correlation between all results was found.

$$M_{cr} = \frac{\pi^3 d\sqrt{(6D_{11} + E_L t d^2)\left[\pi^2 d^2\left(2D_{11} + \frac{E_L t^3}{3} + E_L t d^2\right) + 48L^2\left(2D_{66} + \frac{G_{LT} t^3}{12}\right)\right]}}{6(\pi^2 + 4)L^2} \quad (2.8)$$

Eq. 2.8 applies only to the case of a simply supported beam having a point load at midspan applied at the centroid of the member cross section. Additionally, no differentiation between flange and web properties was made.

Sapkás and Kollár (2002) developed explicit expressions to calculate critical LTB loads. Both simply-supported and cantilever beams under various load conditions were included in this work. The results obtained from these explicit formulas were compared with the previous numerical solutions proposed by Mottram (1992), Zureick et al. (1995), and Lin et al. (1996). It was demonstrated that there was a good agreement between those solutions. Lee et al. (2002) developed a FEM model to predict the LTB load of pGFRP I-beams which predicted the results presented by Lin et al. (1996) with a good agreement.

Qiao et al. (2003) conducted a series of tests on cantilever pGFRP I-beams and proposed analytical solutions to predict the corresponding LTB loads. Additionally, a finite element model was built. It was found that there was a good agreement among the proposed analytical solutions, experimental results, and FEM model.

Ascione et al. (2011) developed a numerical model to predict the LTB load for pGFRP I-beams. The results from the proposed model were validated using results obtained by Roberts (2002). Correia et al. (2011) conducted a series of tests on cantilever pGFRP I-beams concluding that pGFRP structural members were practically governed by deformation criteria instead of material strength criteria.

More recently, Nguyen et al. (2014) conducted 114 tests on simply-supported pGFRP I- and C-beams to study their LTB behaviors. It was found that the experimental results were higher than Nguyen's predictions. This was due to the under-prediction of mechanical properties, E_L and G_{LT}, provided by pultruder. Once again, it was demonstrated that the pultruder's design manual resulted in a conservative design, leading to an increase in material cost. Additionally, the effect of vertical load position was identified through the tests. Ngyuen et al. showed that sections in which the load is applied at the centroid exhibit an LTB capacity about 40% greater than when the load is applied along the top flange.

The explicit nature of the numerical solutions for LTB (such as Eq. 2.8) illustrates the load-pattern dependence of such an approach and, therefore, why it may not be well suited to the structural design process.

Table 2.3 summarizes the experimental programs described in this section. Once again, a relatively small range of cross sections is represented and the majority of testing has been carried out on cantilever specimens. Cantilever members are relatively rare in practice and when they are used, will typically have lateral support at their tip and therefore be restrained from LTB of the sort exhibited in the experimental programs.

Table 2.3 pGFRP profiles tested for studying the lateral torsional buckling

Authors	GFRP Section	Unbraced Length	Test Type
Mottram (1992)	102 x 51 x 6.4 mm I-beam	1500 mm	3-point
Brooks and Turvey (1995)	102 x 51 x 6.4 mm I-beam	1250, 1500, and 1750 mm	cantilever
Turvey (1996a)	40 x 6.3 mm Rectangle-beam	400, 600, 800 and 1000 mm	cantilever
	60 x 6.3 mm Rectangle-beam		
	80 x 6.3 mm Rectangle-beam		
	100 x 6.3 mm Rectangle-beam		
Turvey (1996b)	102 x 51 x 6.4 mm I-beam	500, 1000 and 1500 mm	cantilever
Davalos et al. (1997)	304.8 x 304.8 x 12.7 mm I-beam	4420 mm	3-point
Qiao et al. (2003)	203.2 x 101.6 x 9.5 mm I-beam	1829, 2438, 3048, 3658, 3962 mm	cantilever
	152.4 x 76.2 x 9.5 mm I-beam		cantilever
	101.6 x 101.6 x 6.4 mm I-beam		cantilever
	152.4 x 152.4 x 9.5 mm I-beam		cantilever
Correia et al. (2011)	200 x 100 x10 mm I-beam	2000, 3000, and 4000 mm	cantilever
Nguyen et al. (2014)	120 x 60 x 6 mm I-beam	4064, 3454, 2844, 2438 and 1828 mm	3-point
	120 x 50 x 6 mm C-beam		
	100 x 50 x 6 mm C-beam		
	100 x 30 x 6 mm C-beam		

Dimensions shown are d x b x t for I-beams and d x t for Rectangle-beams; for pGFRP it is typical that $t_f = t_w$.

2.3 INTERACTIVE BUCKLING

Flange and web local buckling may occur when global lateral torsional buckling of pGFRP I-beam starts, resulting in the interaction between FLB, WLB and LTB. Such interaction between buckling modes is referred to as the interactive buckling (Kabir and Sherbourne 1998) or distortional buckling (Barbero and Raftoyiannis 1994) of pGFRP I-sections. In this work, the term interactive buckling is adopted.

2.3.1 Interactive Buckling of pGFRP

Barbero and Raftoyiannis (1994) developed a numerical model to predict the critical interactive buckling load of pGFRP I-beams. The energy method for beam and plate bending proposed by Roberts and Jhita (1983) for isotropic material was used and applied to orthotropic material. In this study, a nonlinear shape function for the web was proposed to account for web buckling occurring in interactive buckling. Additionally, various loading conditions were considered. It was found that: for pGFRP I-beams having high depth-width ratios, LTB was the dominant buckling model; and for those beams having low depth-width ratios, interaction between local and global buckling could occur, resulting in reduced critical buckling loads.

Davalos and Qiao (1997) proposed a numerical method for calculating the critical interactive buckling loads of pGFRP I-beams. In this study, the energy method proposed by Davalos et al. (1997) for LTB was expanded by introducing a fifth order polynomial shape function for the buckled web, accounting for web buckling. The analytical predictions of critical interactive buckling loads were found to have good correlations with the results from FEM model.

Kabir and Sherbourne (1998) conducted an analytical study on the interactive buckling behavior of pGFRP I-beams. In this study, the Rayleigh-Ritz energy method (Bradford and Waters 1988) and plate theory were employed to demonstrate that the linear combination of local and global buckling modes could lead to a significant reduction in the critical failure loads of pGFRP I-beams.

More recently, Insausti et al. (2009) carried out a set of three-point bending tests on pGFRP I-beams to study their lateral buckling behavior. The interaction between local and global buckling modes was observed in the tests and a new equation that accounts for interactive

buckling was proposed. Comparison was also made between the experimentally-determined critical buckling moments and the analytical solutions. A good agreement was found only for those beams having relatively low lateral slenderness. For those beams having high lateral slenderness, critical global LTB loads obtained using the energy method or FEM programs were found to correlate best with experimental results. For those beams with intermediate lateral slenderness, however, there was a lack of research studying the transition from the FLB to the LTB modes, namely the interactive buckling mode.

Once again informing this work is the previous work on axial buckling behavior presented by Cardoso (2014). It was recognized that interaction between local and global buckling modes occurs in 'intermediate' length columns (Barbero and Tomblin 1994; Lane and Mottram 2002) comprised of 'intermediate' or 'slender' plates (Cardoso 2014). It is proposed that this interaction is analogous to that of FLB, WLB and LTB in flexural members and that some of the same approaches to analysis may be adopted (Cardoso et al. 2014a).

2.4 DETERMINATIONS OF BUCKLING LOADS FOR PGFRP I-SECTIONS

Commonly accepted code-like equations for determining the critical buckling loads of pGFRP I-sections are presented in this section, including FLB and LTB. Interactive buckling, however, is not presented due to the lack of accepted design equations.

2.4.1 Determinations of FLB

The following sections summarize current broadly accepted code-like recommendations for determining flange local buckling (FLB) capacity of pGFRP I-sections. In general, the design equation for critical moment to cause FLB takes the form:

$$M_{cr} = f_{cr} S \tag{2.9}$$

Where S is the elastic section modulus about the strong-axis of the member[2], and the critical stress for flange local buckling, f_{cr}, is determined as described in the following sections.

2.4.1.1 ASCE (1984)

To predict the critical buckling stress in the outstand flange of an I-section, two conditions are considered in ASCE (1984): 1) the flange-web connection is simply-supported or 2) the flange-web connection is fixed. In either case, the outside flange is free. Accordingly, two sets of equations are promulgated. For a simply-supported flange-web connection, the critical stress for FLB is calculated as:

$$f_{cr} = \frac{\pi^2}{(b/2)^2 t_f}\left[D_{11}^f \left(\frac{b}{2a}\right)^2 + \frac{12}{\pi^2} D_{66}^f\right] \tag{2.10}$$

In which a is the length of the flange element considered (i.e., length between brace points) and $b/2$ is the outstand width of the flange. For a long plate having a large $2a/b$ ratio, the term $(b/2a)^2$ in Eq. 2.10 can be neglected and the critical buckling stress is conservatively obtained as:

$$f_{cr} = G_{LT}^f \left(\frac{2t_f}{b}\right)^2 \tag{2.11}$$

The formulation given in Eq. 2.11 is also promulgated in ASCE (2012 and 2014). For a fixed flange-web connection, the critical stress for FLB is calculated as:

[2] for an I-section, $S = [[b(d^3 - (d - 2t_f)^3]/6d] + t_w(d - 2t_f)/3$

$$f_{cr} = \frac{\pi^2}{(b/2)^2 t_f}\left[0.935\sqrt{D_{11}^f D_{12}^f} - 0.656 D_{12}^f + 2.082 D_{66}^f\right] \tag{2.12}$$

2.4.1.2 ASCE (2010)

According to ASCE (2010), the critical buckling stress for FLB in an I-section subject to strong-axis flexure is given as:

$$f_{cr} = \frac{4t_f^2}{b^2}\left(\frac{7}{12}\sqrt{\frac{E_L^f E_T^f}{1+4.1\xi}} + \min\{G_{LT}^w, G_{LT}^f\}\right) \tag{2.13}$$

where

$$\xi = \frac{E_T^f {t_f}^3}{b k_r 6} \tag{2.14}$$

and

$$k_r = \frac{E_T^w t_w^3}{6d}\left\{1 - \left[\left(\frac{48 t_f^2 d^2 E_L^w}{11.1\pi^2 t_w^2 b^2 E_L^f}\right)\left(\frac{\min\{G_{LT}^w, G_{LT}^f\}}{1.25\sqrt{E_L^w E_T^w} + E_T^w \nu_{LT} + 2\min\{G_{LT}^w, G_{LT}^f\}}\right)\right]\right\} \tag{2.15}$$

2.4.1.3 EUR 27666 (2016)

In the recently published EUR 27666 (2016) calculation of critical buckling stress for FLB, the flange-web connection is simulated as being elastically restrained. That is, the flange is constrained by the web and the web rotational stiffness is defined as:

$$k_{EUR} = \frac{D_{22}^w}{(d - t_f)}\left[1 - \frac{t_f f_{cr,f}^{ss}\dfrac{1}{E_L^f t_f}}{t_w f_{cr,w}^{ss}\dfrac{1}{E_L^w t_w}}\right] \tag{2.16}$$

Where $f_{cr,f}^{ss}$ and $f_{cr,w}^{ss}$ are the critical buckling stresses of flange (FLB) and web (WLB), respectively, when the flange-web connection is simulated as being simply-supported (superscript, *ss*). In EUR 27666, $f_{cr,f}^{ss}$ can be conservatively estimated as:

$$f_{cr,f}^{ss} = \frac{12D_{66}}{t_f\left(\frac{b}{2}\right)^2} \tag{2.17}$$

Eq. 2.17 is the same as Eq. 2.11.

$$f_{cr,w}^{ss} = \frac{\pi^2}{t_w(d-t_f)}\left[2\sqrt{D_{11}^w D_{22}^w} + 2(D_{12}^w + 2D_{66}^w)\right] \tag{2.18}$$

Using elastic flange-web restraint, the critical buckling stress of FLB is calculated as:

For K ≤ 1 (K is determined in Eq. 2.21):

$$f_{cr} = \frac{\sqrt{D_{11}^f D_{22}^f}}{t_f\left(\frac{b}{2}\right)^2}\left\{K\left[15.1\eta\sqrt{1-\rho} + 6(1-\rho)(1-\eta)\right] + \frac{7(1-K)}{\sqrt{1+4.12\zeta}}\right\} \tag{2.19}$$

For K > 1:

$$f_{cr} = \frac{\sqrt{D_{11}^f D_{22}^f}}{t_f\left(\frac{b}{2}\right)^2}\left[15.1\eta\sqrt{1-\rho} + 6(1-\rho)(K-\eta)\right] \tag{2.20}$$

Where *K*, ζ, ρ and η are determined as follows:

$$K = \frac{2D_{66}^f + D_{12}^f}{\sqrt{D_{11}^f D_{22}^f}} \tag{2.21}$$

$$\zeta = \frac{D_{22}^f}{k_{EUR}\left(\frac{b}{2}\right)} \tag{2.22}$$

$$\rho = \frac{D_{12}^f}{2D_{66}^f + D_{12}^f} \tag{2.23}$$

$$\eta = \frac{1}{\sqrt{1 + (7.22 - 3.55\rho)\zeta}} \tag{2.24}$$

EUR 27666 (2016) also provides a simple estimation for critical FLB stress:

$$f_{cr} = 4G_{LT}^{f}\left(\frac{t_f}{b}\right)^2 \tag{2.25}$$

Eq. 2.25 is the same with Eq. 2.11 in ASCE (1984). Additionally, to calculate the critical FLB moment, an additional reduction factor, χ, is introduced to account for the interaction between local and global buckling behaviors.

2.4.1.4 Other Predictions of FLB

The discrete plate method is often used to analytically determine the critical stress for FLB for an I-section. Using this method, the I-section is divided into five plates: four flange plates and one web plate. Each plate is restrained by the adjacent plates. Therefore, FLB can be studied by focusing on one outstanding flange plate and plate theory can be employed. Timoshenko and Gere (1961) derived the governing equation for an isotropic plate subject to uniform compressive stress:

$$\frac{\partial^4 w}{\partial L^4} + 2\frac{\partial^4 w}{\partial L^2 \partial T^2} + \frac{\partial^4 w}{\partial T^4} = \frac{t f_x}{D}\frac{\partial^2 w}{\partial L^2} \tag{2.26}$$

Where L and T are the longitudinal and transverse axes of the plate (Figure 1.6); $w(L,T)$ is the deflection shape function; D is the flexural stiffness of the isotropic plate; t is the plate thickness; and f_x is the uniform compressive stress in the longitudinal direction of the plate. The flange-web connection is simulated as an elastic restraint. Substituting the general form of the shape function, $w(L,T)$, into the boundary conditions at the free (outer) edge and flange-web connection, two transcendental equations are obtained. The critical stress for FLB can be obtained by numerically solving these. Timoshenko and Gere obtained the critical stress, f_{cr}, in the form of:

$$f_{cr} = k_{cr} \frac{\pi^2 D}{(b/2)^2 t} \tag{2.27}$$

Where k_{cr} is the buckling coefficient, which is dependent on the aspect ratio of the plate.

Leissa (1985) derived the governing equation for FLB for an orthotropic plate:

$$D_{11} \frac{\partial^4 w}{\partial L^4} + 2(D_{12} + 2D_{66}) \frac{\partial^4 w}{\partial L^2 \partial T^2} + D_{22} \frac{\partial^4 w}{\partial T^4} = t f_x \frac{\partial^2 w}{\partial L^2} \tag{2.28}$$

Where D_{11}, D_{22}, D_{12} and D_{66} are the flexural stiffness parameters for an orthotropic plate, which are given in Appendix B. Similarly, substituting the general form of the shape function, *w(L,T)*, into Eq. 2.28, a transcendental equation is obtained. Solving this transcendental equation will yield the analytical approximation for critical buckling stress, although an explicit solution may not be achieved.

2.4.2 Determinations of LTB

The following sections summarize current broadly accepted code-like recommendations for determining lateral torsional buckling (LTB) capacity of pGFRP I-sections. In general, the design equations calculate the critical moment for LTB directly. This, of course can be related back to a critical flange stress using Eq. 2.9.

2.4.2.1 ASCE (1984)

Despite pGFRP being highly orthotropic, ASCE (1984) calculates the nominal moment capacity to cause LTB based on the conventional formulation for an isotropic material that was promulgated by the AISC steel design code of the day. That is:

$$M_n = C_b \sqrt{M_{xc}^2 + \frac{d^2}{4} P_{e2}^2} \tag{2.29}$$

Where C_b is the moment modification factor, accounting for moment gradient along the member, calculated as:

$$C_b = 1.75 + 1.05\left(\frac{M_1}{M_2}\right) + 0.3\left(\frac{M_1}{M_2}\right)^2 \leq 2.3 \tag{2.30}$$

In Eq. 2.29, M_{xc} is given by:

$$M_{xc} = \frac{\pi}{KL_b}\sqrt{EI_2 J} \tag{2.31}$$

and P_{e2} is the weak-axis Euler buckling load for the member:

$$P_{e2} = \frac{\pi^2 E I_2}{(KL_b)^2} \tag{2.32}$$

In Eqs 2.31 and 2.32, KL_b is the weak-axis effective unbraced length for column buckling and I_2 is the weak-axis moment of inertia. Additionally, E and G are modulus of elasticity and shear modulus of an isotropic material. In approximations for orthotropic GFRP material, E and G are taken as E_{LT} and G_{LT}.

2.4.2.2 ASCE (2010)

According to ASCE (2010), the nominal LTB moment of an orthotropic I-beam subject to strong-axis bending is:

$$M_n = C_b\sqrt{\frac{\pi^2 E_L^f I_2 J}{L_b^2} + \frac{\pi^4\left(E_L^f\right)^2 I_2 C_w}{L_b^4}} \tag{2.33}$$

In which all parameters are the same as those defined in Section 2.4.2.1 except the moment modification factor accounting for moment gradient along the member, C_b, is calculated as:

$$C_b = \frac{12.5M_{max}}{2.5M_{max} + 3M_A + 4M_B + 3M_C} \tag{2.34}$$

C_b in Eq. 2.34 is very close to that in Eq. 2.30 and is consistent with the form of equation used in contemporary design codes. J and C_w are the torsional moment of inertia and warping constant calculated for the cross section, respectively.

The nominal LTB moment determined by Eq. 2.33 is derived based on the loading condition of the pure bending (and adjusted by C_b to account for moment gradient) and the load is applied at the shear center of the I-beam. The effect due to vertical loading position, such as top flange or bottom flange, is not considered by ASCE (2010).

2.4.2.3 EUR 27666 (2016)

According to EUR 27666 (2016), the critical LTB moments of a doubly symmetric I-beam subject to uniform and variable bending can be determined using Eq. 2.35 and 2.36, respectively.

$$M_n = \frac{\eta_c}{\gamma_M}\frac{\pi^2}{L_b^2}E_L I_2\sqrt{\frac{C_w}{I_2}\left(1+\frac{G_{LT}}{E_L}\frac{J}{C_w}\frac{L_b^2}{\pi^2}\right)} \tag{2.35}$$

$$M_n = \frac{\eta_c}{\gamma_M}\frac{C_1}{k}\frac{\pi^2}{L_b^2}E_L I_2\left[-C_2 a+\sqrt{\left(\frac{C_2 a}{k}\right)^2+\frac{C_w}{I_2}\left(\frac{1}{k^2}+\frac{G_{LT}}{E_L}\frac{J}{C_w}\frac{L_b^2}{\pi^2}\right)}\right] \tag{2.36}$$

Where η_c is the conversion factor and γ_M is the partial factor, together accounting for the uncertainties in the behaviors of the material. C_1, C_2, and k are the restraint and load coefficients, tabulated for typical cases in Table 13.1 of EUR 27666 (2016). a accounts for the vertical loading position with respect to the centroid of the I-beam. Various loading conditions and the vertical loading position are considered in EUR 27666 (2016).

2.4.2.4 Other Predictions of LTB

In an I-beam exhibiting lateral torsional buckling behavior, any section of this beam simultaneously sustains strong-axis bending, weak-axis bending and twisting of the entire section. Accordingly, Timoshenko and Gere (1961) proposed the governing equations for LTB for an isotropic material:

$$EI_{\xi}\frac{d^2v}{dz^2} = M_{\xi} \tag{2.37}$$

$$EI_{\eta}\frac{d^2u}{dz^2} = M_{\eta} \tag{2.38}$$

$$GJ\frac{d\phi}{dz} - EC_w\frac{d^3\phi}{dz^3} = M_{\zeta} \tag{2.39}$$

Where M_{ξ}, M_{η} and M_{ζ} are the strong-axis bending moment, weak-axis bending moment and twisting moment, respectively, in the local coordinate system, which can be determined based on the loading condition; u and v are the displacements along x and y axes in the global coordinate system; EI_{ξ} and EI_{η} are the bending stiffness about strong- and weak-axis, respectively; ϕ is the rotational angle of the cross section; GJ is the torsional stiffness; and EC_w is the warping stiffness. The local and global coordinate systems are shown in Figure 2.3.

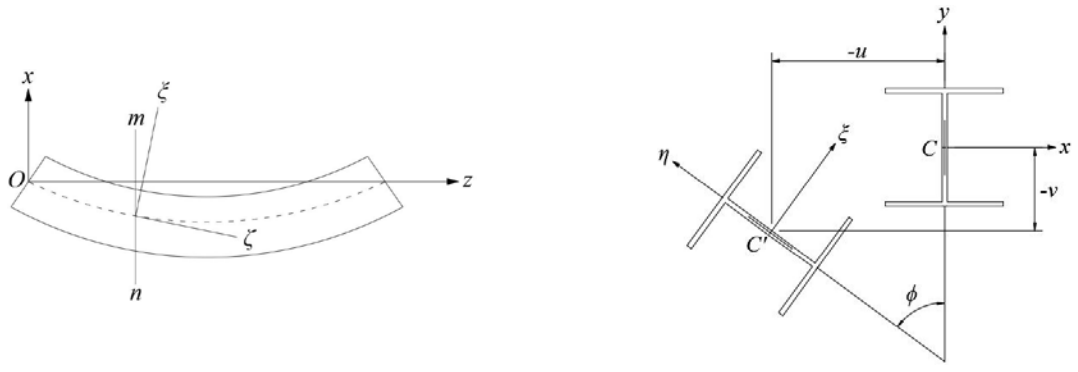

a) Plan view **b) Cross section view**

Figure 2.3 Local and global coordinate systems for LTB of an I-section (Timoshenko and Gere 1961)

Combining Eq. 2.37 – 39, a fourth order differential equation can be obtained. By solving this equation, the critical LTB moment can be numerically determined, although an explicit solution may not be obtained. In a special case of I-beam sustaining pure moment, an explicit solution to LTB is given by Timoshenko and Gere (1961):

$$M_{cr} = \frac{\pi}{L_b}\sqrt{EI_\eta GJ + \left(\frac{\pi E}{L_b}\right)^2 I_\eta C_w} \tag{2.40}$$

Eq. 2.40 is the same with Eq. 2.33, if E is replaced by E_L for an orthotropic material.

3.0 MATERIAL AND GEOMETRIC CHARACTERIZATIONS

3.1 INTRODUCTION TO PULTRUDED GFRP MATERIALS

Fiber Reinforced Polymer (FRP) composites consist of two primary constituents: 1) high strength fiber, which contributes to the principal strength and stiffness along the direction(s) in which they are aligned; and 2) a polymer matrix, which transfers loads between fibers as well as providing environmental and physical protection to fibers (Hyer 2009). Other commonly used constituents, acting as additives, are fillers, catalysts, pigments, coatings, and coupling agents, which are used for formulating and coloring the matrix resin, and improving the bond between fiber and matrix (Mallick 2008; Creative 2015b). Combining all constituents together, FRP composites are able to achieve mechanical and chemical properties superior to those of any constituent alone (Mallick 2008; Barbero 2011).

In the manufacturing of FRP composites, widely used fibers include glass, carbon, and aramid fibers. Among these fibers, glass fibers are the most commonly used because of their low cost, high tensile strength, and high corrosion resistance (Swanson 1997; Mallick 2008; Barbero 2011). Five types of glass fibers are available: types A, C, D, E, and S. In particular, A, C, and D-glass are used in applications where specific alkaline resistance, corrosion resistance, or a low dielectric constant is required, respectively. E and S-glass, from the perspective of their structural behaviors, are preferred in the construction industry (Hyer 2009; Barbero 2011). S-glass exhibits higher strength and modulus than E-glass, and is therefore used where higher structural

performance is required. However, due to the lower material cost, E-glass is typically used in most construction industry composite applications (Barbero 2011).

Carbon fibers possess much higher strength and stiffness, and lower weight, compared with glass fibers. However, due to the high material cost, their applications are typically limited to the aerospace and sporting industries where exceptionally high strength-to-weight ratio is a critical design consideration (Mallick 2008; Barbero 2011). Aramid fibers, having the highest strength-to-weight ratio of all types of fibers, have a relatively low modulus, limiting their use in construction applications (Mallick 2008). Typical properties of these three types of fibers are presented in Table 3.1.

Table 3.1 Typical properties of glass, carbon, and aramid fibers (Barbero 2011)

Fibers	Modulus (GPa)	Tensile strength (GPa)	Elongation (%)	Poisson's ratio	Density (g/cm^3)
E-glass	72	3.45	4.4	0.22	2.55
Carbon (T300)	230	3.53	1.5	0.20	1.75
Aramid (Kevlar 49)	131	3.62	2.8	0.35	1.45

In FRP composites, two categories of polymeric resins are generally used as the matrix: 1) thermosets, which are cured by irreversible chemical reaction; and 2) thermoplastics, which are formed by heating. Although thermoplastics permit repeated heating and reforming, making the material repairable, thermosets are more common in commercial applications due to their low viscosity, ease of processing, and low cost (Swanson 1997). Thermosetting matrix resins contribute little to the tensile strength of FRP composites. Nevertheless, the compressive and in-plane shear strengths of composites are primarily functions of the mechanical properties of matrix resins (Mallick 2008). Therefore, an appropriate selection of thermosetting matrix

material is needed in the practical design process particularly where specific transverse performance is required. The most widely used thermosetting resins are epoxy, unsaturated polyester, and vinyl ester (Hull and Clyne 1996).

Epoxy is versatile and has low shrinkage, excellent corrosion resistance, and high structural performance (Mallick 2008; Barbero 2011). The material cost of epoxy, however, is greater than other resins (Swanson 1997). Additionally, to cure epoxy resin, a relatively long time is needed when compared with polyester and vinyl ester resins (Mallick 2008). Therefore, epoxy is mainly utilized in the aerospace industry (Barbero 2011). Polyester is commonly used because of its high performance-to-cost ratio, short cure time, and low viscosity. Although the mechanical properties of polyester are found to be poorer than those of epoxy, polyester is more widely used in many applications due to its low cost. Additionally, UV resistance can be achieved through UV inhibitors in polyester resins to enable their outdoor applications. Fire resistance can also be improved to some extent by adding fire retardant additives (Mallick 2008; Barbero 2011; Creative 2015b). Vinyl ester has structural performance and cost that fall between epoxy and polyester. In particular, the corrosion resistance and tensile strength of vinyl ester are closer to those of epoxy, while the cure time, viscosity, and shrinkage are closer to those of polyester (Mallick 2008; Barbero 2011). Typical properties of these three types of resins are presented in Table 3.2.

Table 3.2 Typical properties of polyester, vinyl ester, and epoxy resins (Barbero 2011)

Matrix resins	Tensile modulus (MPa)	Tensile strength (MPa)	Compressive strength (MPa)	Tensile elongation (%)
Polyester (isophthalic)	3400	75.9	117.2	3.3
Vinyl ester	3400	82.7	117.1	5.5
Epoxy (8551-7)	4089	99.2	-	4.4

The applications of FRP composites are typically related to the matrix properties, as the change in environmental moisture and operating temperature may have adverse effects on mechanical properties of the matrix, thus influencing the performance of FRP composite (Hyer 2009). For instance, the strength and modulus of polymeric resins will decrease, as operating temperature increases. To improve the performance of resins at elevated temperature, a higher glass transition temperature needs to be achieved and consequently a matrix resin with lower strength and modulus is obtained. That is, a compromise between temperature application and structural performance needs to be made (Barbero 2011).

In this work, the glass fiber reinforced polymer (GFRP) composite made of E-glass fiber reinforcement and polyester matrix is studied. Various manufacturing methods are currently available for GFRP composites. Pultrusion is recognized as a cost-effective method for producing straight profiles with constant cross section of any length (Barbero 2011). In pultruded glass fiber reinforced polymer (pGFRP) composites, a number of continuous glass fibers form a strand. Then, a bundle of parallel strands is twisted together forming a continuous roving (Mallick 2008). Between rovings, continuous strand mats (CSM), which are made of layers of randomly oriented fibers, are used to improve the transverse properties of pGFRP composites. At the outer surfaces, veils (essentially higher quality CSM) are used to improve the appearance and handling, and provide an additional layer of environmental protection to pGFRP composites (Creative 2015b). Thin-plate cross sections may have a single layer of roving in the middle with CSM and a surface veil on both sides, while thicker sections will have multiple rovings, each separated by CSM (Figure 3.1). The layup of the pGFRP is referred to as its ‘architecture’. Fiber architecture has little effect on tensile properties but can significantly affect flexural and

transverse properties as the rovings are located away from the neutral axis of the plate and additional CSM layers are provided.

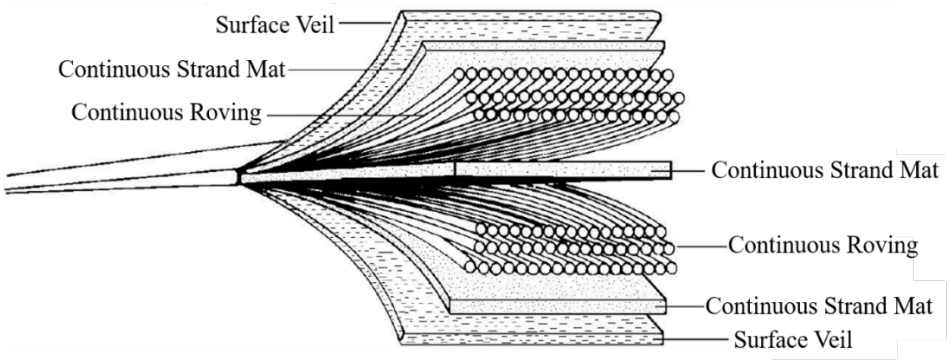

Figure 3.1 Constitution of pultruded profiles showing a two-layer architecture (Creative 2015b)

3.2 THEORETICAL MATERIAL CHARACTERIZATION

To characterize the mechanical properties of pGFRP composites, theoretical predictions based on micromechanics can be used prior to the experimental material tests (Swanson 1997). Using micromechanics, heterogeneous pGFRP composites can be modeled as orthotropic homogeneous materials in which fiber and matrix constituents are described using fiber and matrix volume fractions, respectively. To determine the fiber and matrix volume fractions, two standard test methods are available: ASTM D2584 and ASTM D3171; these are selected based on the matrix type. In both tests, the matrix resin, is removed (by ignition or acid solution, respectively), leaving only the fiber content from which the fiber volume of the original sample is calculated.

Using analytical methods and determined fiber and matrix volumes, theoretical predictions of pGFRP plate axial stiffness may be reliably determined; however, strength predictions are often found to be unreliable due to the back-calculations involved. Various

models are proposed to predict the stiffness of pGFRP composites, including: 1) the simple rule-of-mixtures model; and 2) more complex models, constructed based on the theory of elasticity (Swanson 1997; Cardoso 2014). To determine the strength of pGFRP composites, experimental tests are typically necessary (Barbero 2011).

The rule-of-mixtures approach, using parallel and series models, can be used to predict longitudinal modulus and major Poisson's ratio, and transverse modulus and in-plane shear modulus, respectively. Using this approach, both fiber and matrix are assumed to be linearly elastic isotropic materials (Swanson 1997).

In the rule-of-mixtures parallel model, fiber and matrix are assumed to sustain the same strain under tension (i.e., plane strain). The longitudinal modulus, E_L, and major Poisson's ratio, ν_{LT}, of the pGFRP composite can be derived using constitutive properties of the component materials:

$$E_L = E_f V_f + E_m V_m \tag{3.1}$$

$$\nu_{LT} = \nu_f V_f + \nu_m V_m \tag{3.2}$$

Where, E_f and E_m are the longitudinal modulus of fiber and matrix, respectively; V_f and V_m are the fiber and matrix volume fractions; and ν_f and ν_m are the major Poisson's ratios of fiber and matrix, respectively.

Transverse modulus and in-plane shear modulus can be predicted using a series model and the rule-of-mixtures. In this method, fiber and matrix are assumed to behave in series, carrying the same stress. Again, constitutive properties are used to calculate the transverse modulus, E_T, and in-plane shear modulus, G_{LT}:

$$E_T = \frac{E_f E_m}{V_f E_m + V_m E_f} \tag{3.3}$$

$$G_{LT} = \frac{G_f G_m}{V_f G_m + V_m G_f} \tag{3.4}$$

Where, G_f and G_m are the in-plane shear modulus of fiber and matrix (Swanson 1997).

Since glass fiber is not, in fact, an isotropic material, an improvement for E_L and E_T can be made, if the E_f terms in Eqs 3.1 and 3.3 is replaced by the longitudinal modulus, E_{Lf}, and transverse modulus, E_{Tb}, respectively.

For typical pGFRP materials, using simple rule-of-mixtures models, only longitudinal modulus and major Poisson's ratio can be obtained with acceptable accuracy. The transverse and in-plane shear modulus cannot be accurately determined. Additionally, necessary constitutive properties of the fiber, including transverse modulus, E_{Tb}, major Poisson's ratio, v_f, and in-plane shear modulus, G_f, may not be available. Consequently, using simple models, errors may be introduced when these data are required (Mallick 2008).

To overcome the limitations of rule-of-mixture models and obtain reliable results of mechanical properties of pGFRP composites, an elasticity model can be applied. However, complex numerical analysis is required, impeding its practical application (Cardoso 2014). In this situation, semi-empirical formulas can be used, such as those proposed by Cardoso (2014). Specifically, Cardoso used linear regression based on experimental data to derive the formulas for stiffness of pGFRP composites. This empirical approach was found to be quite accurate for pGFRP materials having similar materials and architecture (from the same manufacturer) but must be applied with caution when varying materials.

3.3 EXPERIMENTAL MATERIAL CHARACTERIZATION

In this work, the pGFRP I-section profiles used in the experimental programs are manufactured by Bedford Reinforced Plastics, located in Bedford PA, USA. The E-glass reinforced sections are made with polyester resin with fire retardant additive. The nominal geometries of all I-sections are 152.4 x 152.4 x 6.35 mm (*d* x *b* x *t*) [native dimensions are 6 x 6 x ¼ inch]. As is typical in many pultruded sections, flange thickness is equal to web thickness. In each of the flange and web elements, three layers of continuous roving are used to provide principal strength and stiffness in the longitudinal direction; four layers of continuous strand mats, separating the longitudinal rovings, enhance the transverse properties; finally, two surface veils improve the appearance and handling, as well as provide additional environmental protection for the pGFRP profiles. The fiber volume fraction is 35-39%, and the matrix volume fraction is 61%-65% (personal correspondence with pultruder).

To evaluate the mechanical properties of the pGFRP profiles considered in this work, a series of material coupon tests are conducted. The test methods include both standard tests specified by ASTM, and non-standard tests that are proposed by researchers. In all tests requiring electrical resistance strain gages, 120 ohm gages produced by Micro-Measurements were used. All strain gages had a gage area of 6.35 x 3.05 mm (length x width), sufficiently large to mitigate any local effects of individual fibers in the surface veils. The following sections report the methods used to obtain different material properties.

3.3.1 Longitudinal and Transverse Tensile Strength and Modulus of Elasticity

The tensile properties of the pGFRP material in the longitudinal and transverse directions are usually considered to be fundamental measures of behavior (Adams et al. 2003) and are those

most commonly (and consistently) reported by manufacturers. A number of experimental studies are conducted to investigate the longitudinal and transverse tensile properties of pGFRP material, including strength and modulus of elasticity. Wang and Zureick (1994) conducted a series of longitudinal tensile tests on pGFRP material to study its tensile behavior. In this test, two types of rectangular strips were cut from pGFRP I-sections and were tested without end tabs. The pGFRP material was identified to behave linearly to failure. Additionally, through analysis of the test results, the use of a tensile coupon without end tabs is suggested, since this simple specimen configuration was shown to achieve satisfactory accuracy. Later, Sonti and Barbero (1996) conducted 34 longitudinal and 15 transverse tensile tests on pGFRP coupons cut from pultruded I-sections made with vinylester resin. Four specimen geometries were used with respect to the sampling locations (flange and web) and fiber orientation (longitudinal and transverse) (see Figure 1.6). Differing from Wang and Zureick (1994), aluminum end tabs were used to prevent material from being damaged by machine grips. In this study, a good agreement was found between experimental and analytical results. In addition, Zureick and Scott (1997), and Kang (2001), following the method proposed by Wang and Zureick (1994), conducted tensile coupon tests to obtain the longitudinal strength and modulus of elasticity of pGFRP material. The test procedures of both groups were determined in accordance with ASTM D3039, and end tabs were not used.

Two standard tensile tests are commonly used: ASTM D3039 and ASTM D638. In both standards, gripping is used to transfer the load to specimen through friction. Straight-sided specimens measuring 250 mm x 15 mm are specified in ASTM D3039, while dog-bone shaped specimens are required in ASTM D638. ASTM D638 specimen dimensions are a function of the material thickness but for pGFRP the overall dimensions will typically be 165 x 19 mm

(thickness less than 7 mm) or 246 x 29 mm (thickness up to 14 mm). Due to the simplicity of the specimen preparation, ASTM D3039 is more widely used by researchers (Cardoso et al. 2014b) although this method was not specifically developed for pGFRP, but rather for layed-up laminates.

In the research literature, only Sonti and Barbero (1996) report “standard” tests of transverse tensile properties. Except for large shapes, it is typically not possible to obtain standard ASTM D3039 or D638 coupons from typical pultruded shapes; the coupon length requirement is too long. The gripping and clear span requirements make obtaining transverse tension properties from pultruded shapes having flange outstands or webs shorter than 250 mm ‘nonstandard’. As was done in this study, smaller-than-standard specimens are sometimes used. From a practical perspective, however, outstand lengths or web heights less than about 75 mm are too small to practically obtain transverse tension and modulus data. Very often, flanges are assumed to have the same transverse properties as webs.

In this work, tension tests were conducted according to ASTM D3039. Ten longitudinal (5 from web and 5 from flange) and 5 transverse (all from web) rectangular coupons are cut from a randomly selected sample beam to investigate the longitudinal and transverse tensile strength and modulus of elasticity of the pGFRP beams used in this study. The geometry of the longitudinal coupon, 250 x 15 x 6.35 mm, is determined in accordance with ASTM D3039. Due to the web height being only 139 mm, the transverse specimens use a nonstandard geometry, 127 x 15 x 6.35 mm. The flange outstands are less than 75 mm, thus no transverse specimen could be extracted. Tests were performed on a servo hydraulic 600 kN capacity universal test machine (Figure 3.2). The load is transferred through a pair of aluminum grips which are demonstrated to provide sufficient lateral pressure to prevent slippage between the coupon and grips without

damaging the coupon as steel grips have been observed to do; the specimens are untabbed. The aluminum grips are, themselves, supported in the UTM's steel hydraulic grips. Additionally, a 'clip-gage' strain extensometer having a gage length of 50.8 mm is used to monitor the strain in the longitudinal tensile test, while an electrical resistance strain gage is used in the transverse test. Loading was applied at a displacement-controlled rate of 0.1 mm/min to ensure a nearly constant strain rate during the test. The cross-head displacement, coupon strain and applied load are recorded. The ultimate tensile strength is calculated as (ASTM D3039):

$$F_L = \frac{P_{max}}{A} \tag{3.5}$$

Where P_{max} is the maximum tensile force and A is the cross-sectional area of the specimen. The tensile modulus of elasticity, E_L, is calculated as the secant modulus between 25% and 50% of the ultimate strain for the longitudinal tests and between strains of 0.001 and 0.003 for transverse tests as (ASTM D3039):

$$E_L = \frac{\Delta\sigma}{\Delta\varepsilon} \tag{3.6}$$

Where, $\Delta\sigma$ and $\Delta\varepsilon$ are the change in calculated stress (Eq. 3.5) and measured strain, respectively.

Figure 3.2 Tensile test set-up

3.3.2 Transverse Flexural Strength and Modulus of Elasticity

Since standard coupons for obtaining transverse tensile properties, particularly for flange elements, are difficult or impossible to obtain from typical pGFRP profiles, an alternative approach is required for investigating the transverse properties of flange elements in pGFRP sections. In this work, a simple non-standard test method proposed by Ganga Rao (personal correspondence) and similar to that adopted by Cardoso et al. (2014b) for box sections is adopted. The test configuration for obtaining modulus of elasticity is shown in Figure 3.3. The top flange of the specimen, cut from a randomly selected pGFRP I-section, is loaded under flexure using known free-weights. A pair of rollers transferred the load to the top flange, while the bottom flange was fully supported. Ideally, the two top flange elements behave as identical cantilevers.

Four strain gages are used to measure the strain change throughout the test. Beam theory is employed to calculate the stress, σ, at the location at which the strain is measured:

$$\sigma = \frac{M}{S_{flange}} = \frac{3Pa}{wt^2} \tag{3.7}$$

Where, S_{flange} is the elastic section modulus of flange and all other dimensions are shown in Figure 3.3. With stress, the stress-strain curve is determined and the modulus of elasticity, E_{Tb}, of the flange in the transverse direction is obtained.

To obtain transverse modulus, free weights are used to ensure utmost precision. To obtain transverse strength, the same geometry is employed in a UTM and the specimen is tested to failure, defined as the maximum load attained. The transverse strength, F_{Tb}, is also determined from Eq. 3.7 but with the length a taken as the distance from the point of application of the load to the face of the web. The determination of F_{Tb} may be affected by crushing or crippling of the web, calculations must be made using specimens not exhibiting such behavior.

The transverse properties, E_{Tb} and F_{Tb}, obtained through this non-standard approach are flexural properties, rather than tensile properties. Nonetheless, in this work, they are adopted as approximations for flange transverse properties.

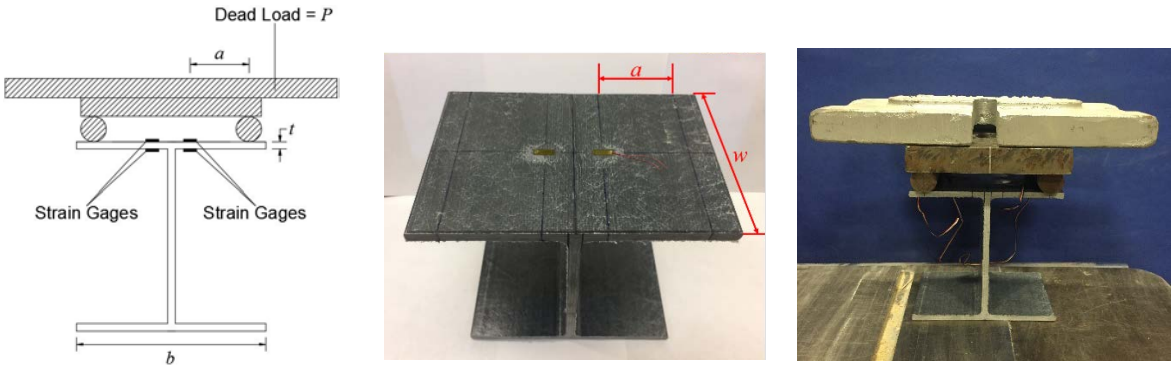

a) Schematic of test set-up **b) Top flange showing strain gages** **c) Test arrangement under load**

Figure 3.3 Non-standard test for transverse flexural modulus of flange

In order to compare the transverse flexural modulus of the flange with that of web, the transverse flexural modulus of web is also obtained by conducting a similar nonstandard test proposed by Cardoso et al. (2014b) shown in Figure 3.4. Specimen geometry is the same as the flange test. However, to maintain the stability of the free-weight, an aluminum bar having rectangular cross-section is used instead of rollers to apply the load. Through the bar, the load is transferred to the flange, producing a constant moment over the height of the web. Two strain gages are installed at the center of both faces of the web to measure the strain. Beam theory is, again, used to calculate the stress, σ, at the location where strain is measured:

$$\sigma = \frac{M}{S_{web}} = \frac{6Pa}{wt^2} \tag{3.8}$$

Where, S_{web} is the elastic section modulus of web and all other dimensions are shown in Figure 3.4. With the stress-strain curve determined, the modulus of elasticity of the web in the transverse direction, E_{Tb}, can be obtained.

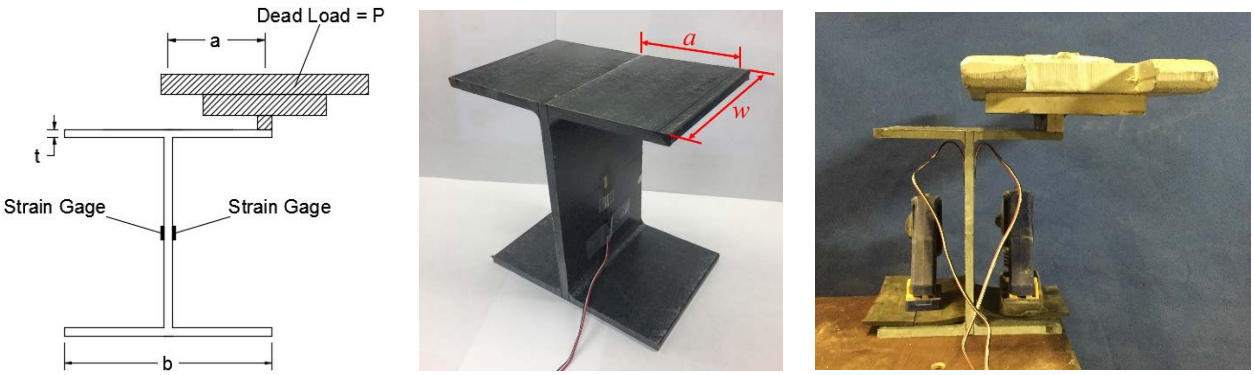

a) Schematic of test set-up **b) Web showing strain gage** **c) Test arrangement under load**

Figure 3.4 Non-standard test for transverse flexural modulus of web

3.3.3 Longitudinal Compressive Strength and Modulus of Elasticity

Four tests are currently available to obtain the compressive properties of pGFRP materials: 1) end loading test (ASTM D695); 2) shear loading test (ASTM D3410); 3) combined loading test (ASTM D6641); and 4) honeycomb core sandwich beam test (ASTM D5467). Regardless of the test type used, failure modes involving load eccentricity, stress concentration, and Euler buckling should be avoided, as these issues could lead to inaccurate compressive response (Adams et al. 2003). Each test has a fundamentally different loading mechanism as shown in Figure 3.5.

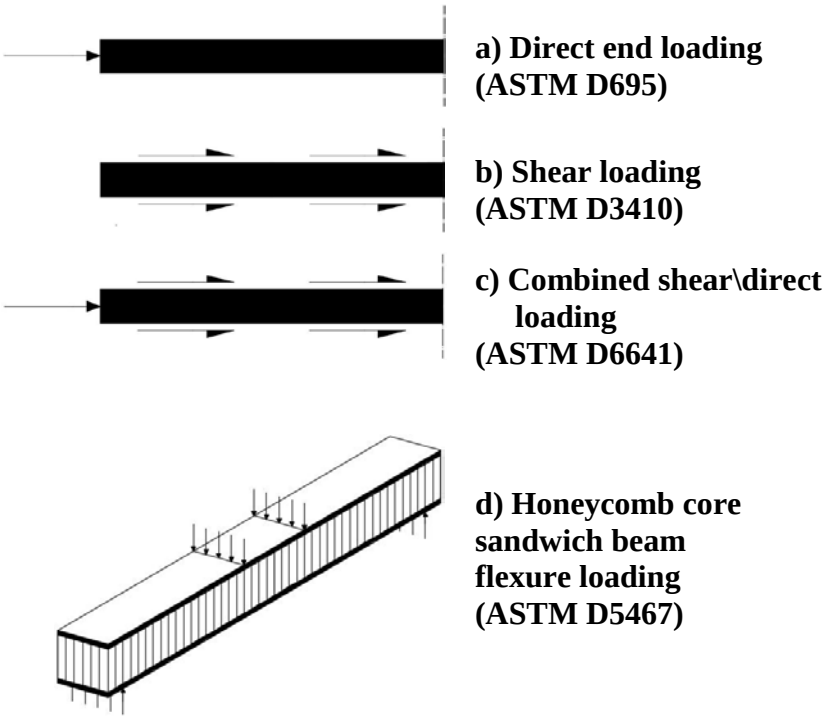

Figure 3.5 Loading mechanisms
(Figures a, b, and c: Hodgkinson 2000; Figure d: Hofer and Rao 1977)

ASTM D695 end loading tests are most appropriate for prism or cylindrical specimens. Plate specimens such as pGFRP materials require the additional use of a lateral support jig.

Applications and modifications to the ASTM D695 standard test method can be found in many studies. In earlier versions of D695 (pre-1996), tabbed specimens were prescribed. Gurdal and Starbuck (1988) modified the method to be used without tabs. This specimen geometry was adopted into D695 in 1996. Barbero et al. (1999) demonstrated compressive tests of pGFRP materials without tabs and a good correlation was found between coupon test and full-section compression tests. Correia et al. (2011) and Cardoso et al. (2014b) carried out end-loaded compressive tests on rectangular coupons according to ASTM D695 but with no lateral support provided. The specimens were sized to mitigate buckling and simply loaded by the flat loading platens of the test machine. In each study, compressive strength and modulus were obtained.

Due to the high orthotropy and local stress concentrations, specimens under direct end loading often fail by end crushing (Hodgkinson 2000; Adams 2002). Consequently, the bearing strength at the specimen end rather than the compressive strength is obtained (Barbero et al. 1999). To avoid end crushing, shear loading, as specified in ASTM D3410, is used. In the test fixture adopted in D3410 (Figure 3.6). Compressive stress is introduced by friction between the specimen and flat wedge grips. Both tabbed and untabbed straight-sided specimen with various thickness are permitted (Adams et al. 2003).

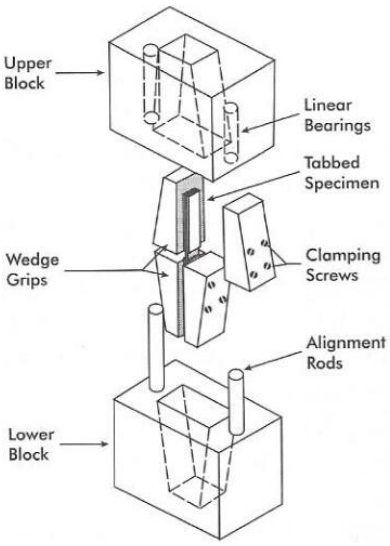

a) Schematic of test set-up (Adams et al. 2003)

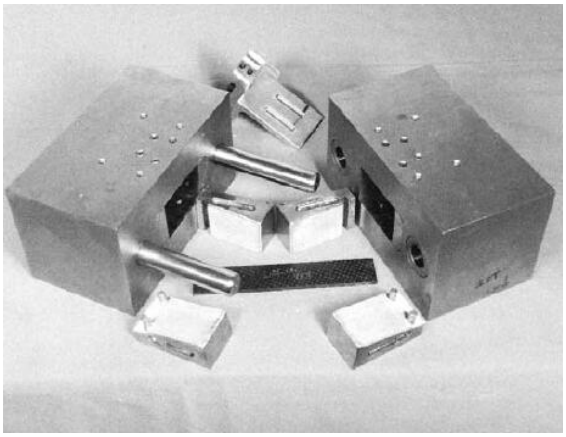

b) Test fixture (ASTM D3410-03)

Figure 3.6 Shear loading test fixture

Tabs, usually bonded at both ends of the specimen, are commonly employed in shear loading tests to improve the uniformity of the stress distribution (Adams 2002). A stress concentration, however, is induced at the end of the tabs (Bogetti et al. 1988). Compliant tab material and shallow chamfer angles are found to decrease this stress concentration (Tan and Knight 1994; Adams and Xie 1995). However, using more compliant tab material, the shear load cannot be adequately transferred to the specimen, and thus, a compromise between shear load transfer and stress concentration needs to be made (Adams 2002).

Numerous experimental studies have been performed to evaluate the effectiveness of the ASTM D3410 test method. Zureick and Scott (1997) conducted 108 pGFRP coupon tests in accordance with ASTM D3410 to obtain the longitudinal compressive modulus of elasticity and strength. The coupon length was determined such that buckling would not occur. End tabs were shown to be unnecessary in preliminary tests. In addition, despite supposedly identical fiber architecture, a difference in compressive properties between flange and web elements was

identified, indicating the fiber reinforcement was not uniformly placed throughout the cross section in the manufacturing process. Zureick and Steffen (2000), Butz (1997) and Kang (2001) have all reported acceptable results using this test method.

Utilizing the features of both the end loading and shear loading tests, the "Wyoming combined loading test" was developed and adopted in ASTM D6641 (Adams and Welsh 1997). The combined loading test fixture is shown in Figure 3.7. Both shear loading (through the friction between specimen and grips) and end loading mechanisms are employed for load transfer. The ratio between shear and end loading can be controlled by adjusting the clamping force in the grips through fixture bolts. Both tabbed and untabbed straight-sided specimens are permitted in this test with the use of tabs determined by the fiber architecture of the specimen (Adams and Welsh 1997).

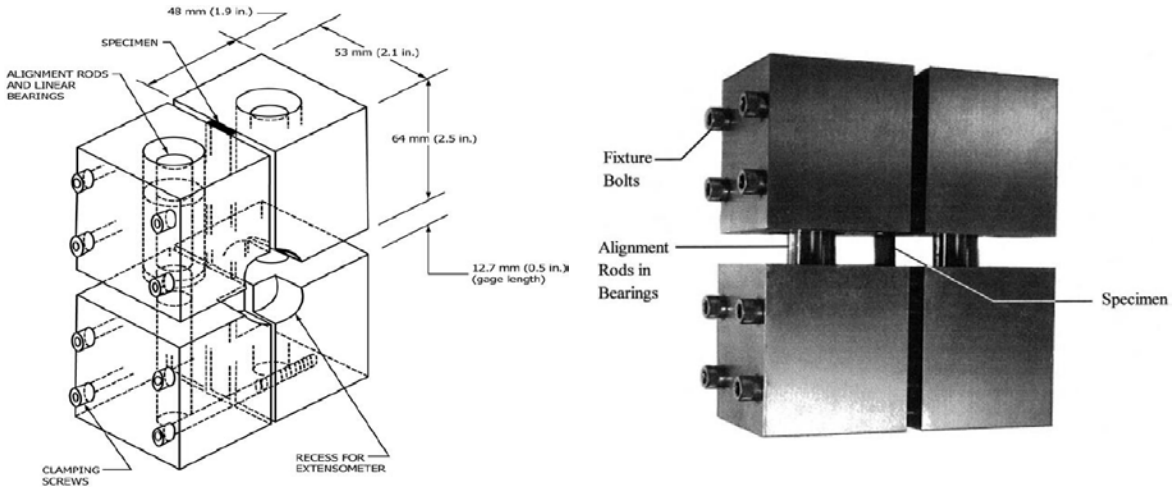

a) Schematic of test set-up **b) Test fixture**

Figure 3.7 Combined loading test fixture (ASTM D6641)

An experimental program was conducted by Adams and Welsh (1997), comparing the three tests in which it was found that the combined loading test provides more consistent results

of compressive strength. Considering the issues of stress concentrations in the shear loading test and end crushing in end loading tests, the combined loading test was considered as the most attractive method for testing straight-sided specimens without end tabs (Adams and Welsh 1997; Adams 2002).

Finally, the honeycomb core sandwich beam test specified in ASTM D5467 can be used to establish the compression behavior of a pGFRP plate. In this test, the GFRP material under investigation is fabricated and installed as the compressive skin on a sandwich panel to be tested in four-point flexure. To ensure that the compression skin fails, aluminum core material and a metallic tension skin are typically used. Using beam theory, the compressive strength and modulus of elasticity can be obtained with a high degree of reliability. However, the sandwich beam test requires specific fabrication of the specimen, resulting in expensive material cost and, while proposed (Hofer and Rao 1977), is not known to have been used to establish compression properties of pCFRP materials. The test is regularly used to establish properties of GFRP sandwich panels.

Due to the relative complexity of the ASTM tests and the availability of the test fixtures required, the use of longer non-standard specimens in an ASTM D695 arrangement demonstrated by Correia et al. (2011) and Cardoso et al. (2014a) was used in the present study to determine the compressive strength and modulus of pGFRP composite. In this test, direct end loading is applied to the 50.8 (tall) x 12.7 x 6.35 mm specimen (Figure 3.8); no lateral support or end tabs are used. Load is applied using displacement control at a rate of 0.1 mm/min to ensure quasi-static loading. Specimen dimensions mitigate buckling although occasionally the specimen will split through its 6.35 mm thickness and buckle (cripple); results from such tests are not included in compression results.

Figure 3.8 Compressive test set-up

3.3.4 In-Plane Shear Modulus of Elasticity

For the determination of shear properties of pGFRP materials, a number of test methods have been proposed and are practiced by many researchers. Standardized and non-standard shear test methods include: 1) Iosipescu shear test (ASTM D5379); 2) ±45° tensile test (ASTM D3518); 3) rail shear test (ASTM D4255); 4) short beam test (ASTM D2344): 5) V-notched rail shear test (ASTM D7078); 6) 10° off-axis test; 7) plate-twist test (ASTM D3044); and 8) thin-walled tube torsion test (Chaterjee et al. 1993; Hodgkinson 2000).

The first four tests, shown in Figure 3.9, have seen numerous theoretical and practical practices in past decades. Of these, the Iosipescu shear test (ASTM 5379) is considered to be the most reliable method, since in this test accurate shear strength and modulus are obtained and a pure shear stress distribution is achieved (Adams and Lewis 1997). It has been observed, however, that results from the Iosipescu test (which uses a relatively small specimen) are affected by local fiber or resin content (Sonti et al. 1995 and Sonti and Barbero 1996) and a

larger test specimen is recommended for pGFRP materials (Scott 1997, Zureick and Scott 1997, Zureick and Steffen 2000, and Kang 2001).

The rail shear test (ASTM D4255) is also capable of generating a pure shear stress as well as determining shear strength and modulus, particularly when a V-notch is introduced into the specimen (ASTM D7078). However, the expensive cost of the test fixture and material preparation makes the wide use of this test method prohibitive (Adams and Lewis 1997; Hodgkinson 2000).

The short beam test (ASTM D2344), using a simple test fixture and specimen preparation, has gained prominence in material screening and quality control, even though a pure shear stress distribution in the specimen is not produced. The shear stress-strain curve cannot be determined, and thus, the use of this test is limited to where the shear modulus is not required (Adams et al. 2003; Adams 2005).

The ±45° tensile test (ASTM D3518) is also popular among researchers due to the simplicity of the test fixture and specimen preparation. In this test method the stress state in specimen is complex and higher shear strength tends to result due to fiber scissoring (Adams 2005; Hodgkinson 2000).

The off-axis test is theoretically similar to the ±45° tensile test. However, compared with ±45° tensile test, more strain gages and transformation of stress and strain are required (Hodgkinson 2000). Additionally, small errors in off-axis angle could lead to inaccurate shear response (Chaterjee et al. 1993). The plate-twist test, adopted from the shear test for plywood (ASTM D3044), is found to yield the shear modulus for pGFRP material, although shear strength cannot be determined through this test (Hodgkinson 2000). The thin-walled tube torsion test is

reported as an ideal test method for investigating the shear strength and modulus of composite material. However, its application is limited to circular profiles (Adams 2005).

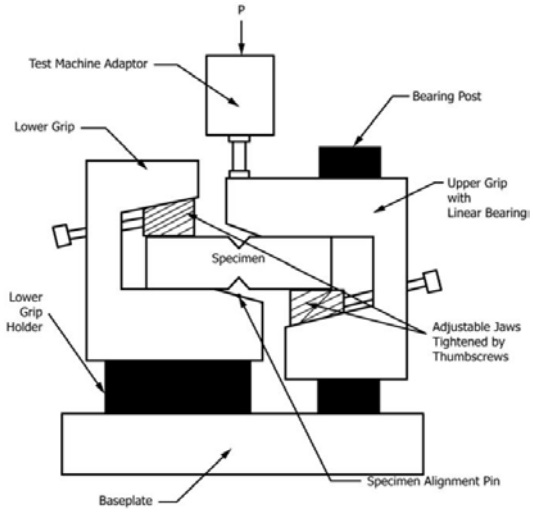

a) Iosipescu shear test (ASTM D5379)

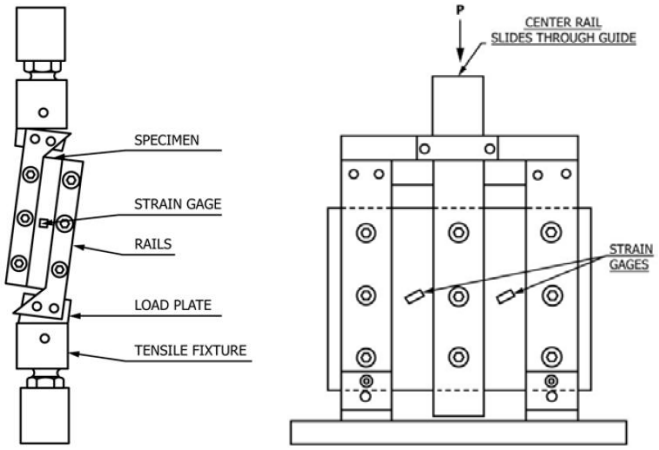

b) Two rail and three rail shear tests (ASTM D4255)

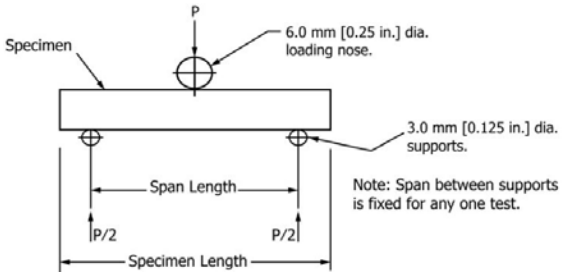

c) Short beam test (ASTM D2344)

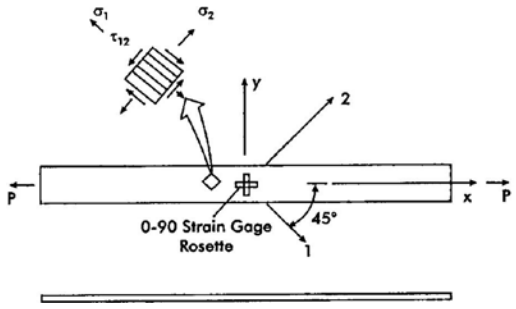

d) ±45° tensile test (Adams et al. 2003)

Figure 3.9 Shear test set-ups

In this work, considering the availability of the test fixture and the required specimen preparation of each test, the ±45° tensile test (ASTM D3518) is used to obtain the shear modulus of pGFRP material. The specimens having nonstandard dimensions of 157 x 15 x 6.35 mm

(length x width x thickness) are obtained from the web of the pGFRP I-section. Shear strength, however, is not investigated, as it is not needed for the purpose of this work.

The test procedure is determined in accordance with ASTM D3518. In the ±45° tensile test, the coupon is cut and loaded along an axis oriented 45° to the fiber direction, resulting in a biaxial stress state of the lamina (σ_1 and σ_2) which further induces a shear stress (τ_{12}) (Figure 3.10). End tabs are not required and specimen size is determined so as to ensure that edge and end effects are negligible (Hodgkinson 2000). Thus, a uniform shear stress distribution is achieved throughout the cross section except for areas near edges (Chaterjee et al. 1993). The induced longitudinal shear stress, τ_{12}, and strain, γ_{12}, are related to the applied tensile stress, σ_x, and the longitudinal and transverse strains, ε_x and ε_y, respectively (Rosen 1972). The equations for calculating shear stress and strain are as follows:

$$\tau_{12} = \sigma_x/2 \tag{3.9}$$

$$\gamma_{12} = \varepsilon_x - \varepsilon_y \tag{3.10}$$

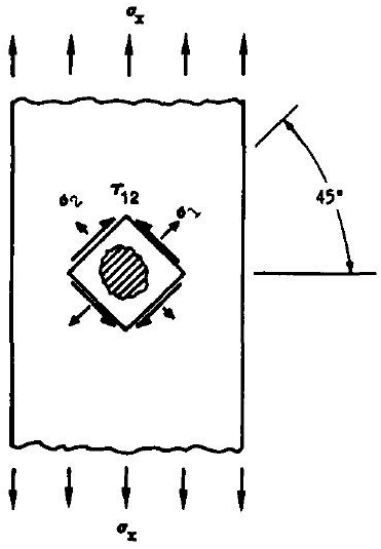

Figure 3.10 ± 45° tensile test specimen (Adam et al. 2003)

With the shear stress and strain determined, the shear stress-strain curve can be plotted, from which shear modulus can be obtained:

$$G = \frac{\sigma_x}{2(\varepsilon_x - \varepsilon_y)} \tag{3.11}$$

Like the direct tension tests, while the ±45° tensile test specimens are smaller, there is a requirement for specimen length that cannot be met in sections having small flange outstands or shallow webs. The test set-up is shown in Figure 3.11.

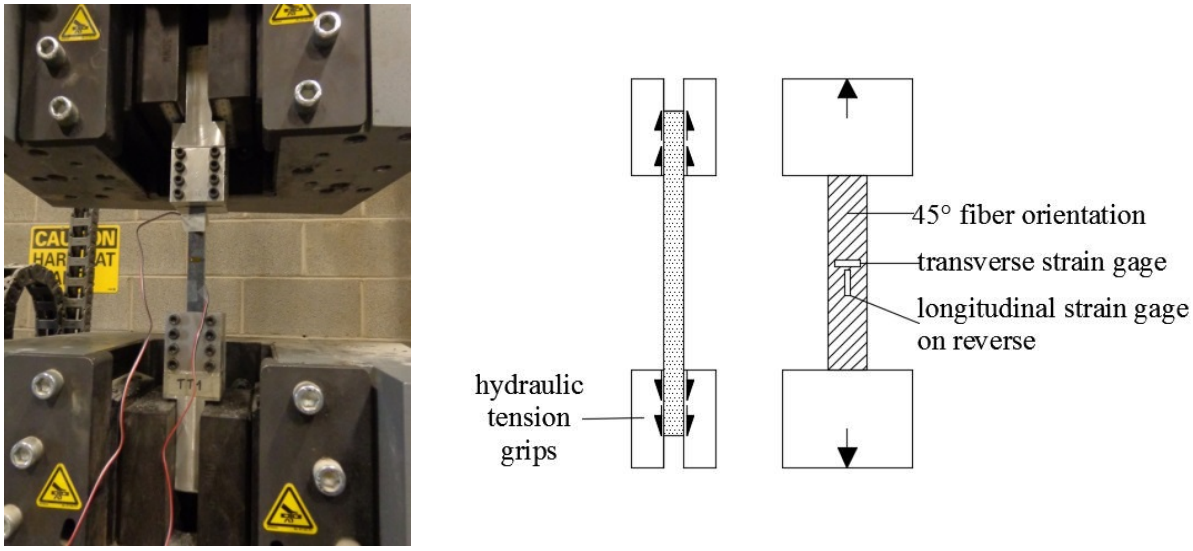

Figure 3.11 Shear test set-up (Image at right: after Cardoso et al. 2014)

3.3.5 Summary

Using the material tests described in this chapter, mechanical properties of the pultruded GFRP I-section profiles were obtained as given in Table 3.3. In general (and as expected), the properties obtained from experimental tests are higher than those provided by manufacturer and exceed the minimum requirements of ASCE (2010). It is noted, however the experimentally

determined shear modulus is less that that reported by the manufacturer. A similar finding is reported by Cardoso (2014) who tested different pGFRP materials from the same manufacturer.

Table 3.3 Mechanical properties of pGFRP profiles

Mechanical Properties	Test Method	Experimental Results		Manufacturer Reported (2012)	ASCE (2010) Minimum Requirement
		Flange (COV)	Web (COV)		
E_{Lt} (MPa)	ASTM D3039	24490 (0.09)	26470 (0.04)	17200	20685
F_{Lt} (MPa)		300 (0.12)	310 (0.10)	207	207
E_{Tt} (MPa)	ASTM D3039	-	8028 (0.06)	5500	5516
F_{Tt} (MPa)		-	52 (0.09)	48	48
E_{Tb} (MPa)	Non-standard (Section 3.3.2)	9444 (0.04)	8289 (0.03)	5500	-
F_{Tb} (MPa)		89 (0.06)	-	69	-
E_{Lc} (MPa)	ASTM D695	31219 (0.09)	31250 (0.08)	17200	20685
F_{Lc} (MPa)		329 (0.14)	227 (0.07)	207	207
G_{LT} (MPa)	ASTM D3518	-	2882 (0.03)	3100	2758

3.4 GEOMETRIC CHARACTERIZATION

Five different section geometries (Figure 3.12) are used in the experimental programs presented in Chapters 5, 6, and 7. All sections are cut from [nominal native dimensions and beam designation] 6 x 6 x ¼ I-beams, using a vertical band saw to cut both flanges simultaneously. Fourteen beams were prepared: four 6 x 6 x ¼ (original section, requiring no cutting), three 6 x 5 x ¼, four 6 x 4 x ¼, two 6 x 3 x ¼, and one 6 x 2 x ¼ section. The resulting nominal and measured geometries of each I-beam are presented in Table 3.4. The flange slenderness ratios range from 12 to 4.

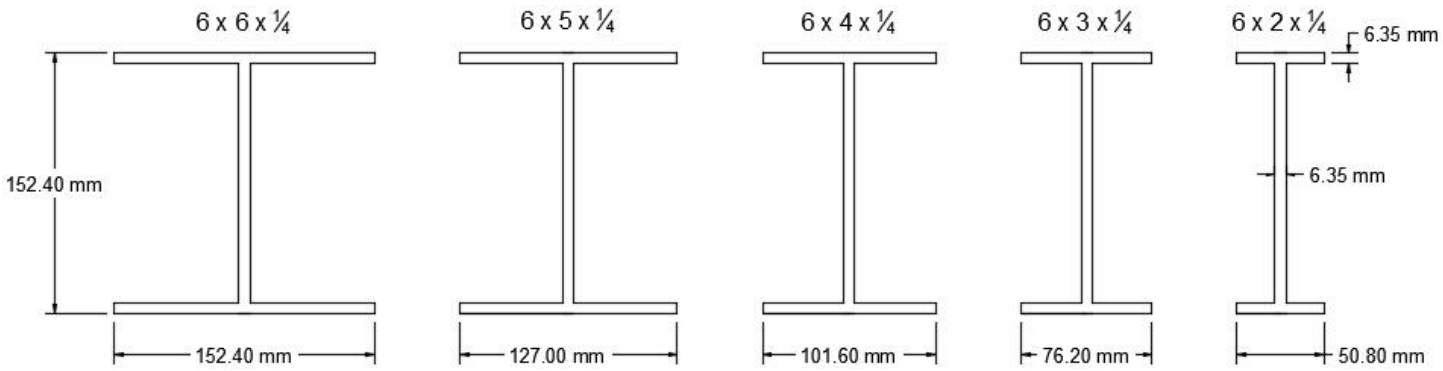

Figure 3.12 Section geometries of FLB and LTB test specimens

Table 3.4 Section dimensions of all pGFRP I-beams

Sections	*weight* (N/mm)	*d* (mm)		*b* (mm)		t_w (mm)		t_f (mm)		$b/2t_f$	
	nominal	nominal	actual	nominal	actual	nominal	actual	nominal	actual	nominal	actual
FLB6-1	0.051	152.40	153.70	152.40	152.10	6.35	6.37	6.35	6.40	12.00	11.88
FLB6-2	0.051	152.40	154.09	152.40	152.17	6.35	6.27	6.35	6.37	12.00	11.95
FLB5-1	0.042	152.40	153.74	127.00	127.57	6.35	6.39	6.35	6.25	10.00	10.21
FLB5-2	0.042	152.40	153.97	127.00	127.21	6.35	6.33	6.35	6.27	10.00	10.15
FLB4-1	0.034	152.40	153.09	101.60	102.55	6.35	6.23	6.35	6.09	8.00	8.41
FLB4-2	0.034	152.40	153.19	101.60	102.38	6.35	6.34	6.35	6.15	8.00	8.32
FLB4-3	0.034	152.40	153.14	101.60	99.84	6.35	6.24	6.35	6.11	8.00	8.17
FLB3	0.025	152.40	152.98	76.20	76.93	6.35	6.29	6.35	6.14	6.00	6.27
LTB6-1	0.051	152.40	153.83	152.40	152.32	6.35	6.38	6.35	6.37	12.00	11.95
LTB6-2	0.051	152.40	153.68	152.40	152.14	6.35	6.30	6.35	6.39	12.00	11.90
LTB5	0.042	152.40	153.33	127.00	128.13	6.35	6.24	6.35	6.09	10.00	10.52
LTB4	0.034	152.40	153.19	101.60	102.45	6.35	6.28	6.35	6.11	8.00	8.38
LTB3	0.025	152.40	153.05	76.20	76.86	6.35	6.39	6.35	6.18	6.00	6.22
LTB2	0.016	152.40	152.76	50.80	52.46	6.35	6.30	6.35	6.18	4.00	4.24

The data presented in Tables 3.3 and 3.4 will be used throughout the experimental programs. Further relevant discussion is presented in the chapters describing the specific tests.

4.0 FINITE STRIP METHOD

In this study, to predict the critical buckling loads for flange local buckling (FLB) and lateral torsional buckling (LTB), elastic buckling analysis is conducted using the constrained finite strip method (FSM) implemented in CUFSM (Li and Schafer 2010). Consequently, a general buckling mode can be decomposed into local, global, and interactive buckling behaviors with their corresponding contributions identified (Ádány and Schafer 2008). In this chapter, the FSM is presented and the modeling procedure using CUFSM is discussed.

4.1 INTRODUCTION

The finite strip method (FSM), first developed by Cheung (1976), has seen much theoretical progress and a number of practical applications over the past decades. Typically used for "thin-walled" sections, common applications can be found in bridges (Figure 4.1a) and slabs or plates (Figure 4.1b) with regular cross sections (Li et al. 1986).

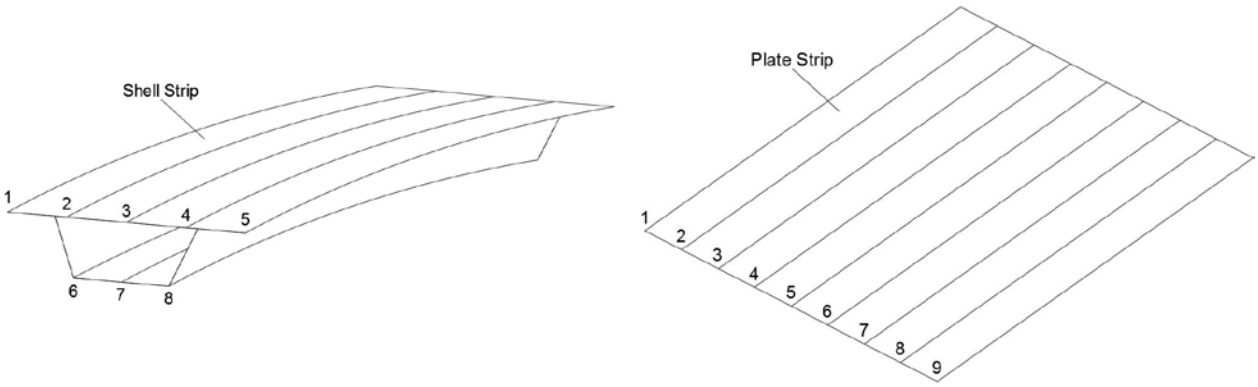

a) box girder bridge (shell strip) **b) slab (plate strip)**

Figure 4.1 Applications of FSM (after Cheung 1976)

The FSM is demonstrated to be applicable for both isotropic and anisotropic materials with arbitrary shaped plates (Azizian and Dawe 1985; Tham and Szeto 1990; Cheung and Akhras 1993). Compared with the well-established finite element method (FEM), the FSM results in considerably fewer degrees of freedom in the analytical procedure and consequently requires less computational cost, while still achieving satisfactory accuracy (Cheung and Chan 1981). The reduction of the degrees of freedom is realized on the basis that the FSM employs both polynomial functions and continuously differentiable series to construct the displacement functions for the transverse and longitudinal directions, respectively, rather than using polynomial functions for all directions as required in the FEM (Cheung 1976). Differentiable series, such as spline functions (B-3 spline and X-spline), are used to describe the displacement fields in the longitudinal directions of the strips (Cheung 1976; Tham and Szeto 1990). For instance, the displacement function $w(x,y)$ can be constructed by multiplying the B-3 spline function, $\varphi_i(y)$, by the conventional beam shape functions, $N(x)$, (Kong and Cheung 1993):

$$w(x,y) = \sum_{i=-1}^{m+1} [N(x)]\varphi_i(y)\{\alpha\}_i \tag{4.1}$$

Where, $\{a\}_i$ is the unknown parameter for the i^{th} member of B-3 spline function. The general expression of the B-3 spline function is presented in Figure 4.2. Through the use of spline functions, the compatibility requirement at the nodes is satisfied (Li et al. 1986).

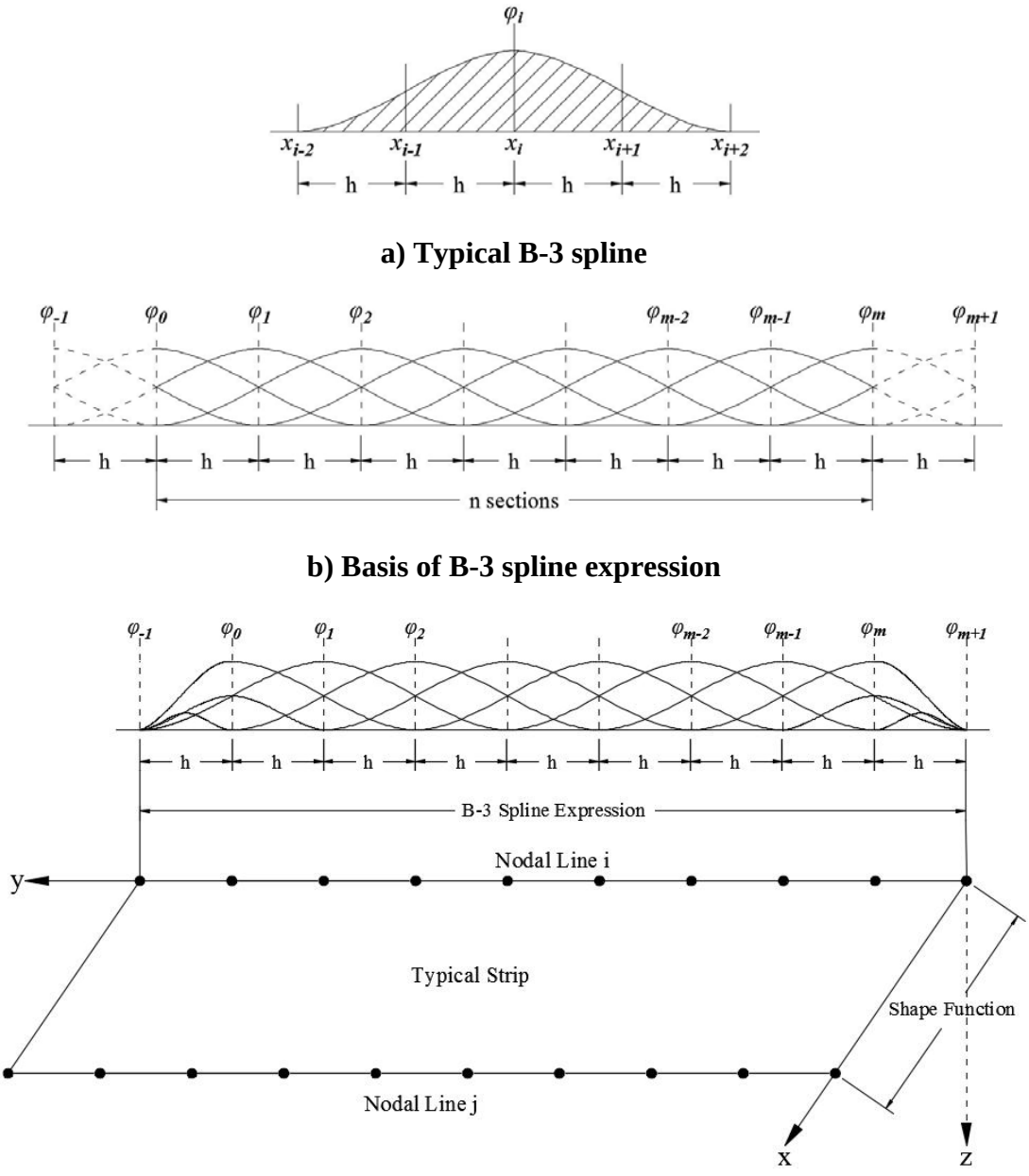

a) Typical B-3 spline

b) Basis of B-3 spline expression

c) Displacement functions for typical strip

Figure 4.2 Displacement function constructed using B-3 spline (after Kong and Cheung 1993)

With the displacement functions determined, the principle of minimum potential energy is used to conduct the stability analysis. A general form of the total potential energy is given by Azizian and Dawe (1985):

$$\Pi = U + W \tag{4.2}$$

Where, U is the strain energy in the strip, W is the potential energy of the external load, and Π is the total potential energy. Minimizing the potential energy yields a standard eigenvalue problem, as described by Tham and Szeto (1990):

$$|K_s - \lambda K_G| = 0 \tag{4.3}$$

Where, K_S and K_G are the stiffness and geometric matrices, respectively; and λ is the eigenvalue which indicates the critical buckling load. Additionally, the buckling modes are defined by the eigenvectors.

4.2 MODELING USING CUFSM

In this work, CUFSM (Li and Schafer 2010) is used to implement the FSM and predict the critical buckling loads for: flange local buckling (FLB), lateral torsional buckling (LTB), and the interaction between FLB and LTB. In the latest version of CUFSM, the constrained FSM is implemented, through which the modal decomposition and modal identification can be performed quantitatively (Li and Schafer 2010). That is, a general buckling mode can be decomposed into basic buckling modes (local, global, interaction) with the corresponding contributions identified quantitatively.

To use CUFSM, material properties, obtained from the material characterization tests discussed in Chapter 3 are required. In particular, those along the longitudinal direction of the

pGFRP I-section used in this work are defined along the y-axis in CUFSM, while the transverse direction is defined as the x-axis. Next, the sectional properties are defined using the control nodes (nodes 1 to 21 for section 6x6 shown in Figure 4.3) at the center lines of each element (two flanges and one web). With the material and nodes determined, the elements, representing the plate strips, can be created. In addition, the element mesh can be improved by using the Double Element function in CUFSM, providing a convenient approach to improve the accuracy of the stability analysis.

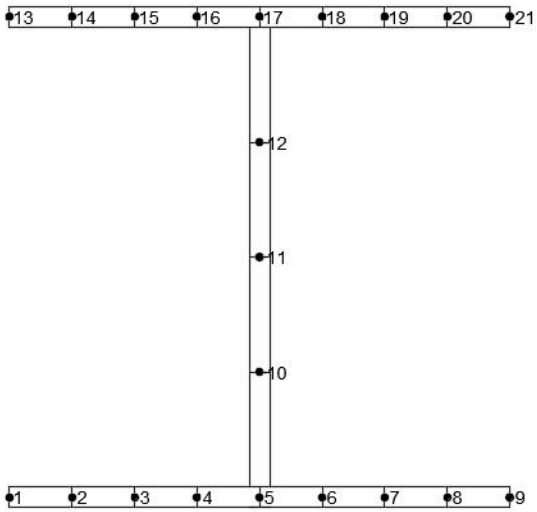

Figure 4.3 FSM model

With the finite strip model constructed, the moment is applied to generate unit compressive and tensile stress at top and bottom of the simply-supported beam. No lateral support is provided along the length of the beam. The stability analysis is conducted using the prescribed section having an arbitrary length through which both local and global buckling can be captured. The beam longitudinal slenderness ratio, L_b/r_y, increases as the length of the beam increases. Accordingly, three buckling modes of interest can be obtained as shown in Figure 4.4

for an example 6 x 6 x ¼ section. FLB-dominated behavior will occur for beams having small longitudinal slenderness ratios (L_b/r_y < 20). LTB is the dominant buckling mode for beams having large longitudinal slenderness ratios (L_b/r_y > 49). Between these limits, interaction between local and global buckling will have a significant effect on the critical buckling moment capacity for beams having intermediate slenderness ratios (20 < L_b/r_y < 49). Moreover, the contributions of the basic modes (local and global) are quantitatively identified for beam having varying longitudinal slenderness ratios, as presented in Figure 4.5. Similarly, it can be seen that the dominant buckling mode transitions from FLB to LTB as the longitudinal slenderness ratio increases and significant interaction will occur for beams having intermediate longitudinal slenderness ratios. The FSM analysis shown in Figures 4.4 and 4.5 is intended to be demonstrative; it was conducted considering only one buckling half wave to occur on the beam. In this case, the interactive buckling shown is incomplete since it captures only a single half-wave length. While correct for LTB, in the range of intermediate slenderness, local FLB minima will occur at integer multiples of the FLB critical half wave length (shown to occur at $L_b/r_y \approx 7$ or $L_b \approx 248$ mm). Interaction between buckling modes occurs in the region of intermediate slenderness but may not be captured in a simple FSM analysis.

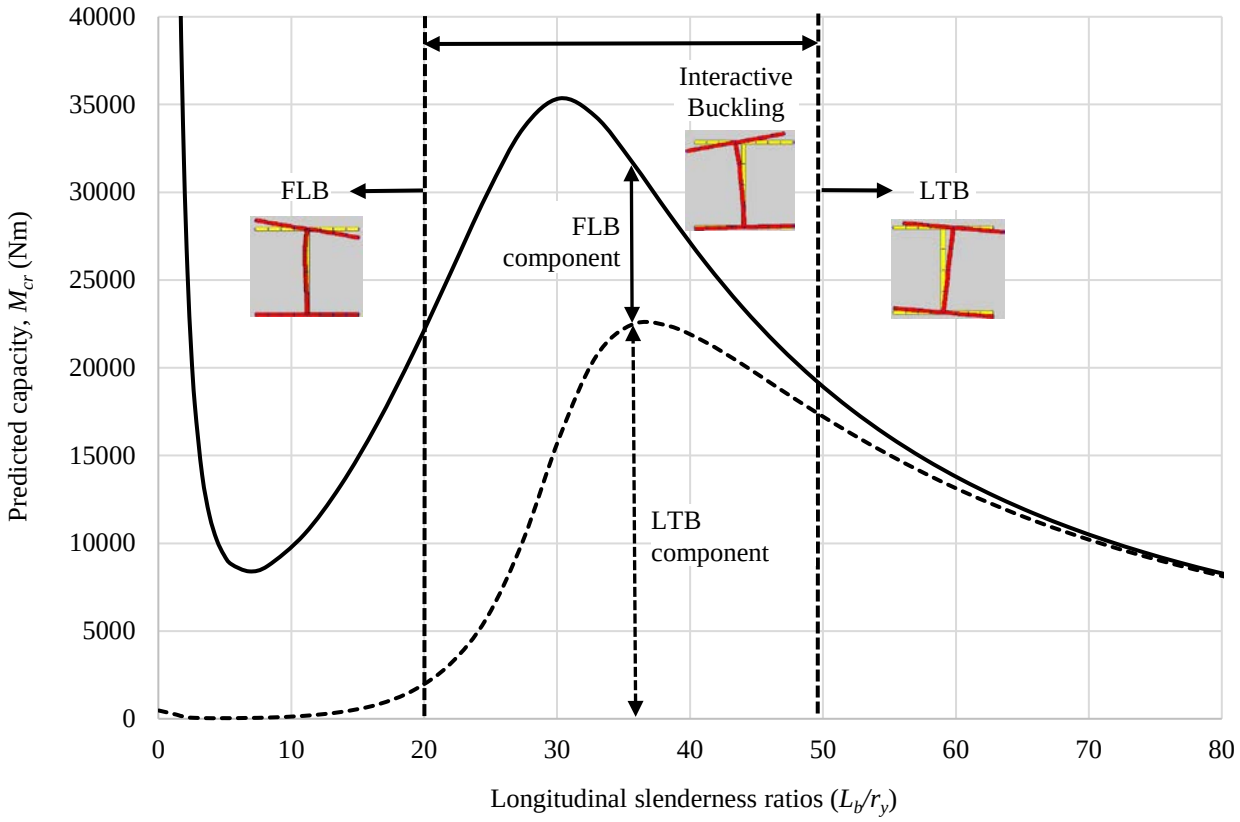

Figure 4.4 Example of critical buckling modes for 152.4 x 152.4 x 6.35 (6 x 6 x ¼) I-section

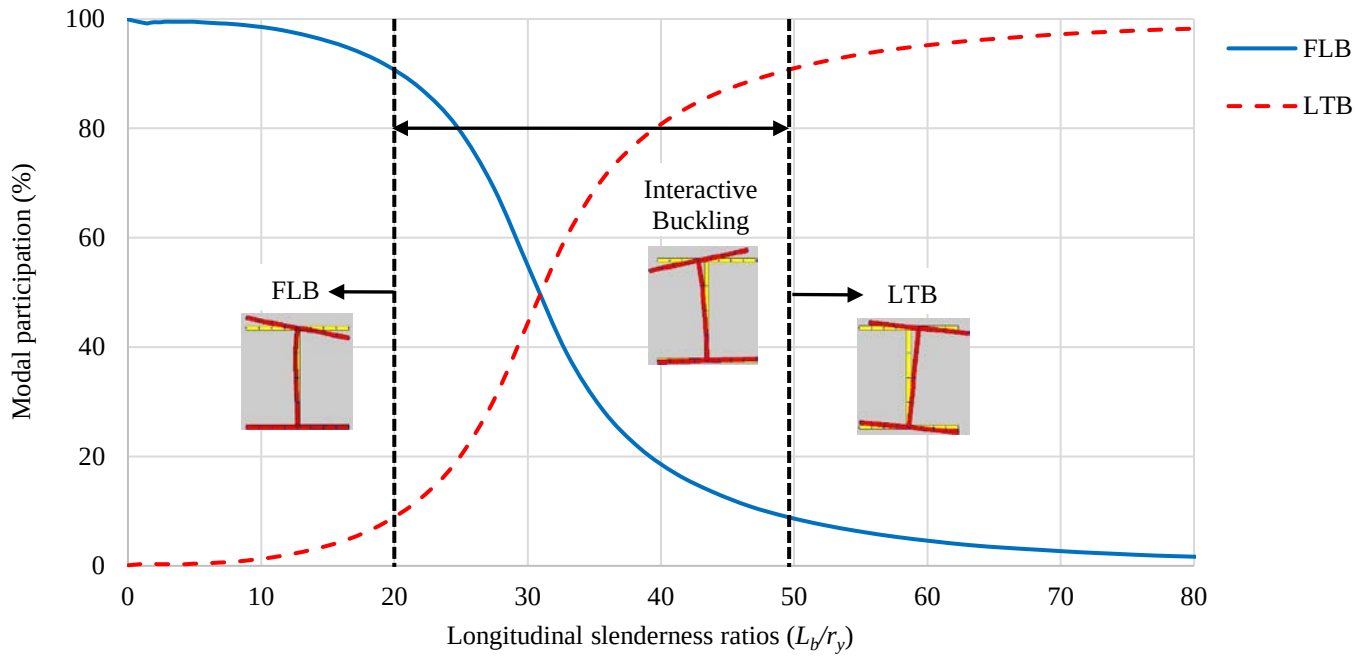

Figure 4.5 Example of modal participation for 152.4 x 152.4 x 6.35 (6 x 6 x ¼) I-section

4.3 SUMMARY OF MODELING

Using CUFSM (Li and Schafer 2010), the predictions for the critical FLB and LTB moments for each test specimen (described in Chapter 5 and 6, respectively) are obtained as described above and are summarized in Tables 4.1 and 4.2. In particular, the half-wave length of each buckling mode, needed in calculating the critical moments, is determined based on the test configurations used and the analytical results provided by CUFSM. For instance, for FLB 6 (described in Chapter 5) having spans of 2900 mm and 2200 mm, the lengths of the constant moment regions are 900 mm and 600 mm, respectively. These values are greater than the critical half-wave length, 248 mm, determined by CUFSM. 3.5 or 2.5 half-waves may theoretically occur in the constant moment region of FLB 6 having spans of 2900 mm and 2200 mm, respectively. The corresponding critical moments are determined at the half-wave length of 248 mm, yielding 8395 Nm. On the other hand, for the LTB tests, described in Chapter 6, the half-wave length is considered to be the entire beam length.

Table 4.1 FSM predictions of critical moments for FLB for test specimens described in Chapter 5

Specimen	Span (mm)	Critical half wave length (mm)	Constant moment length (mm)	M_{cr} (Nm)
FLB6	2900	248	900	8395
	2600		800	
	2200		600	
	1800		400	
FLB5	2900	215	900	10048
	2600		800	
	2200		600	
	1800		400	
FLB4	2900	182	900	12591
	2600		800	
	2200		600	
	1800		400	
FLB3	2900	149	900	16862
	2200		600	

Table 4.2 FSM predictions of critical moments for LTB for test specimens described in Chapter 6

Specimen	Span (mm)	M_{cr} (Nm)
LTB6	2896	8385
	2438	11380
	2134	14398
	1829	18805
	1524	25352
LTB5	2896	5118
	2438	6921
	2134	8771
	1829	11554
	1524	15967
LTB4	2896	2845
	2438	3797
	2134	4778
	1829	6269
	1524	8683
LTB3	2896	1401
	2438	1822
	2134	2253
	1829	2907
	1524	3971
LTB2	2896	580
	2438	724
	2134	868
	1829	1080
	1524	1421

5.0 FLANGE LOCAL BUCKLING BEHAVIOR

5.1 EXPERIMENTAL PROGRAM

An experimental program was conducted to study the flange local buckling (FLB) behavior of thin-walled pGFRP I-beams subject to flexure. Four-point bending tests having different constant moment and shear span lengths were employed (Figure 5.1). The spans were selected to accentuate FLB while mitigating, to the extent possible, lateral torsional buckling (LTB). The 900 kN-capacity test set-up used is shown in Figure 5.2a. Load was applied slowly in displacement control in order to ensure a controlled elastic response and no damage to the beams. Lateral supports (Figure 5.2b) were provided at both reaction points and along the span as required. The load points also provided some degree of lateral support although – due to the presence of a ball joint loading the spreader beam in the loading apparatus – this support cannot be fully relied upon.

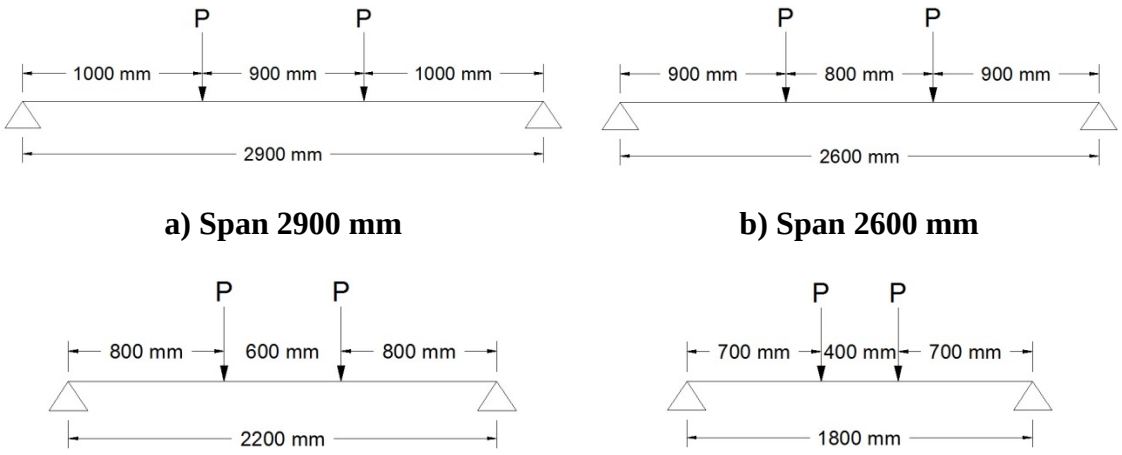

a) Span 2900 mm **b) Span 2600 mm**

c) Span 2200 mm **d) Span 1800 mm**

Figure 5.1 Four-point bending tests span arrangements for FLB tests

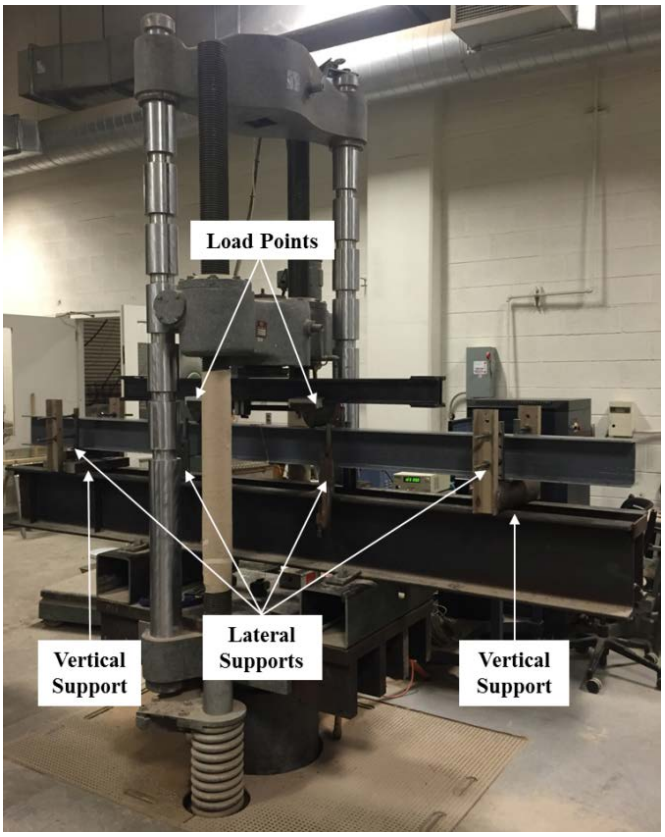

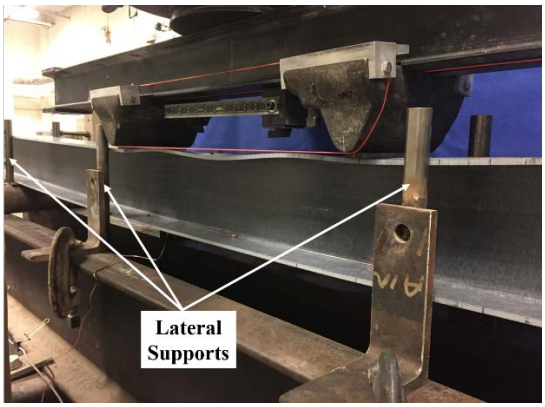

a) Test set-up of four-point bending tests **b) Lateral supports**

Figure 5.2 Test set-up of FLB tests

Eight specimens having four section geometries were used: two 6 x 6 x ¼ (FLB6-1 and FLB6-2), two 6 x 5 x ¼ (FLB5-1 and FLB5-2), three 6 x 4 x ¼ (FLB4-1, FLB4-2 and FLB4-3), and one 6 x 3 x ¼ (FLB3). Measured and nominal specimen dimensions are presented in Table 3.4. Measured material properties are provided in Table 3.3. Four flange slenderness ratios, *b/2t* = 6, 8, 10 and 12, are included in this work (Table 3.4), whereas only two slenderness ratios of 8 and 12 have been reported previously (see Section 2.1).

Each specimen was tested under each of the four span conditions shown in Figure 5.1, except that FLB3 was only tested under spans of 2900 and 2200 mm. Additionally, each specimen was tested in two orientations such that each flange was tested as the compression flange. Therefore, each specimen geometry, except for section FLB3, had no less than four tests under each span geometry (two specimens x two orientations). Tests were controlled so that no damage to the pGFRP material occurred, permitting retests and reuse of the specimens.

In each test, the constant moment region between the load locations was effectively a multiple of the expected FLB half wave length and the shear span was selected to be sufficiently short to mitigate LTB while being sufficiently long to mitigate shear failure under the anticipated applied loads. Electrical resistance strain gages located on the top surface of the compression flange near the flange tips were used to assess the onset of FLB behavior (thereby establishing the critical FLB load). Flange strains are linear until the onset of buckling and begin to diverge as the flange bends due to local buckling (Figure 2.1a). A representative example of such strain data is shown in Figure 5.3b for specimen FLB5-1 tested over 2600 mm (shown in Figure 5.3a) indicating buckling at an applied force P_{cr} of 12.98 kN plus the self weight of the beam (0.042 N/mm; see Table 3.4). Digital images were used to confirm buckling behavior and to obtain the half wave length of the resulting buckles. A representative image from FLB5 tested over a span

of 2600 mm is shown in Figure 5.3a in which three half-sine buckles are seen over the 800 mm constant moment region.

a) Buckling in constant moment region showing 3 half sine buckles over the 800 mm constant moment region

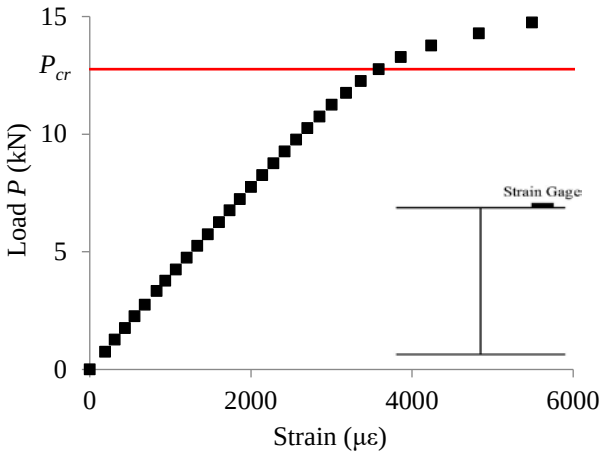

b) Flange strain showing buckling at an load *P* of 12.98 kN

Figure 5.3 Flange local buckling (FLB5 over 2600 mm span)

5.2 EXPERIMENTAL RESULTS

Using the aforementioned combination of test configurations, 62 four-point bending tests were conducted: 16 tests on FLB6, 22 on FLB5, 20 on FLB4, and 4 on FLB3. The test results are presented in Table 5.1. The average values of FLB buckling load are calculated and all coefficients of variation (COV) are found to be less than 0.10, except for those obtained from the tests on FLB3, indicating that the tests demonstrated repeatability and confirming that no damage accumulated in the specimens. FLB3 was found to fail in a manner dominated by LTB rather than FLB due to the relatively low flange slenderness ratio ($b/2t$ = 6) and high longitudinal slenderness ratio, L_b/r_y. Based on this result planned tests of a smaller section, FLB2, having $b/2t$

= 4, were not conducted. Flange stresses were calculated by dividing applied moment by section modulus (Eq. 2.9) calculated using nominal section dimensions. Images and flange stress-strain curves for all specimens are reported in Appendix A.1.

The four-point bending tests began with specimen of FLB6 (*b/2t = 12*) with lateral supports only provided at the reaction points. In these tests, interaction between FLB and LTB was not identified. However, in the initial test of the more slender specimen FLB5 (*b/2t = 10*), apparent interaction between FLB and LTB was observed over a span of 2900 mm, resulting in a lower-than-anticipated critical bending moment. This interaction was verified in the test of FLB5 having a span of 1800 mm. In Table 5.3, an asterisk is used to denote those tests in which such FLB-LTB interaction was observed. Following these tests, additional lateral supports located close to the load points (Figure 5.2b) were used for all subsequent specimens having $b/2t \leq 10$.

The experimentally determined critical FLB moments, M_{cr}, are plotted against the flange slenderness ratios, *b/2t*, in Figure 5.4. From the results of FLB6, FLB5 and FLB4, it can be seen that the critical FLB moment generally increases as flange slenderness ratio decreases. However, the dominant failure mode may transition from FLB to LTB when flange slenderness continues to decrease. In this case, the ratio of longitudinal slenderness to flange slenderness effectively increases. This phenomenon was observed in the tests on FLB3: significant LTB behaviors were observed and one FLB3 specimen failed due to LTB (a significant LTB 'snap through' damaged the flange-web interface stopping testing of this section). Additionally, the significantly lower capacity of the LTB5* specimens that exhibited interactive buckling is evident in Figure 5.4, indicating how interaction with LTB reduces FLB capacity.

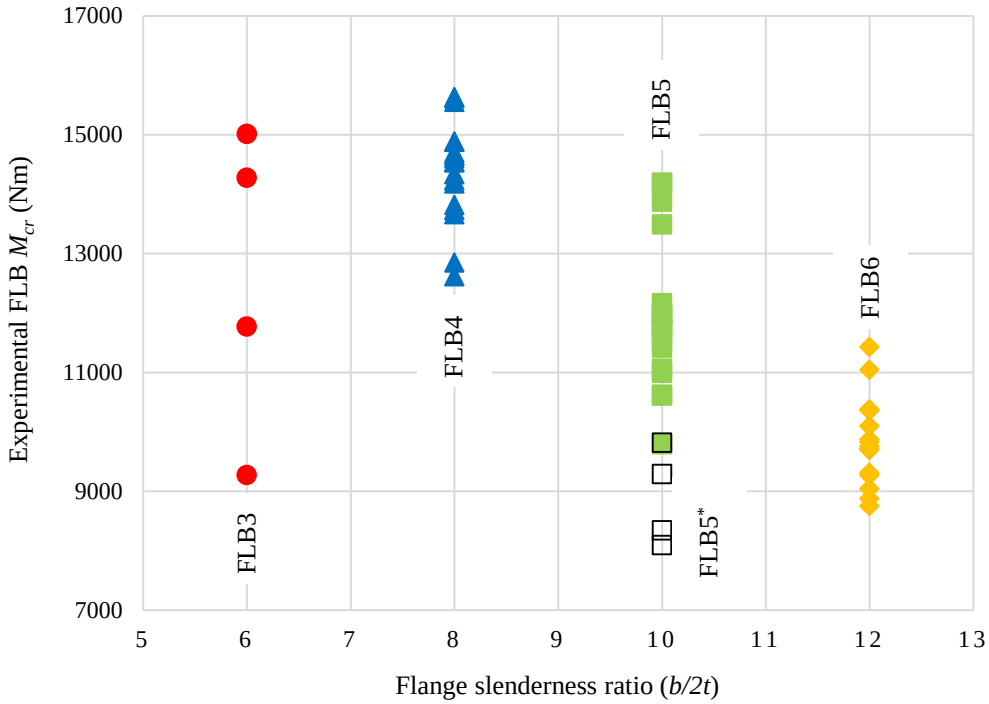

Figure 5.4 Experimentally determined critical FLB moments versus flange slenderness ratios

Table 5.1 Experimental results and predictions of flange local buckling specimens

Specimen	Span	Shear Span	Experiment		$M_{cr\,FLB}$ (Nm) predictions calculated with nominal section dimensions and $E_{L,t}$							
					ASCE (2010)		EUR 27666 (2016)		Kollár (2003)		FSM	
	mm	mm	M_{cr} (Nm)	Average M_{cr} (Nm) (COV)	M_{cr}	pred / exp	M_{cr}	pred / exp	M_{cr}	pred / exp	M_{cr}	pred / exp
FLB6	2900	1000	8879	9304 (0.06)	6945	0.75	6078	0.65	7195	0.77	8395	0.90
			9754									
			8754									
			9829									
	2600	900	9313	9330 (0.03)	6945	0.74	6078	0.65	7195	0.77	8395	0.90
			9043									
			9268									
			9696									
	2200	800	10371	10680 (0.07)	6945	0.65	6078	0.57	7195	0.67	8395	0.79
			9871									
			11045									
			11431									
	1800	700	10101	10140 (0.03)	6945	0.68	6078	0.60	7195	0.71	8395	0.83
			10363									
			9716									
			10381									
FLB5	2900	1000	11944	11259 (0.08)	8141	0.72	6883	0.61	8419	0.75	10048	0.89
			9794									
			11769									
			11794									
			10994									
FLB5*	2900	1000	8344	8219 (0.02)	8141	0.99	6883	0.84	8419	1.02	10048	1.22
			8094									
FLB5	2600	900	11713	11432 (0.05)	8141	0.71	6883	0.60	8419	0.74	10048	0.88
			10611									
			11983									
			11421									
	2200	800	11546	11351 (0.06)	8141	0.72	6883	0.61	8419	0.74	10048	0.89
			10626									
			11066									
			12166									
	1800	700	13492	13548 (0.07)	8141	0.60	6883	0.51	8419	0.62	10048	0.74
			13877									
			14192									
			11987									
			14192									
FLB5*	1800	700	9817	9555 (0.04)	8141	0.85	6883	0.72	8419	0.88	10048	1.05
			9292									
FLB4	2900	1000	14235	14485 (0.06)	9932	0.69	7774	0.54	10256	0.71	12591	0.87
			13735									
			14335									
			15635									
			9285**									

Table 5.1 (continued)

Specimen	Span	Shear Span	Experiment		$M_{cr\,FLB}$ (Nm) predictions calculated with nominal section dimensions and $E_{L,t}$							
	mm	mm	M_{cr} (Nm)	Average M_{cr} (Nm) (COV)	ASCE (2010)		EUR 27666 (2016)		Kollár (2003)		FSM	
					M_{cr}	pred / exp	M_{cr}	pred / exp	M_{cr}	pred / exp	M_{cr}	pred / exp
	2600	900	14653	14215 (0.06)	9932	0.70	7774	0.55	10256	0.72	12591	0.89
			14698									
			14653									
			12853									
	2200	800	14180	14060 (0.09)	9932	0.71	7774	0.55	10256	0.73	12591	0.90
			15620									
			13820									
			12620									
	1800	700	15554	14668 (0.04)	9932	0.68	7774	0.53	10256	0.70	12591	0.86
			14539									
			14889									
			14540									
			13664									
			14884									
			14609									
FLB3	2900	1000	11776	11776 (0.21)	12826	1.09	6941	0.59	13235	1.12	16862	1.43
			9276									
			14276									
	2200	800	15015[1]	15015[1]	12826	0.85	6941	0.46	13235	0.88	16862	1.12

[*] interaction of FLB and LTB observed;
[1] only one test was conducted due to LTB failure and damage to beam.

As summary of the average critical FLB moments of each specimen geometry (including all spans) are presented in Table 5.2.

5.3 COMPARISONS WITH STANDARDS, NUMERICAL AND FSM MODELING

Experimentally determined critical FLB moments were compared with the values obtained through various numerical analyses, as shown in Table 5.1. The average values of test results from specimens under each span are also presented in Table 5.1. Additionally, a summary of the average critical FLB moments of each specimen geometry (including all spans) is presented in

Table 5.2 and Figure 5.5. The error bars of the experimental results in Figure 5.5 represent one standard deviation. In all analyses nominal section dimensions (Table 3.4) and measured material properties (Table 3.3) were used.

Two widely-used design guides, ASCE (2010) and EUR 27666 (2016) (see Section 2.4.1), were used to evaluate the experimental results. It was found that both design guides provide conservative predictions of critical FLB moment. Moreover, Kollár's solutions (see Appendix C) also provided conservative predictions, as compared with experimental results. The finite strip method, implemented using CUFSM (Li and Schafer 2010) and described in Chapter 4, was found to have good agreement with the experimental results. Through this comparative study, it is found that all predictions underestimate the FLB behavior of pGFRP I-sections. The implication of this underestimation is that the calibration of material resistance factors (so-called φ factors) through reliability analyses may result in unreasonably high values. While perhaps appropriate for the conservative equations being used, this misrepresents the actual material reliability (Cardoso et al. 2014a). As is seen in Figure 5.5, FLB predictions of pultruded I-shapes exhibit considerable variability. This demonstrates the need of developing a new formula having improved prediction of critical FLB moment capacity of pGFRP I-sections.

Table 5.2 Average critical FLB moments of each specimen geometry

Specimen	Experiment	$M_{cr\,FLB}$ (Nm) predictions calculated with nominal section dimensions and $E_{L,t}$									
	M_{cr} (Nm)	ASCE (2010)		EUR 27666 (2016)		Kollár (2003)		FSM		Eq. 5.16	
		M_{cr}	pred/exp	M_{cr}	pred/exp	M_{cr}	pred/exp	M_{cr}	pred/exp	M_{cr}	pred/exp
FLB6	9863	6945	0.70	6078	0.62	7195	0.73	8395	0.85	8522	0.86
FLB5*	8887	8141	0.92	6883	0.77	8419	0.95	10048	1.13	9975	1.12
FLB5	11898	8141	0.68	6883	0.58	8419	0.71	10048	0.84	9975	0.84
FLB4	14357	9932	0.69	7774	0.54	10256	0.71	12591	0.88	12056	0.84
FLB3	13396	12826	0.96	6941	0.52	13235	0.99	16862	1.26	15341	1.15

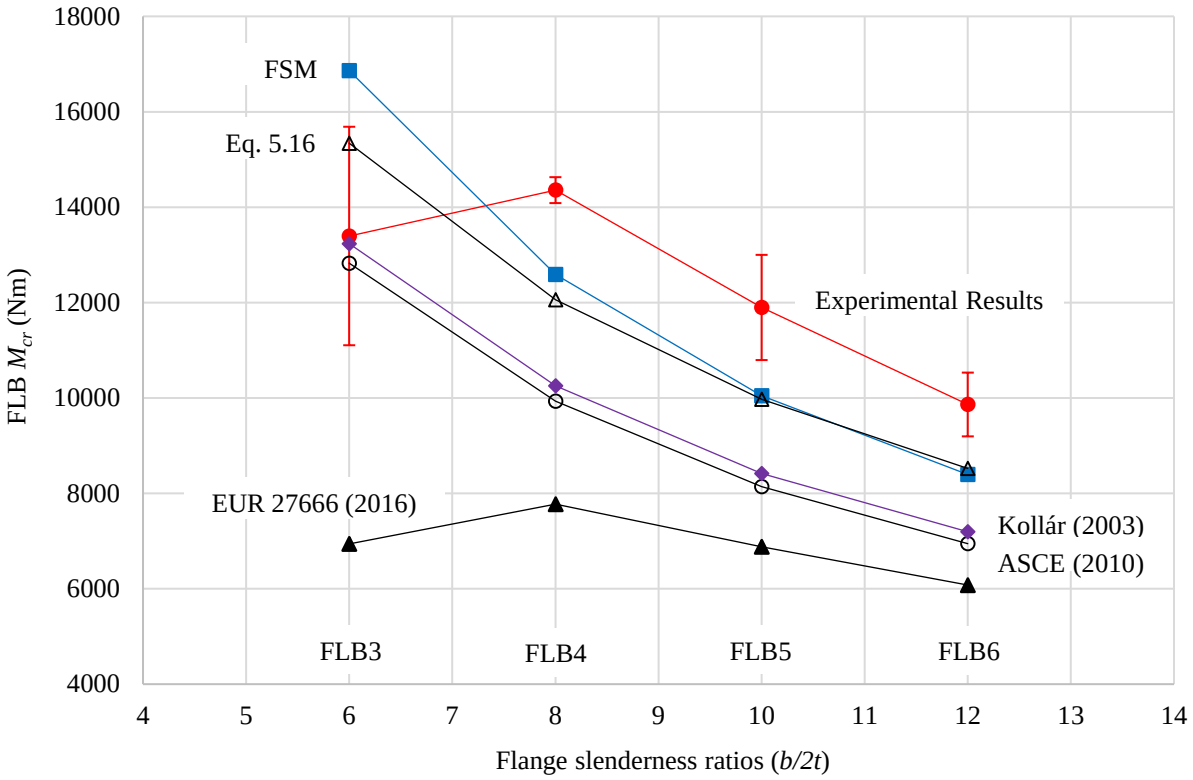

Figure 5.5 Average critical FLB moments versus flange slenderness ratios

5.4 ANALYTICAL STUDY OF FLANGE LOCAL BUCKLING

5.4.1 Formulations

Following the approach described by Cardoso (2014) for concentrically loaded column members, the plate theory (Bleich 1952) and the energy method (Leissa 1985) were used to derive explicit equations for flange local buckling (FLB) of pGFRP I-sections subject to flexure. In the following, $t = t_w = t_f$.

Referring to Figure 5.6, in plate theory, both the flange outstands and the web can be considered as individual plates restrained by the adjacent plates, allowing the investigation of FLB to be accomplished by only studying the individual plates rather than analyzing the full

cross sections. The flange outstand plate is considered to be elastically restrained by the web with elastic rotational spring constant *k* about the longitudinal (*x*) axis at the flange-web interface, free at the outside edge of the flange and simply supported in the transverse (*y*) direction. Additionally, the flange plate loading is approximated as a uniform compression load, f_x, across its entire width. This is an important and nontrivial simplification since the compression flange is subject to both axial compression and a small through-thickness strain gradient resulting from flexure of the overall section (about the *y* axis). Additionally, this condition implies no bending about *z* axis as would occur in the case of LTB. The boundary conditions of a flange outstand are shown in Figure 5.6.

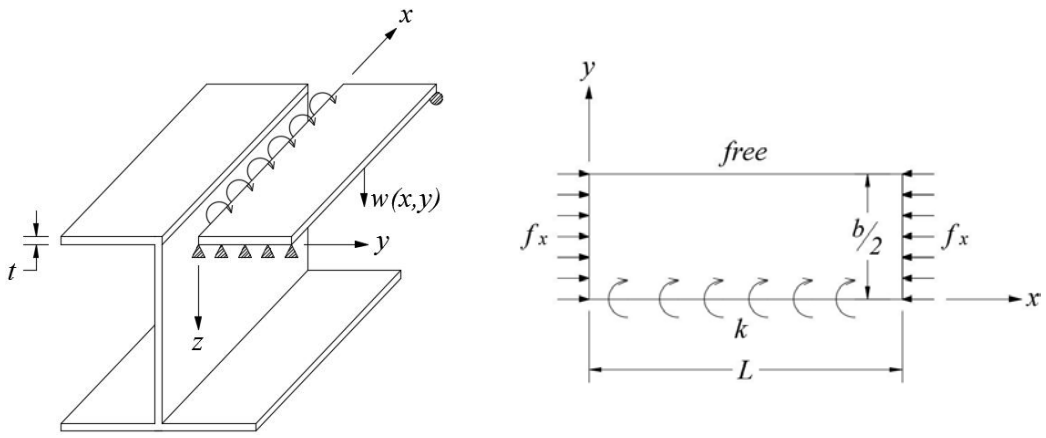

a) Flange outstand plate **b) Plan view**

Figure 5.6 Coordinate system and boundary conditions for flange outstand plate

With plate boundaries established, the energy method is applied to obtain FLB loads for the flange plate that is subject to uniform compression which corresponds to the I-beam being subject to a constant bending moment. The strain energy of an orthotropic plate, *U*, and potential energy of the in-plane force, *W*, under a uniform compression load are given by (Leissa 1985):

$$U = \frac{1}{2}\int_0^{b/2}\int_0^{L}\left[D_{11}^f\left(\frac{\partial^2 w}{\partial x^2}\right)^2 + D_{22}^f\left(\frac{\partial^2 w}{\partial y^2}\right)^2 + 2D_{12}^f\frac{\partial^2 w}{\partial x^2}\frac{\partial^2 w}{\partial y^2} + 4D_{66}^f\left(\frac{\partial^2 w}{\partial x \partial y}\right)^2\right]dxdy \quad (5.1)$$

$$W = -\frac{1}{2}\int_0^{b/2}\int_0^{L} t f_x\left(\frac{\partial^2 w}{\partial x^2}\right)^2 dxdy \quad (5.2)$$

Where $w(x, y)$ is the shape function for the buckled flange plate; D_{ij} are the flexural stiffness parameters for a homogenous orthotropic plate, which are defined in Appendix B; t is the flange thickness; $b/2$ is the flange outstand width; L is the half wave length of the buckled flange plate in the longitudinal direction; and f_x is the uniform compressive stress. The state of equilibrium is achieved when the total potential energy is zero:

$$U + W = 0 \quad (5.3)$$

Substituting Eqs. 5.1 and 5.2 into 5.3, the expression for compression stress, f_x, is obtained:

$$f_x = \frac{\frac{1}{2}\int_0^{b/2}\int_0^{L}\left[D_{11}^f\left(\frac{\partial^2 w}{\partial x^2}\right)^2 + D_{22}^f\left(\frac{\partial^2 w}{\partial y^2}\right)^2 + 2D_{12}^f\frac{\partial^2 w}{\partial x^2}\frac{\partial^2 w}{\partial y^2} + 4D_{66}^f\left(\frac{\partial^2 w}{\partial x \partial y}\right)^2\right]dxdy}{\frac{1}{2}\int_0^{b/2}\int_0^{L} t\left(\frac{\partial^2 w}{\partial x^2}\right)^2 dxdy} \quad (5.4)$$

The critical FLB stress, f_{cr}, is obtained when substituting the critical half wave length, $L = L_{cr}$, into Eq. 5.4.

In order to derive the explicit equation for critical FLB stress using Eq. 5.4, an appropriate shape function for the buckled flange plate needs to be determined. In this work, sinusoidal and second order polynomial functions are selected to approximate the buckled shape in the longitudinal and transverse directions, respectively:

$$w(x, y) = \sin\left(\frac{\pi x}{L}\right)(c_1 y + c_2 y^2) \quad (5.5)$$

Where c_1 and c_2 are constant coefficients. The selected shape function, $w(x,y)$, needs to respect the boundary conditions of the flange plate at the flange-web interface, including:

$$(w)_{y=0} = 0 \tag{5.6}$$

$$-(D_{12}^{f}\frac{\partial^2 w}{\partial x^2} + D_{22}^{f}\frac{\partial^2 w}{\partial y^2})_{y=0} = -k\frac{\partial w}{\partial y} \tag{5.7}$$

Where *k* is the spring constant simulating the rotational restraint at flange-web interface, which is given by Kollár (2003) as:

$$k_{Kollár} = \left(\frac{1}{2}\right)\frac{4D_{22}^{w}}{(d-t)}\left[1 - \frac{\left(t_f f_{cr,ss}^{f}\right)a_{11}^{f}}{\left(t_w f_{cr,ss}^{w}\right)a_{11}^{w}}\right] \tag{5.8}$$

Where a_{11}^{f} and a_{11}^{w} account for the thickness and material properties of flange and web, respectively. In this case, $a_{11}^{f} = a_{11}^{w}$, since the flange and web have the same thickness and material properties. $f_{cr,ss}^{f}$ and $f_{cr,ss}^{w}$ are the critical buckling stresses of a simply supported orthotropic plate under uniform compression, which are given by Kollár (2003) as:

$$f_{cr,ss}^{f} = \frac{12D_{66}^{f}}{t_f\left(\frac{b}{2}\right)^2} \tag{5.9}$$

$$f_{cr,ss}^{w} = \frac{\pi^2}{t_w(d-t)^2}\left[13.9\sqrt{D_{11}^{w}D_{22}^{w}} + 11.1(D_{12}^{w} + 2D_{66}^{w})\right] \tag{5.10}$$

According to Kollár (2003), the initial factor "*1/2*" in Eq. 5.8 is used to account for the fact that the web restrains two flange outstands and such restraint is equally divided between these. However, in this work the "*1/2"* factor is omitted as demonstrated in Section 5.4.3 below. Therefore, the spring constant, *k*, is taken as twice that proposed by Kollár (2003):

$$k = \frac{4D_{22}^{w}}{(d-t)}\left[1 - \frac{\left(t_f f_{cr,ss}^{f}\right)a_{11}^{f}}{\left(t_w f_{cr,ss}^{w}\right)a_{11}^{w}}\right] \tag{5.11}$$

Substituting the shape function *w* defined in Eq. 5.5 into boundary conditions, Eqs. 5.6 and 5.7, yields:

$$c_2 = \frac{kc_1}{2D_{22}^f} \tag{5.12}$$

Using Eq. 5.12, the shape function, *w*, can be further expressed as:

$$w(x,y) = \sin\left(\frac{\pi x}{L}\right)\left(c_1 y + \frac{kc_1}{2D_{22}^f} y^2\right) \tag{5.13}$$

In Eq. 5.13, it can be seen that there is only one constant coefficient, c_1, remaining and this will be cancelled out in the calculation in Eq. 5.4. Substituting Eq. 5.13 into Eq. 5.4, the compressive stress, f_x, can be obtained in terms of the half wave length, *L*. In order to obtain the critical FLB stress, f_{cr}, the critical half wave length, L_{cr}, is determined by taking the first derivative of f_x with respect to *L* and setting this equal to zero:

$$L_{cr} = \pi\left(\frac{b}{2}\right)\left[D_{11}^f\left(\frac{1}{20D_{22}^f} + \frac{D_{22}^f}{3k^2\left(\frac{b}{2}\right)^2} + \frac{1}{4k\left(\frac{b}{2}\right)}\right)\right]^{\frac{1}{4}} \tag{5.14}$$

Substituting L_{cr} into the expression of f_x (Eq. 5.4) the critical FLB stress, f_{cr}, can be obtained, as presented in Eq. D.1. Eq. 5.15 is a simplification of Eq. D.1 to better accommodate application in a design office. Details of the simplification process are presented in Appendix D.

$$f_{cr} = \frac{60L_{cr}^2 k^2 D_{22}^f}{t\left(\frac{b}{2}\right)^2 \pi^2\left(20\left(D_{22}^f\right)^2 + 15D_{22}^f\left(\frac{b}{2}\right)k + 3\left(\frac{b}{2}\right)^2 k^2\right)} + \frac{16D_{66}^f}{t\left(\frac{b}{2}\right)^2} + \frac{D_{11}^f \pi^2}{tL_{cr}^2} - \frac{2k}{3t\left(\frac{b}{2}\right)} \tag{5.15}$$

Finally, the critical FLB moment can be determined as:

$$M_{cr\ FLB} = f_{cr} S \tag{5.16}$$

Where *S* is the elastic section modulus of the cross section.

Predictions of experimental specimen FLB capacity based on Eq. 5.16 are shown in Table 5.2 and Figure 5.5 and discussed further in Section 5.4.2 below. These predictions are seen to better represent the observed behavior than other formulations except the FSM.

5.4.2 Validation of Eq. 5.16

Eq. 5.16 was validated using experimental results available in the literature (see Chapter 2.1) and compared with analytical results from finite strip method (FSM) analyses (as described in Chapter 4), as presented in Table 5.3. The tests conducted by Bank et al. (1996) and Pecce and Cosenza (2000) were selected, since all necessary material properties and test results were provided in these studies. It can be seen that both FSM and Eq. 5.16 have generally conservative predictions when compared with the reported experimental results, although Eq. 5.16 shows an excellent correlation with FSM analysis, with absolute differences less than 2%.

Table 5.3 Comparisons with additional experimental results

Authors	$b = d$ (mm)	t (mm)	$b/2t$	L (mm)	E_L (MPa)	E_T (MPa)	G_{LT} (MPa)	v_{LT}	M_{cr} (Nm)	FSM		Eq. 5.16	
										M_{cr} (Nm)	$\frac{\text{pred}}{\text{exp}}$	M_{cr} (Nm)	$\frac{\text{pred}}{\text{exp}}$
Bank et al. (1996)	203	9.5	11	2740	24010	7530	2630	0.31	34213	24978	0.73	25488	0.74
	203	12.7	8	2740	24610	10270	3660	0.33	69663	75424	1.08	74738	1.07
Pecce and Cosenza (2000)	102	6.4	8	1400	22000	7500	2400	0.30	9806	7031	0.72	6996	0.71

Additionally, Eq. 5.16 was validated using the experimental results obtained in this work and compared with the analytical results from both FSM analysis and Kollár's solution. Kollár's equations are widely accepted as the 'exact' solutions by many researchers. The comparisons between experimental and analytical results are presented in Table 5.2 and Figure 5.5. It can be seen that for FLB6, FLB5 and FLB4 which have relatively large flange slenderness ratios (ranging from 12 to 8), FSM analysis, Kollár's solution and Eq. 5.16 provide conservative predictions of critical FLB moments. Moreover, FSM analysis and Eq. 5.16 show better predictions of experimental data than Kollár's solution. The absolute difference between FSM

analysis and Eq. 5.16 for I-sections having a flange slenderness ranging from 12 to 8 is less than 5%. For FLB3 having the smallest flange slenderness ratio ($b/2t$ = 6), FSM analysis and Eq. 5.16 both result in unconservative predictions of critical FLB moments. The low experimentally determined FLB moment for FLB3 is caused by the interaction between local and global buckling. Such interaction has a greater effect on critical FLB moment for those I-sections having small flange slenderness ratios as well as large longitudinal ratios as will be discussed in Chapter 7.

5.4.3 Determination of Elastic Spring Constant

In early design guides for composite materials, such as ASCE (1984), the flange outstands are assumed to be simply-supported or fixed at the flange-web interface, leading to significant under- or over-predictions of critical FLB moment capacities of pGFRP I-sections, respectively. In order to improve the characterization of the boundary condition at the flange-web interface and to achieve a more accurate prediction of critical FLB moment, an elastic rotational spring constant, k, is introduced to simulate the elastic restraining effect at flange-web interface. The determination of k is critical in predicting the FLB moment capacities of pGFRP I-sections. However, there is a lack of a uniformly accepted description of k. In EUR 27666 (2016), k (Eq. 2.16) is defined in a form essentially identical to that proposed by Kollár (Eq. 5.8) but lower by a factor of 2 (when the flange and web plates have the same properties). This partially explains the poor predictive capacity of the EUR 27666 equations as demonstrated in Tables 5.1, 5.2 and Figure 5.5. In an early study, Barbero and Raftoyiannis (1993) adopted the transverse bending stiffness of the web, $(D_{22})_{web}$, as the definition of k. In this case, k is greater than that prescribed

by EUR 27666 (2016) and Kollár (2003) and consequently leads to a higher prediction of critical FLB moment.

In this study, the *k* factor proposed by Kollár (2003) (Eq. 5.8) is adopted with a modification. According to Kollár, the elastic restraint at the flange-web interface is equally divided between the two flange outstands and thus, a factor of "*1/2*" should be applied to *k*. However, in this work, it is demonstrated that by neglecting the "*1/2*" factor (as is done in Eq. 5.16), a better correlation can be found between the experimental results and analytical predictions of critical FLB moment, as shown in Table 5.2.

It is universally observed that when FLB occurs, the two compression flange outstands of an I-section rotate in the same direction as a single element experiencing an elastic rotational restraint, *k*, as shown in Figure 5.7a. That is, the flange remains continuous over the web interface. In contrast, Figure 5.7b shows a different case, in which the two flange outstands rotate in opposite directions in which case they both experience an elastic restraint of *k/2* (assuming the degree of rotation to be the same; otherwise each outstand is restrained by some fraction of *k* in which the fractions sum to *k*). These two buckling mechanisms of flange outstands may be represented using parallel and series circuit diagrams, respectively, as presented in Figure 5.7. In the parallel circuit, the two resistors, *R1* and *R2*, have the same voltage, *V*, while in the series circuit, *R1* and *R2* each have a voltage that is a fraction of *V* (assuming *R1 = R2*, each resistor has a voltage of *V/2*). As demonstrated in this work, the two flange outstands are restrained in the manner similar to the two resistors in the parallel circuit. That is, both flange outstands experience the same elastic restraint, *k*. Thus, the factor of "*1/2*" in Eq. 5.8 is inappropriate and the *k* defined in Eq. 5.11 is used. Additionally, this *k* factor is validated through experimental and analytical results, as presented previously in Section 5.4.2.

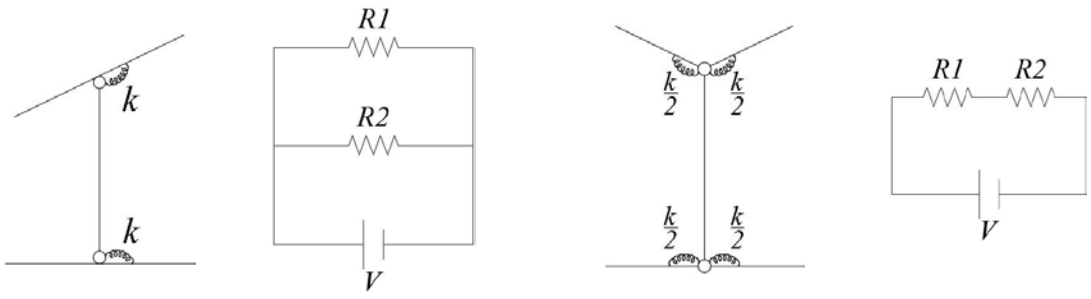

a) Two flange outstands restrained by web as a whole element (EUR 27666 2016) and parallel circuit analogy

b) Two flange outstands restrained by web as two independent elements and series circuit analogy

Figure 5.7 Modelling of the elastic rotational restraint at flange-web interface

5.4.4 Corrections to Predictions Accounting for Test Geometry

In Table 5.1 and Figure 5.5, it can be seen that analytical predictions of critical FLB moments are lower than experimental results for FLB6, FLB5 and FLB4 that were dominated by FLB behavior in tests. Such under-prediction may be an indication that the constant moment region in the test was not, in fact, an integer multiple of the natural buckling half wave length. If the constant moment region is not an integer multiple of the natural half wave length, the response of the beam will be stiffer and a higher buckling moment is expected. This effect can be seen in Figure 4.4 in the region in which only FLB is predicted ($L_b/r_y < 20$). There is a local minimum capacity at $L_b/r_y = 7$ which corresponds to the critical half wave length of the compression flange, $L_{cr} = 248$ mm (Table 4.1). As the length varies from this value, the buckling capacity increases.

In the experimental set-up, the loading points are effectively points of inflection of the resulting FLB wave and thus impose a half wave length. This effect is addressed through an analytical

study. The theoretical number of the half waves, n, over a constant moment region length, L, is given as:

$$n = \frac{L}{L_{cr}} \tag{5.17}$$

Where L_{cr} is the critical half wave length calculated using Eq. 5.14. Due to loading boundary conditions, n must be an integer; therefore, the experimentally observed half wave length, $L_{provided}$, from the observed number of half waves, n, is calculated as:

$$L_{provided} = \frac{L}{n} \tag{5.18}$$

Substituting $L_{provided}$ in place of L_{cr} in Eq. 5.15, an improved estimate of the critical FLB moment can be calculated, as presented in Table 5.4. It can be seen that using the experimentally observed half wave length, $L_{provided}$, the critical FLB moments are slightly increased, as is expected.

Therefore, in order to further improve the accuracy of the proposed FLB predictions in Section 5.4.1, a more accurate estimation of actual half wave length may be used if sufficient information is known. Knowing the boundary conditions constraining an unbraced length of a beam flange, L, Eq. 5.17 may be used to estimate the theoretical number of the half waves, n, that should develop. Rounding both up and down to the nearest integers, and applying Eq. 5.18, two possible values of *in situ* half wave length result. Applying both these in Eq. 5.15 in place of L_{cr} yields the predicted FLB capacities for the constrained unbraced length; the lower value controls the design but will still exceed the value of M_{cr} calculated with L_{cr}.

Table 5.4 Comparisons between experimental and analytical $M_{cr\ FLB}$

Specimen	L_b	n	L_{cr} (Eq. 5.15)	$L_{provided}$	Experiment	$M_{cr\ FLB}$ (Nm) predictions calculated with nominal section dimensions and $E_{L,t}$			
	mm		mm	mm	M_{cr} (Nm)	Eq. 5.16 (L_{cr})		Eq. 5.16 ($L_{provided}$)	
						M_{cr}	pred/exp	M_{cr}	pred/exp
FLB6	900	4	216	225	9304	8522	0.92	8539	0.92
	800	4	216	200	9330	8522	0.91	8592	0.92
	600	3	216	200	10680	8522	0.80	8592	0.80
	400	2	216	200	10140	8522	0.84	8592	0.85
FLB5	900	5	191	180	11259	9975	0.89	10022	0.89
	800	4	191	200	11432	9975	0.87	9998	0.87
	600	3	191	200	11351	9975	0.88	9998	0.88
	400	2	191	200	13548	9975	0.74	9998	0.74
FLB4	900	5	166	180	14485	12056	0.83	12144	0.84
	800	5	166	160	14215	12056	0.85	12088	0.85
	600	4	166	150	14060	12056	0.86	12200	0.87
	400	2	166	200	14668	12056	0.82	12511	0.85

6.0 LATERAL TORSIONAL BUCKLING BEHAVIOR

6.1 EXPERIMENTAL PROGRAM

Three-point bending tests were conducted to study the lateral torsional buckling (LTB) behavior of thin-walled pGFRP I-sections subject to flexure. The simply supported spans (Figure 6.1) and resulting longitudinal slenderness ratios, L_b/r_y (Table 6.1), were selected to capture the global lateral buckling phenomenon while mitigating, to the extent possible, flange local buckling behavior. The 900 kN-capacity test set-up is illustrated in Figure 6.2. Lateral support was only provided at the beam simple supports (Figure 6.2a). Loading was applied through a "two-pin link" at midspan (Figure 6.2b) which provides minimal lateral restraint to LTB; thus the unbraced length, L_b is assumed to be the simple span length. In this work, the load is appied at the top flange of the I-beam, which has been shown to result in a reduction of nearly 30% in the obtained critical load as compared with loading at the shear center (Nguyen et al. 2014). This loading position is specifically considered in the design equations for critical LTB moment proposed by EUR 27666 (2016), while in ASCE (2010), the proposed LTB equation assumes the load is applied at shear center.

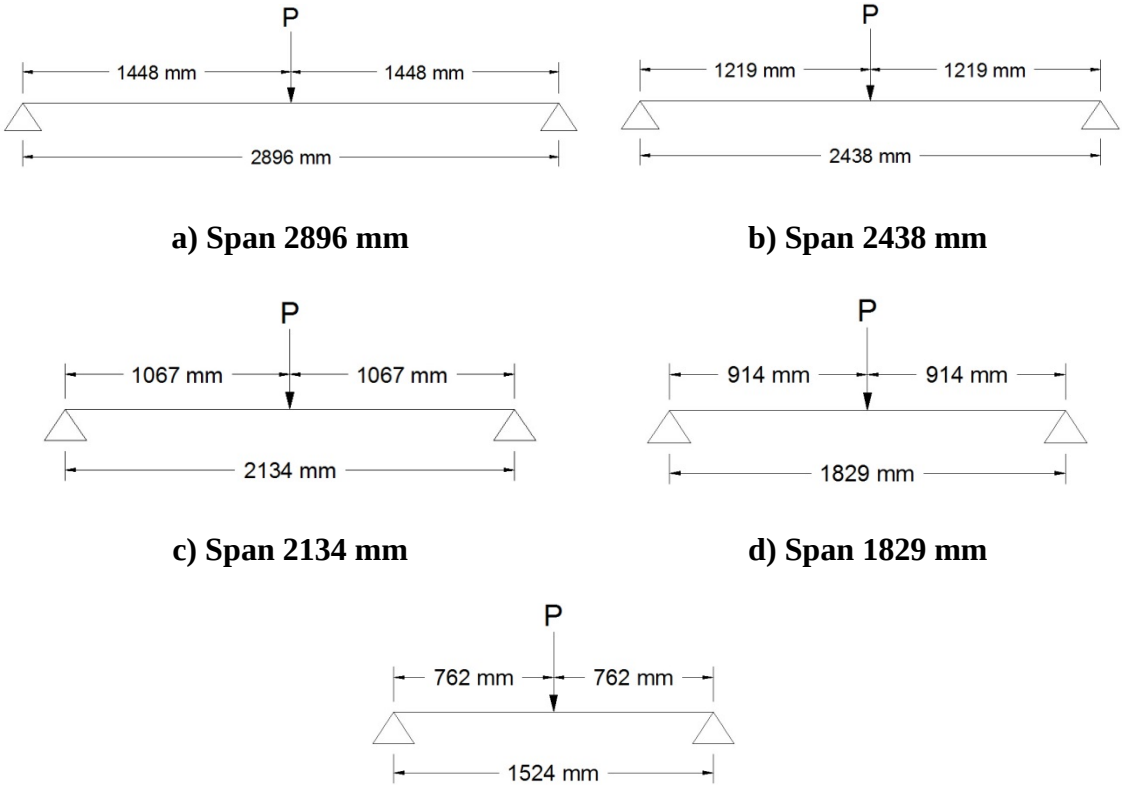

a) Span 2896 mm **b) Span 2438 mm**

c) Span 2134 mm **d) Span 1829 mm**

e) Span 1524 mm

Figure 6.1 Three-point bending tests span arrangements for LTB tests

Table 6.1 Longitudinal slenderness ratios of LTB specimens

Specimen	Section geometries *d* x *b* x *t*	r_y (mm)	Nominal L_b/r_y for test spans				
			L_b = 2896 mm	2438 mm	2134 mm	1829 mm	1524 mm
LTB6	152.4 x 152.4 x 6.35 mm	36.45	79	67	59	50	42
LTB5	152.4 x 127.0 x 6.35 mm	29.47	98	83	72	62	52
LTB4	152.4 x 101.6 x 6.35 mm	22.61	128	108	94	81	67
LTB3	152.4 x 76.2 x 6.35 mm	15.94	182	153	134	115	96
LTB2	152.4 x 50.8 x 6.35 mm	9.62	301	253	222	190	158

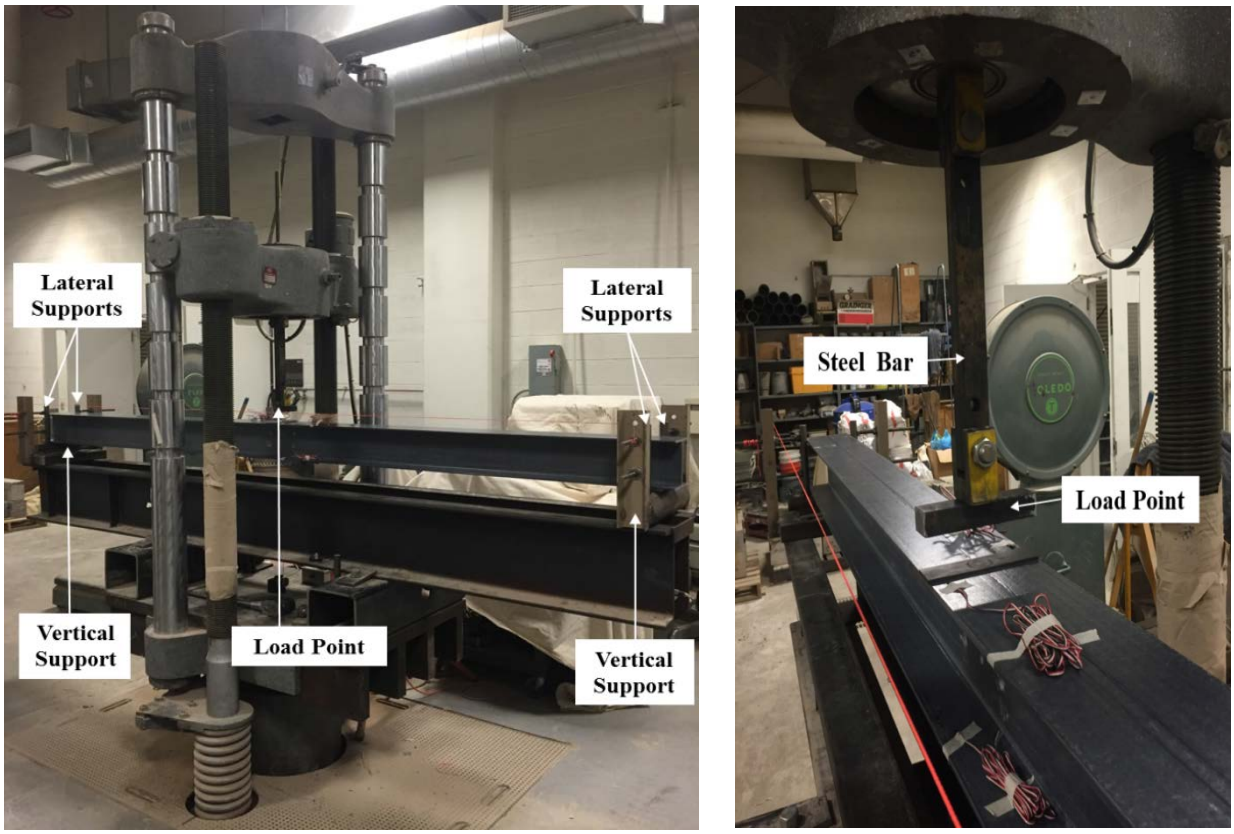

a) Overall view of test set-up **b) Two-pin link**

Figure 6.2 Test set-up of three-point bending tests

Six specimens having five section geometries were used: two 6 x 6 x ¼ (LTB6-1 and 6-2), one 6 x 5 x ¼ (LTB5), one 6 x 4 x1/4 (LTB4), one 6 x 3 x ¼ (LTB3) and one 6 x 2 x ¼ (LTB2). Measured and nominal specimen dimensions are presented in Table 3.4. Measured material properties are provided in Table 3.3. The two LTB6 specimens were also used to investigate the effect of test/load history on the specimens. No effect from retesting specimens in this study was found since LTB deflections were controlled to result in only low elastic stresses in the pGFRP I-sections. Therefore, the LTB5 to LTB2 section geometries were only tested using one specimen. Each specimen was tested in two orientations such that both flanges are tested as the compression flange. Additionally, each specimen was tested over five clear span lengths (Figure

6.1), beginning with the longest (lowest buckling load) in all cases. In this experimental program, 25 different longitudinal slenderness ratios, ranging from 42 to 301, were included, as indicated in Table 6.1. This range was believed to be sufficient to capture pure LTB behavior and interaction of LTB with FLB. Once again, this is seen in Figure 4.4 for the LTB6 specimens for which the tested values of L_b/r_y range from 42 to 79.

LVDT position transducers, electrical resistance strain gages, and digital images were used to capture the onset of LTB so as to establish the critical LTB load. Lateral displacements at mid-span are constant until the onset of LTB and begin to increases rapidly as the beam buckles laterally (Figure 2.1b). A representative example of such lateral displacement (LTB3 tested over a span of 2896 mm) is shown in Figure 6.3. The applied load versus lateral displacement plot for this test (Figure 6.3b) indicates buckling at an applied force P_{cr} of 2.65 kN (plus the self weight of the beam). In Figure 6.3b, it can be seen that there exists an initial lateral displacement due to seating of the load and beam imperfections; this apparent displacement is an artifact of the test set-up and method of displacement measurement and is neglected when determining the critical LTB moment.

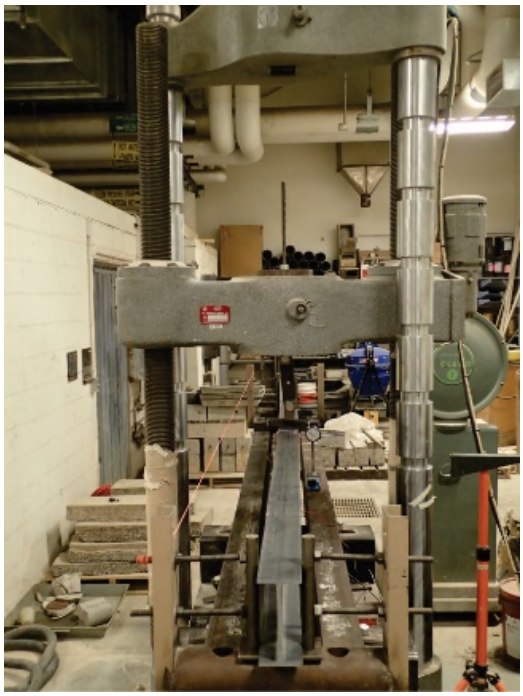

a) Lateral torsional buckling of pGFRP I-section

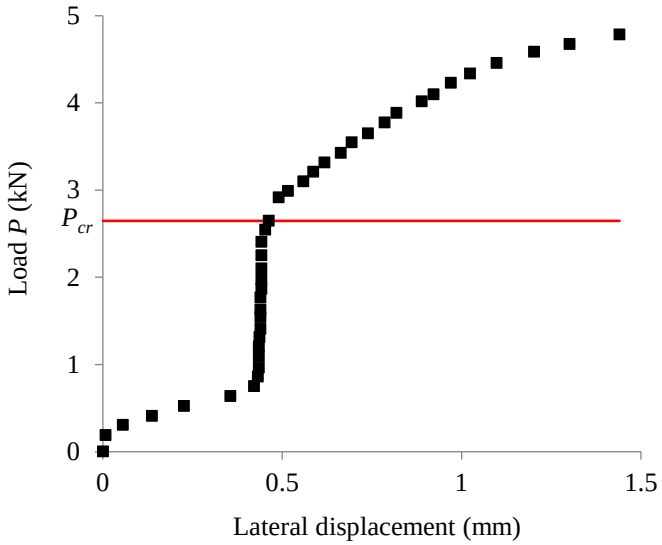

b) Lateral displacement at mid-span showing buckling at an load of 2.65 kN

Figure 6.3 Lateral torsional buckling (LTB3 over spans of 2896 mm)

6.2 EXPERIMENTAL RESULTS

In the experimental program, 86 three-point bending tests were conducted: 24 tests on LTB6, 15 on LTB5, 11 on LTB4, 19 on LTB3 and 17 on LTB2. The test results are presented in Table 6.2 and Figures 6.4. Images and flange stress-strain and load-lateral displacement curves for all specimens are reported in Appendix A.2.

The averages and coefficients of variation (COV) of tests results are shown in Table 6.2. The COVs are uniformly equal to or less than 0.10, except for those tests on LTB2 having the two greatest spans of 2896 and 2438 mm; the greater variation in this very slender specimen may be due to the initial imperfections in the specimen and the relatively low applied loads achieved.

In particular, the process of cutting the flanges to fabricate LTB2 (see Section 3.4) was found to result in some sweep and camber, presumably resulting from the release of residual stresses in this specimen having lower weak axis stiffness.

The experimentally determined critical LTB moments, M_{cr}, are plotted against the longitudinal slenderness ratios, L_b/r_y, in Figure 6.4. From the plot of LTB6, LTB5, LTB4 and LTB2, it can be seen that critical LTB moment generally increases, as the longitudinal slenderness decreases. Due to the initial imperfections of LTB3, the relationship between critical LTB moment and longitudinal slenderness is not as evident as in other tests.

Table 6.2 Experimental results and predictions of lateral torsional buckling specimens

Specimen	Span	Experiment		$M_{cr\ LTB}$ (Nm) predictions calculated with nominal section dimensions and $E_{L,t}$									
	mm	M_{cr} (Nm)	Average M_{cr} (Nm) (COV)	ASCE (2010)		EUR 27666 (2016)		Sapkás and Kollár (2002)		FSM		Eq. 6.16	
				M_{cr}	pred / exp	M_{cr}	pred / exp	M_{cr}	pred / exp	M_{cr}	pred / exp	M_{cr}	pred / exp
LTB6	2896	3230	3316 (0.05)	11775	3.55	7017	2.12	6749	2.04	8388	2.53	7467	2.25
		3257											
		3279											
		3215											
		3599											
		2639*											
	2438	4056	4153 (0.05)	16242	3.91	9556	2.30	9213	2.22	11378	2.74	10197	2.46
		4040											
		4092											
		4082											
		4062											
		4647											
		4093											
	2134	5320	5022 (0.06)	20939	4.17	12224	2.43	11635	2.32	14404	2.87	13054	2.60
		4736											
		5260											
		4773											
		3582*											
	1829	6368	6195 (0.02)	28172	4.55	16332	2.64	15266	2.46	18809	3.04	17466	2.82
		6136											
		6152											
		6124											
	1524	6988	7058 (0.01)	40162	5.69	23141	3.28	21006	2.98	25354	3.59	24783	3.51
		7127											
LTB5	2896	3252	3257 (0.01)	7080	2.17	4311	1.32	4205	1.29	5119	1.57	4570	1.40
		3275											
		3264											
		3236											
	2438	4093	4093 (0)	9673	2.36	5786	1.41	5649	1.38	6920	1.69	6155	1.50
		4093											
	2134	3825	3822 (0)	12397	3.24	7335	1.92	7094	1.86	8775	2.30	7813	2.04
		3821											
		3821											
	1829	5313	5315 (0.03)	16587	3.12	9716	1.83	9276	1.75	11557	2.17	10369	1.95
		5312											
		5518											
		5115											
	1524	5118	5112 (0)	23531	4.60	13662	2.67	12771	2.50	15968	3.12	14606	2.86
		5106											
LTB4	2896	3598	3590 (0)	3886	1.08	2455	0.68	2424	0.68	2846	0.79	2587	0.72
		3581											
	2438	3560	3431 (0.05)	5225	1.52	3220	0.94	3177	0.93	3796	1.11	3407	0.99
		3302											
	2134	4065	4143 (0.03)	6627	1.60	4019	0.97	3939	0.95	4780	1.15	4261	1.03
		4292											

Table 6.2 (continued)

Specimen	Span	Experiment		$M_{cr\ LTB}$ (Nm) predictions calculated with nominal section dimensions and $E_{L,t}$									
	mm	M_{cr} (Nm)	Average M_{cr} (Nm) (COV)	ASCE (2010)		EUR 27666 (2016)		Sapkás and Kollár (2002)		FSM		Eq. 6.16	
				M_{cr}	pred / exp	M_{cr}	pred / exp	M_{cr}	pred / exp	M_{cr}	pred / exp	M_{cr}	pred / exp
		4070											
	1829	4293	4187 (0.04)	8780	2.10	5244	1.25	5096	1.22	6271	1.50	5575	1.33
		4082											
	1524	4733	4743 (0)	12343	2.60	7272	1.53	6968	1.47	8684	1.83	7750	1.63
		4752											
LTB3	2896	1943	1897 (0.05)	1886	0.99	1272	0.67	1269	0.67	1403	0.74	1329	0.70
		1793											
		1957											
		759**											
		669*											
	2438	1767**	1095 (0.02)	2467	2.25	1609	1.47	1602	1.46	1824	1.67	1688	1.54
		1075											
		1101											
		1109											
	2134	1909	1865 (0.04)	3070	1.65	1956	1.05	1939	1.04	2257	1.21	2057	1.10
		1901											
		1786											
	1829	1727	1788 (0.04)	3990	2.23	2483	1.39	2447	1.37	2913	1.63	2620	1.47
		1843											
		1725											
		1857											
	1524	2044	2045 (0)	5506	2.69	3349	1.64	3272	1.60	3980	1.95	3546	1.73
		2043											
		2048											
LTB2	2896	409	419 (0.19)	767	1.83	580	1.39	583	1.39	581	1.39	599	1.43
		501											
		346											
	2438	681	587 (0.11)	961	1.64	700	1.19	703	1.20	725	1.24	725	1.24
		565											
		550											
		550											
	2134	952	964 (0.02)	1157	1.20	817	0.85	818	0.85	869	0.90	848	0.88
		976											
	1829	815	893 (0.10)	1448	1.62	990	1.11	987	1.10	1082	1.21	1030	1.15
		919											
		826											
		1011											
	1524	1368	1323 (0.07)	1918	1.45	1265	0.96	1253	0.95	1423	1.08	1320	1.00
		1367											
		1192											
		1365											

* Premature failure due to test set-up.

** Significant outlier determined using Grubbs' test ($\alpha = 0.05$); data not included in averages.

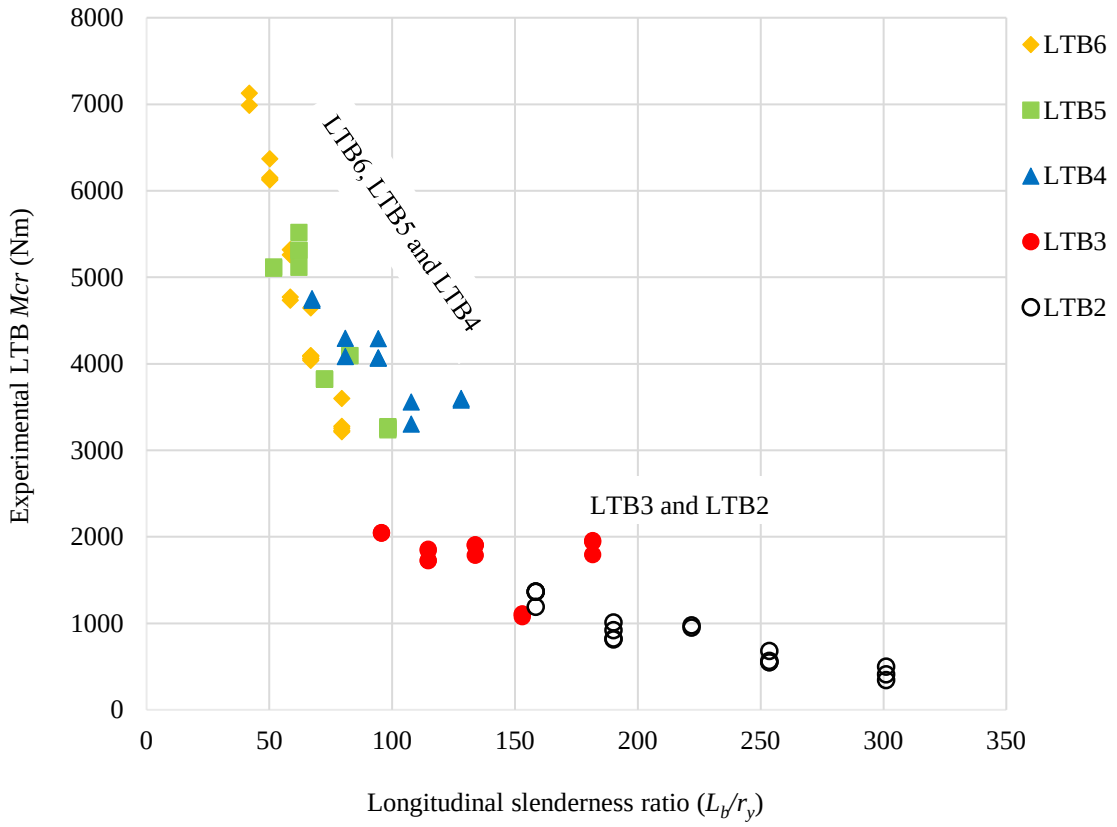

Figure 6.4 Critical LTB moments versus longitudinal slenderness ratios

6.3 COMPARISONS WITH STANDARDS, NUMERICAL AND FSM MODELING

Experimental results were compared with the critical LTB moments provided by design guides (ASCE 2010 and EUR 27666 2016), Sapkás and Kollár's (2002) solution and FSM modeling, as presented in Table 6.2 and Figures 6.5 – 6.9. The error bars of the experimental results in Figures 6.5 – 6.9 represent one standard deviation. The averages of experimental results are also presented in Table 6.2.

Two design guides, ASCE (2010) and EUR 27666 (2016), were used to predict the test results. Using ASCE (2010) the critical LTB moments were obtained assuming that the load was

applied at the shear center of an I-section, which is expected to lead to an overestimation of moment capacities on the order of 40% for the specimens loaded at their top flange (Nguyen et al. 2014). Additionally, Sapkás and Kollár's solution and FSM analysis were also used to predict the experimental data.

Generally, ASCE, EUR 27666, Sapkás and Kollár's solution and FSM analysis provide unconservative predictions of critical LTB moment. The over-prediction results partially from the interaction between and FLB, WLB and LTB observed in the tests. The interaction is found to affect the LTB behavior, leading to a reduction in the critical LTB moment. Such interaction is more significant for specimens having greater flange slenderness ratios, such as LTB6 and LTB5. For more compact sections, such as LTB4, LTB3 and LTB2, the LTB predictions become much better as FLB is mitigated. As seen in summary of prediction accuracy given in Table 6.3, the flange slenderness ratio $b/2t = 8$ appears to separate observed behaviors and therefore predictive capacity of LTB equations.

Specimen and test set-up imperfections also impact the observed overestimation of capacity (calculated for "perfect" specimens). The sensitivity of LTB tests to imperfections has also been noted by other researchers (Mottram 1992).

Table 6.3 Summary of ratios of predicted to experimental capacity for LTB tests

Slenderness ratio	Ratios	ASCE (2010)[1]	EUR 27666 (2016)	Sapkás and Kollár (2002)	FSM	Eq. 6.16
b/2t > 8 LTB6 and 5	average	3.74	2.19	2.08	2.56	2.34
	COV	0.29	0.27	0.25	0.25	0.28
b/2t ≤ 8 LTB4, 3 and 2	average	1.76	1.14	1.13	1.29	1.20
	COV	0.29	0.26	0.26	0.28	0.27

[1] ASCE does not account for the reduction in capacity expected when the load is applied at top flange. A reduction in predicted capacity of approximately 30% is expected to account for this effect (Nguyen et al. 2014)

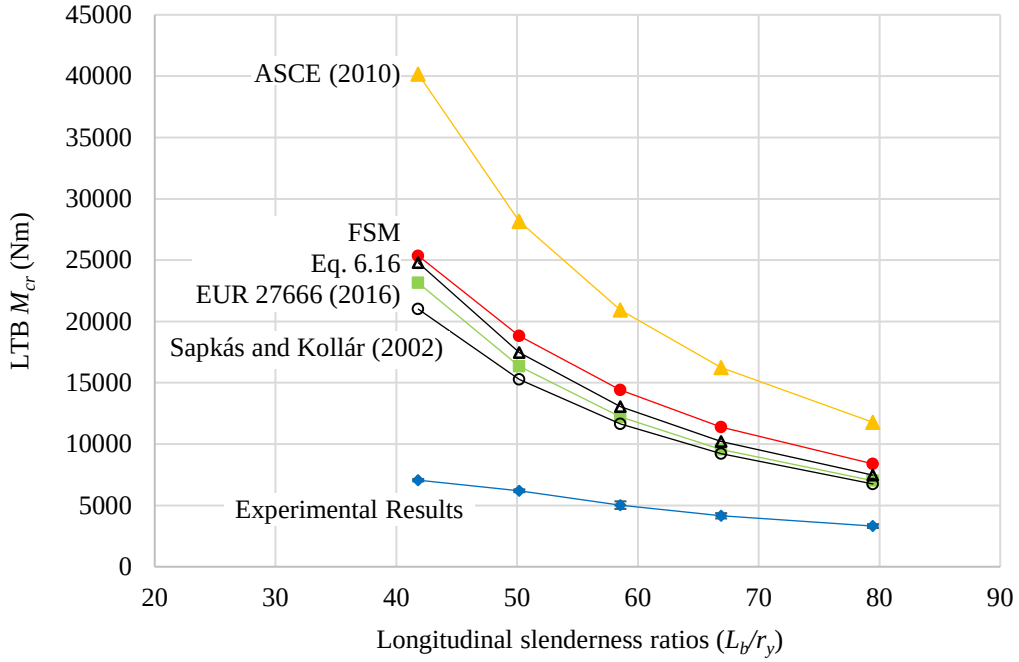

Figure 6.5 Critical LTB moments versus longitudinal slenderness ratios for LTB6

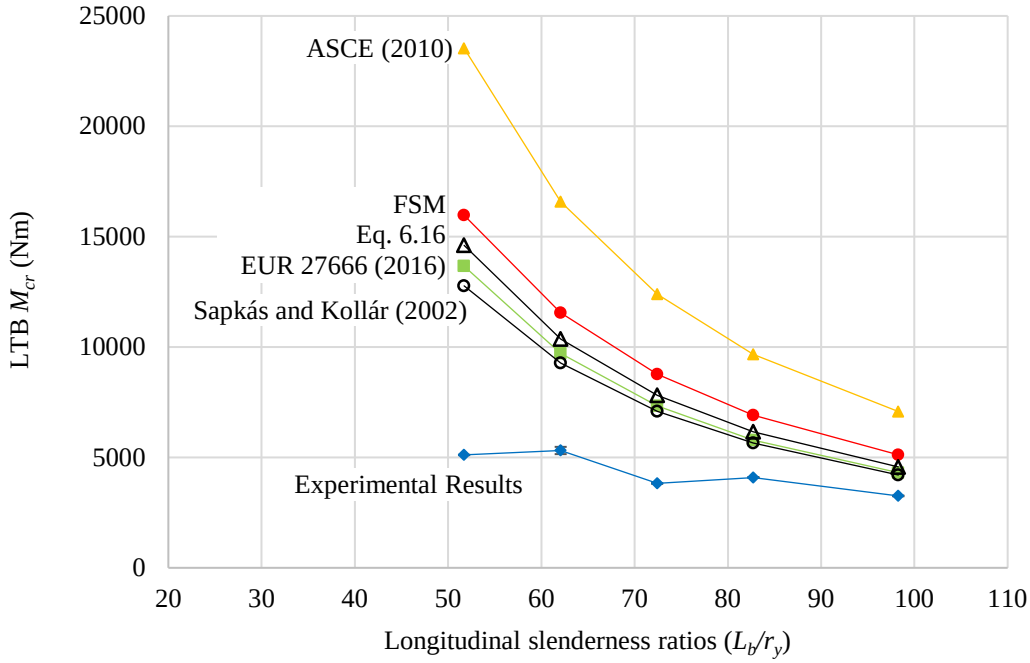

Figure 6.6 Critical LTB moments versus longitudinal slenderness ratios for LTB5

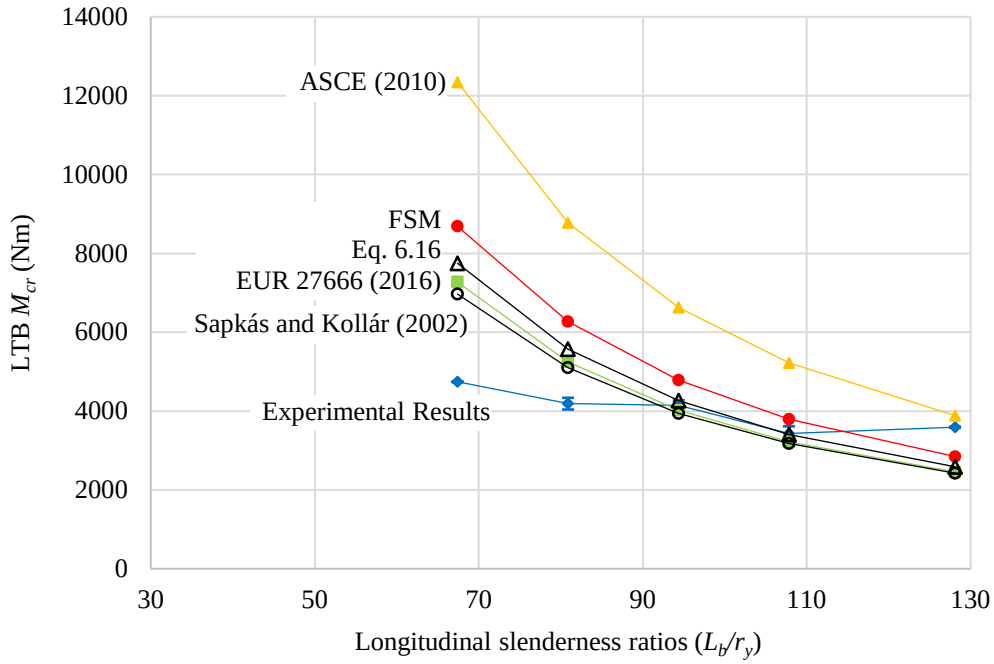

Figure 6.7 Critical LTB moments versus longitudinal slenderness ratios for LTB4

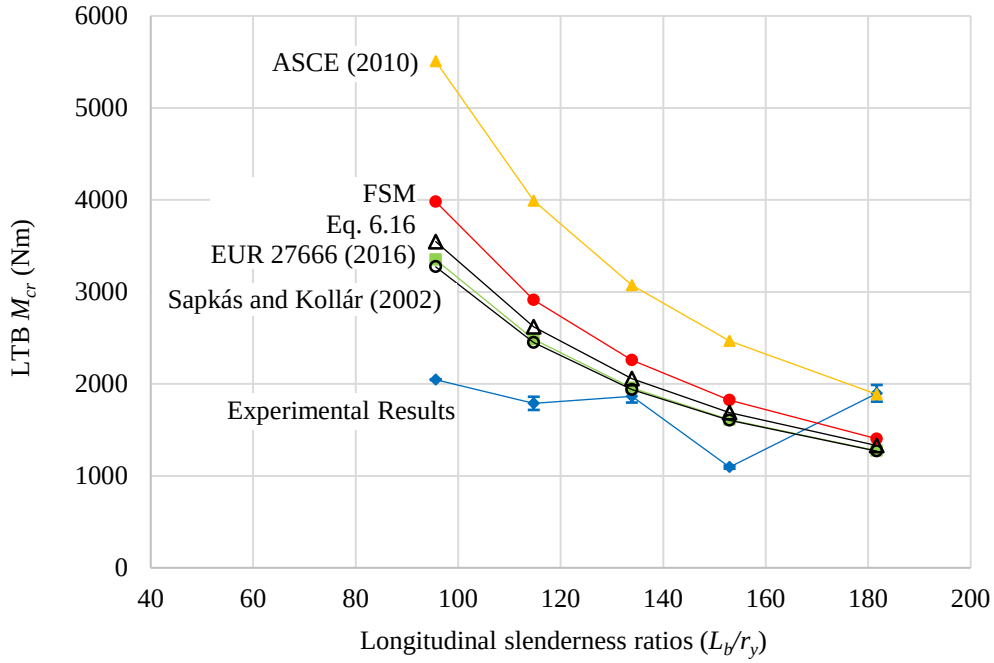

Figure 6.8 Critical LTB moments versus longitudinal slenderness ratios for LTB3

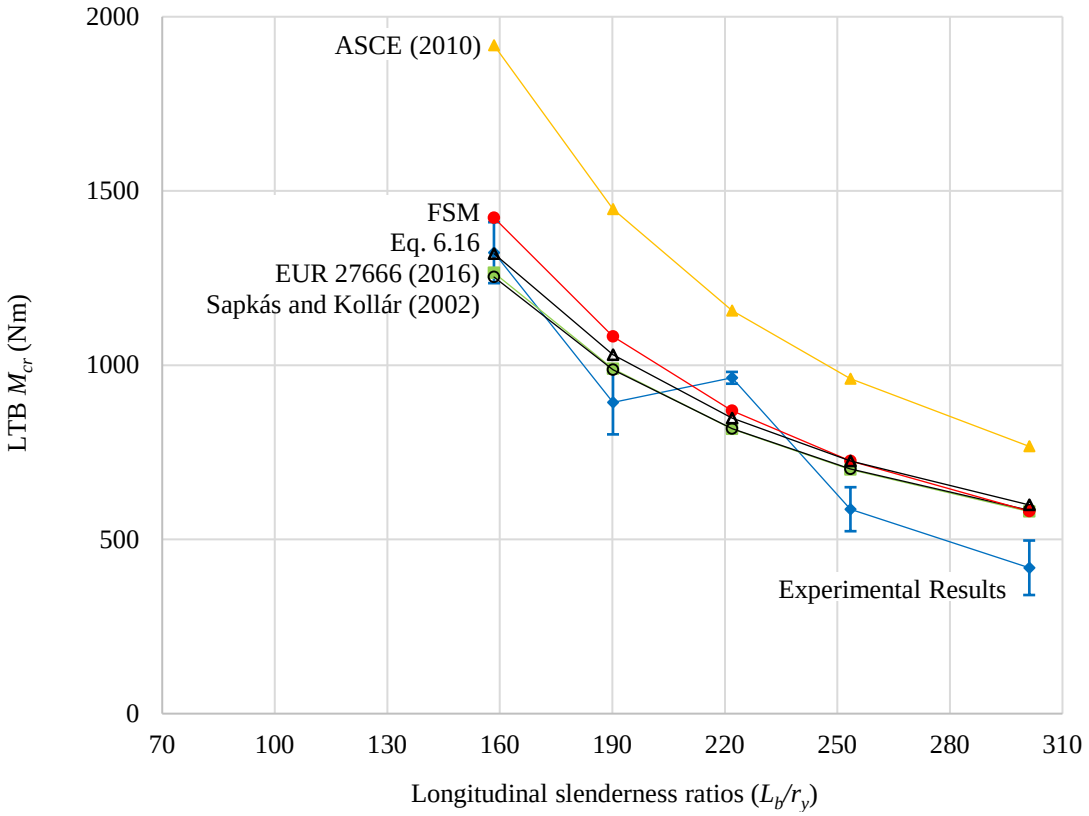

Figure 6.9 Critical LTB moments versus longitudinal slenderness ratios for LTB2

6.4 ANALYTICAL STUDY OF LATERAL TORSIONAL BUCKLING

6.4.1 Formulations

The energy method proposed by Timoshenko and Gere (1961) for LTB of an I-section made of isotropic material is used to develop the equation for LTB of a pGFRP I-beam. The LTB behavior of an I-section can be decomposed into: strong-axis bending, weak-axis bending, torsion and warping of the beam. The critical LTB load can be found through the state of equilibrium between the internal strain energy and external virtual work that are produced in the LTB behaviors; that is:

$$U - W = 0 \tag{6.1}$$

Since the terms will balance, the energy involved in the strong-axis bending of the section can be excluded from this analysis. Only the weak-axis bending, torsion and warping of the I-beam need to be considered in Eq. 6.1. The global and local coordinate systems are presented in Figure 6.10. The displacements in *x*, *y* and *z* directions are represented as *u*, *v* and *w*, respectively. In the following, $t = t_w = t_f$.

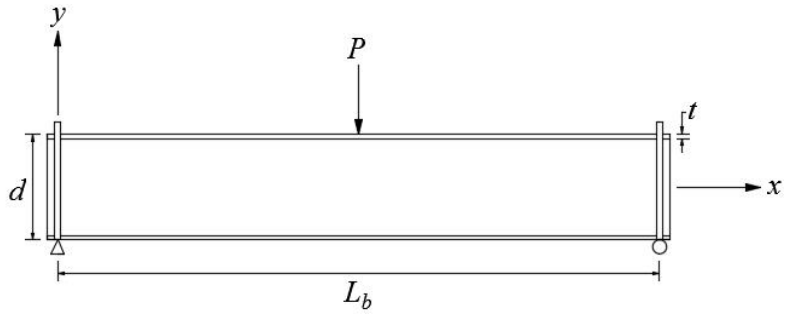

a) Global coordinate system (elevation)

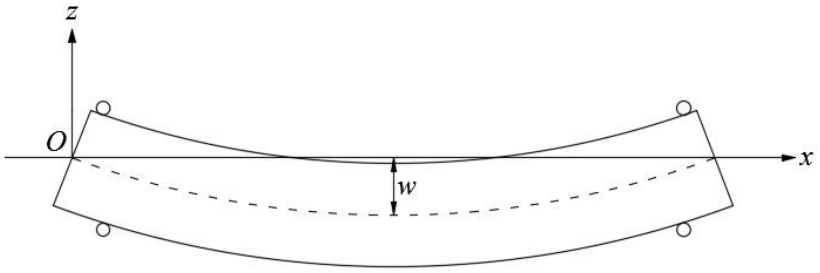

b) Plan view of LTB

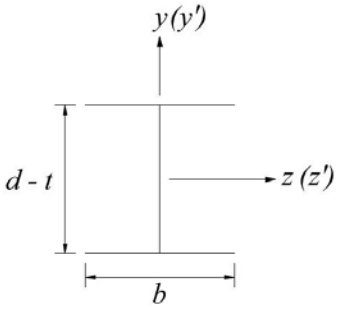

c) Cross section view without LTB

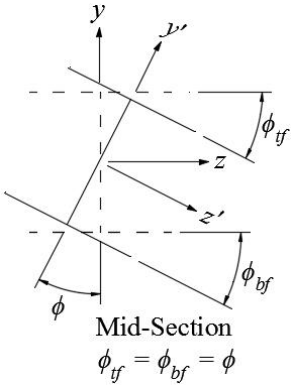

d) Cross section view with torsion

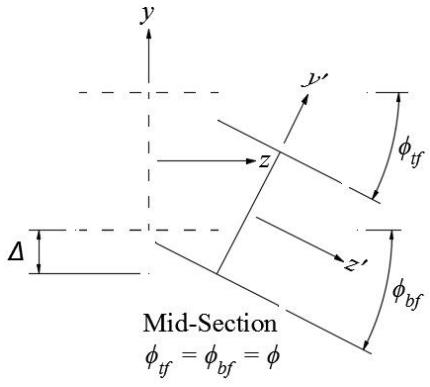

e) Cross section view with torsion and weak-axis (*y'*-axis) bending

Figure 6.10 Global (*x*, *y*, *z*) and local (*x*, *y'*, *z'*) coordinate systems in LTB of I-beam

The strain energy corresponding to weak-axis (*y'*-axis) bending, torsion and warping of I-beam are (Timoshenko and Gere 1961):

$$U_{weak-axis\ bending} = \frac{1}{2} E_L I_{y'} \int_0^{L_b} \left(\frac{d^2 w}{dx^2}\right)^2 dx \tag{6.2}$$

$$U_{torsion} = \frac{1}{2} G_{LT} J \int_0^{L_b} \left(\frac{\partial \phi}{\partial x}\right)^2 dx \tag{6.3}$$

$$U_{warping} = \frac{1}{2} E_L C_w \int_0^{L_b} \left(\frac{\partial^2 \phi}{\partial x^2}\right)^2 dx \tag{6.4}$$

Where E_L is the longitudinal modulus of elasticity; $I_{y'}$ is the moment of inertia about the local weak-axis *y'*; and, together, $E_L I_{y'}$ is the weak-axis bending stiffness of the beam. In pure LTB of an I-beam, $E_L I_{y'} = E_L I_y$, since the geometry at any section is assumed to be unchanged. G_{LT} is the shear modulus; J is the section torsional constant; C_w is the section warping constant; ϕ is the section torsional angle; and L_b is the laterally unbraced length of a beam.

In this work, following Timoshenko's method, the vertical displacement produced in the strong-axis bending is excluded from the energy analysis. Only the vertical displacement introduced by weak-axis (*y'*-axis) bending (Δ in Figure 6.10e) is used to calculate the external virtual work. Δ is given as (Timoshenko and Gere 1961):

$$\Delta = \phi \frac{d^2 w}{dx^2} x dx \tag{6.5}$$

Furthermore, the work by load P resulting from LTB along the entire span is:

$$W = P \int_0^{L_b} \phi \frac{d^2 w}{dx^2} x dx \tag{6.6}$$

Additionally, the effect of vertical load position is considered by introducing an additional vertical displacement to the load P:

$$W_{load\ position\ effect} = P\frac{a(\phi^2)_{x=\frac{L_b}{2}}}{2} \tag{6.7}$$

Where a is the distance from the location of application of load to the shear center, defined in Figure 6.11; and $(\phi)_{x=Lb/2}$ is the rotational angle at the mid-section where the load P is applied.

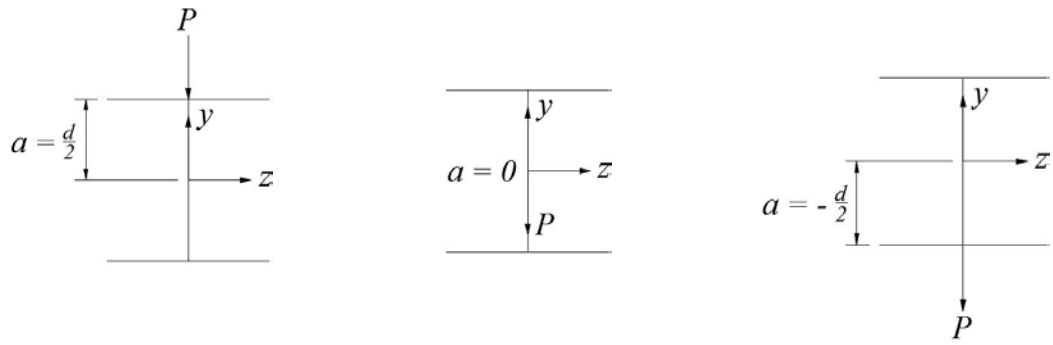

a) Load at top flange **b) Load at shear center** **c) Load at bottom flange**

Figure 6.11 Vertical load positions

Substituting Eqs. 6.2, 6.3, 6.4, 6.6 and 6.7 into Eq. 6.1, yields:

$$\frac{1}{2}E_L I_{y'}\int_0^{L_b}\left(\frac{d^2w}{dx^2}\right)^2 dx + \frac{1}{2}G_{LT}J\int_0^{L_b}\left(\frac{\partial\phi}{\partial x}\right)^2 dx + \frac{1}{2}E_L C_w\int_0^{L_b}\left(\frac{\partial^2\phi}{\partial x^2}\right)^2 dx$$

$$= P\int_0^{L_b}\phi\frac{d^2w}{dx^2}xdx + P\frac{a(\phi^2)_{x=\frac{L_b}{2}}}{2} \tag{6.8}$$

Additionally, the weak-axis bending behavior of the I-beam can be expressed as (Timoshenko and Gere 1961):

$$EI_{y'}\frac{d^2w}{dx^2} = M_{y'} \tag{6.9}$$

Where $M_{y'}$ is the weak-axis bending moment, which is calculated as:

$$M_{y'} = \frac{P}{2}\left(\frac{L_b}{2} - x\right)\phi \tag{6.10}$$

Thus, Eq. 6.9 can be expressed as:

$$EI_{y'}\frac{d^2w}{dx^2} = \frac{P}{2}\left(\frac{L_b}{2} - x\right)\phi \tag{6.11}$$

Substituting Eq. 6.11 into Eq. 6.8, yields:

$$\frac{1}{2}EI_{y'}\int_0^{L_b}\left[\frac{\frac{P}{2}\left(\frac{L_b}{2}-x\right)\phi}{EI_{y'}}\right]^2 dx + \frac{1}{2}G_{LT}J\int_0^{L_b}\left(\frac{\partial\phi}{\partial x}\right)^2 dx + \frac{1}{2}E_L C_w\int_0^{L_b}\left(\frac{\partial^2\phi}{\partial x^2}\right)^2 dx$$

$$= P\int_0^{L_b}\phi\left[\frac{\frac{P}{2}\left(\frac{L_b}{2}-x\right)\phi}{EI_{y'}}\right]xdx + P\frac{a(\phi^2)_{x=\frac{L_b}{2}}}{2} \tag{6.12}$$

In order to obtain an explicit equation for critical LTB load, an appropriate shape function which respects the boundary conditions at both ends of the beam needs to be selected. In this work, a sinusoidal function is used to simulate the rotational angle, ϕ, along the laterally buckled I-beam:

$$\phi = c\sin\left(\frac{\pi x}{L_b}\right) \tag{6.13}$$

Where c is a constant coefficient. At both ends ($x = 0$ and L_b), $\phi = 0$ and at midspan, ϕ = c. Thus, the boundary conditions are satisfied. Substituting Eq. 6.13 into Eq. 6.12 and replacing $E_L I_{y'}$ with $E_L I_y$, the critical load, P_{cr}, can be obtained:

$$P_{cr} = \frac{48E_L I_y\pi^2}{L_b^3(6+\pi^2)}\left[-a + 2\sqrt{\frac{a^2}{4} + \frac{(6+\pi^2)}{192E_L I_y}(C_w E_L\pi^2 + G_{LT}JL_b^2)}\right] \tag{6.14}$$

The critical LTB moment is given as:

$$M_{cr} = \frac{1}{4}P_{cr}L_b = \frac{12}{6+\pi^2}\frac{\pi^2}{L_b^2}E_L I_y\left[-a + 2\sqrt{\frac{a^2}{4} + \frac{6+\pi^2}{192E_L I_y}(C_w E_L\pi^2 + G_{LT}JL_b^2)}\right] \tag{6.15}$$

In order to expand the applicable range of Eq. 6.15, the effect of moment gradient under various loading conditions is considered using the moment modification factor, C_b (defined in Eq. 2.34). Thus, the critical LTB moment that accounts for various loading conditions is:

$$M_{cr} = \frac{C_b}{1.32}\frac{12}{6+\pi^2}\frac{\pi^2}{L_b^2}E_L I_y\left[-a + 2\sqrt{\frac{a^2}{4} + \frac{6+\pi^2}{192E_L I_y}(C_w E_L \pi^2 + G_{LT} J L_b^2)}\right] \quad (6.16)$$

It is seen that Eq. 6.16 has a similar form to Eq. 2.38, which is the critical LTB load for a doubly symmetric I-beam subject to variable bending given by EUR 27666 (2016).

6.4.2 Validation of Eq. 6.16

Eq. 6.16 was first validated using experimental results available in the literature (see Chapter 2.2), as presented in Table 6.4. The tests conducted by Nguyen et al. (2015) were selected, since necessary material properties and test results were provided in this study. It can be seen that both FSM and Eq. 6.16 provide conservative predictions of critical LTB moments when compared with experimental results from Nguyen's study. Additionally, Eq. 6.16 is found to have a better agreement with experimental results over FSM. Such discrepancy between FSM and Eq. 6.16 mainly result from the low assumed material properties E_T (adopted from the manufacturer's design manual) used in FSM, while E_T is not required in Eq. 16.

Table 6.4 Comparisons with additional experimental results

Author	b (mm)	d (mm)	t (mm)	L_b (mm)	L_b/r_y	E_L (MPa)	G_{LT} (MPa)	Experiment	FSM		Eq. 6.16	
								M_{cr} (Nm)	M_{cr} (Nm)	pred / exp	M_{cr} (Nm)	pred / exp
Nguyen et al. (2015)	60	120	6	4064	322	30600	4200	732	518	0.71	626	0.86
	60	120	6	3454	274	30600	4200	933	624	0.67	737	0.79
	60	120	6	2844	225	30600	4200	1166	788	0.68	905	0.78
	60	120	6	2438	193	30600	4200	1262	956	0.76	1076	0.85
	60	120	6	1828	145	30600	4200	1732	1411	0.81	1538	0.89

Eq. 6.16 was also validated using the experimental results obtained in this work and the analytical predictions from both FSM analysis and Sapkás and Kollár's solutions, as presented in Table 6.2 and Figures 6.5 – 6.9. It is found that Eq. 6.16 provides conservative predictions of critical LTB moments for I-beams having relatively large lateral slenderness ratios and small flange slenderness ratios (see Tables 6.2 and 6.3). This trend is similar to that of Sapkás and Kollár's solutions and FSM analysis. The absolute differences between Eq. 6.16 and FSM analysis are less than 11%.

The uniform over-prediction of experimentally observed capacity suggests that the interaction between FLB, WLB and LTB is affecting LTB capacity. This interaction is addressed in the following chapter.

7.0 INTERACTIVE BUCKLING BEHAVIOR

7.1 EXPERIMENTAL RESULTS

The interaction between local (FLB and WLB) and global (LTB) buckling, namely interactive buckling, was observed in this study in the initial four-point bending test on FLB5 over a span of 2900 mm and verified in another test on FLB5 over a span of 1800 mm. In order to mitigate the undesired lateral displacement and such interaction, additional lateral supports were applied in the subsequent FLB tests. By comparing the test results obtained with and without lateral supports, it can be found that the critical FLB moment decreases when additional lateral supports are not applied (see Figure 5.4). Therefore, the interaction between local and global buckling results in a reduction in the critical FLB moment.

Additionally, various extents of interaction between local and global buckling were observed in all three-point bending tests. An example is shown in Figure 7.1. Such interaction results in a reduced critical LTB moment and poor performance of predictive models, as presented in Section 6.3.

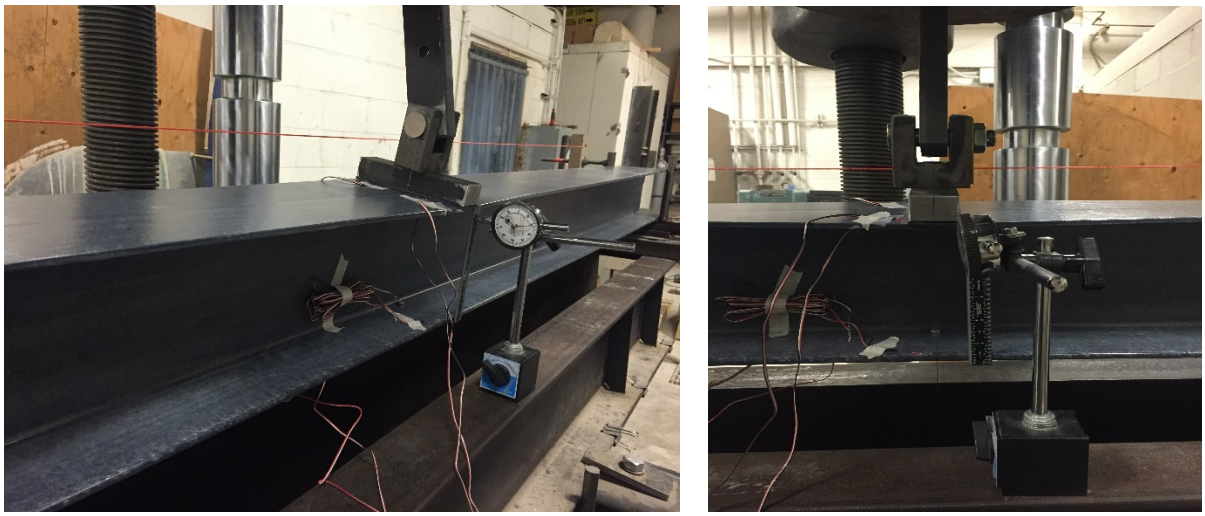

a) LTB of LTB6 **b) FLB of LTB6**

Figure 7.1 Interaction between local and global buckling (LTB6 under span of 2896 mm)

7.1.1 Summary of Experimental Behaviors

Figure 7.2 summarizes the observed experimental behaviors based on flange ($b/2t$) and beam (L_b/r_y) slenderness ratios. The marked differentiation between LTB and interaction behavior apparently demarked by $b/2t$ less than or greater than 8 is clear. LTB was mitigated in most FLB tests so no direct conclusion can be made regarding L_b/r_y, however specimens as short as L_b/r_y = 42 demonstrated some interaction effects (LTB6 under span of 1524 mm).

Figure 7.3 extends the data shown in Figure 7.2 by including the observed buckling capacity, M_{cr}, normalized by the flexural capacity of the cross section, SF_{Lt}, in which S is the elastic section modulus of the section and F_{Lt} is the longitudinal strength of the pGFRP. In this image, black represents LTB failure, blue is FLB and red is interactive buckling. The effects of both local and global slenderness on capacity is easily seen. The further detrimental effects of buckling interaction are also evident in the reduced capacities of specimens having high local slenderness although lower global slenderness. Finally, it is noted that the reduction in capacity

for anisotropic pGFRP due to buckling effects is more significant than for isotropic materials such as steel. In this study, the highest capacity achieved was M_{cr}/SF_{Lt} = 0.577.

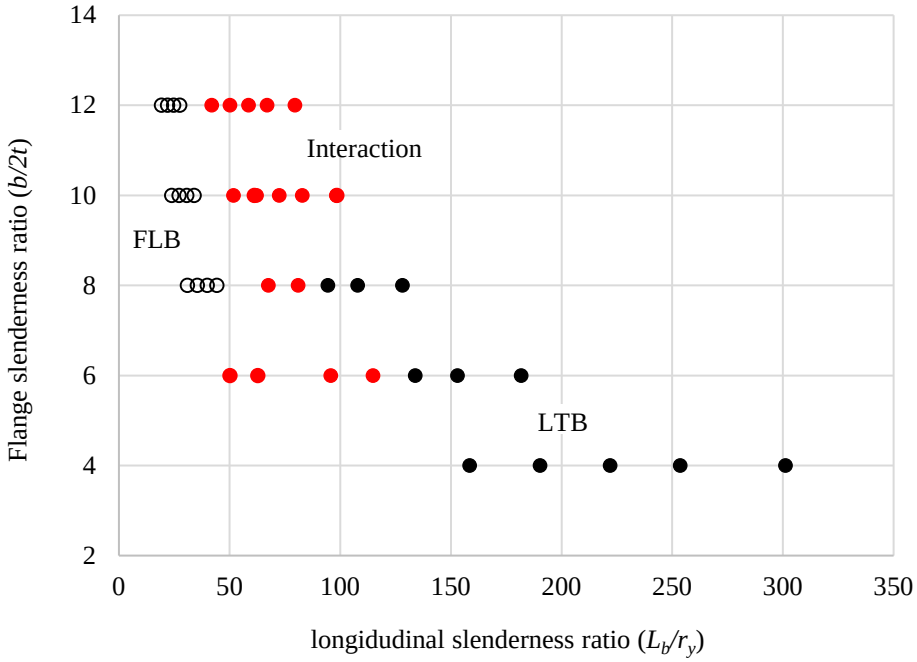

Figure 7.2 Nature of observed buckling failures

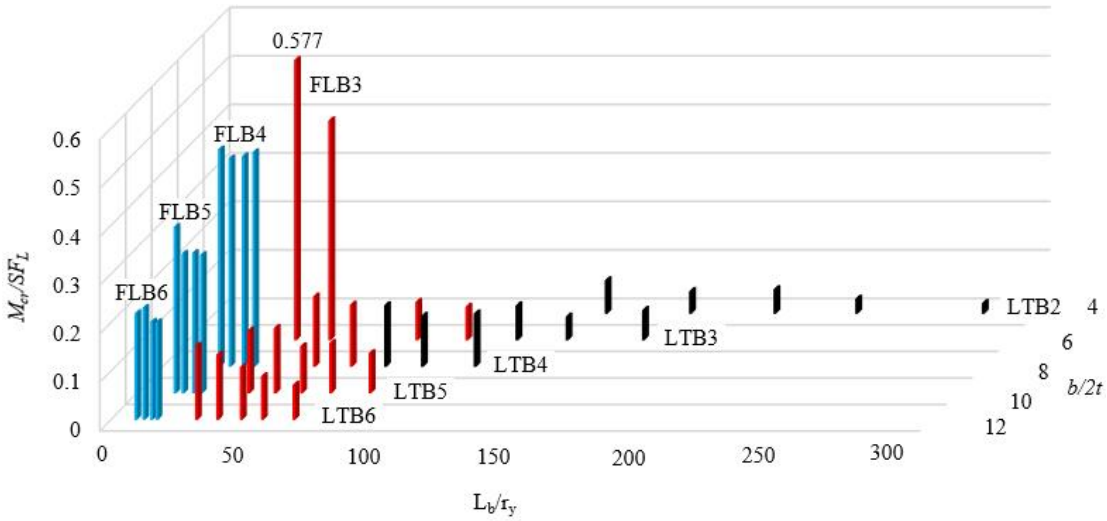

Figure 7.3 Experimentally determined critical buckling moments versus longitudinal and flange slenderness ratios

7.2 ANALYTICAL STUDY OF INTERACTIVE BUCKLING

7.2.1 Formulations

The energy method proposed by Timoshenko and Gere (1961) is used to develop the equation for critical LTB moment of pGFRP I-sections. In pure LTB behavior, both the flange and web plates at any section of the I-beam are assumed to have infinitely small curvatures and the angles between them are assumed to be fixed. That is, the geometry of the cross section does not change in LTB behavior. This assumption permits the energy analysis to be conducted on the LTB behavior of the entire beam, rather than on each flange and web element. This was done in Chapter 6. However, in interactive buckling, the interaction between local (FLB and WLB) and global (LTB) buckling results in a changed geometry of the cross section. The energy analysis needs to be conducted on each flange and web element specifically. Following the method proposed by Roberts and Jhita (1983) for isotropic material, in interactive buckling behavior of an I-section, the top and bottom flanges will sustain [global] strong-axis bending as plates and [global] weak-axis bending as beams, while the web will sustain weak-axis bending as a plate. The critical interactive buckling load is determined through the state of equilibrium of the total potential energy:

$$U = 0 \tag{7.1}$$

In this work, a third order polynomial proposed by Hancock et al. (1980) is used to simulate the laterally buckled web:

$$w_{web} = \left[c_1 + c_2\left(\frac{y}{d-t}\right) + c_3\left(\frac{y}{d-t}\right)^2 + c_4\left(\frac{y}{d-t}\right)^3\right]\sin\left(\frac{\pi x}{L_b}\right) \tag{7.2}$$

Where c_1, c_2, c_3 and c_4 are constant coefficients; $d - t$ is the height of web plate; and L_b is the laterally unbraced length of the beam. Axis and displacement notations are presented in Figure

7.4. The displacements in *x*, *y* and *z* directions are represented as *u*, *v* and *w*, respectively. Throughout this discussion, "strong axis" refers to flexure about the global *z* axis and "weak axis" refers to flexure about the global *y* axis regardless of the orientation of the flange or web element.

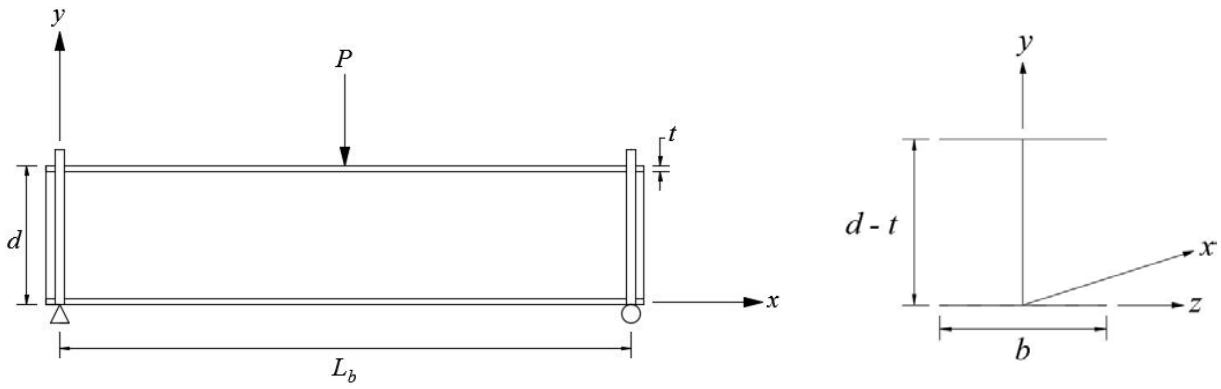

a) Coordinate system **b) Cross section**

Figure 7.4 Axis and displacement notations

With the shape function of web defined, the lateral displacements and rotational angles of the top and bottom flanges are obtained through compatibility conditions at the flange-web interfaces:

$$w_{tf} = (w_{web})_{y=d-t} \tag{7.3}$$

$$w_{bf} = (w_{web})_{y=0} \tag{7.4}$$

$$\phi_{tf} = \left(\frac{\partial w_{web}}{\partial y}\right)_{y=d-t} \tag{7.5}$$

$$\phi_{bf} = \left(\frac{\partial w_{web}}{\partial y}\right)_{y=0} \tag{7.6}$$

Differing from LTB of an I-section, the top and bottom flanges in interactive buckling have different rotational angles due to the buckled web, as shown schematically in Figure 7.5.

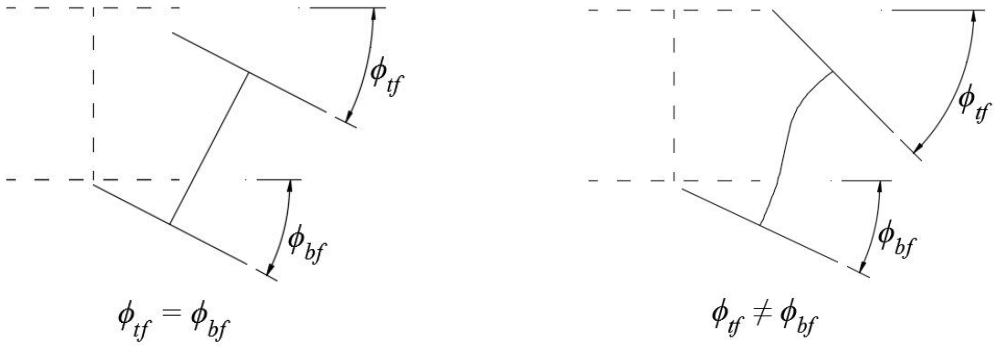

a) LTB **b) Interactive buckling**

Figure 7.5 Rotational angles of top and bottom flanges

Additionally, vertical displacements of top and bottom flanges are assumed to be based on a rigid body rotation of the flange (Roberts and Jhita 1983; Barbero and Raftoyiannis 1994):

$$v_{tf} = -z\phi_{tf} \tag{7.7}$$

$$v_{bf} = -z\phi_{bf} \tag{7.8}$$

With the shape functions determined, the potential energy corresponding to orthotropic flanges and web can be developed as shown below. In this process, the weak-axis bending of the web and strong-axis bending of the flanges are analyzed using plate theory, while the weak-axis bending of the flanges is addressed using beam theory (Roberts and Jhita 1983; Leissa 1985).

7.2.1.1 Web

For the web in bending, normal (f_x) and shear (f_{xy}) stresses are included. Vertical stress (f_y) introduced by load, P, is applied at the midspan section ($x = L_b/2$). The potential energy involved in web weak-axis bending is:

$$(U_{web})_{bending}^{weak} = \frac{1}{2}\int_0^{(d-t)}\int_0^{L_b} t\left[f_x^w\left(\frac{\partial w_{web}}{\partial x}\right)^2 + 2f_{xy}^w\left(\frac{\partial w_{web}}{\partial x}\frac{\partial w_{web}}{\partial y}\right)^2\right]dxdy$$

$$+\frac{1}{2}\int_0^{(d-t)}\left[tf_y^w\left(\frac{\partial w_{web}}{\partial y}\right)^2\right]_{x=\frac{L_b}{2}}dy$$

$$+\frac{1}{2}\int_0^{(d-t)}\int_0^{L_b}\left[D_{11}^w\left(\frac{\partial^2 w_{web}}{\partial x^2}\right)^2 + D_{22}^w\left(\frac{\partial^2 w_{web}}{\partial y^2}\right)^2 + 2D_{12}^w\frac{\partial^2 w_{web}}{\partial x^2}\frac{\partial^2 w_{web}}{\partial y^2}\right.$$

$$\left. + 4D_{66}^w\left(\frac{\partial^2 w_{web}}{\partial x \partial y}\right)^2\right]dxdy \tag{7.9}$$

Where t is the thickness of web plate; $(d - t)$ is the height of the web; L_b is the lateral unbraced length of beam; D_{ij} are the flexural stiffness parameters given in Appendix B for the web and/or flange plate as indicated; and f_x, f_y, and f_{xy} are the inplane stresses in the web, defined as:

$$f_x^w = \frac{Pxy}{2I}\ for\ 0 \le x \le \frac{L_b}{2} \tag{7.10}$$

$$f_y^w = -\frac{P(y + \frac{d}{2} - a)}{d - t}\ for\ x = \frac{L_b}{2} \tag{7.11}$$

$$f_{xy}^w = -\frac{P}{2(d - t)}\ for\ 0 \le x \le \frac{L_b}{2} \tag{7.12}$$

Where I is the moment of inertia of the entire I-section about its strong-axis, which is given as:

$$I = \frac{1}{12}[bd^3 - (b - t)(d - 2t)^3] \tag{7.13}$$

Additionally, a is the distance from shear center to the load point shown in Figure 6.6. Due to the symmetry of the I-beam and midspan loading, in Eqs. 7.10 – 7.12, only the stresses in half of the span ($0 \le x \le L_b/2$) are needed.

7.2.1.2 Top Flange

For the top flange in bending, only normal stress (f_x) is considered. Additionally, the buckled flange is assumed to be linear in the transverse direction at any section as shown in Figure 7.5. Thus, for the top flange, the second variation of the shape function vanishes with respect to the [global] strong-axis. The potential energy involved in top flange [global] strong-axis bending is:

$$\left(U_{tf}\right)_{bending}^{strong} = \frac{1}{2}\int_{-\frac{b}{2}}^{\frac{b}{2}}\int_{0}^{L_b} tf_x^{tf}\left(\frac{\partial v_{tf}}{\partial x}\right)^2 dxdz + \frac{1}{2}\int_{-\frac{b}{2}}^{\frac{b}{2}}\int_{0}^{L_b}\left[D_{11}^{tf}\left(\frac{\partial^2 v_{tf}}{\partial x^2}\right)^2 + 4D_{66}^{tf}\left(\frac{\partial^2 v_{tf}}{\partial x \partial z}\right)^2\right] dxdz \quad (7.14)$$

Where b is the width of flange; and f_x^{tf} is the normal stress at the top flange, which is given as:

$$f_x^{tf} = \frac{Pb_w x}{4I} \quad for\ 0 \le x \le \frac{L_b}{2} \quad (7.15)$$

Where I is defined in Eq. 7.13. The potential energy involved in top flange [global] weak-axis bending is:

$$(U_{tf})_{bending}^{weak} = \frac{1}{2}\int_{-b/2}^{b/2}\int_{0}^{L_b} tf_x^{tf}\left(\frac{\partial w_{tf}}{\partial x}\right)^2 dxdz + \frac{1}{2}E_L I_y^{tf}\int_{-b/2}^{b/2}\int_{0}^{L_b}\left(\frac{\partial^2 w_{tf}}{\partial x^2}\right)^2 dxdz \quad (7.16)$$

Where $E_L I_y^{tf}$ is the weak-axis bending stiffness of flange. I_y^{tf} is calculated as:

$$I_y^{tf} = \frac{tb^3}{12} \quad (7.17)$$

7.2.1.3 Bottom Flange

For the bottom flange in bending, only normal stress (f_x) is considered and the calculations are the same as the top flange (Eqs. 7.14 and 7.16) substituting bottom flange properties. The normal stress in the bottom flange is calculated as:

$$f_x^{bf} = -\frac{Pb_w x}{4I} \quad for\ 0 \le x \le \frac{L_b}{2} \tag{7.18}$$

The total potential energy of the section is therefore:

$$U = (U_{web})_{bending}^{weak} + (U_{tf})_{bending}^{strong} + (U_{tf})_{bending}^{weak} + (U_{bf})_{bending}^{strong} + (U_{bf})_{bending}^{weak} = 0 \tag{7.19}$$

Through Eq. 7.19, a quadratic form in terms of constant coefficients (c_1, c_2, c_3 and c_4) is obtained. Transforming this quadratic into matrix form, yields:

$$[c_1 \quad c_2 \quad c_3 \quad c_4][\mathbf{A}]\begin{bmatrix} c_1 \\ c_2 \\ c_3 \\ c_4 \end{bmatrix} = 0 \tag{7.20}$$

Where **A** is a 4x4 symmetric matrix in terms of *P*. If Eq. 7.20 is solvable, the determinant of matrix **A** is zero:

$$\det(\mathbf{A}) = 0 \tag{7.21}$$

The critical buckling load, P_{cr}, is given by the minimum positive solution of Eq. 7.21. Additionally, the critical interactive buckling moment for midspan flexure is given as:

$$M_{cr} = \frac{P_{cr} L_b}{4} \tag{7.22}$$

In order to expand the applicable range of Eq. 7.22, the effect of moment gradient under various loading conditions can be considered using the moment modification factor, C_b (defined in Eq. 2.34). Thus, the critical interactive buckling moment that accounts for various loading conditions is:

$$M_{cr} = \frac{C_b}{1.32}\frac{P_{cr} L_b}{4} \tag{7.23}$$

7.2.2 Validations

The critical interactive buckling moments of pGFRP I-sections defined by Eq. 7.23 were validated using the experimental results obtained in this work and compared with the analytical LTB solutions from Eq. 6.16, as presented in Table 7.1 and Figures 7.6 – 7.10.

In Figures 7.6 and 7.7, showing predictions for LTB6 and LTB5 having the largest flange slenderness ratios of $b/2t$ = 12 and 10, respectively, it can be seen that when compared with Eq. 6.16 for pure LTB, Eq. 7.23 provides the lower predictions of critical buckling moments. Although the critical interactive buckling moments provided by Eq. 7.23 remain unconservative when compared with experimental results, the reduction of the critical buckling moment due to the interaction is, indeed, captured. Additionally, the effect of the interaction, represented by the amount of reduction in critical buckling moment, tends to become greater, as the lateral slenderness of the section decreases; that is as the ratio of flange slenderness to global slenderness increases. The low experimental results for LTB6 and LTB5 obtained in the tests may be partially due to the imperfections in both specimens and test configurations.

In Figures 7.8 and 7.9, it can be seen that for sections LTB4 and LTB3 having moderate flange slenderness ratios of $b/2t$ = 8 and 6, respectively, the differences between the critical interactive buckling moments provided by Eq. 7.23 and the critical LTB moments by Eq. 6.16 tend to decrease, as the lateral slenderness ratios increase. That is, for sections having relatively large lateral slenderness ratios, the interaction between local and global buckling behaviors tends to have a smaller effect on critical buckling moment and the pure LTB behavior tends to dominate the failure mode. This phenomenon is verified by both experimental observations and analytical comparisons: for LTB4 and LTB3 having relatively large lateral slenderness ratios (under spans of 2896, 2438 and 2134 mm), essentially pure LTB behaviors were observed in

tests and the analytical LTB solutions provide generally conservative predictions when compared with experimental results, as presented in Table 7.1. On the other hand, for LTB4 and LTB3 having relatively smaller lateral slenderness ratios (under spans of 1829 and 1524 mm), the interaction between local and global buckling tends to have a greater effect on critical buckling moment. Thus, the LTB predictions are shown to be unconservative, while the predictions by Eq. 7.23, accounting for the effect of the interaction, are found to show improved agreement with test results.

Finally, in Figure 7.10, it can be seen that for LTB2, the interactive buckling moments by Eq. 7.23 are generally higher than LTB moments by Eq. 6.16, demonstrating that LTB is the dominant behavior for this section having very small flange slenderness ratio, $b/2t$ = 4. This phenomenon was also observed in the tests in so far as, despite the large variation observed, LTB2 was dominated by pure LTB behavior. Additionally, it is worth noting that for LTB2 having the smallest lateral slenderness ratios (under the smallest span of 1524 mm), the interactive buckling moment prediction is found to be lower than LTB prediction, indicating that the effect of the interaction between local (likely only WLB for this specimen) and global buckling can still lead to a reduction in critical buckling moment even at such a low longitudinal slenderness ratio (L_b/r_y = 42).

In conclusion, compared with pure LTB predictions by Eq. 6.16, the critical interactive buckling moment of pGFRP I-sections proposed in this work (Eq. 7.23) captures the moment reduction due to the interaction between local and global buckling behaviors. Additionally, the effect of the interaction increases, as the lateral longitudinal slenderness ratio decreases and the flange slenderness increases.

Table 7.1 Comparisons between experimental and analytical buckling moments

Specimen	Spans (mm)	Experiment	Eq. 6.16		Eq. 7.23	
		Average M_{cr} (Nm)	M_{cr} (Nm)	pred/exp	M_{cr} (Nm)	pred/exp
LTB6	2896	3316	7467	2.25	5858	1.77
	2438	4153	10197	2.46	7793	1.88
	2134	5022	13054	2.60	9732	1.94
	1829	6195	17466	2.82	12473	2.01
	1524	7058	24783	3.51	15983	2.26
LTB5	2896	3257	4570	1.40	3711	1.14
	2438	4093	6155	1.50	4853	1.19
	2134	3822	7813	2.04	6017	1.57
	1829	5315	10369	1.95	7722	1.45
	1524	5112	14606	2.86	10198	1.99
LTB4	2896	3590	2587	0.72	2225	0.62
	2438	3431	3407	0.99	2821	0.82
	2134	4143	4261	1.03	3436	0.83
	1829	4187	5575	1.33	4358	1.04
	1524	4743	7750	1.63	5787	1.22
LTB3	2896	1613	1329	0.82	1275	0.79
	2438	1263	1688	1.34	1532	1.21
	2134	1865	2057	1.10	1799	0.96
	1829	1788	2620	1.47	2205	1.23
	1524	2045	3546	1.73	2856	1.40
LTB2	2896	419	599	1.43	733	1.75
	2438	587	725	1.24	812	1.38
	2134	964	848	0.88	894	0.93
	1829	893	1030	1.15	1019	1.14
	1524	1323	1320	1.00	1224	0.93

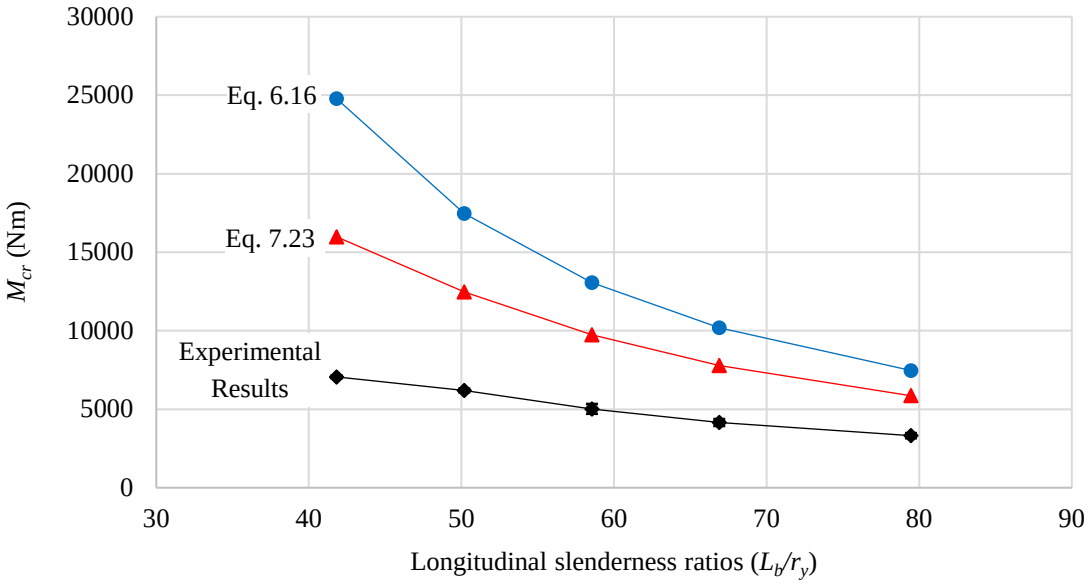

Figure 7.6 Critical buckling moments versus longitudinal slenderness ratios for LTB6

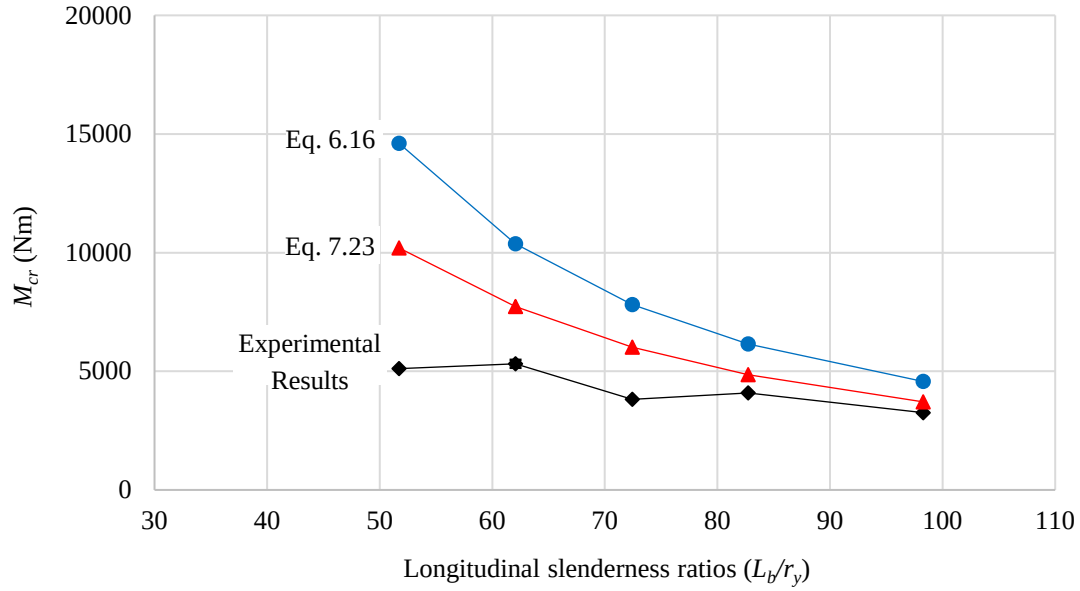

Figure 7.7 Critical buckling moments versus longitudinal slenderness ratios for LTB5

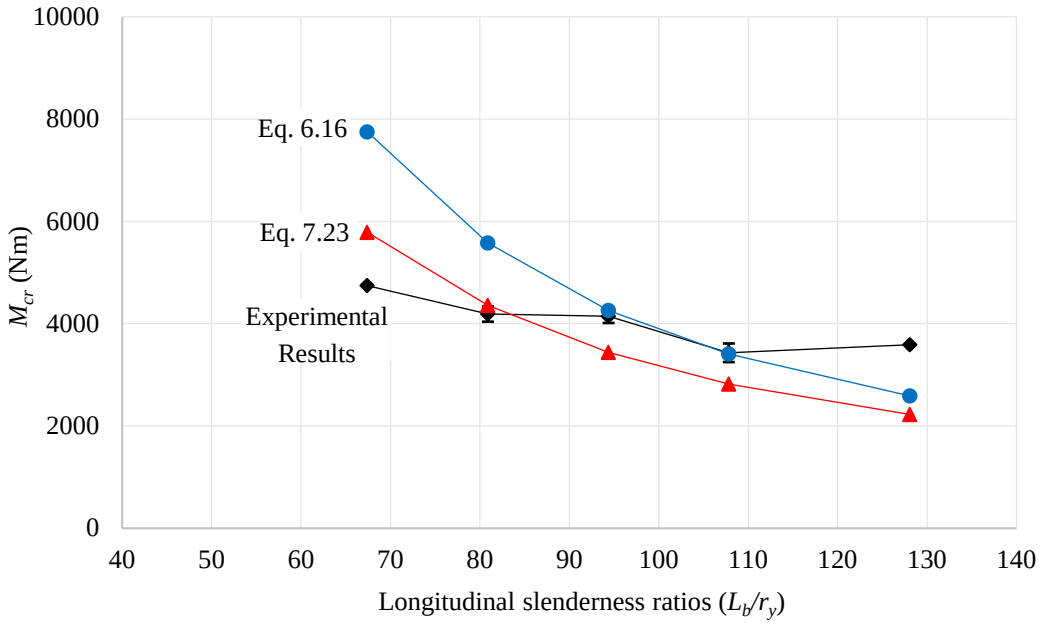

Figure 7.8 Critical buckling moments versus longitudinal slenderness ratios for LTB4

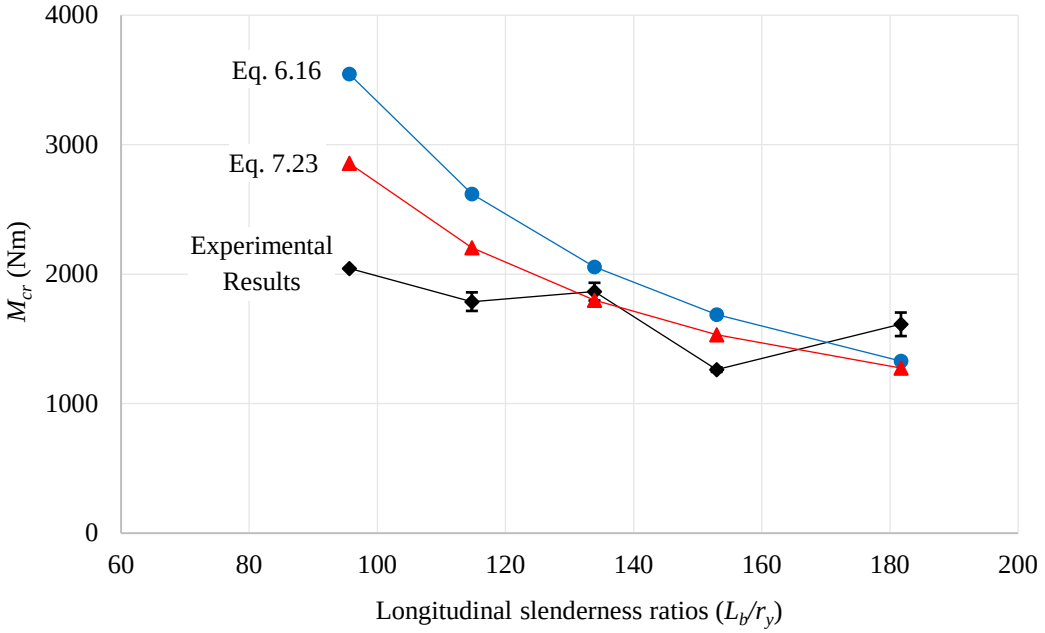

Figure 7.9 Critical buckling moments versus longitudinal slenderness ratios for LTB3

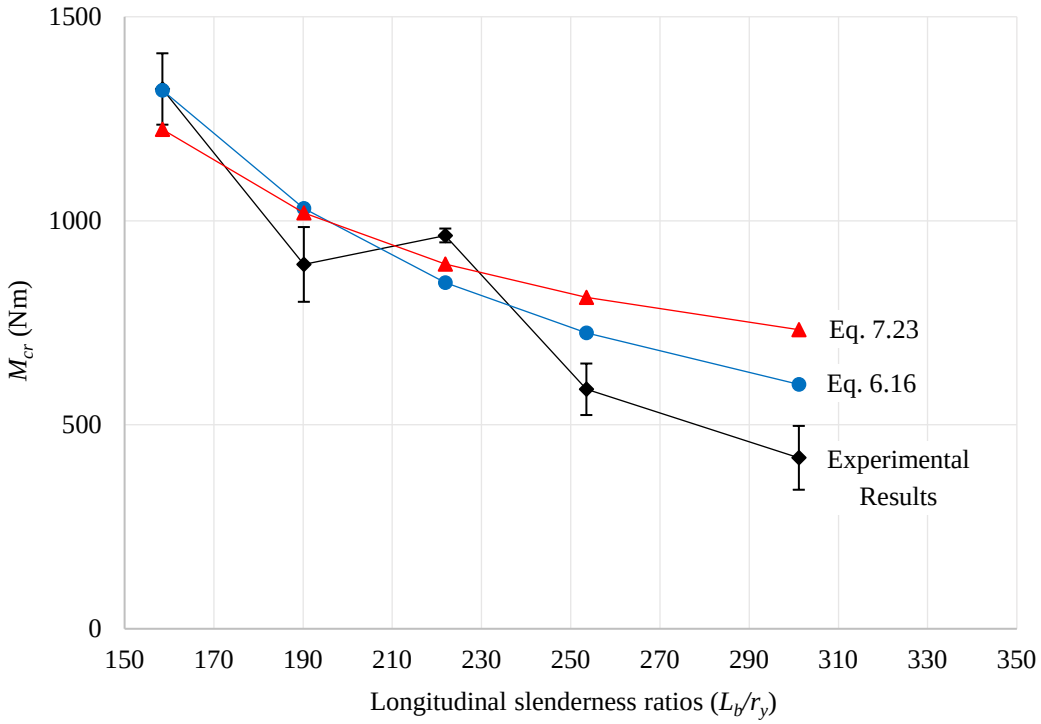

Figure 7.10 Critical buckling moments versus longitudinal slenderness ratios for LTB2

8.0 CONCLUSIONS

In this work, the stability behavior of pultruded glass fiber reinforced polymer (pGFRP) I-sections subject to flexure was addressed. An extensive review of stability behaviors of pGFRP members, including: flange local buckling (FLB), global lateral torsional buckling (LTB) and interaction between local and global buckling (interactive buckling) behaviors, was carried out. Two experimental programs were conducted: 62 four-point bending tests to investigate FLB behavior and 86 three-point bending tests to investigate LTB behavior. Interactive buckling behavior was observed in both series of tests and was shown to be quite prevalent in results from the LTB tests. Analytical studies were presented and non-empirical design formulas derived using energy methods were proposed with respect to the buckling behaviors observed in the experimental program. Supporting the experimental work, a series of material characterization tests were carried out to evaluate the mechanical properties of the pGFRP materials used. The findings and conclusions drawn from this work as well as the recommendations for future research are presented in the following sections.

8.1 EXPERIMENTAL FINDINGS

8.1.1 Material Characterizations

In order to establish the most convenient and inexpensive test methods for pGFRP composite materials, both standard tests specified by ASTM and non-standard tests proposed by researchers were discussed regarding their required test fixtures, coupon preparation and dimensions, limitations and perceived reliability. Many ASTM standard test methods for composite materials, were found to require specific test fixtures and/or coupon geometries, leading to an increase in cost and complexity of test equipment and coupon preparations. In many cases, specimen geometry is considerably larger than what may be extracted fro typical pGFRP sections. Furthermore, it is proposed that these limitations and complexity of standard test methods may represent a barrier to development of new materials, particularly beyond so-called highly-developed communities, or a barrier to small or pilot research programs. In such circumstance, non-standard tests, were proposed. Generally, non-standard tests require no complex test fixtures and the desired material properties can be efficiently obtained. In this work, the test methods (including both standard and non-standard tests) that can be readily conducted using typically available test equipment as well as those requiring simple material preparations were recommended. Additionally, the recommended test methods were demonstrated in an experimental program and found to yield acceptable results with satisfactory accuracy, while requiring no special test fixtures.

Transverse properties of pGFRP sections are difficult to obtain using standard tests. In this work two tests involving simple flange and/or web bending were demonstrated. These are illustrated in Figures 3.3 and 3.4.

8.1.2 FLB Tests

Flange local buckling behavior of pGFRP I-sections was investigated through an experimental program. 62 four-point bending tests having different constant moment and shear spans were conducted. It is found that the critical FLB moment increases as flange slenderness decreases. Experimentally determined critical FLB moments were compared with results by design guides (ASCE 2010; EUR 27666 2016), numerical (Kollár 2003) and FSM modeling (Li and Schafer 2010). All sources were found to provide generally conservative predictions of critical FLB moments, while FSM was found to have the best correlation with experimental results.

The underestimation of FLB capacity by both design standards may be viewed as being conservative, although this impacts the calibration of calibration of material resistance factors (so called φ factors) through reliability analyses and may lead to unreasonably high values. Although such calibration results in conservative design equations, the actual material reliability is misrepresented. This may lead to a) an increase in material cost in practical applications; or b) unrealistic expectations form the design community regarding the reliability and consistency of pGFRP materials having a relatively high value material resistance factor. For this reason, improved prediction of critical FLB moment capacity of pGFRP I-sections is needed.

8.1.3 LTB Tests

Lateral torsional behavior of pGFRP I-sections was studied through an experimental program. 86 three-point bending tests having different spans were conducted. It is found that the critical LTB moment generally increases as longitudinal slenderness decreases and flange slenderness increases. Experimentally determined critical LTB moments were compared with results by design codes (ASCE 2010; EUR 27666 2016), numerical (Sapkás and Kollár 2002) and FSM

modeling (Li and Schafer 2010). All approaches were found to provide generally unconservative predictions of critical LTB moments for sections LTB6, LTB5, LTB4 and LTB3 having large flange slenderness ratios, $b/2t$ = 12, 10, 8, 6, respectively; while for section LTB2 having relatively smaller flange slenderness ratio, $b/2t$ = 4, the analytical solutions were found to have a good agreement with experimental results. Such over-predicted critical LTB moments were partially due to the neglect of the interaction between local and global buckling. As described in Section 7.1, very significant interaction effects (LTB capacity reduced due to interaction with FLB) were observed in the LTB tests; these were most pronounced when $b/2t > 8$.

8.2 ANALYTICAL PREDICTIONS

8.2.1 FLB

An explicit equation (Eq. 5.16) for predicting the critical FLB moment of pGFRP I-sections subject to flexure was proposed. To derive this equation, plate theory and energy method were used. Additionally, the critical half wave length, L_{cr}, for FLB was also addressed (Eq. 5.14). Short unsupported flange lengths that are not an integer multiple of L_{cr} will have an increased critical buckling load as described in Section 5.4.4. Eq. 5.16 was validated using the experimental results obtained in this work and other studies in available literature and analytical solutions from ASCE (2010), EUR 27666 (2016), Kollár's equation (2003), and FSM analysis. A good agreement was found between Eq. 5.16 and experimental results. The absolute differences between Eq. 5.16 and FSM were less than 5% for sections FLB6, FLB5 and FLB4 which were observed to be dominated by FLB behavior. Finally, Eq. 5.16 shows an improved accuracy over existing code-like equations as well as the "exact" solutions by Kollár (2003).

8.2.1.1 Revision to Kollár Assumptions

Flange local buckling predictions are significantly affected by the elastic rotational restraint provided to the flange at the flange-web interface. The accuracy in estimation of such restraining effect (described by a spring constant *k*) is, therefore, critical in predicting FLB behaviors. In this work, a revision was made to the *k* factor proposed by Kollár (2003). It is demonstrated that using the revised *k* factor, given by Eq. 5.11, a better correlation is found between the experimental results and analytical predictions of critical FLB moment (see Section 5.4.3).

8.2.2 LTB

An explicit equation (Eq. 6.16) for predicting the critical LTB moment of pGFRP I-sections subject to flexure was proposed. To derive this equation, Timoshenko's energy method (Timoshenko and Gere 1961) for an isotropic I-section was adopted and revised to account for the anisotropic nature of pGFRP. Eq. 6.16 has a similar form to the critical LTB moment capacity (Eq. 2.38) given by EUR 27666 (2016). Eq. 6.16 was validated using experimental results obtained in this work and other studies in available literature as well as the analytical solutions by other sources (ASCE 2010; EUR 27666 2016; Sapkás and Kollár's equation 2002; and FSM analysis). Eq. 6.16 was found to have a good agreement with experimental results for section LTB2 which has the smallest flange slenderness ratio, $b/2t = 4$, and was, therefore, observed to be dominated by LTB behavior. The absolute differences between Eq. 6.16 and FSM were less than 11% for all sections that were considered.

8.2.3 Interactive Buckling

An explicit equation (Eq. 7.23)–accounting for anisotropic material properties–for interactive buckling was proposed based on the energy method proposed by Roberts and Jhita (1983) for isotropic material. Eq. 7.23 was validated using the experimental results obtained in this work and compared with the analytical LTB solutions using Eq. 6.16. It is found that Eq. 7.23 captures the moment reduction due to the interaction between local and global buckling. Therefore, Eq. 7.23 shows an improvement over Eq. 6.16 and provides more accurate predictions in practice. The effect of the interaction increases, as the longitudinal slenderness (L_b/r_y) decreases and the flange slenderness ($b/2t$) increases. Additionally, it is worth noting that the interactive buckling behavior of pGFRP I-sections were also investigated by Barbero and Raftoyiannis (1994) and Davalos and Qiao (1997). However, in these two studies, the lateral bending of the two flanges (bending as beams) is neglected, leading to a significant reduction in critical buckling moments, while in this work, the lateral bending of the flanges is considered, providing an improved prediction on interactive buckling moment.

8.3 FUTURE RESEARCH

In order to further improve the predictions of flexural stability of pGFRP I-sections, future research is needed, as presented in the following.

In using ASTM D695 to evaluate the compressive properties of pGFRP materials (see Section 3.3.3), end crushing often occurs and a lower bound compressive strength is obtained. To improve the accuracy of this test, future work is needed in regard of preventing the end crushing mode as well as ensuring the vertical alignment of the specimen.

In the FLB test, the constant moment region was found not to be an integer multiple of natural buckling half wave length and consequently, a stiffer buckling response was obtained. To mitigate such effect, a longer constant moment region (requiring a longer specimen) are recommended in four-point bending test.

In both FLB and LTB tests specimen imperfections lead to a reduction in critical buckling moment, although this was not considered in this work. To achieve a more accurate evaluation of the critical buckling moment in experiments, specimen imperfection needs to be assessed in future work. The effect of imperfections become more pronounced for more slender sections. Cardoso (2104), for instance, addressed imperfections in column specimens *post priori* in his work. This is more complex for flexure and *a priori* determination of imperfections remains a challenge.

In the method of predicting the critical FLB moment, the flange outstand is assumed to be subject to uniform compressive stress and consequently, the bending behavior of the flange plate is neglected. Compressive behavior of the plate is assumed to be a function of compressive modulus (often tensile modulus is used) which is a function of fiber volume ratio, However, flange buckling is a flexural behavior and the flexural behavior of pGFRP is highly dependent on both fiber volume ratio and fiber architecture. To improve the simulation of the flange plate, flexural modulus is needed in the place of the tensile or compressive modulus prescribed in existing design guides. Additionally, standard flexure tests of pGFRP materials must be interpreted correctly accounting for (at least) fiber volume ratio, fiber architecture and the variation of fiber architecture. Specifications regarding these material complexities need to be proposed for manufacturers.

The rotational restraint at flange-web interface, defined by a spring constant *k*, is critical in predicting the FLB behavior of pGFRP I-sections. However, there is a lack of a uniformly accepted description of *k* and no accepted means of determining this value. Therefore, a more accurate and reliable *k* factor is needed in the future work.

In addition, longitudinal shear failure of the flange-to-web interface has been identified in other studies and was observed in specimen FLB3. The presence of longitudinally oriented distress, leading to this type of failure may lead to a reduction of *k* factor as well as the critical FLB moment capacity of the beam. Thus, future work is needed to study the limit state of shear strength of the flange-to-web and how this behavior may impact the rotational restraint inherent at this interface.

Finally, various methods of predicting the critical interactive buckling moment have been proposed in past decades, such as Barbero and Raftoyiannis (1994), Davalos and Qiao (1997), Kabir and Sherbourne (1998) and Insausti et al. (2009). However, due to the complexities in these methods, it is difficult to adopt these methods to practical applications in design office. Therefore, a more concise design equation having satisfactory accuracy is needed in the future. While this work moved in this direction, the resulting equations remain inadequate to the purpose.

APPENDIX A

EXPERIMENTAL RESULTS

A.1 FOUR-POINT BENDING TESTS

In this work, 62 four-point bending tests were conducted as reported in Chapter 5. Images and flange stress-strain curves for all specimens are reported in this section. The strain gage layout on the compression flange is shown in Figure A.1. Compressive strain readings are taken as positive.

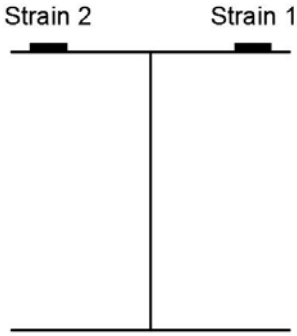

Figure A.1 Strain gage layout on the compression flange for four-point bending tests

Specimen: FLB6-2	Span: 2900 mm	Date: 8/10/2015
	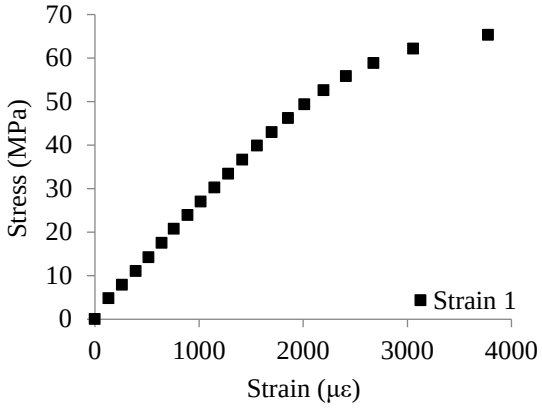	
M_{cr} = 8879 Nm		

Specimen: FLB6-1	Span: 2900 mm	Date: 8/12/2015
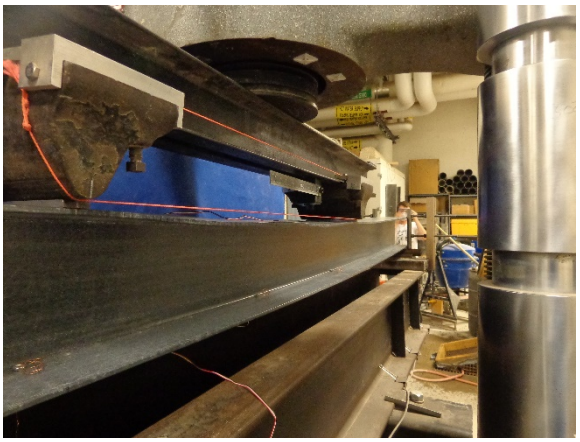	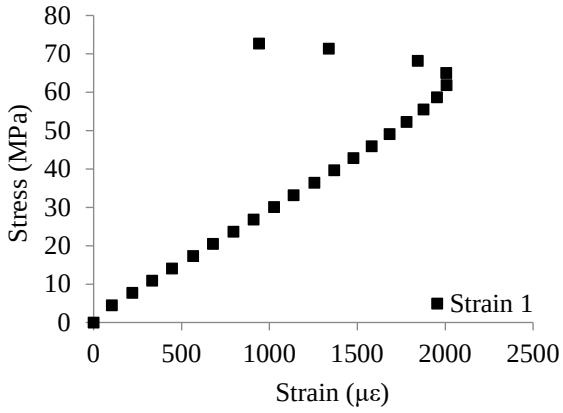	
M_{cr} = 9754 Nm		

Specimen: FLB6-1	Span: 2900 mm	Date: 8/11/2015
	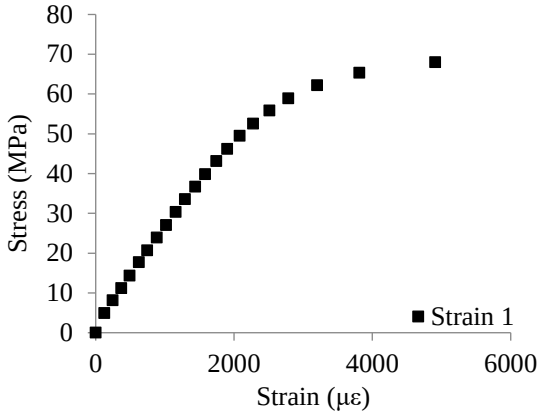	
M_{cr} = 8754 Nm		

Specimen: FLB6-2	Span: 2900 mm	Date: 8/11/2015
	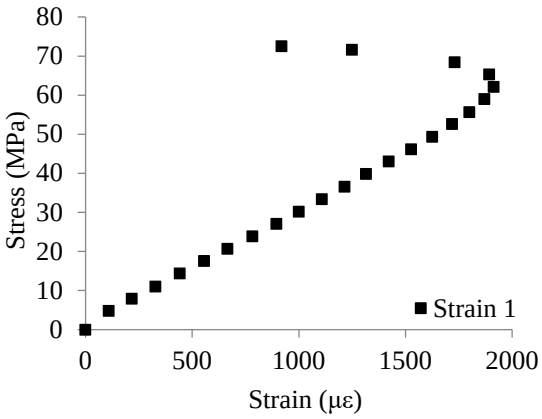	
M_{cr} = 9829 Nm		

Specimen: FLB6-2	Span: 2600 mm	Date: 8/7/2015
	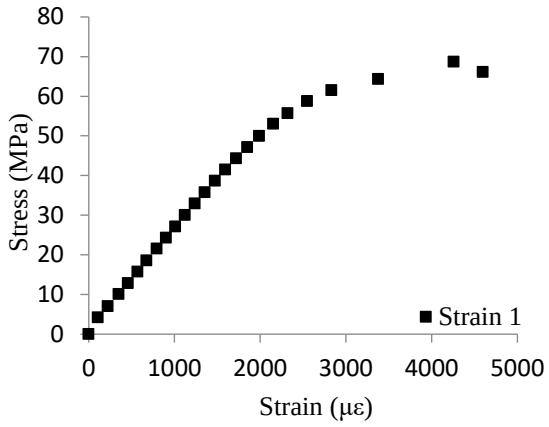	
M_{cr} = 9313 Nm		

Specimen: FLB6-2	Span: 2600 mm	Date: 8/7/2015
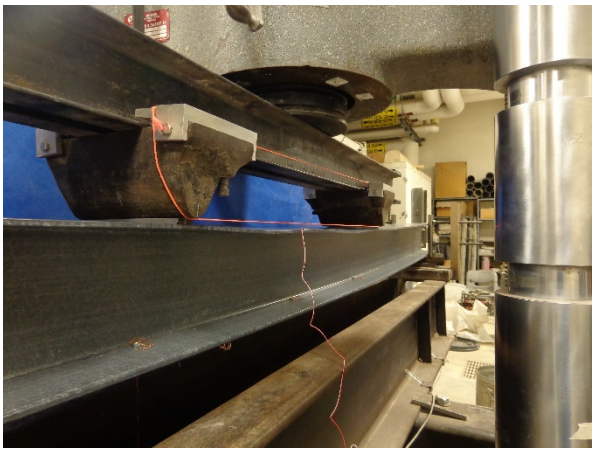	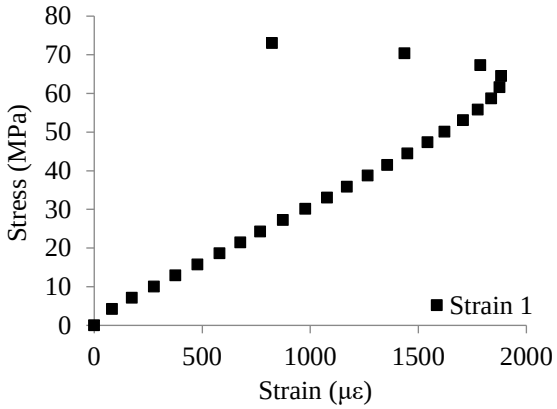	
M_{cr} = 9043 Nm		

Specimen: FLB6-1	Span: 2600 mm	Date: 8/3/2015
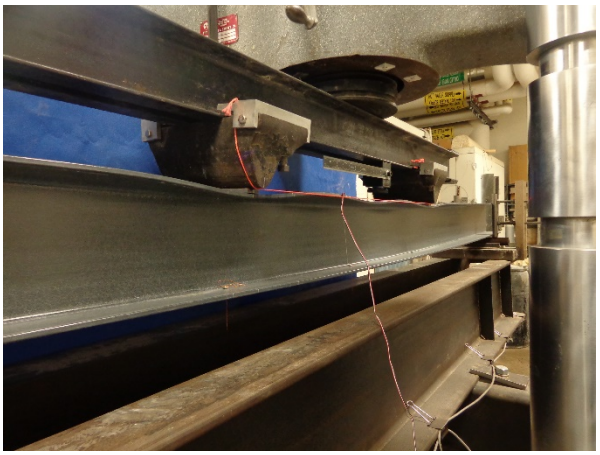	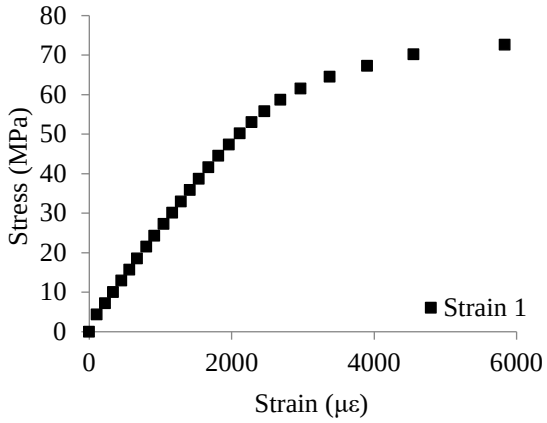	
M_{cr} = 9268 Nm		

Specimen: FLB6-1	Span: 2600 mm	Date: 8/7/2015
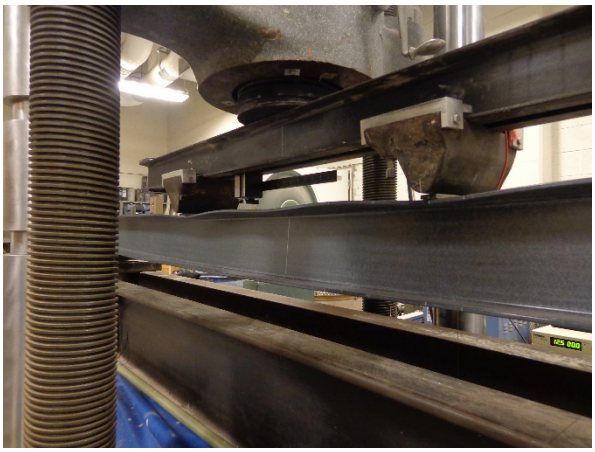	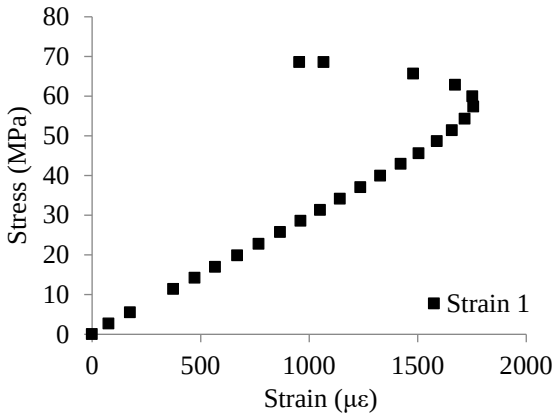	
M_{cr} = 9696 Nm		

Specimen: FLB6-1	Span: 2200 mm	Date: 8/12/2015
	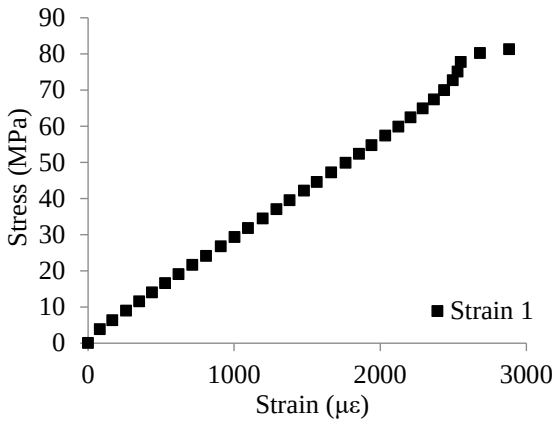	
M_{cr} = 10371 Nm		

Specimen: FLB6-1	Span: 2200 mm	Date: 8/12/2015
	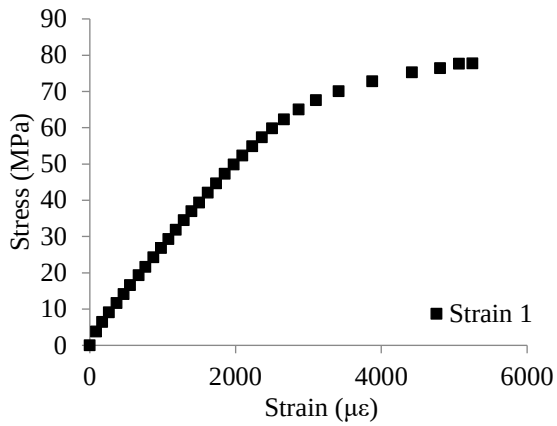	
M_{cr} = 9871 Nm		

Specimen: FLB6-2	Span: 2200 mm	Date: 8/13/2015
	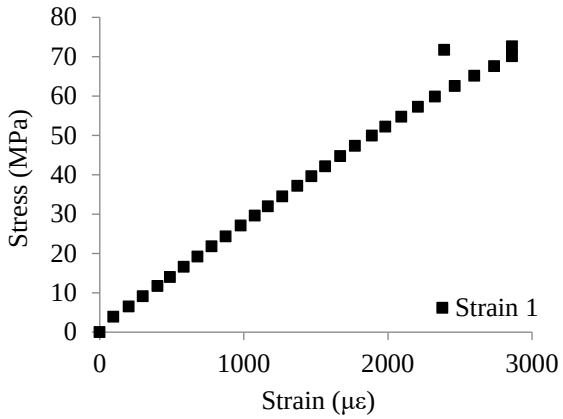	
M_{cr} = 11045 Nm		

Specimen: FLB6-2	Span: 2200 mm	Date: 8/13/2015
	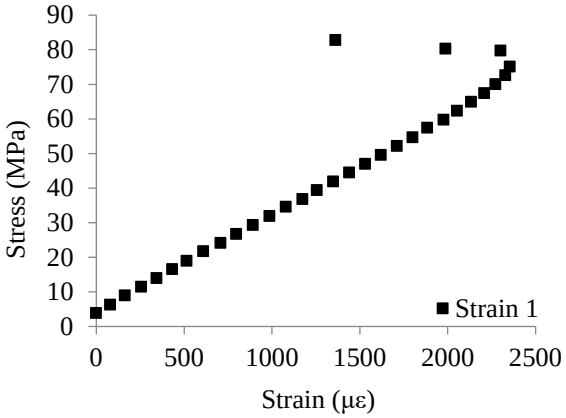	
M_{cr} = 11431 Nm		

Specimen: FLB6-1	Span: 1800 mm	Date: 8/14/2015
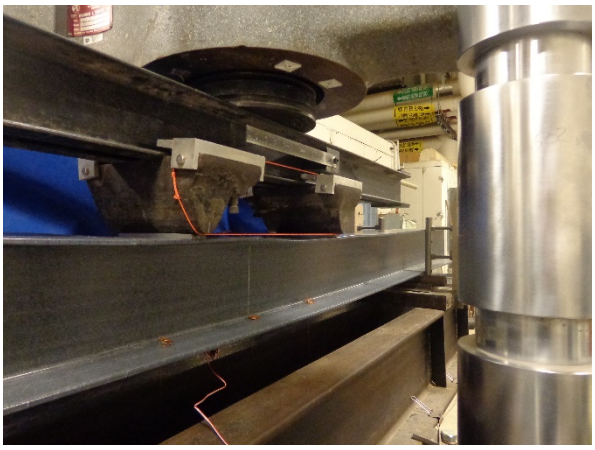	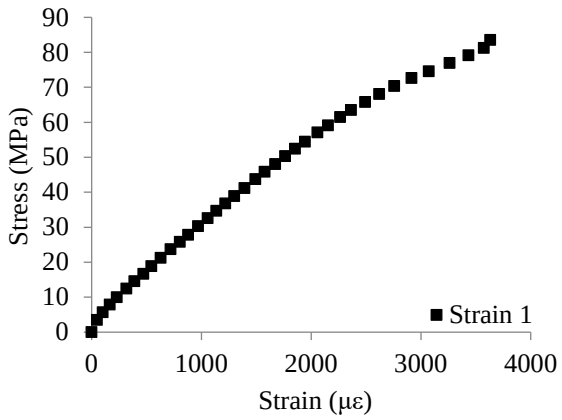	
M_{cr} = 10101 Nm		

Specimen: FLB6-1	Span: 1800 mm	Date: 8/14/2015
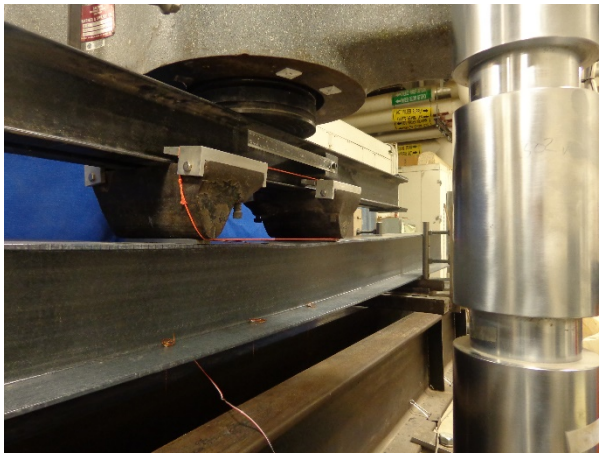	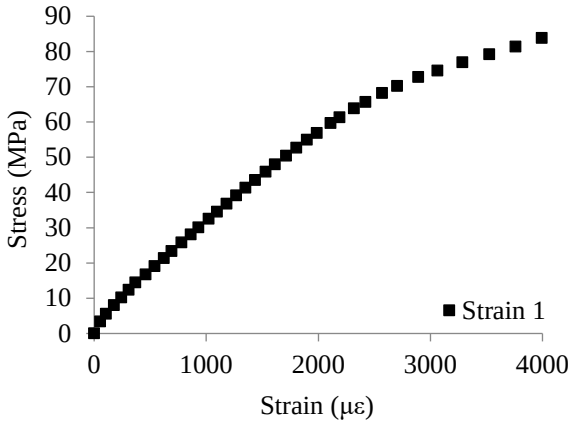	
M_{cr} = 10363 Nm		

Specimen: FLB6-2	Span: 1800 mm	Date: 8/14/2015
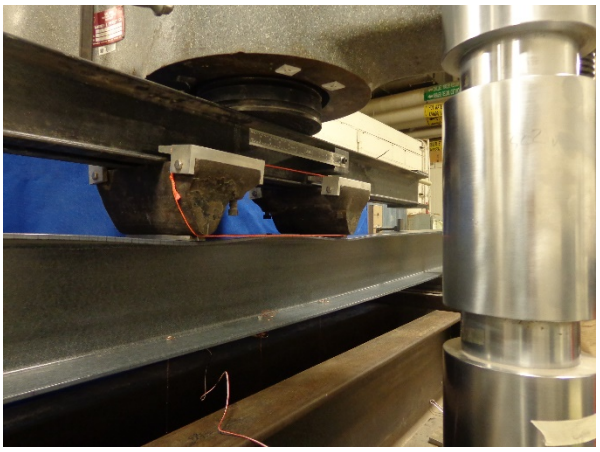	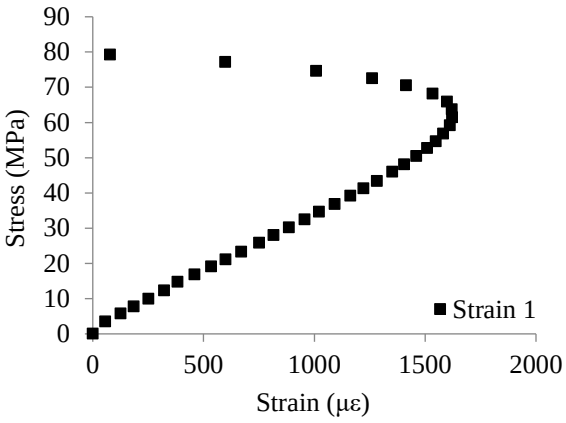	
M_{cr} = 9716 Nm		

Specimen: FLB6-2	Span: 1800 mm	Date: 8/13/2015
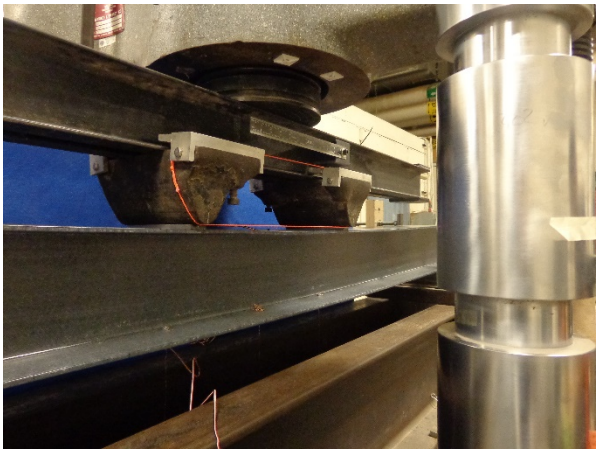	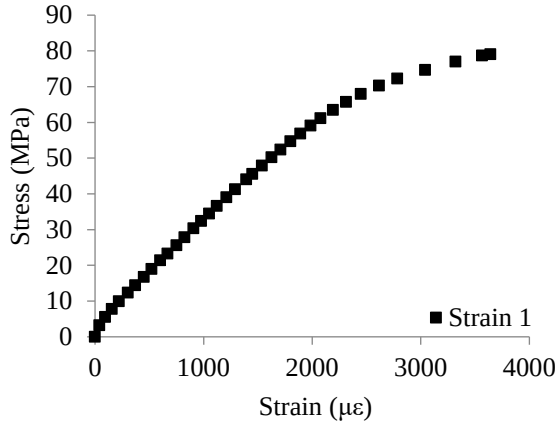	
M_{cr} = 10381 Nm		

Specimen: FLB5-1	Span: 2900 mm	Date: 9/15/2015
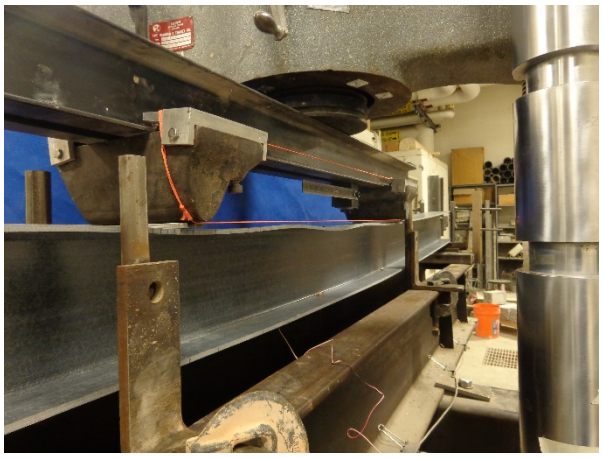	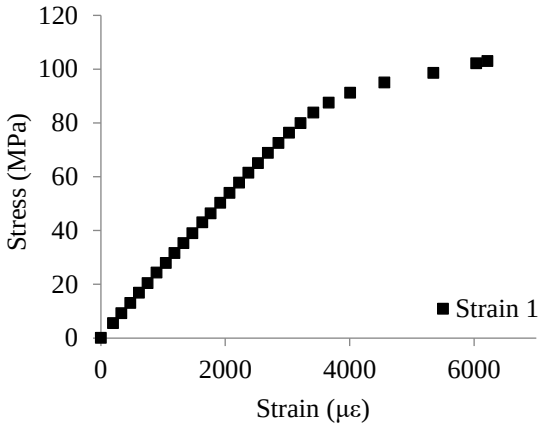	
M_{cr} = 11944 Nm		

Specimen: FLB5-1	Span: 2900 mm	Date: 9/15/2015
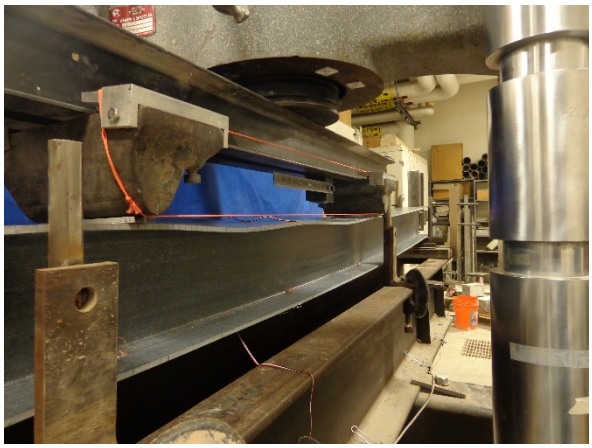	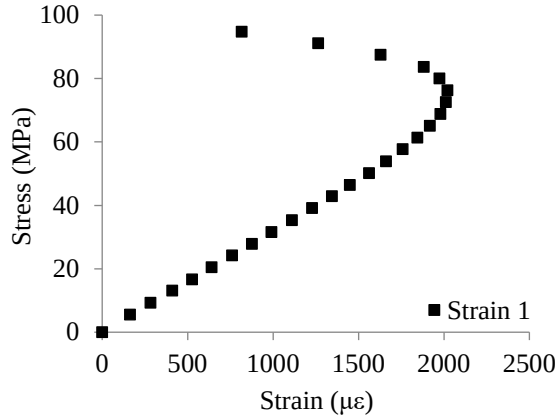	
M_{cr} = 9794 Nm		

Specimen: FLB5-2	Span: 2900 mm	Date: 9/11/2015
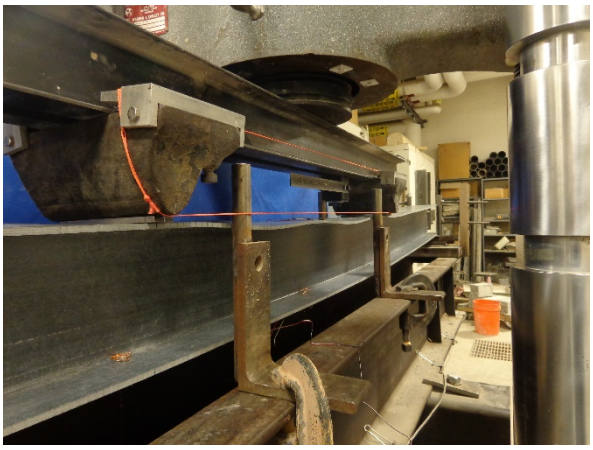	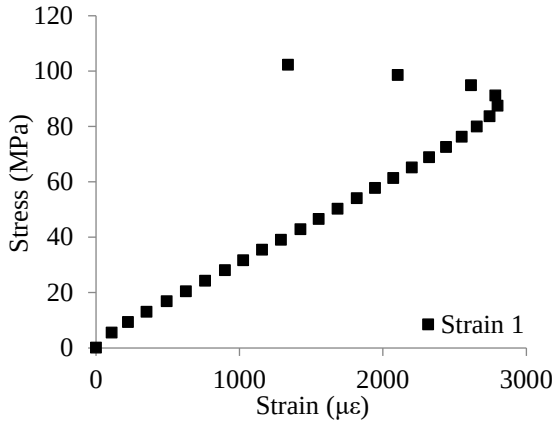	
M_{cr} = 11794 Nm		

Specimen: FLB5-2	Span: 2900 mm	Date: 9/11/2015
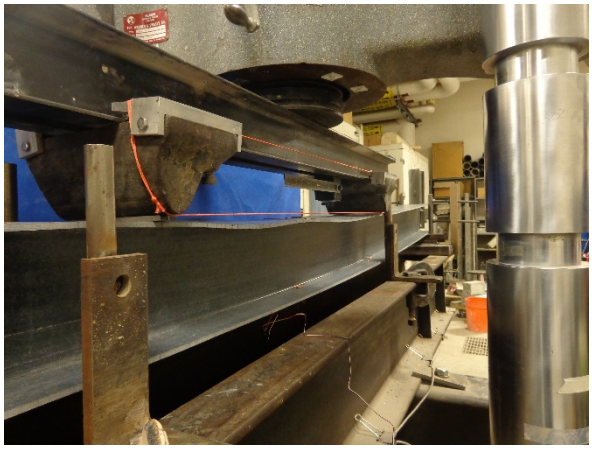	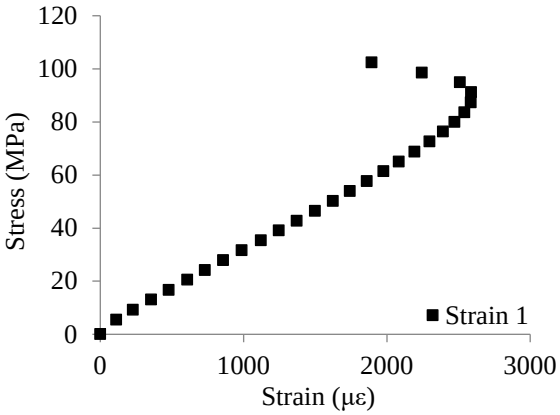	
M_{cr} = 11769 Nm		

Specimen: FLB5-2	Span: 2900 mm	Date: 9/14/2015
	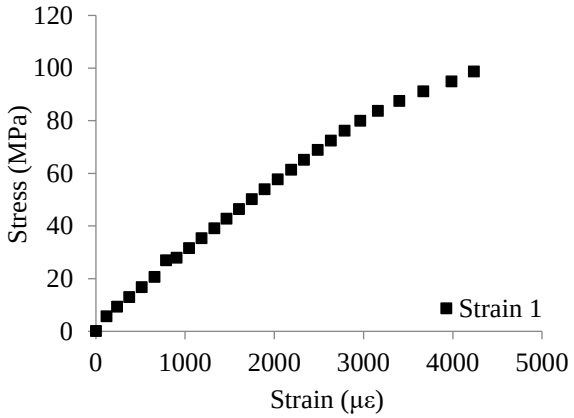	
M_{cr} = 10994 Nm		

Specimen: FLB5-1	Span: 2900 mm	Date: 8/19/2015
	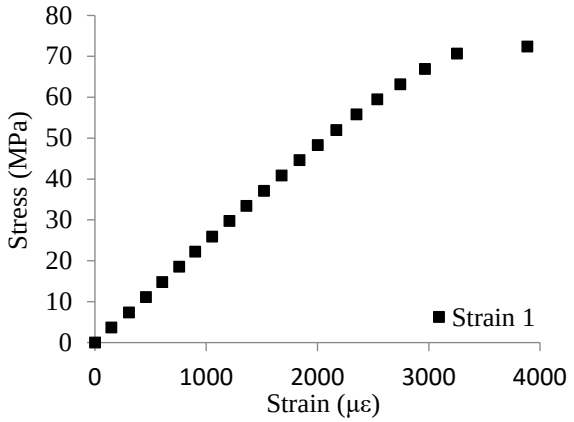	
M_{cr} = 8344* Nm		

Specimen: FLB5-1	Span: 2900 mm	Date: 9/14/2015
	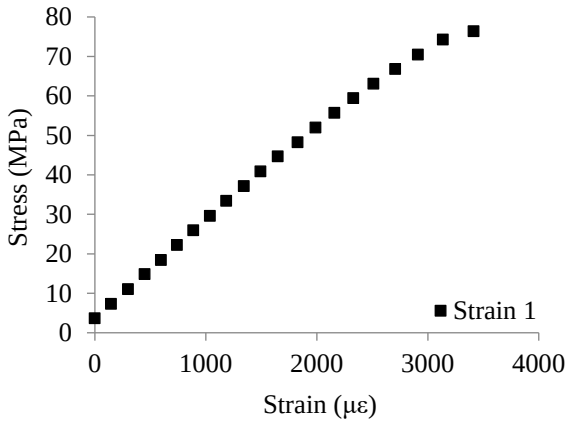	
M_{cr} = 8094* Nm		

Specimen: FLB5-1	Span: 2600 mm	Date: 9/17/2015
	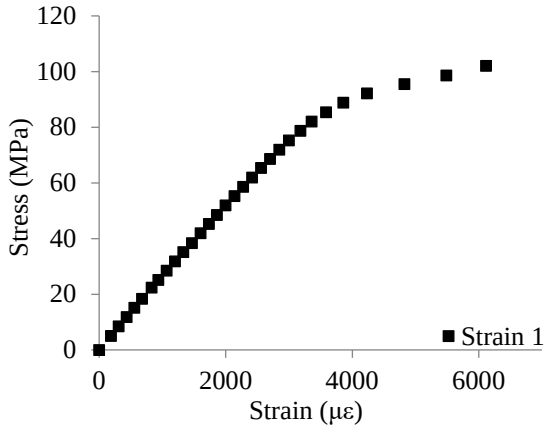	
M_{cr} = 11713 Nm		

Specimen: FLB5-1	Span: 2600 mm	Date: 9/17/2015
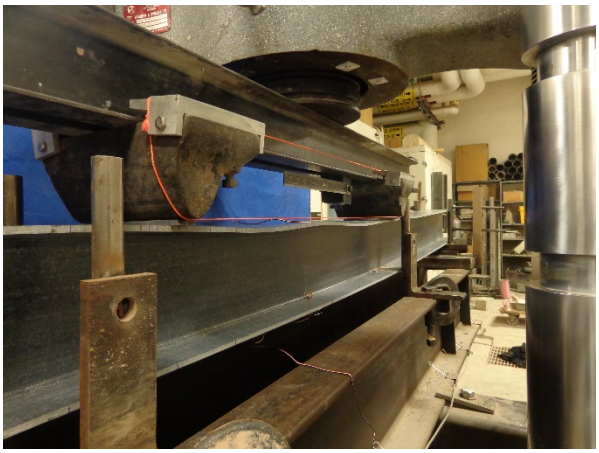	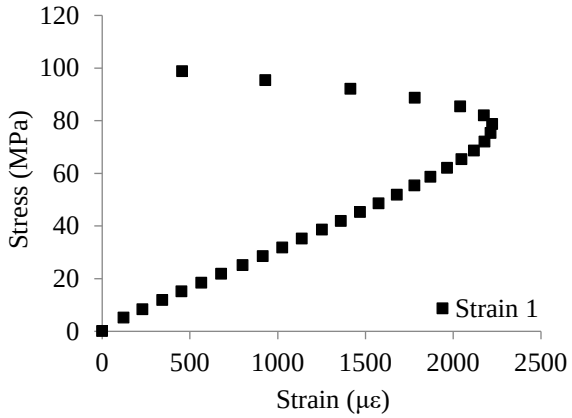	
M_{cr} = 10611 Nm		

Specimen: FLB5-2	Span: 2600 mm	Date: 9/17/2015
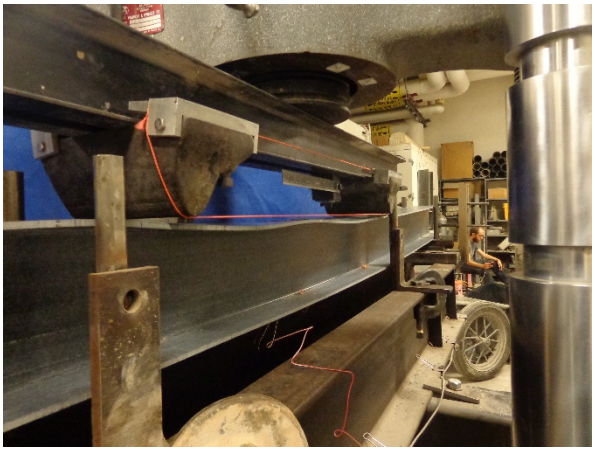	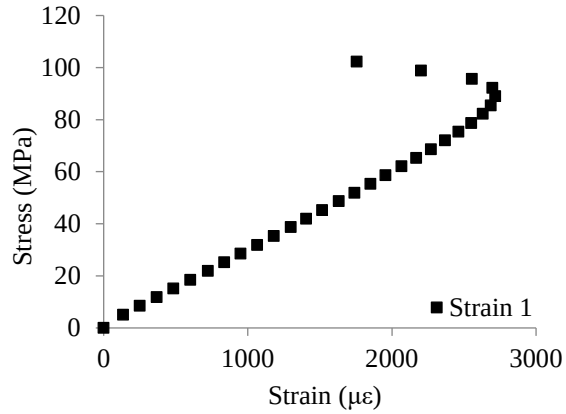	
M_{cr} = 11983 Nm		

Specimen: FLB5-2	Span: 2600 mm	Date: 9/18/2015
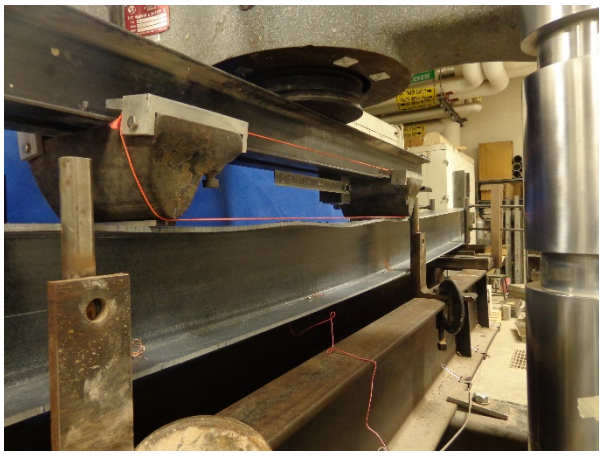	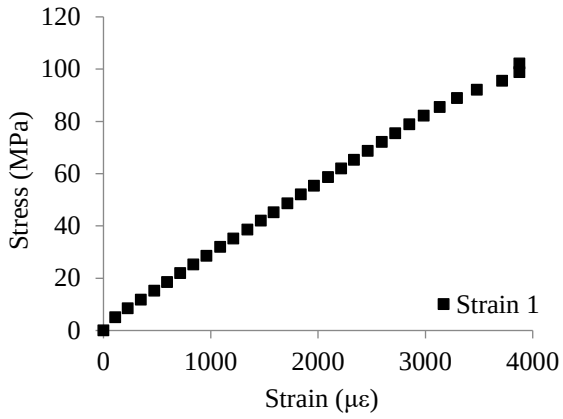	
M_{cr} = 11421 Nm		

Specimen: FLB5-1	Span: 2200 mm	Date: 9/18/2015
	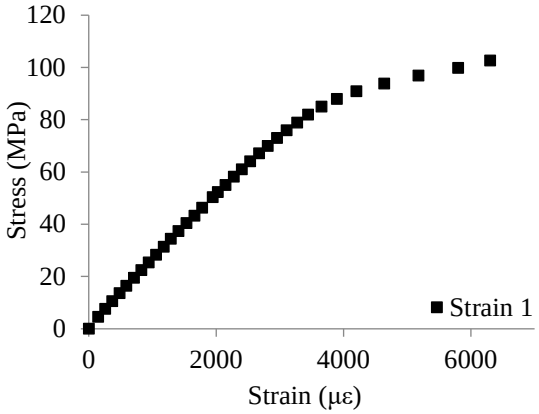	
M_{cr} = 11546 Nm		

Specimen: FLB5-1	Span: 2200 mm	Date: 9/21/2015
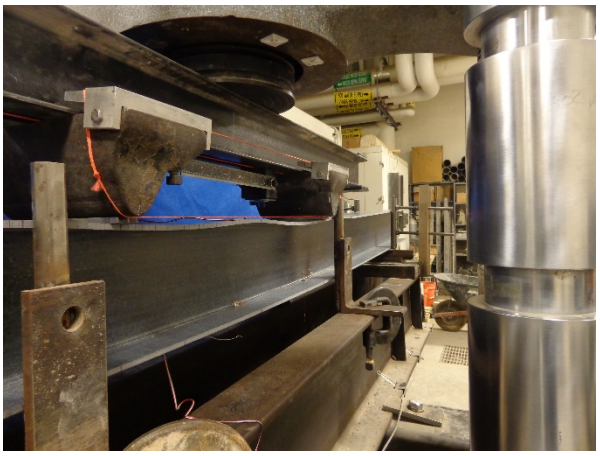	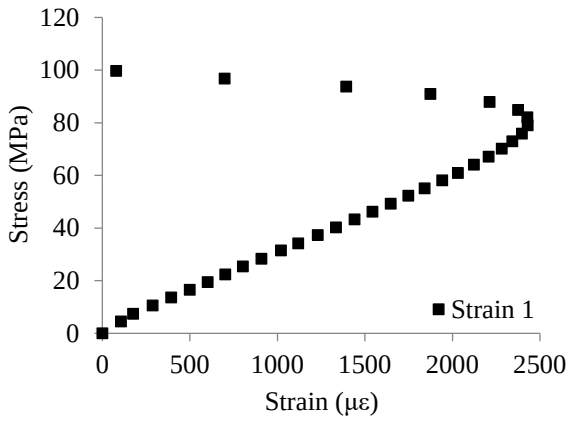	
M_{cr} = 10626 Nm		

Specimen: FLB5-2	Span: 2200 mm	Date: 9/21/2015
	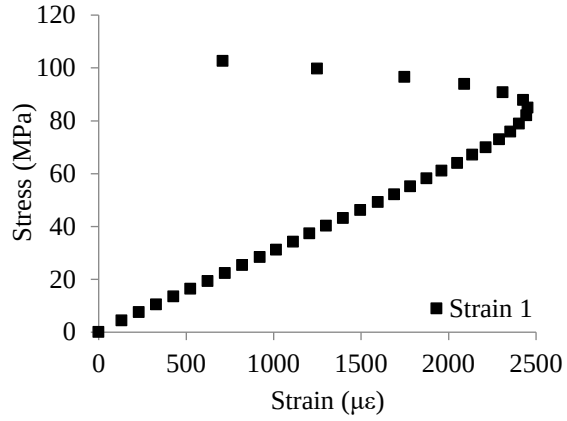	
M_{cr} = 11066 Nm		

Specimen: FLB5-2	Span: 2200 mm	Date: 9/22/2015
	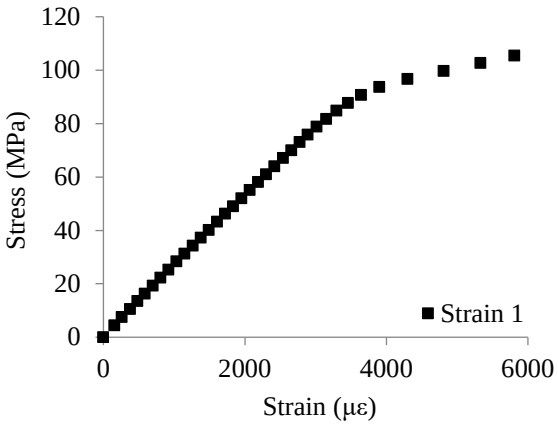	
M_{cr} = 12166 Nm		

Specimen: FLB5-1	Span: 1800 mm	Date: 9/29/2015
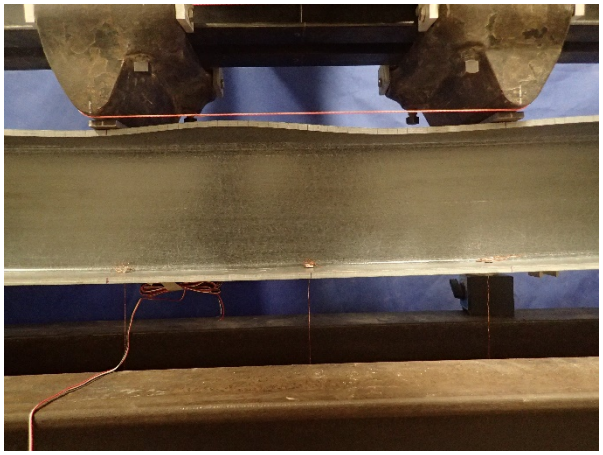	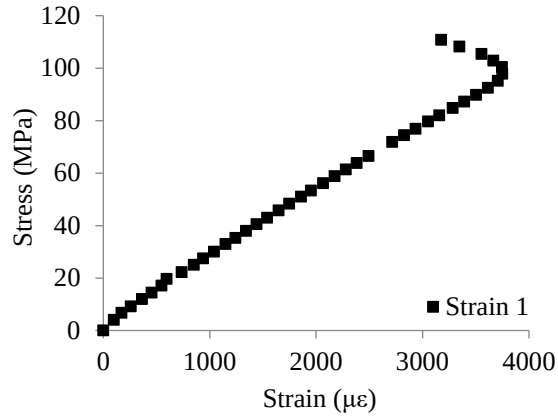	
M_{cr} = 13492 Nm		

Specimen: FLB5-1	Span: 1800 mm	Date: 9/29/2015
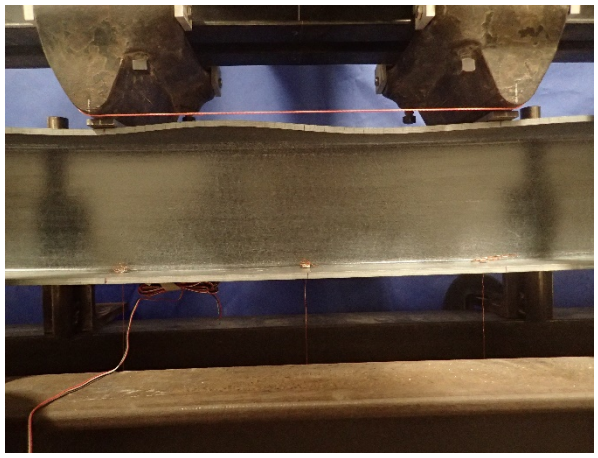	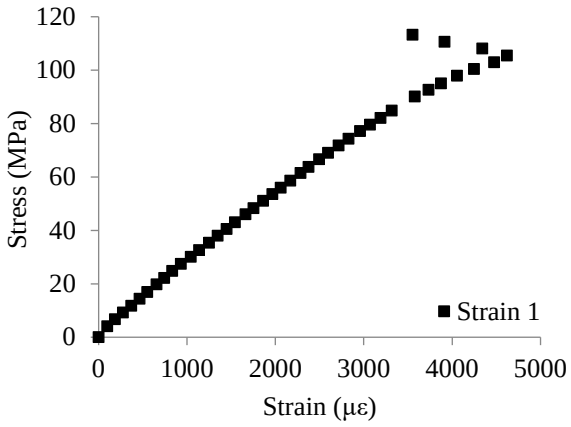	
M_{cr} = 13877 Nm		

Specimen: FLB5-1	Span: 1800 mm	Date: 9/29/2015
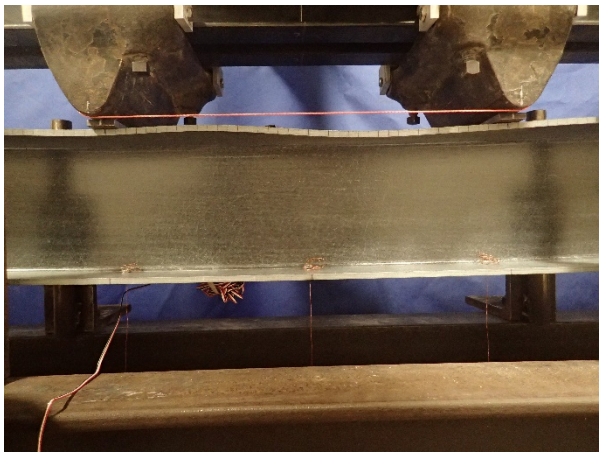	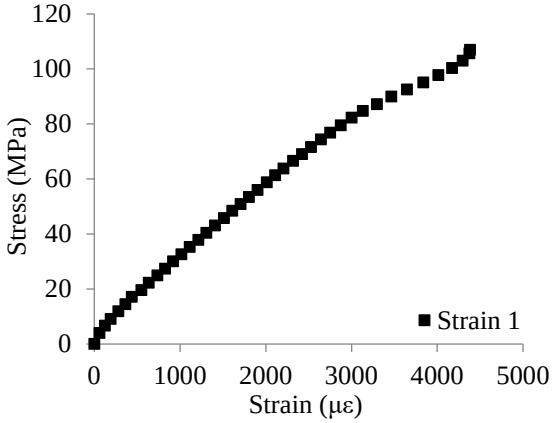	
M_{cr} = 14192 Nm		

Specimen: FLB5-2	Span: 1800 mm	Date: 10/1/2015
	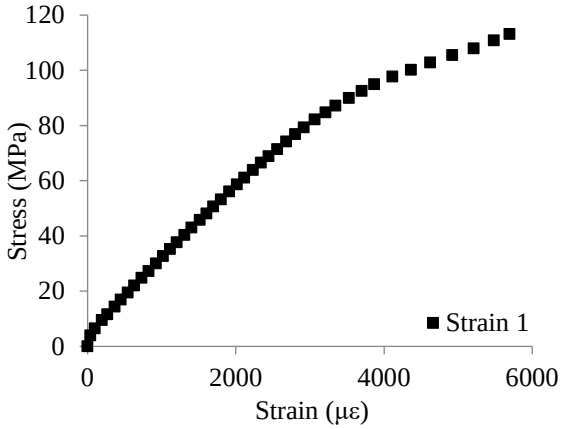	
M_{cr} = 11987 Nm		

Specimen: FLB5-2	Span: 1800 mm	Date: 10/1/2015
	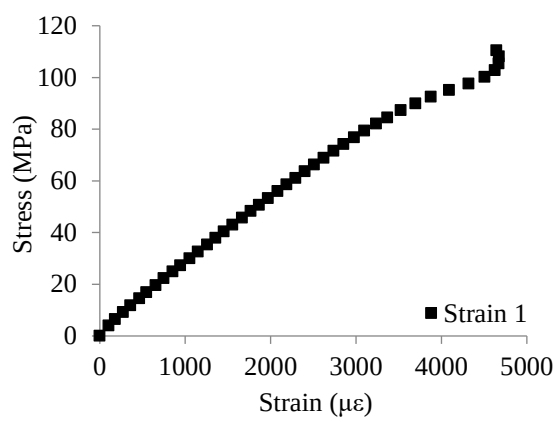	
M_{cr} = 14192 Nm		

Specimen: FLB5-1	Span: 1800 mm	Date: 9/22/2015
	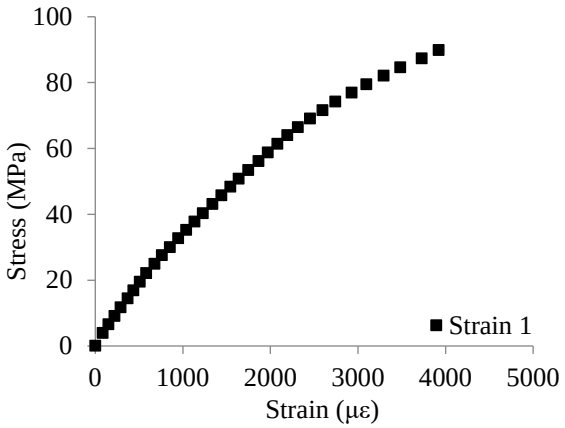	
M_{cr} = 9817* Nm		

Specimen: FLB5-2	Span: 1800 mm	Date: 9/22/2015
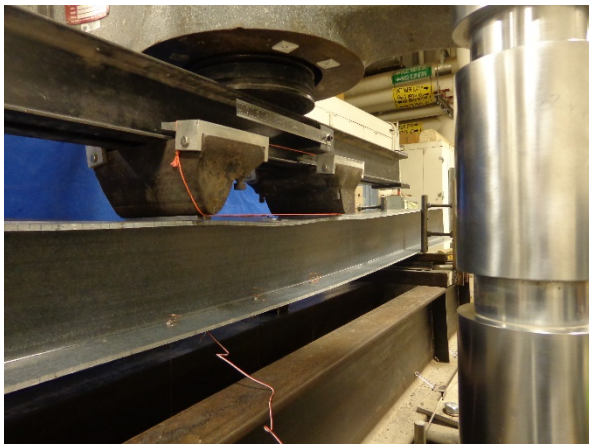	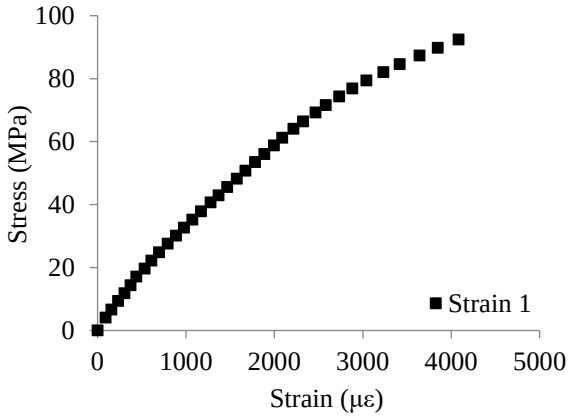	
M_{cr} = 9292* Nm		

Specimen: FLB4-1	Span: 1800 mm	Date: 10/7/2015
	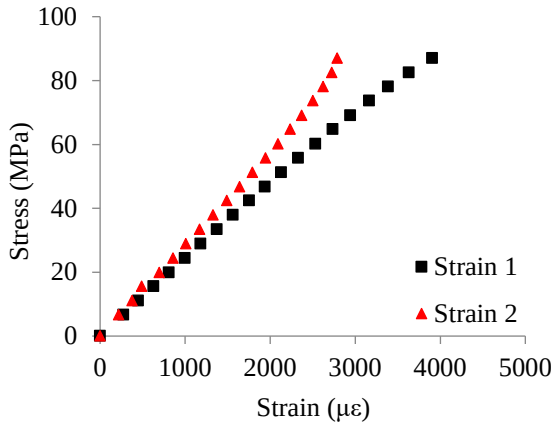	
M_{cr} = 9285 Nm (LTB Failure)		

Specimen: FLB4-2	Span: 2900 mm	Date: 10/9/2015
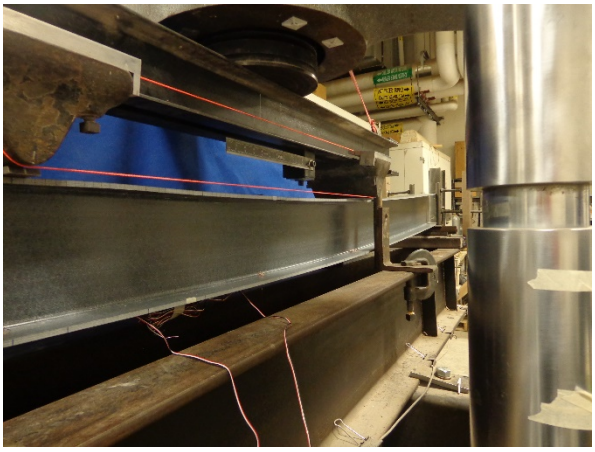	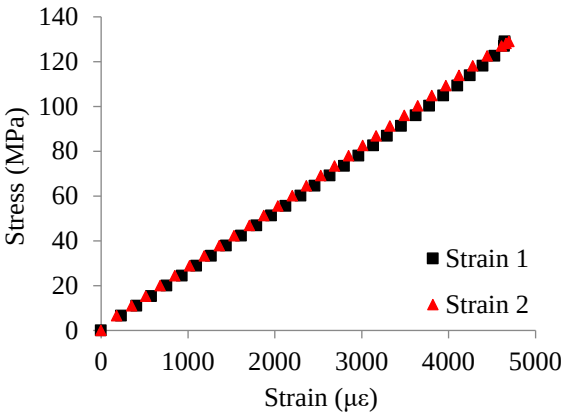	
M_{cr} = 14235 Nm		

Specimen: FLB4-2	Span: 2900 mm	Date: 10/9/2015
	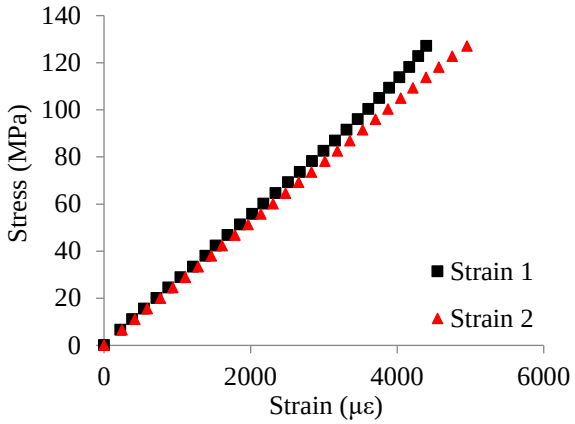	
M_{cr} = 13735 Nm		

Specimen: FLB4-3	Span: 2900 mm	Date: 11/2/2015
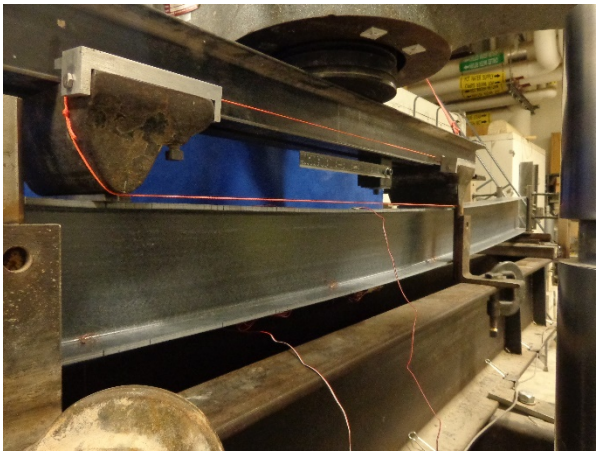	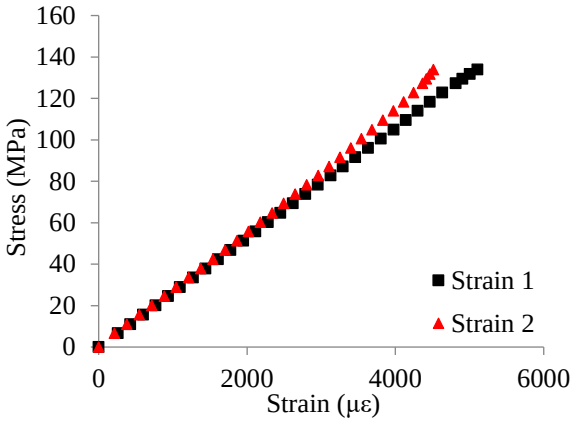	
M_{cr} = 14335 Nm		

Specimen: FLB4-3	Span: 2900 mm	Date: 11/2/2015
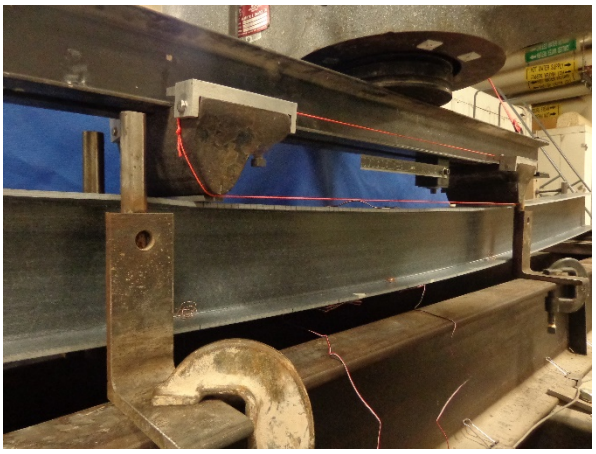	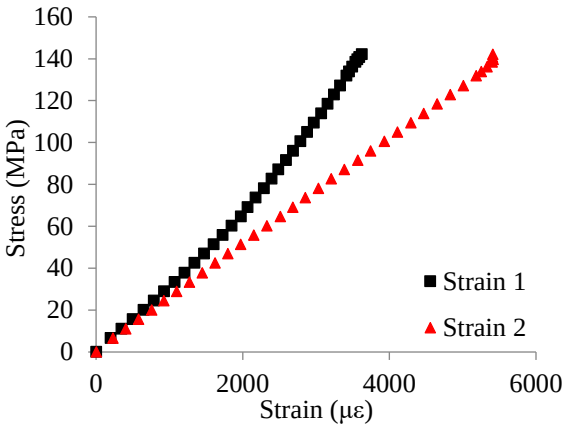	
M_{cr} = 15635 Nm		

Specimen: FLB4-2	Span: 2600 mm	Date:10/12/2015
	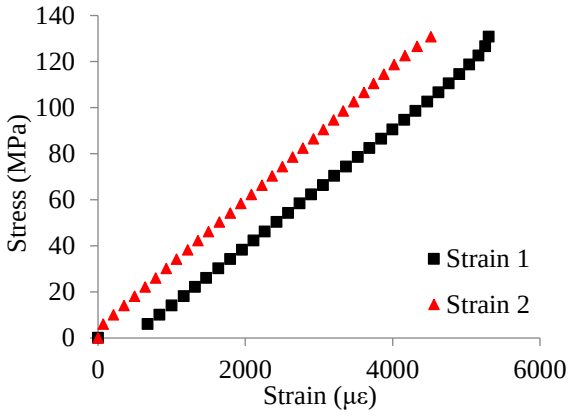	
M_{cr} = 14653 Nm		

Specimen: FLB4-2	Span: 2600 mm	Date:10/12/2015
	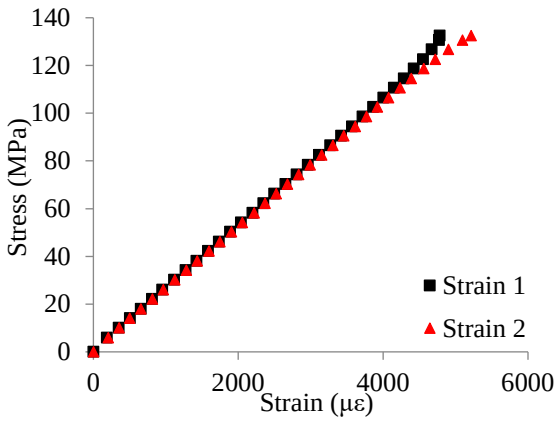	
M_{cr} = 14698 Nm		

Specimen: FLB4-3	Span: 2600 mm	Date: 11/5/2015
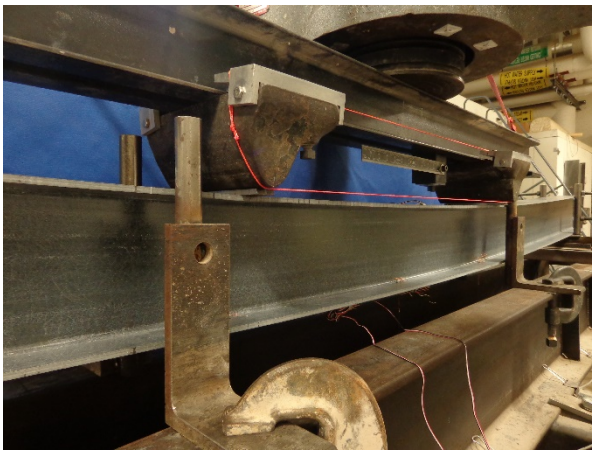	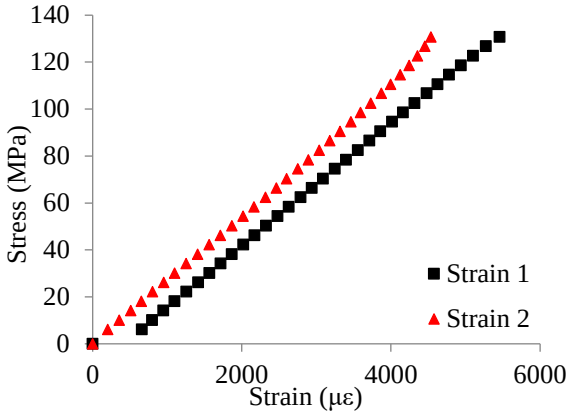	
M_{cr} = 14653 Nm		

Specimen: FLB4-3	Span: 2600 mm	Date: 11/6/2015
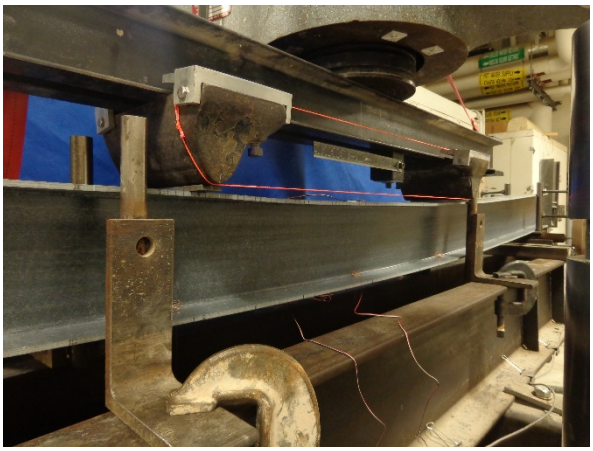	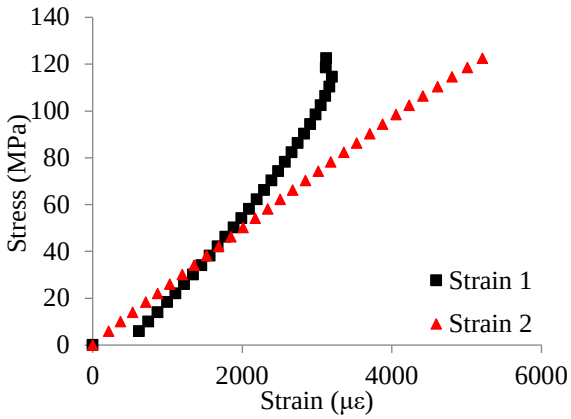	
M_{cr} = 12853 Nm		

Specimen: FLB4-2	Span: 2200 mm	Date:10/13/2015
	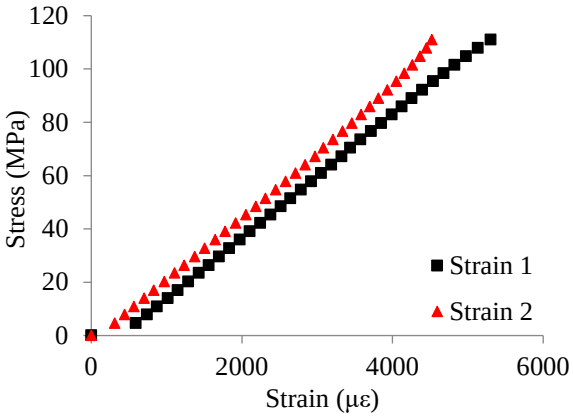	
M_{cr} = 14180 Nm		

Specimen: FLB4-2	Span: 2200 mm	Date:10/13/2015
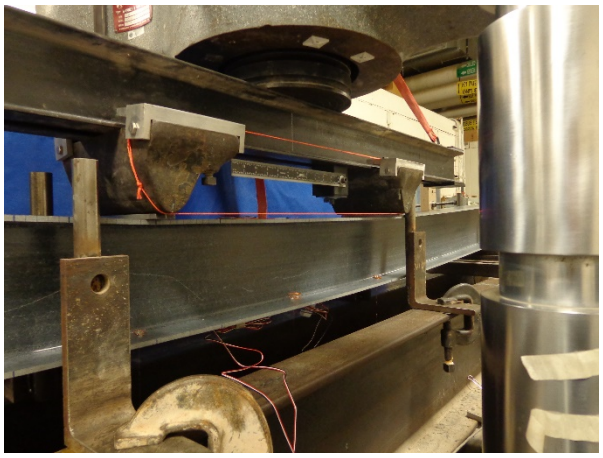	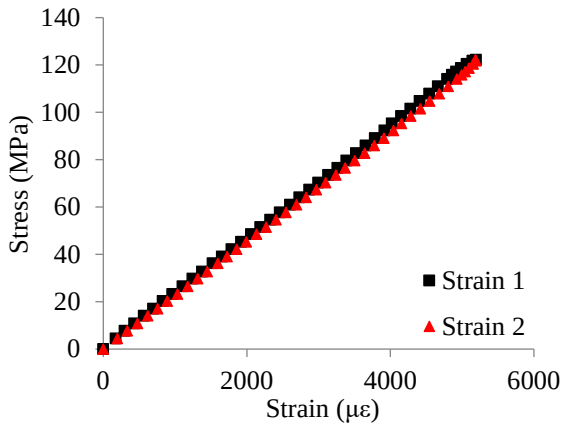	
M_{cr} = 15620 Nm		

Specimen: FLB4-3	Span: 2200 mm	Date: 11/5/2015
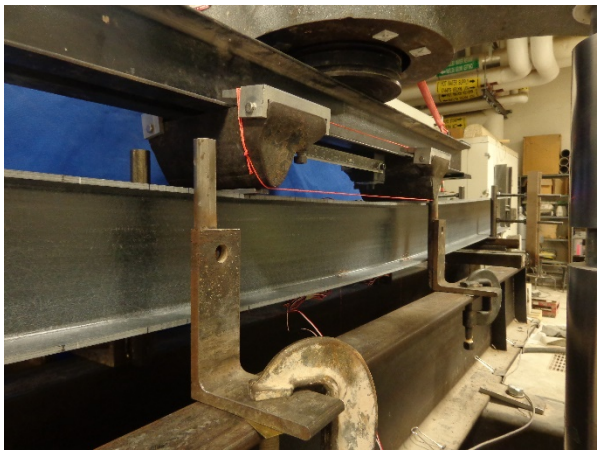	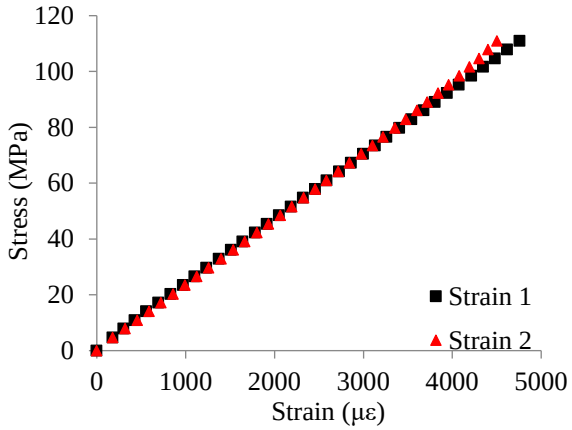	
M_{cr} = 13820 Nm		

Specimen: FLB4-3	Span: 2200 mm	Date: 11/5/2015
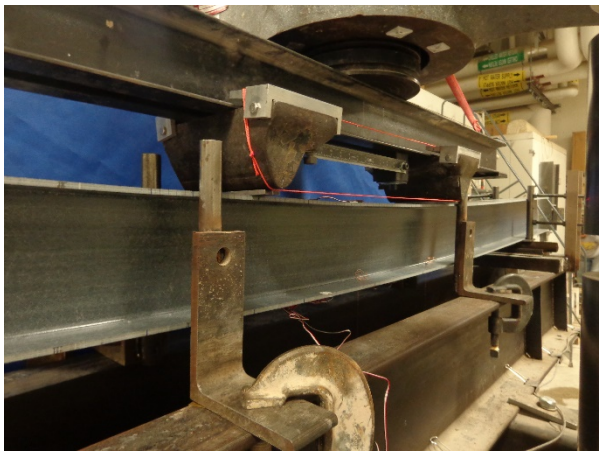	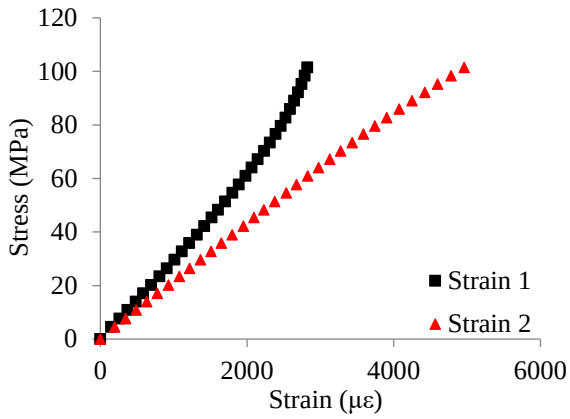	
M_{cr} = 12620 Nm		

Specimen: FLB4-2	Span: 1800 mm	Date:10/14/2015
	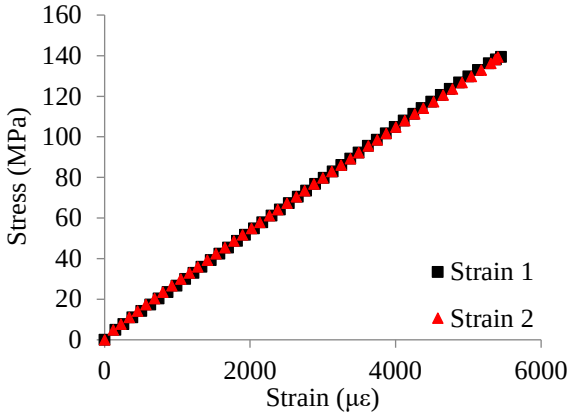	
M_{cr} = 15554 Nm		

Specimen: FLB4-3	Span: 1800 mm	Date: 11/6/2015
	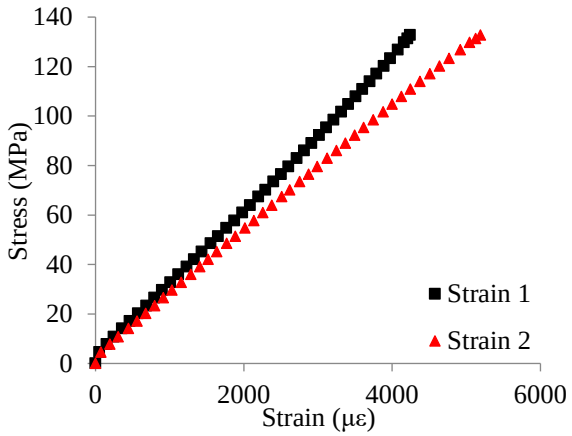	
M_{cr} = 14539 Nm		

Specimen: FLB4-2	Span: 1800 mm	Date:3/23/2016
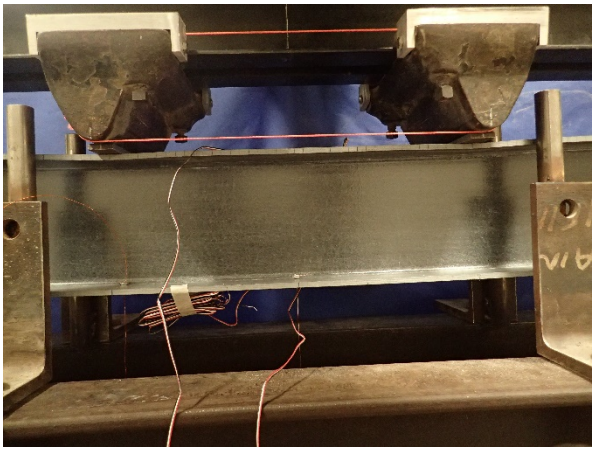	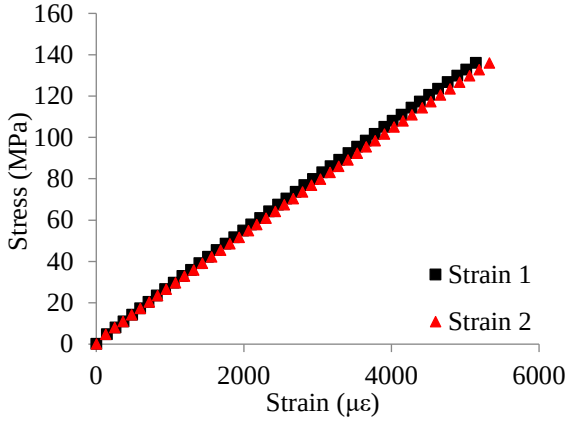	
M_{cr} = 14889 Nm		

Specimen: FLB4-2	Span: 1800 mm	Date:10/15/2015
	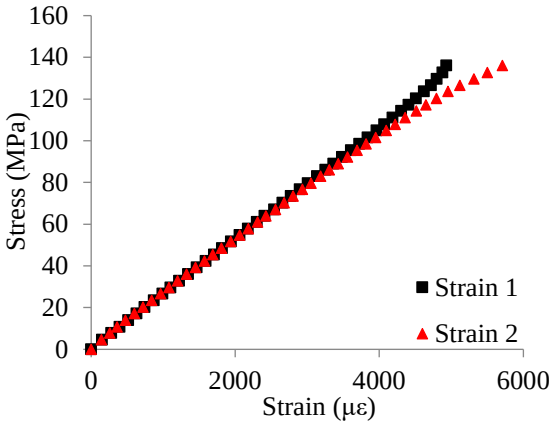	
M_{cr} = 14540 Nm		

Specimen: FLB4-3	Span: 1800 mm	Date: 11/6/2015
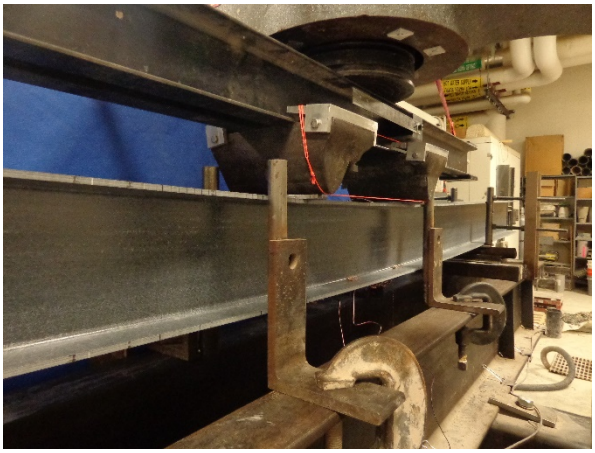	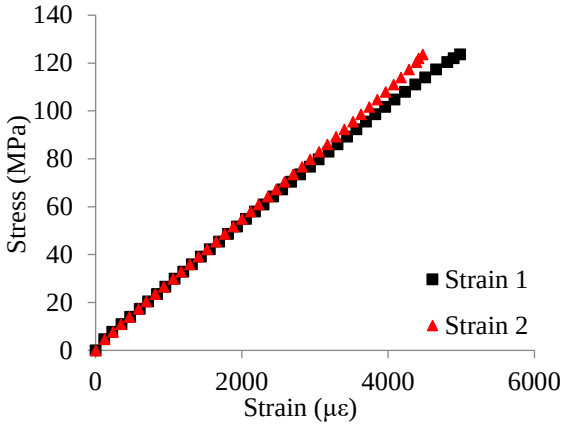	
M_{cr} = 13664 Nm		

Specimen: FLB4-2	Span: 1800 mm	Date: 3/23/2016
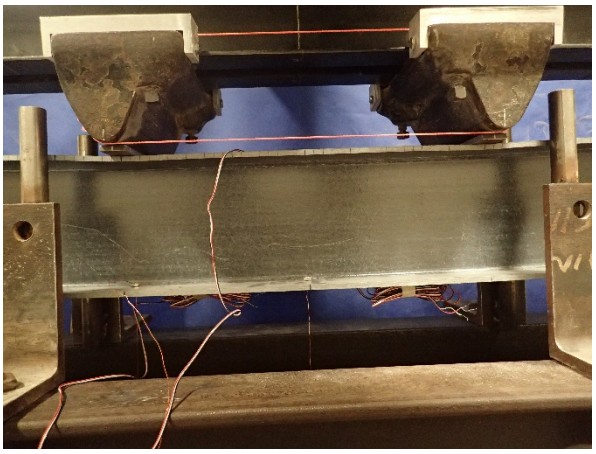	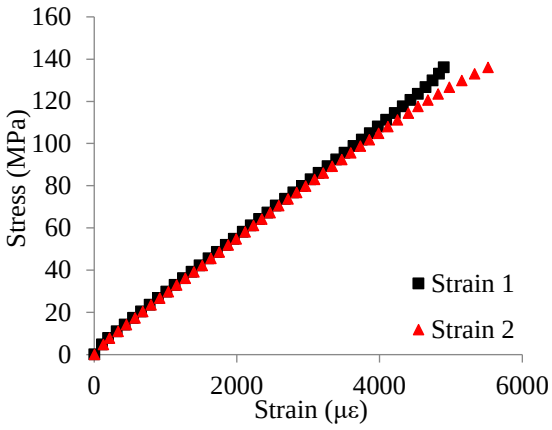	
M_{cr} = 14884 Nm		

Specimen: FLB4-3	Span: 1800 mm	Date:3/23/2016
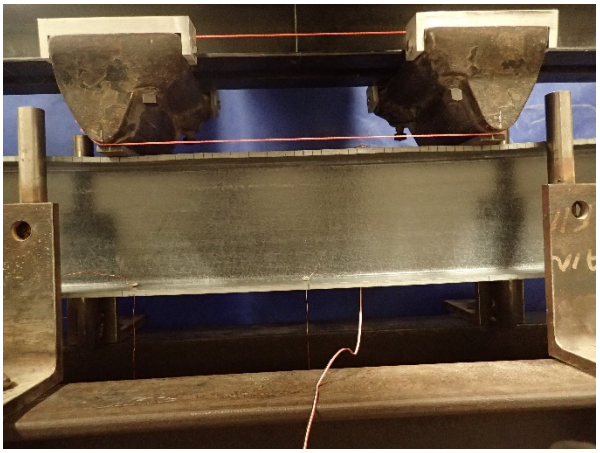	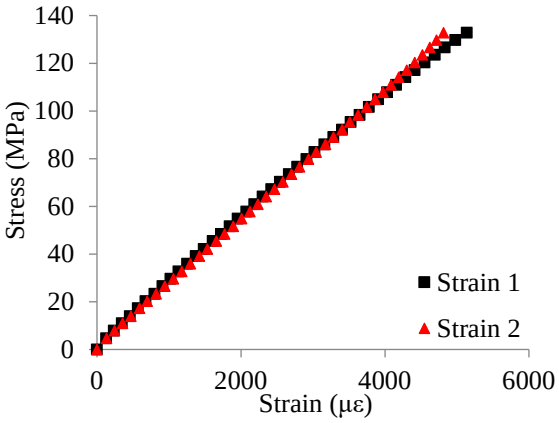	
M_{cr} = 14609 Nm		

Specimen: FLB3-1	Span: 2900 mm	Date: 11/2/2016
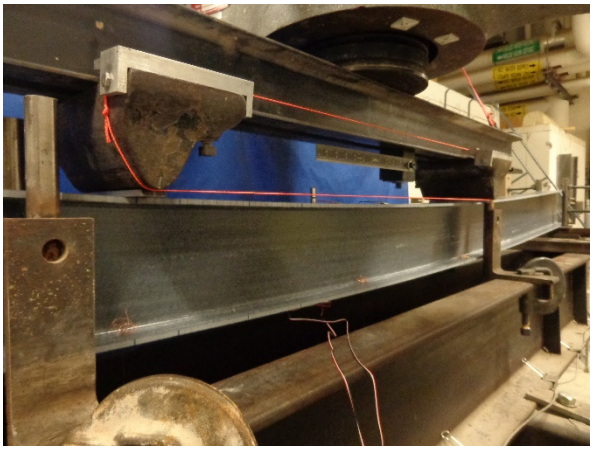	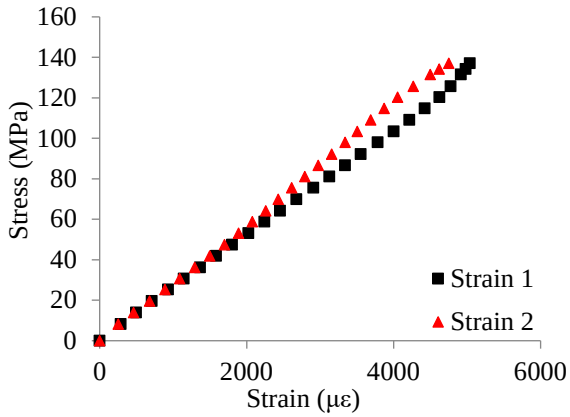	
M_{cr} = 11776 Nm		

Specimen: FLB3-1	Span: 2900 mm	Date: 11/3/2016
	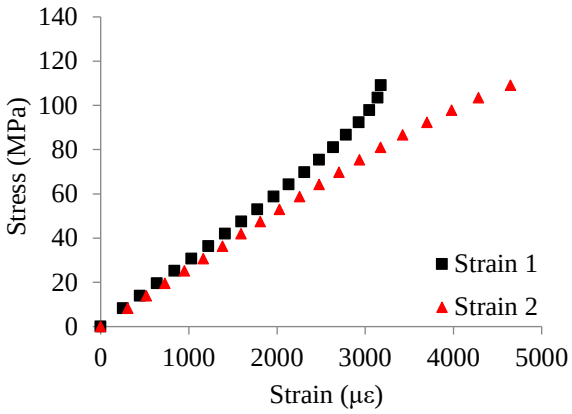	
M_{cr} = 9276 Nm		

Specimen: FLB3-1	Span: 2900 mm	Date: 11/3/2016
	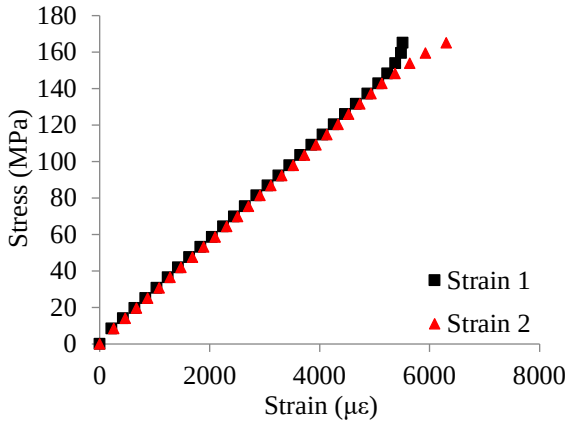	
M_{cr} = 14276 Nm		

Specimen: FLB3-1	Span: 2200 mm	Date:11/3/2016
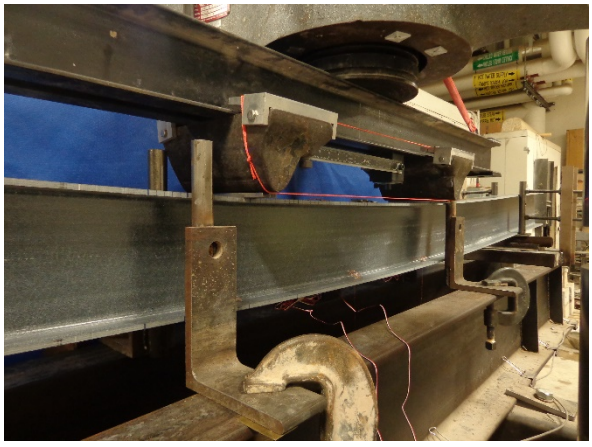	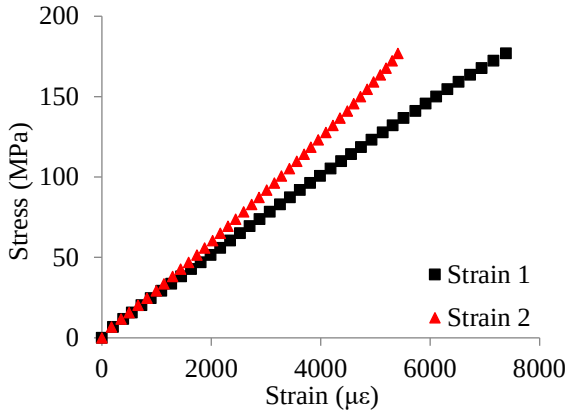	
M_{cr} = 15015 Nm		

A.2 THREE-POINT BENDING TESTS

In this experimental program, 86 three-point bending tests were conducted as reported in Chapter 6. Images, load-lateral displacement curves and flange stress-strain curves for all specimens are reported in this section. The strain gage layout on the compression flange is shown in Figure A.2. Tensile and compressive strain readings are taken as positive and negative, respectively.

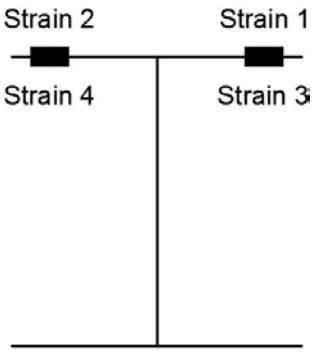

Figure A.2 Strain gage layout on the compression flange for three-point bending tests

Specimen: LTB6-2	Span: 2896 mm	Date:1/6/2016
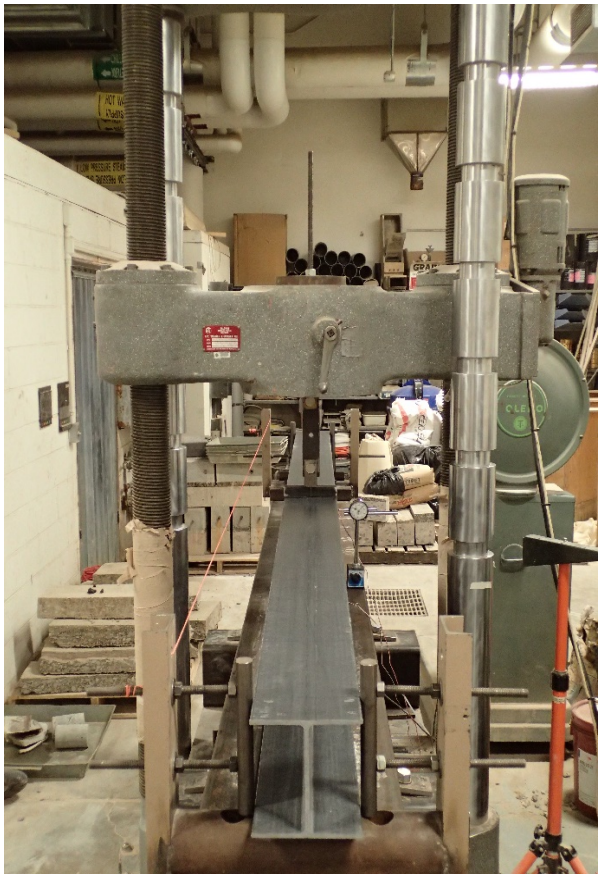	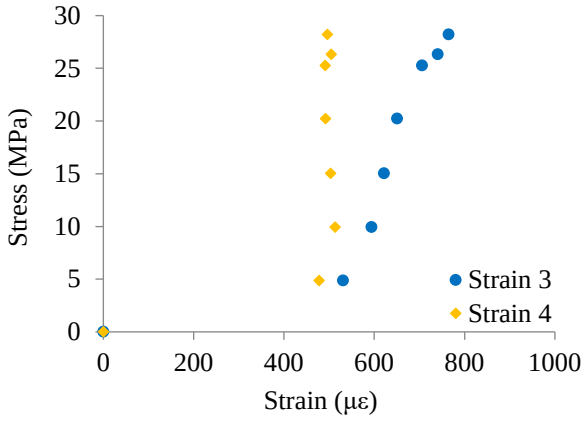 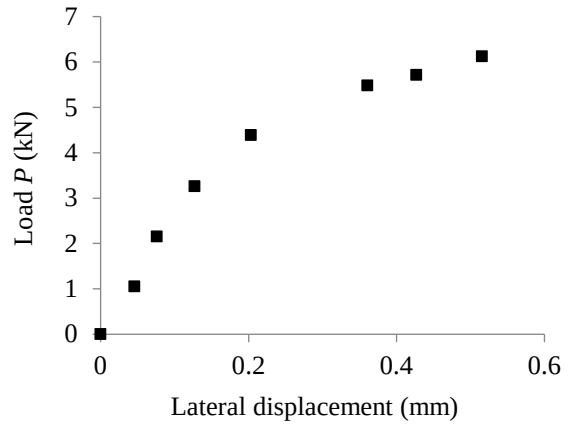	
M_{cr} = 3230 Nm		

Specimen: LTB6-2	Span: 2896 mm	Date:1/8/2016
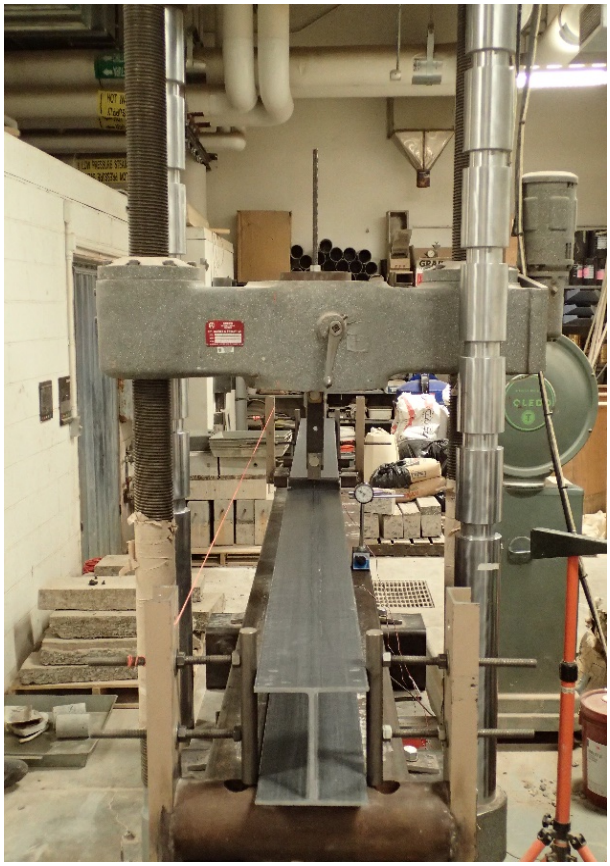	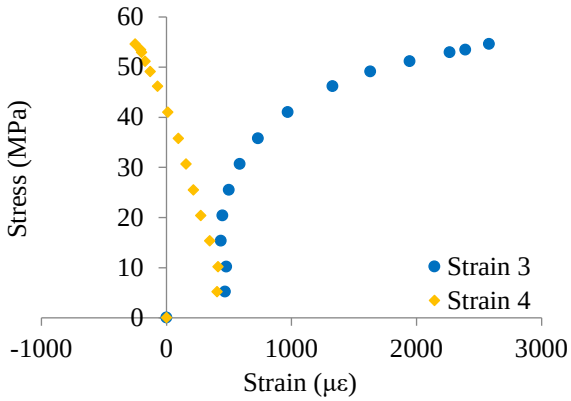	
	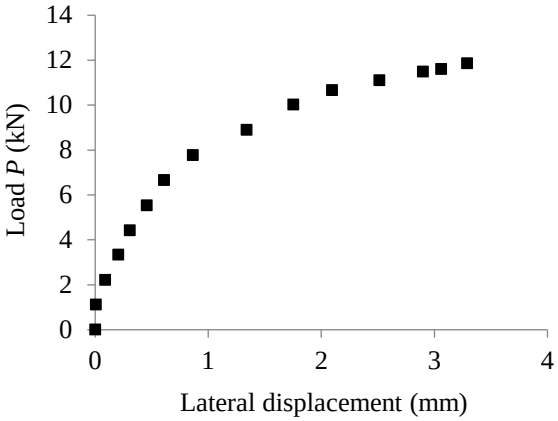	
M_{cr} = 3257 Nm		

Specimen: LTB6-2	Span: 2896 mm	Date:2/16/2016
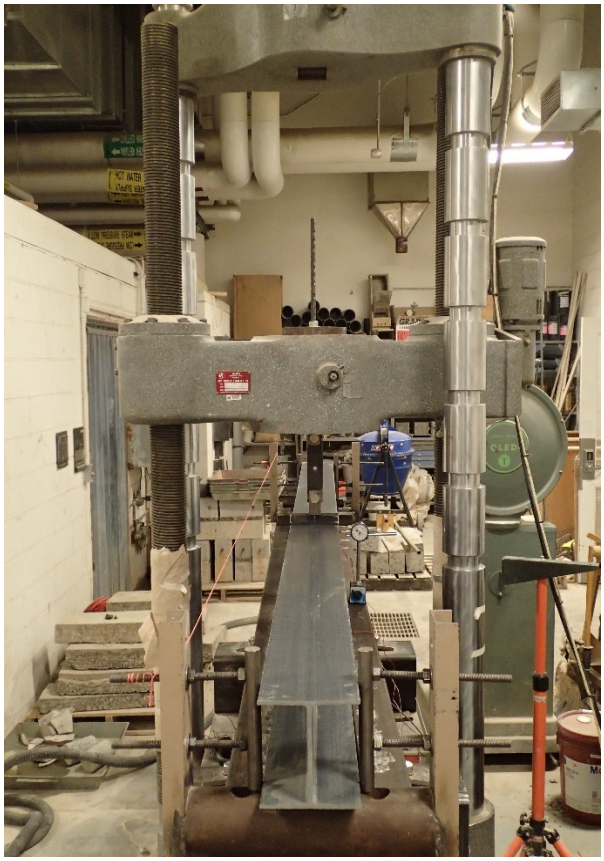	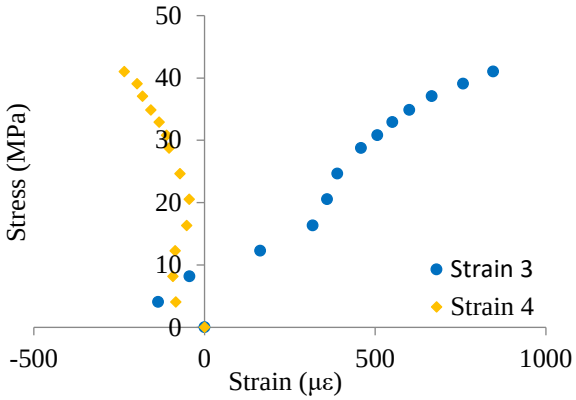 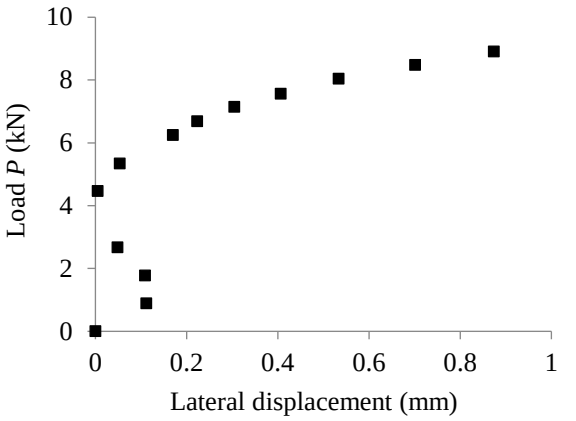	
M_{cr} = 3279 Nm		

Specimen: LTB6-2	Span: 2896 mm	Date:1/12/2016
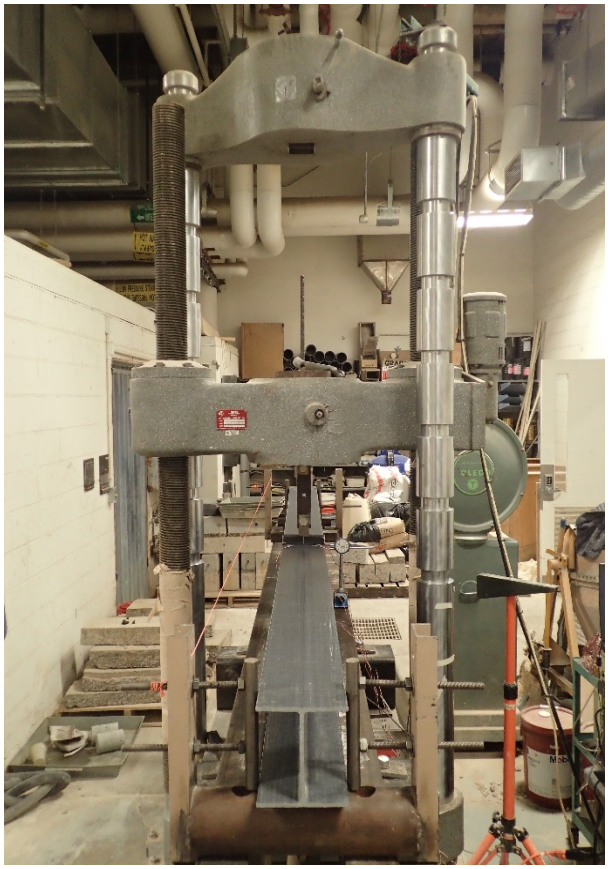	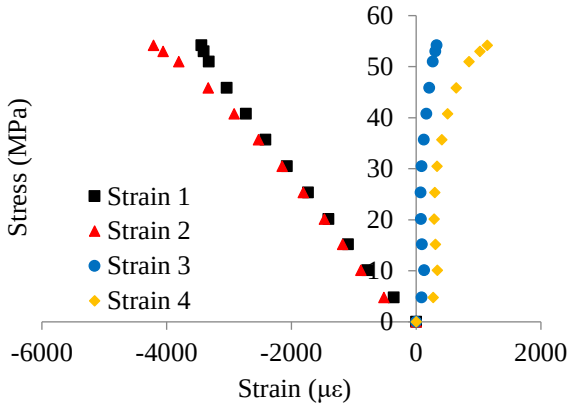 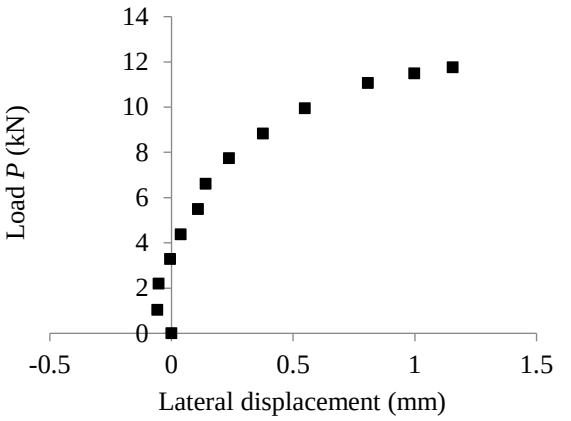	
M_{cr} = 3215 Nm		

Specimen: LTB6-2	Span: 2896 mm	Date:2/16/2016
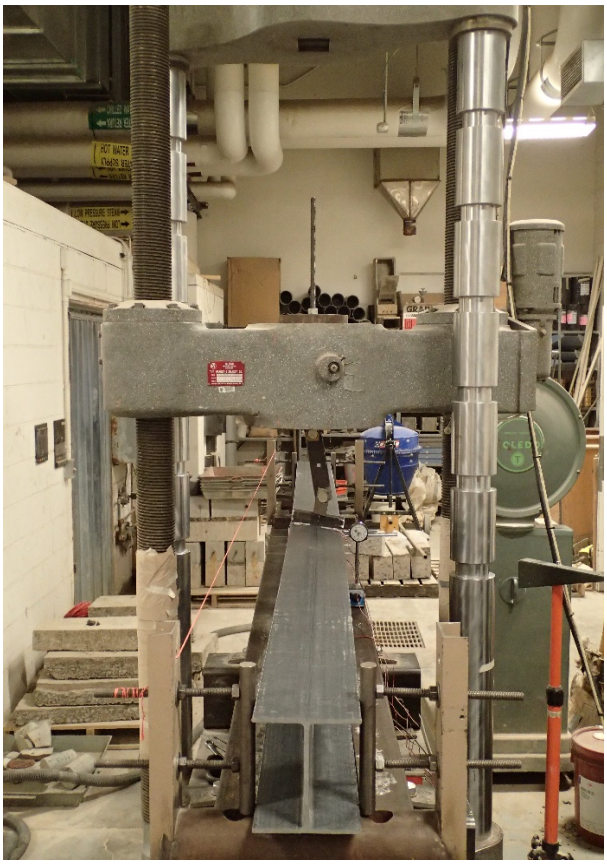	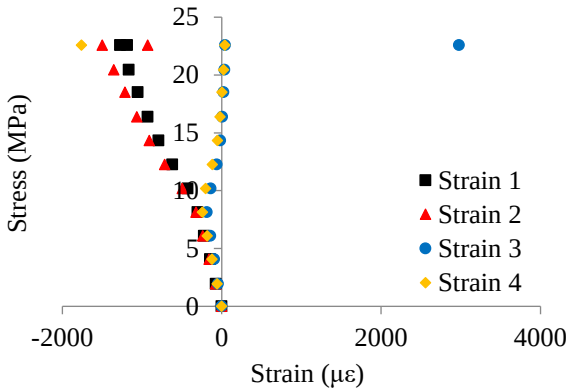	
	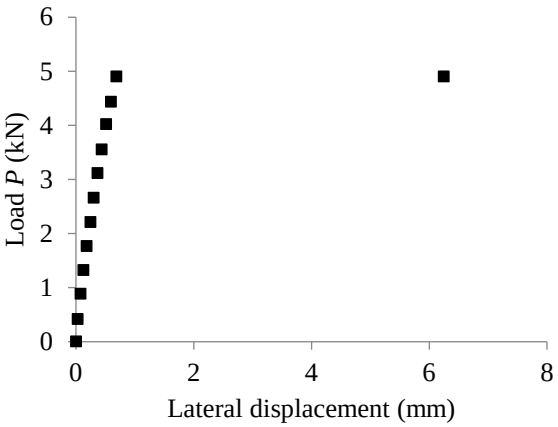	
M_{cr} = 3599 Nm		

Specimen: LTB6-2	Span: 2896 mm	Date:2/16/2016
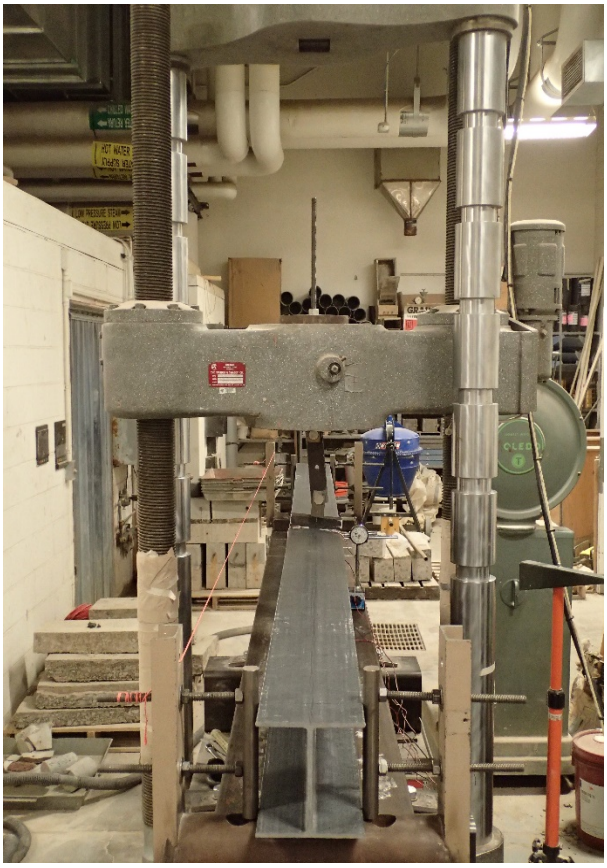	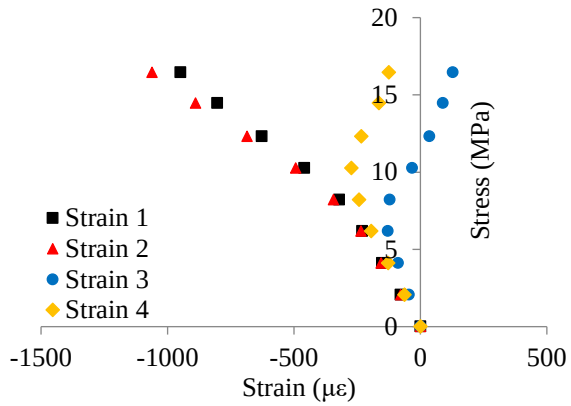	
	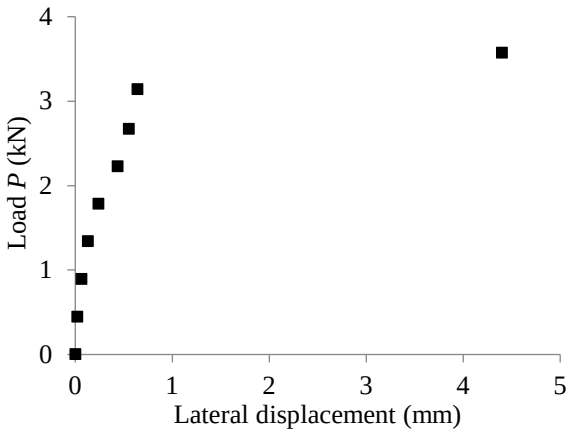	
M_{cr} = 2639 Nm		

Specimen: LTB6-1	Span: 2438 mm	Date:12/18/2015
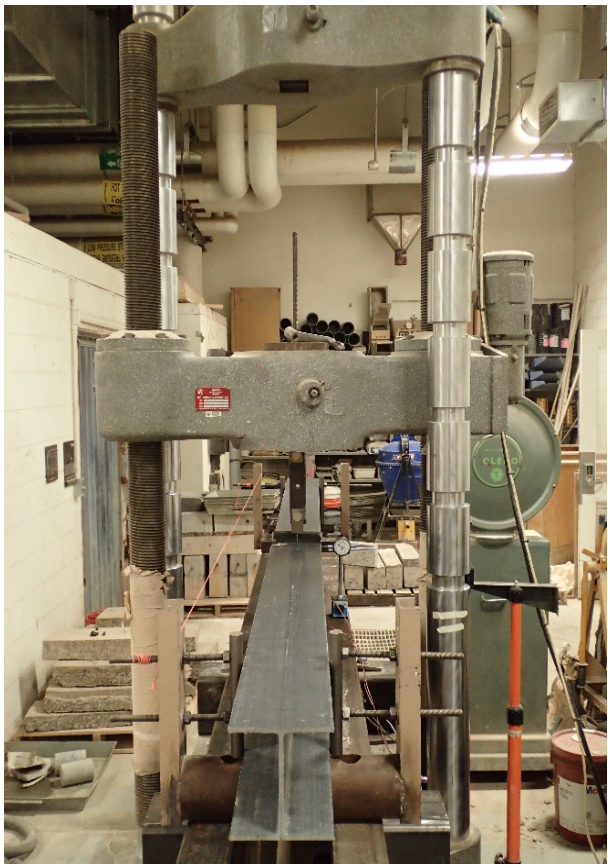	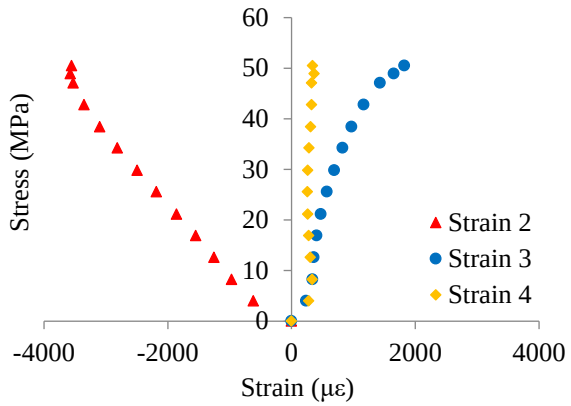	
	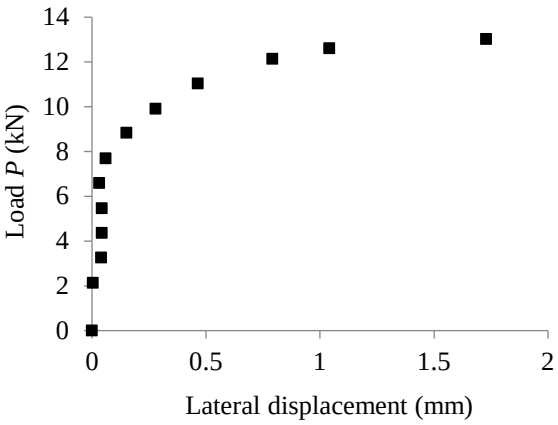	
M_{cr} = 4056 Nm		

Specimen: LTB6-2	Span: 2438 mm	Date:1/12/2016
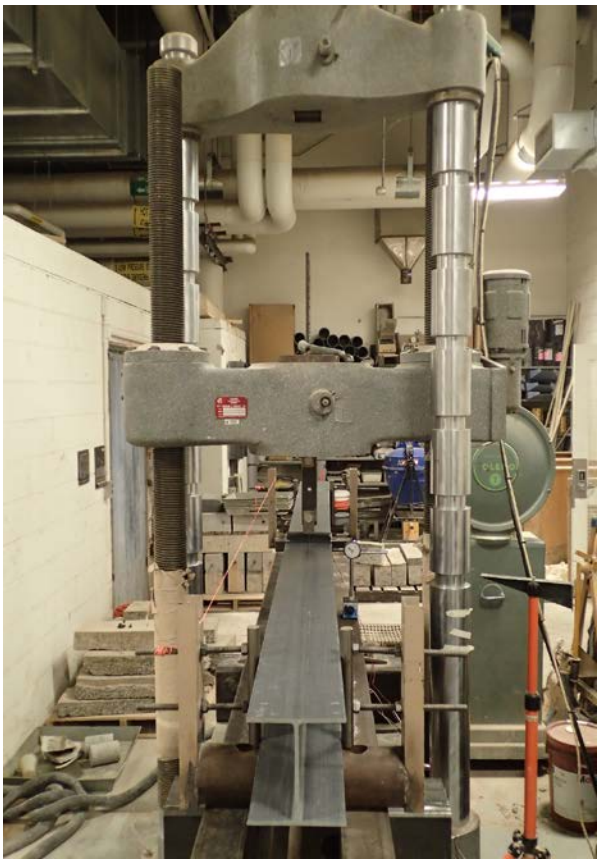	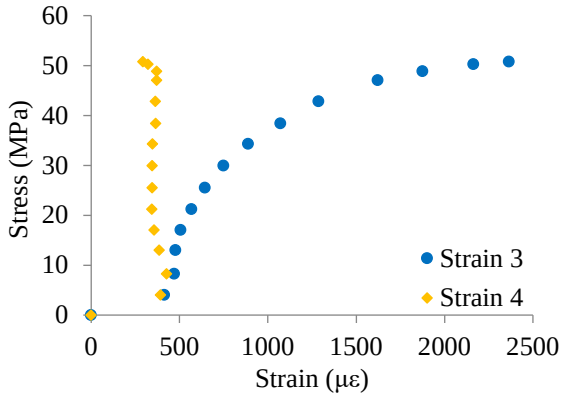 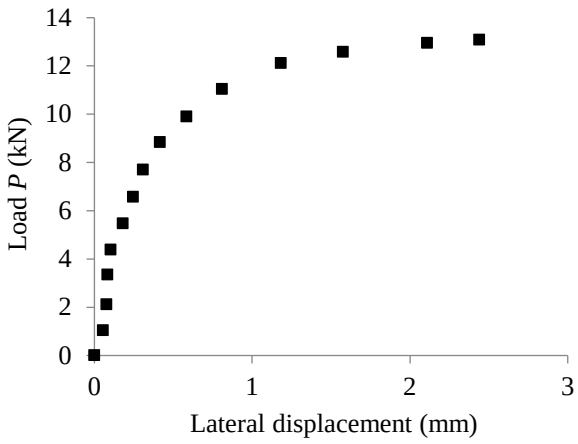	
M_{cr} = 4040 Nm		

Specimen: LTB6-2	Span: 2438 mm	Date:2/18/2016
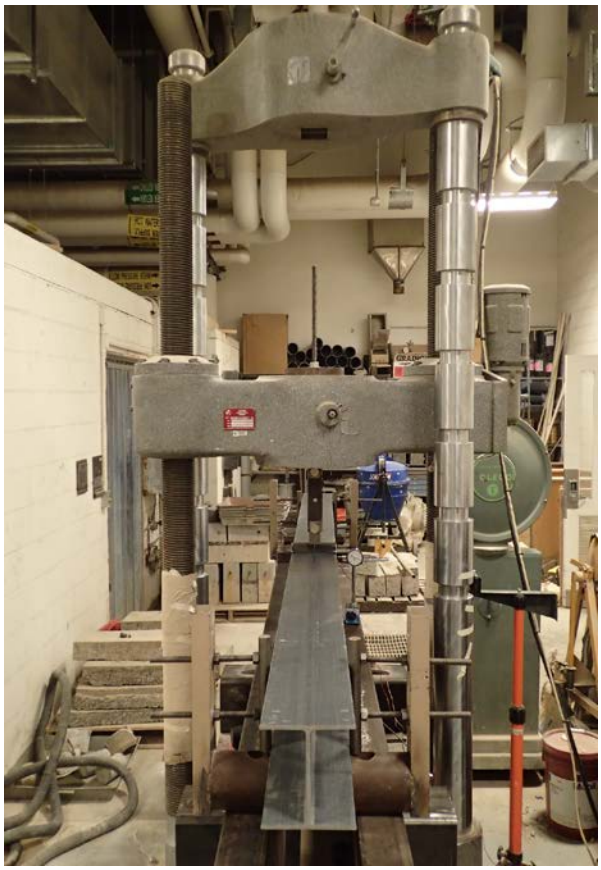	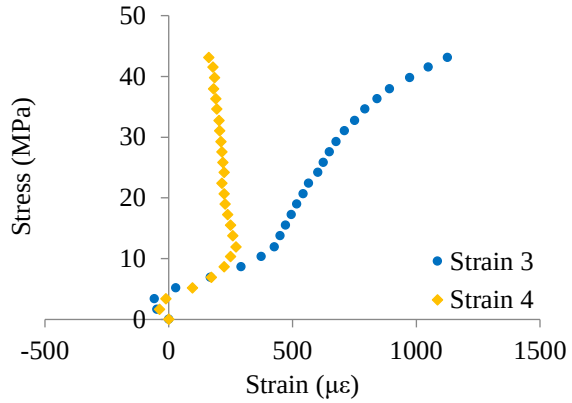 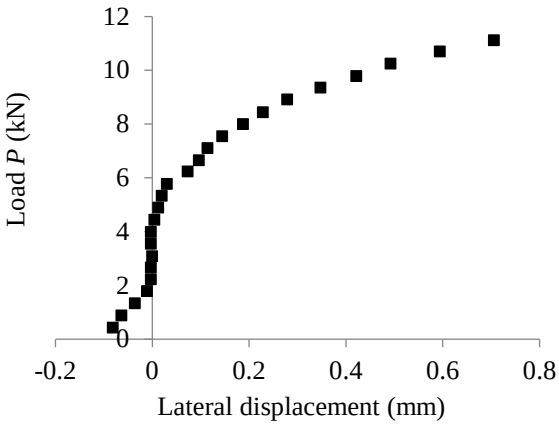	
M_{cr} = 4092 Nm		

Specimen: LTB6-2	Span: 2438 mm	Date:1/12/2016
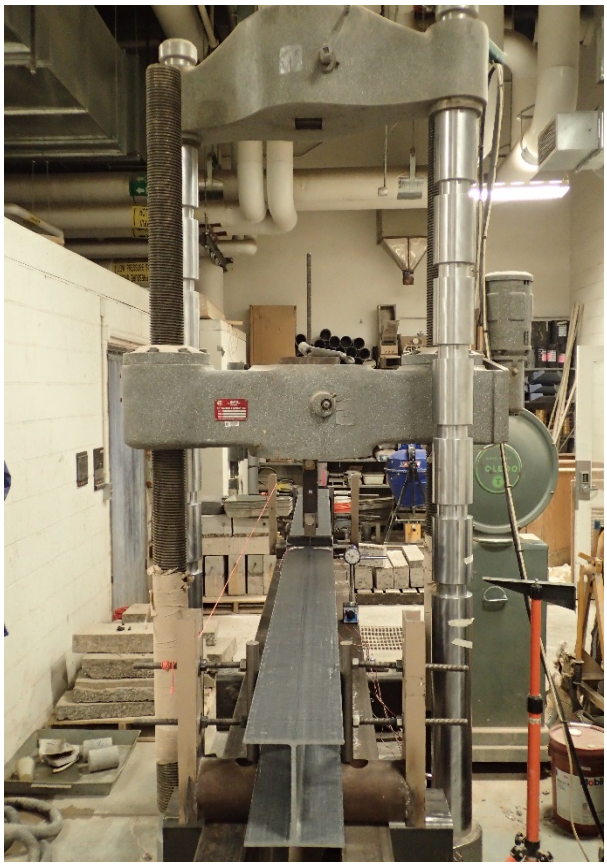	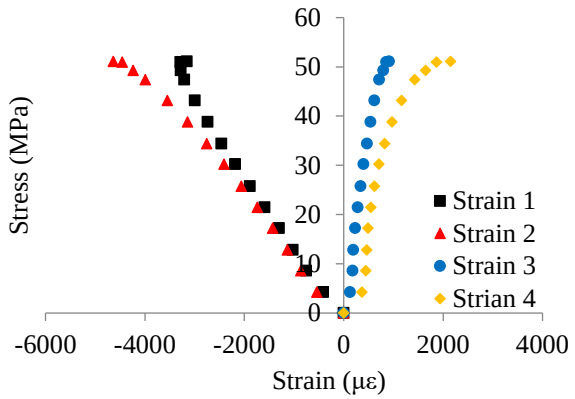 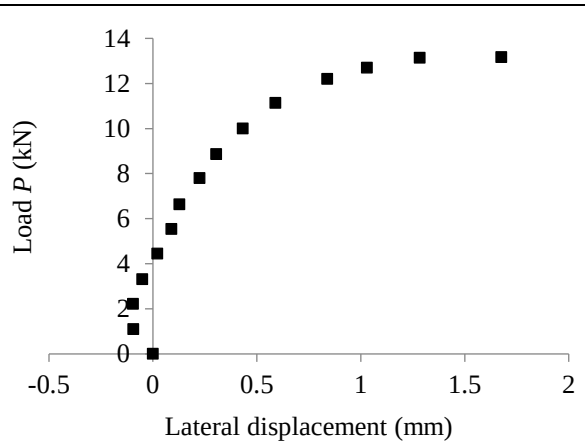	
M_{cr} = 4082 Nm		

Specimen: LTB6-2	Span: 2438 mm	Date:2/18/2016
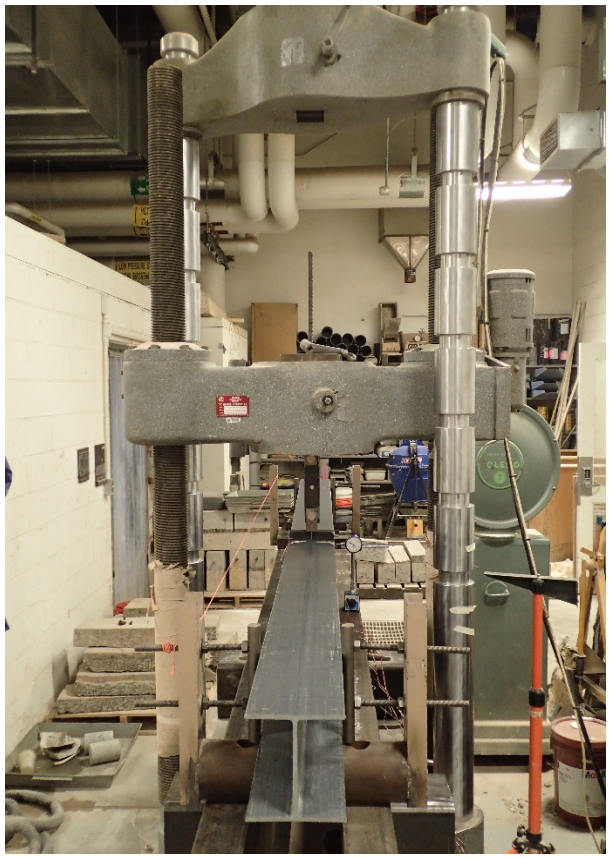	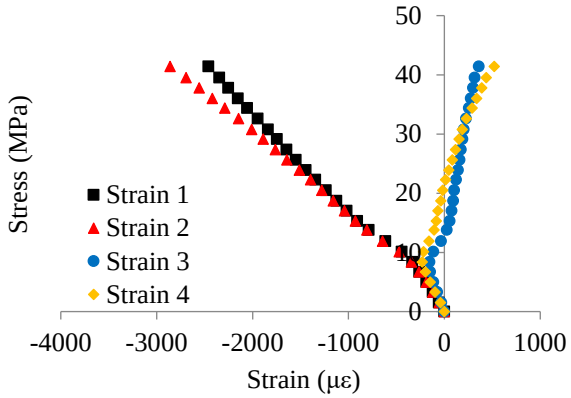	
	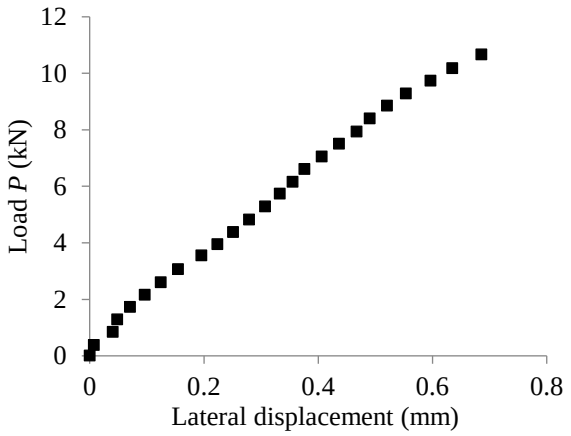	
M_{cr} = 4062 Nm		

Specimen: LTB6-2	Span: 2438 mm	Date:2/18/2016
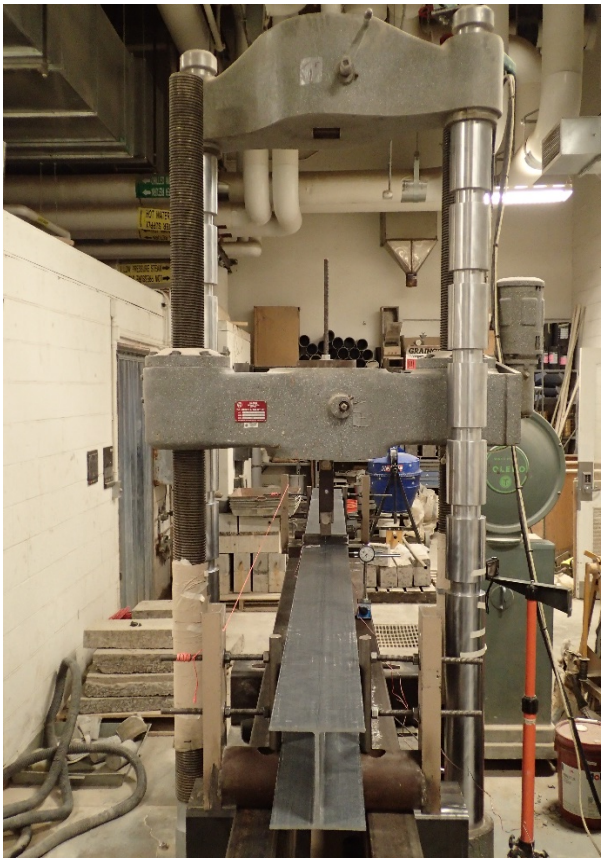	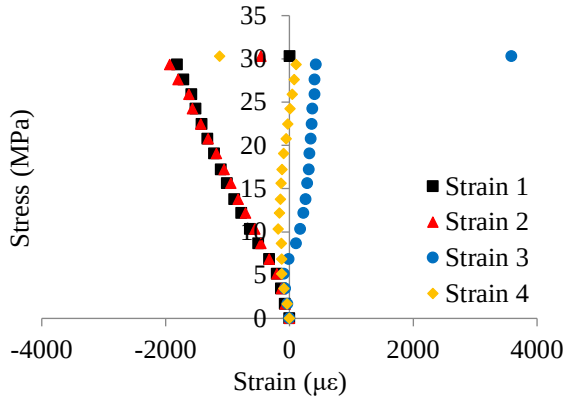	
	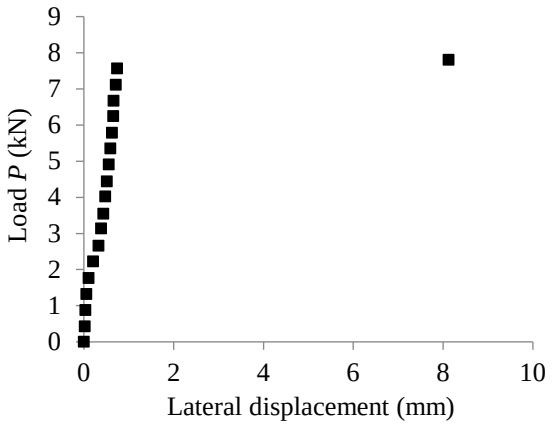	
M_{cr} = 4647 Nm		

Specimen: LTB6-2	Span: 2438 mm	Date:2/18/2016
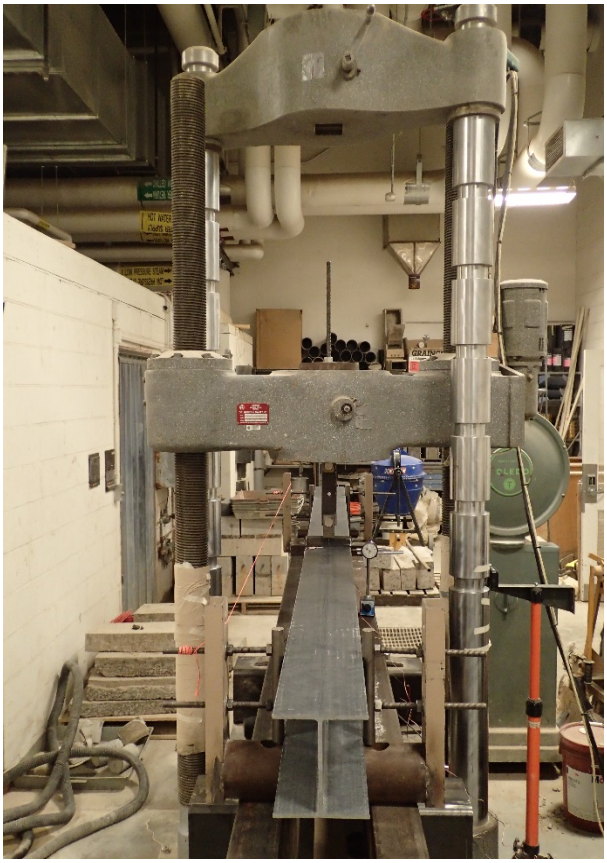	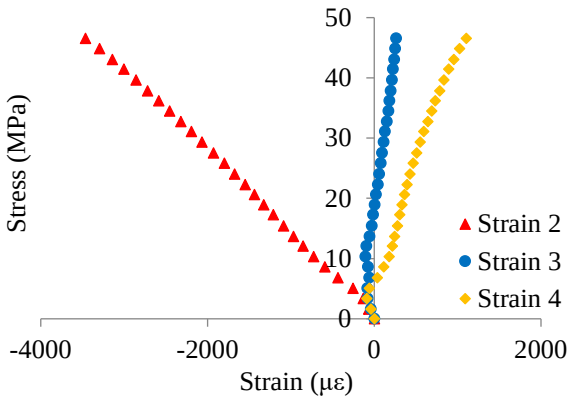 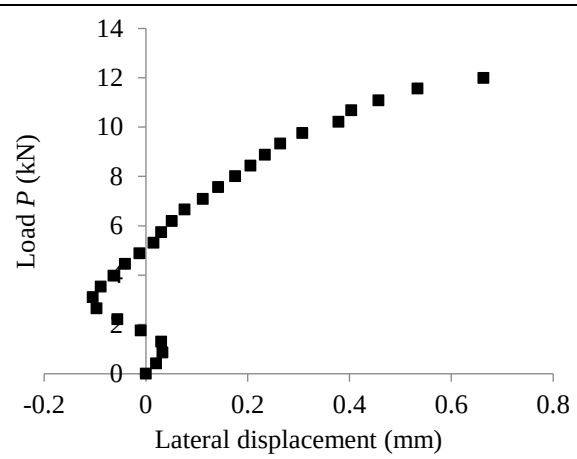	
M_{cr} = 4093 Nm		

Specimen: LTB6-2	Span: 2134 mm	Date:1/14/2016
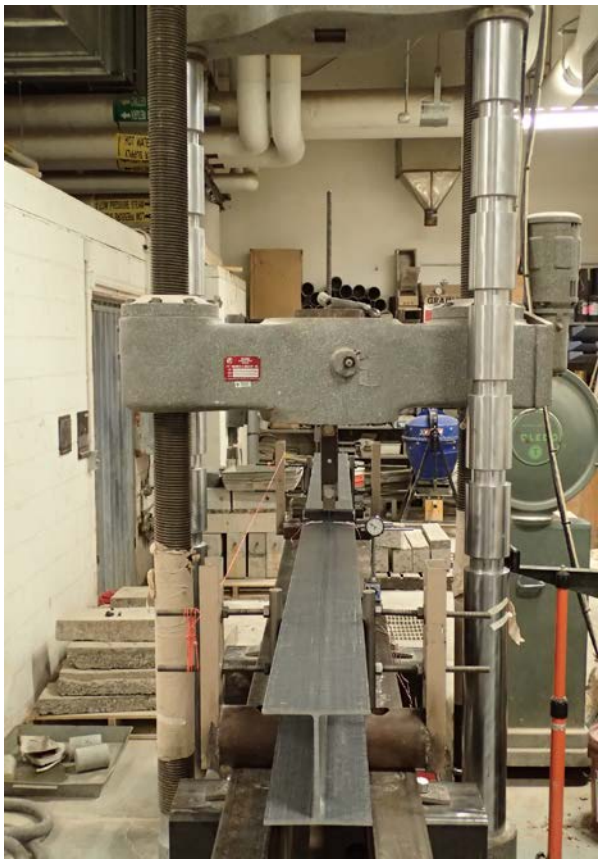	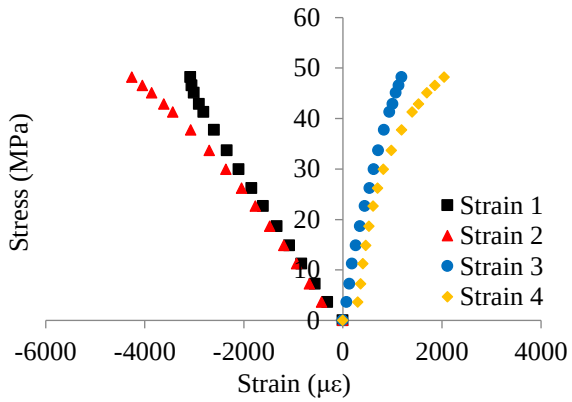	
	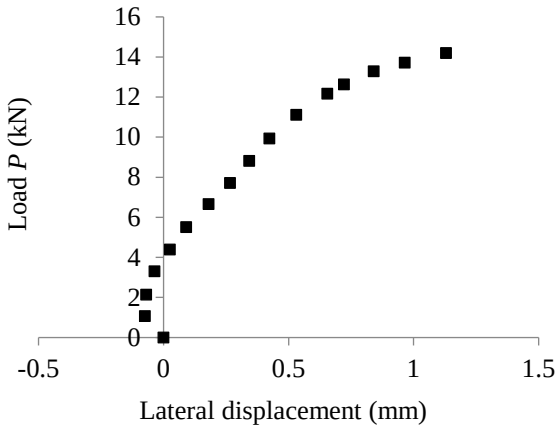	
M_{cr} = 5320 Nm		

Specimen: LTB6-2	Span: 2134 mm	Date:1/14/2016
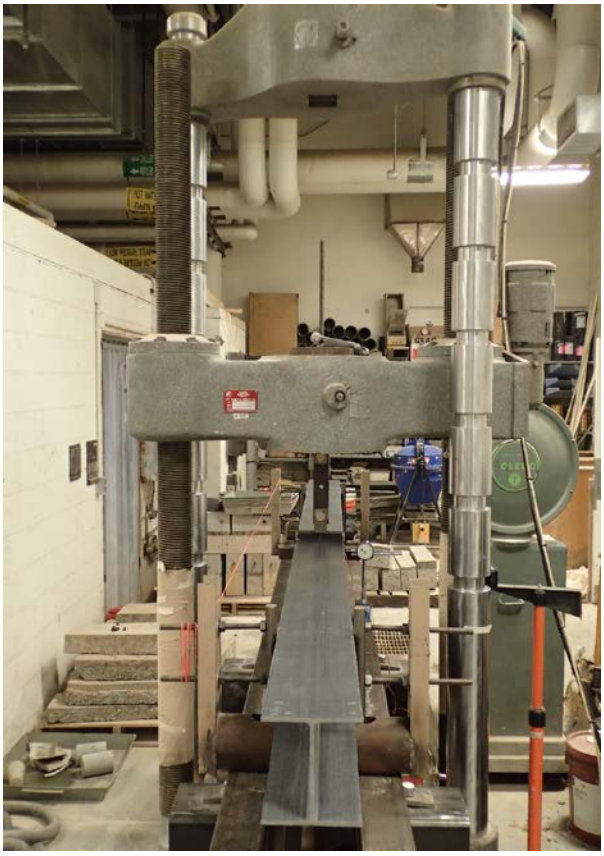	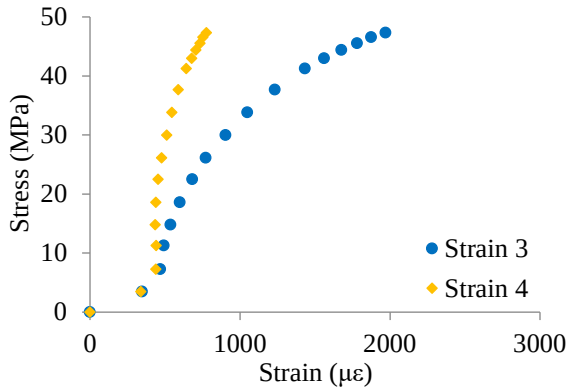 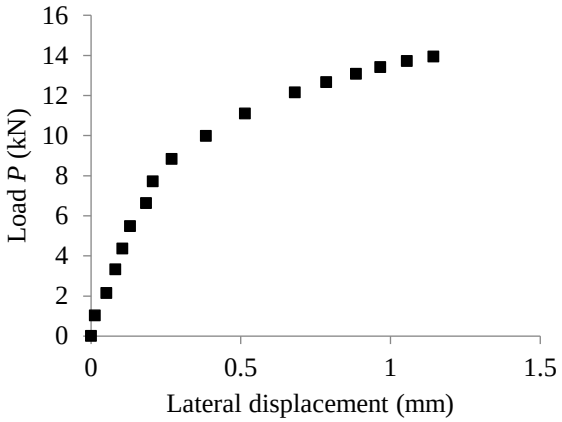	
M_{cr} = 4736 Nm		

Specimen: LTB6-2	Span: 2134 mm	Date:2/19/2016
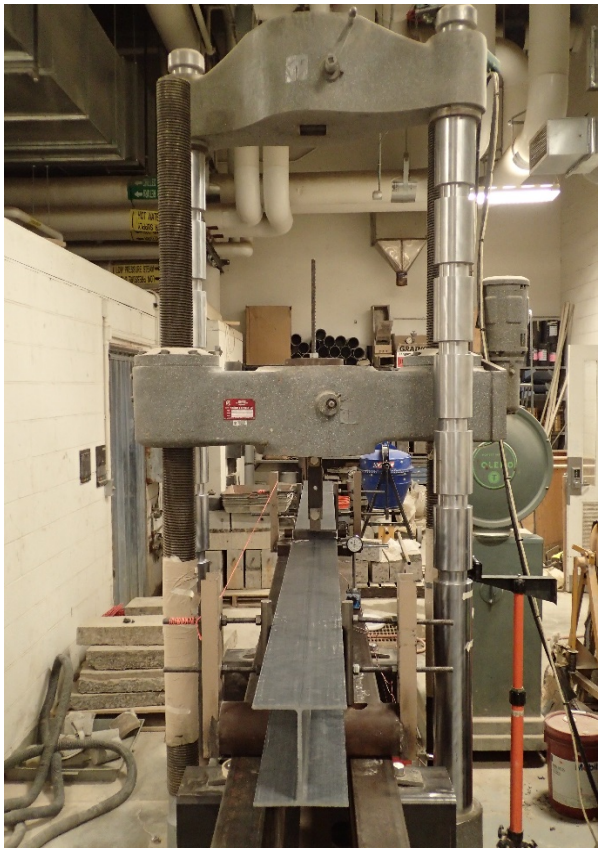	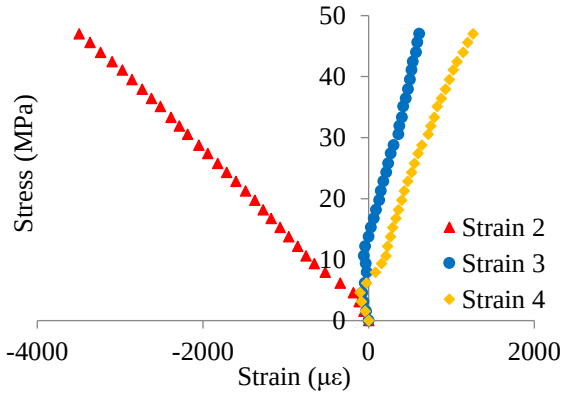 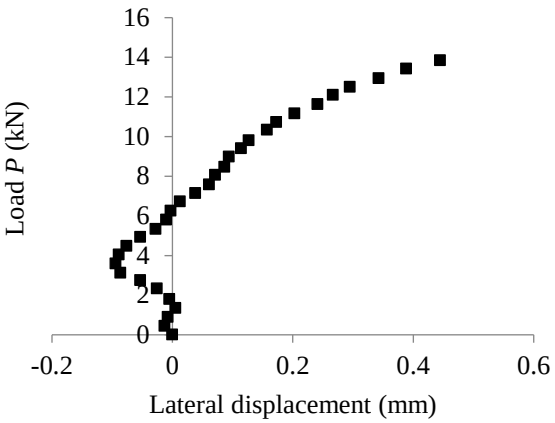	
M_{cr} = 5260 Nm		

Specimen: LTB6-2	Span: 2134 mm	Date:2/19/2016
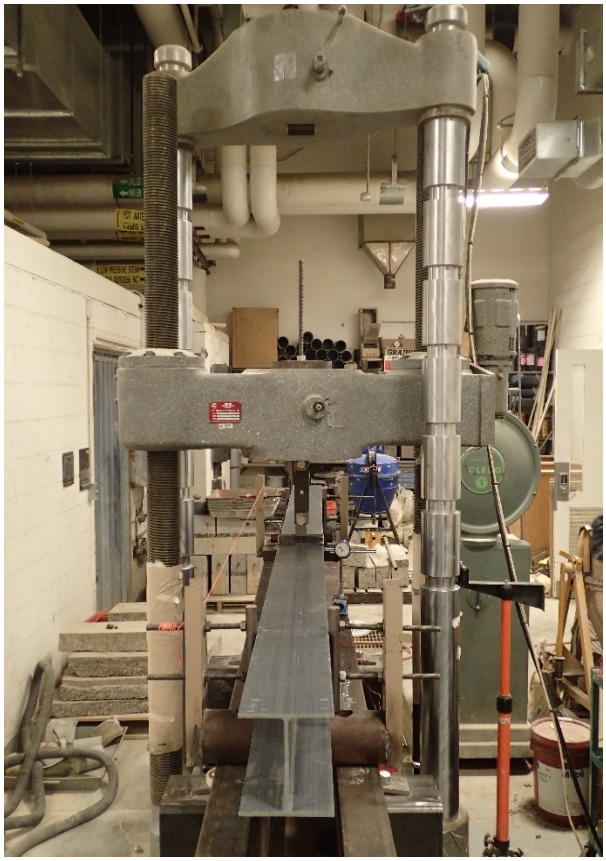	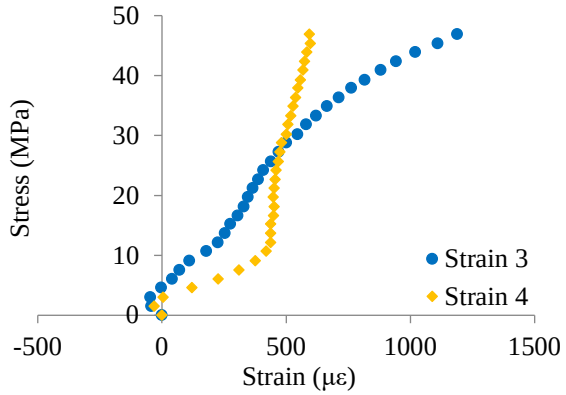 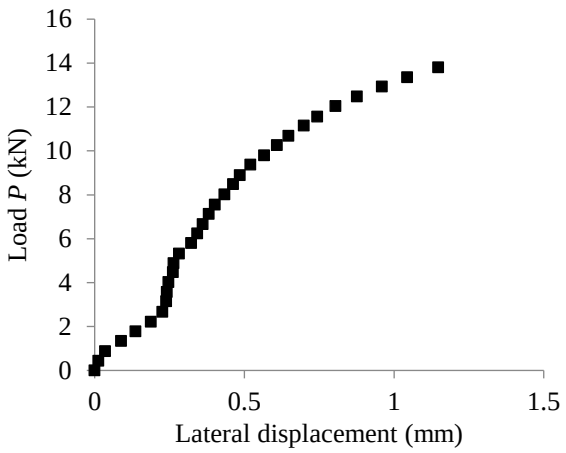	
M_{cr} = 4773 Nm		

Specimen: LTB6-2	Span: 2134 mm	Date:2/19/2016
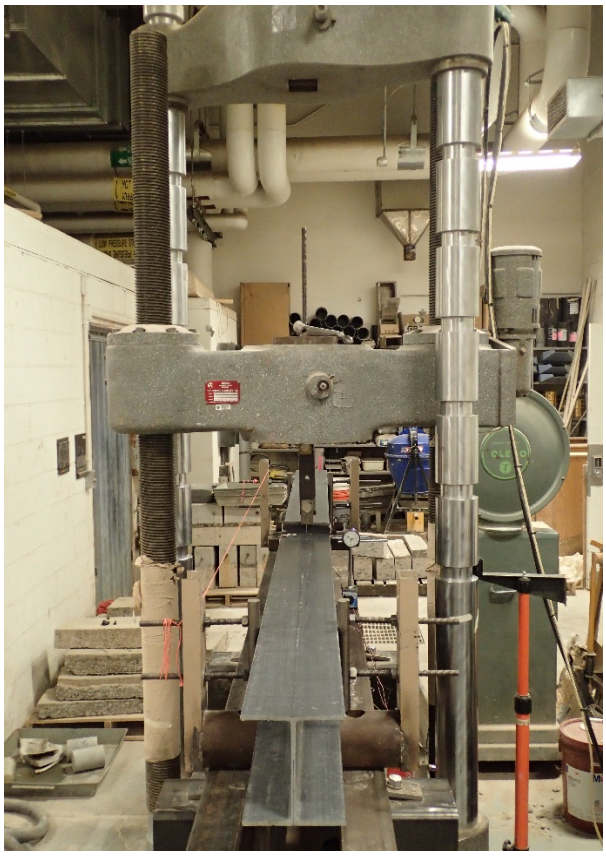	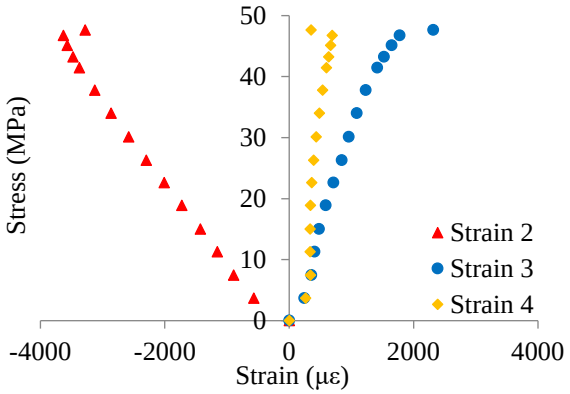 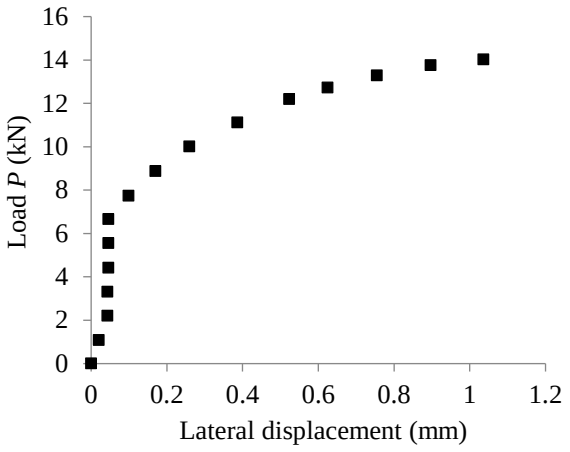	
M_{cr} = 3582 Nm		

Specimen: LTB6-2	Span: 1829 mm	Date:2/23/2016
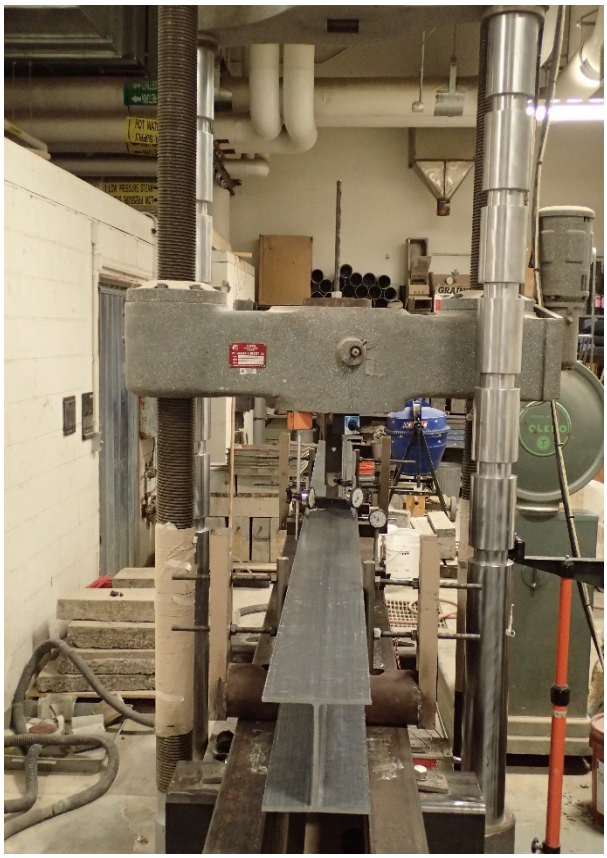	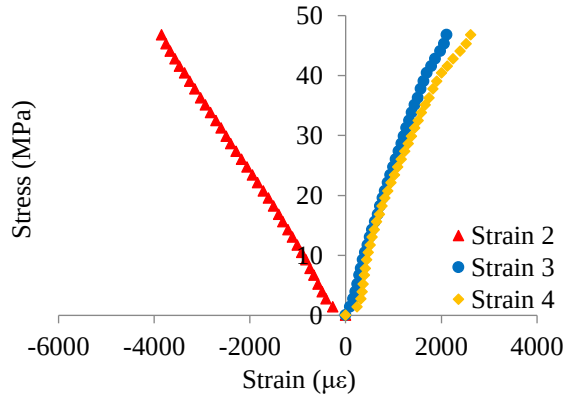 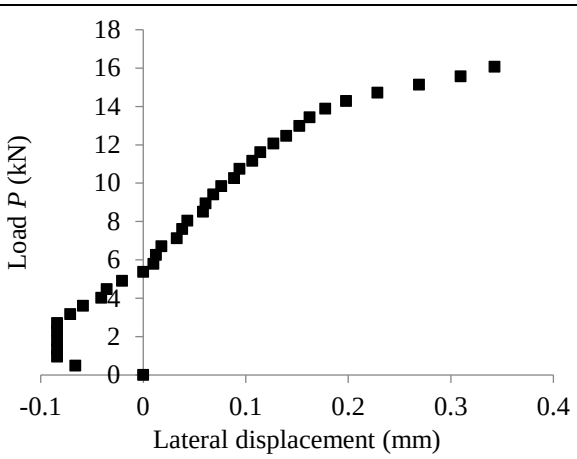	
M_{cr} = 6368 Nm		

Specimen: LTB6-2	Span: 1829 mm	Date:2/22/2016
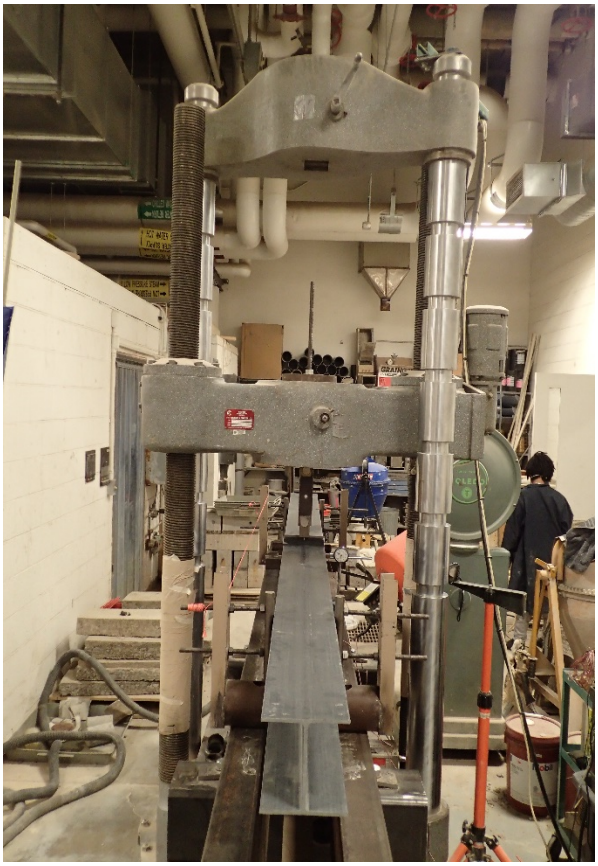	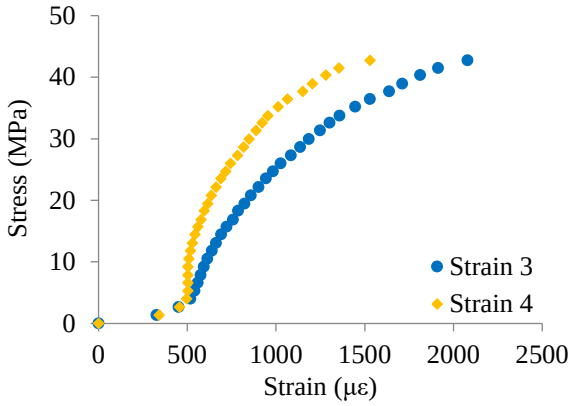 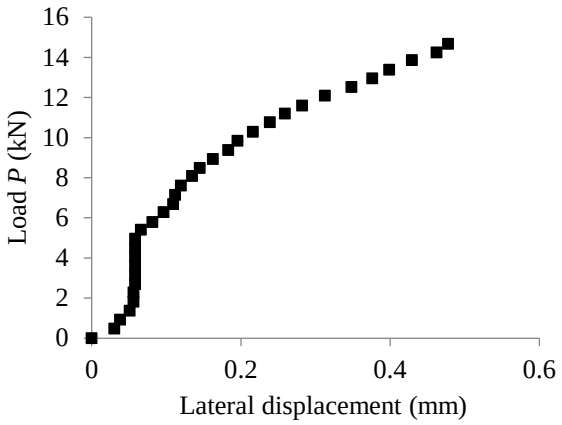	
M_{cr} = 6136 Nm		

Specimen: LTB6-2	Span: 1829 mm	Date:2/23/2016
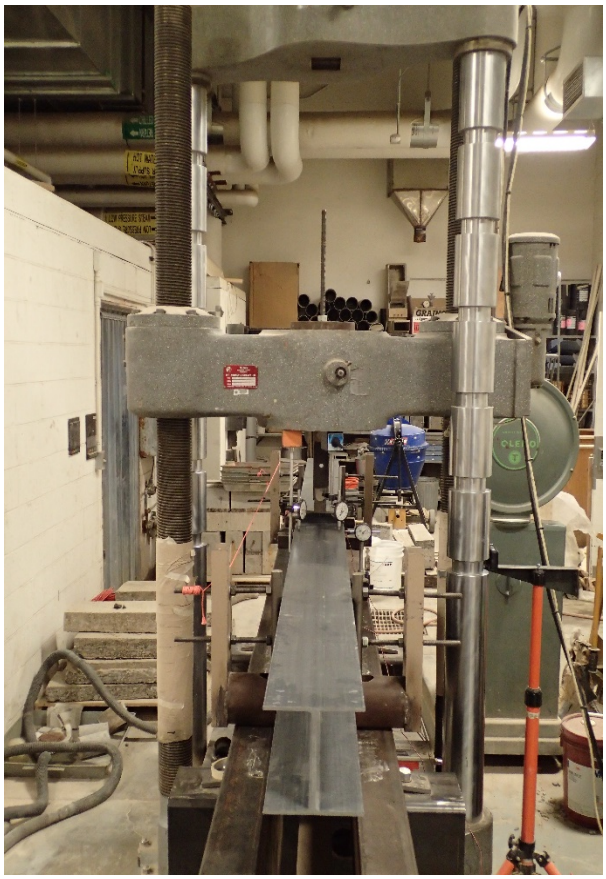	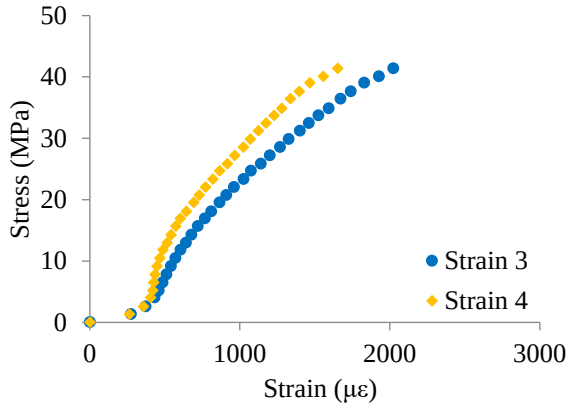 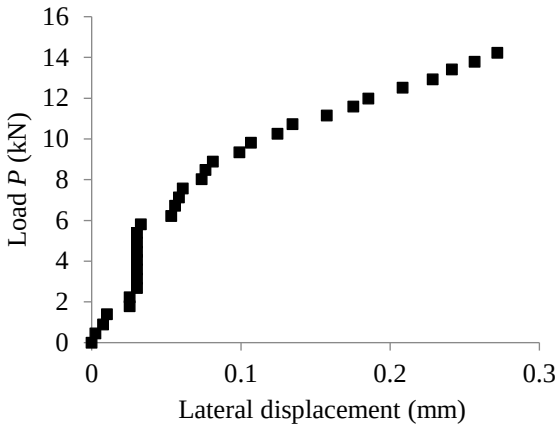	
M_{cr} = 6152 Nm		

Specimen: LTB6-1	Span: 1829 mm	Date:3/17/2016
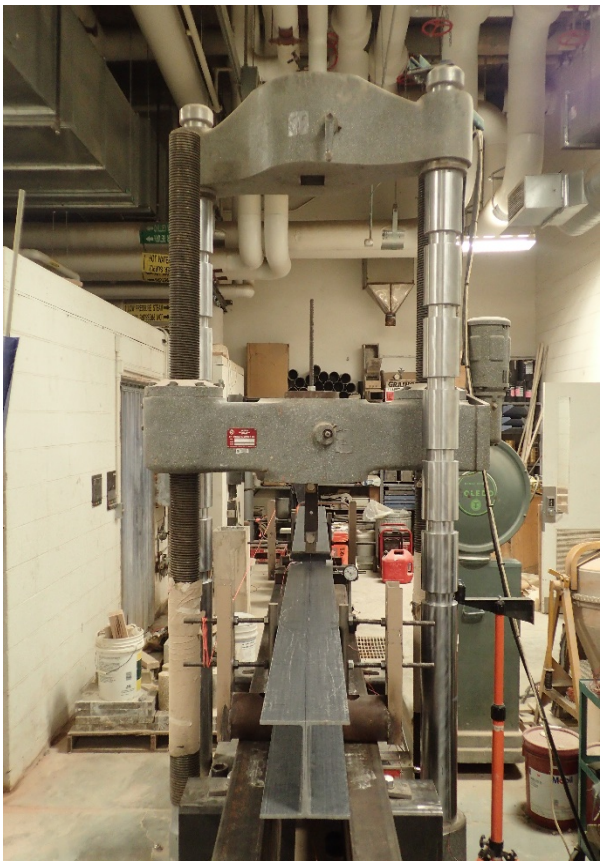	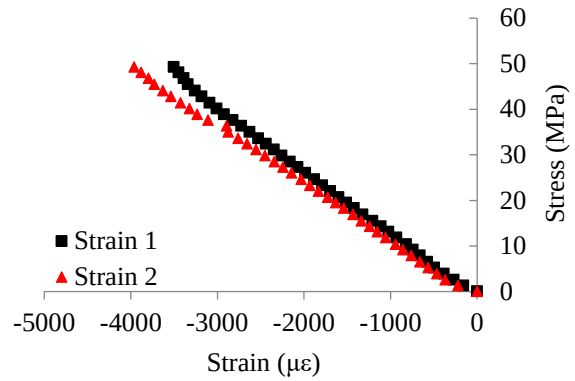	
	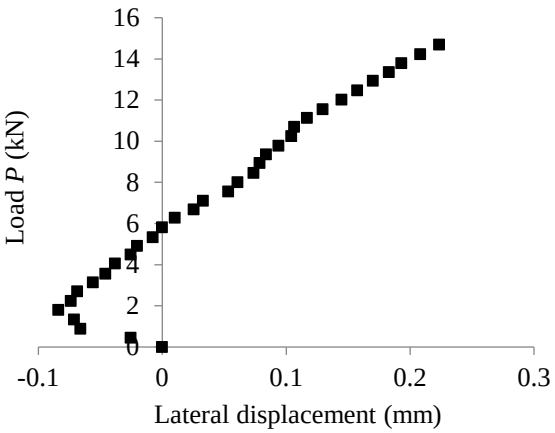	
M_{cr} = 6124 Nm		

Specimen: LTB6-2	Span: 1524 mm	Date:2/23/2016
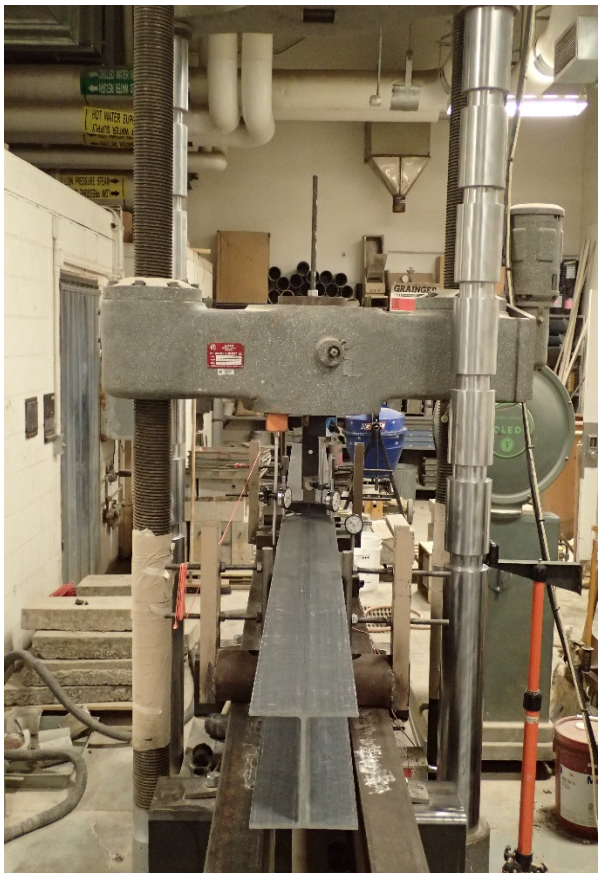	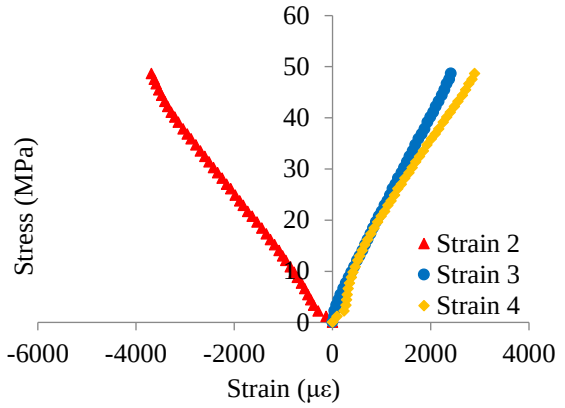	
	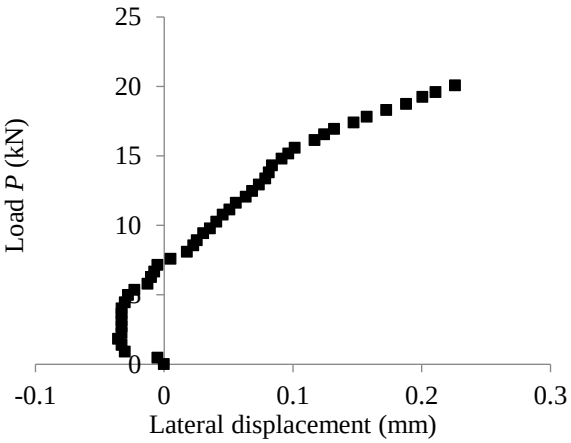	
M_{cr} = 6988 Nm		

Specimen: LTB6-2	Span: 1524 mm	Date:2/24/2016
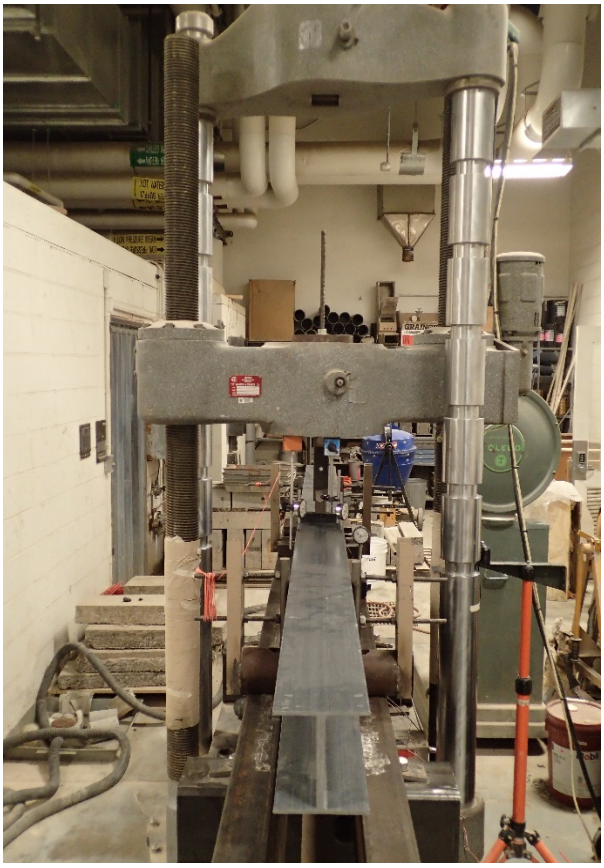	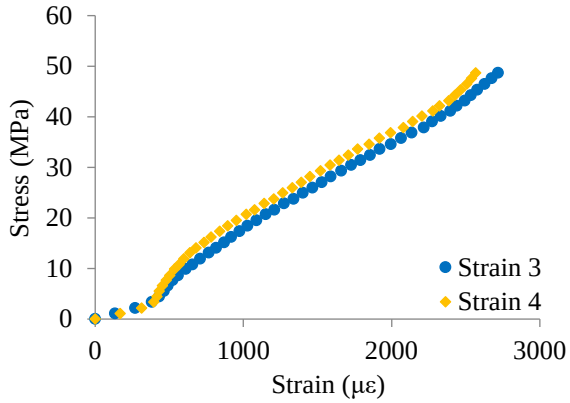	
	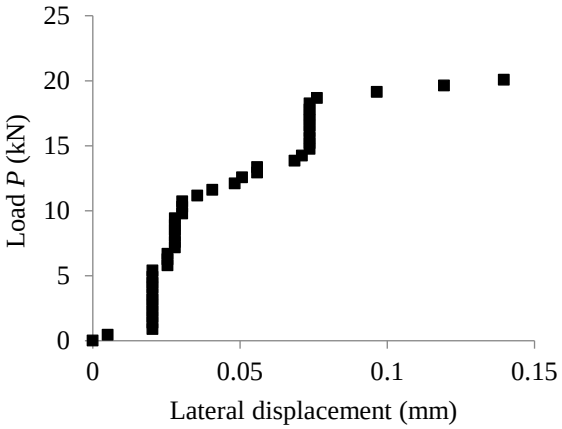	
M_{cr} = 7127 Nm		

Specimen: LTB5	Span: 2896 mm	Date:1/19/2016
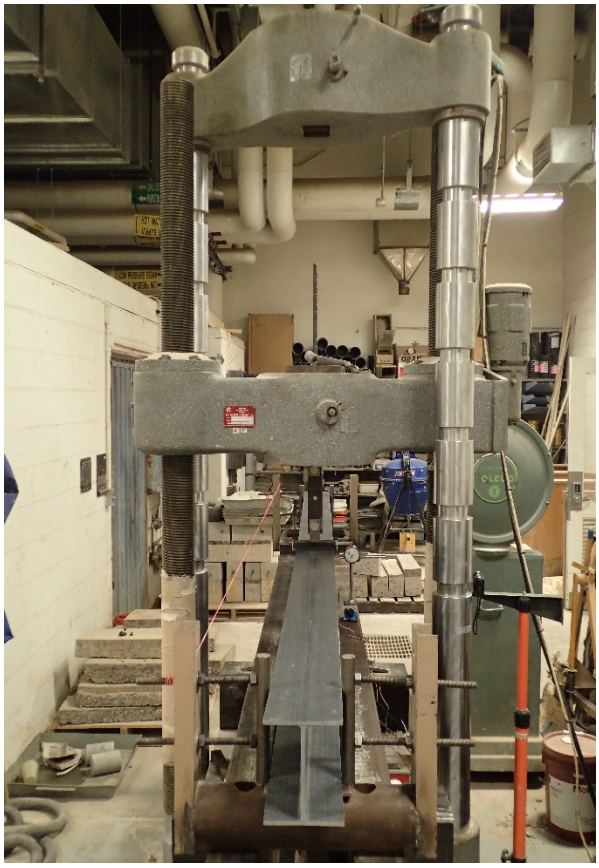	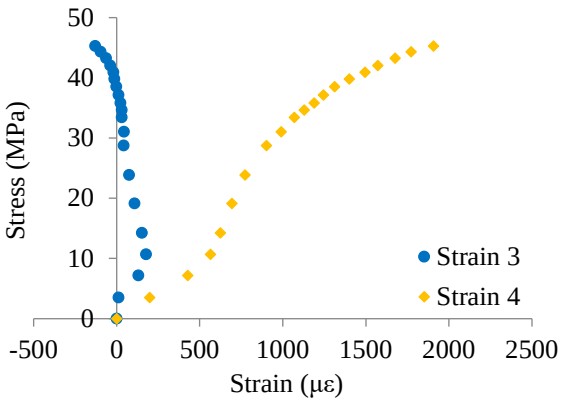	
	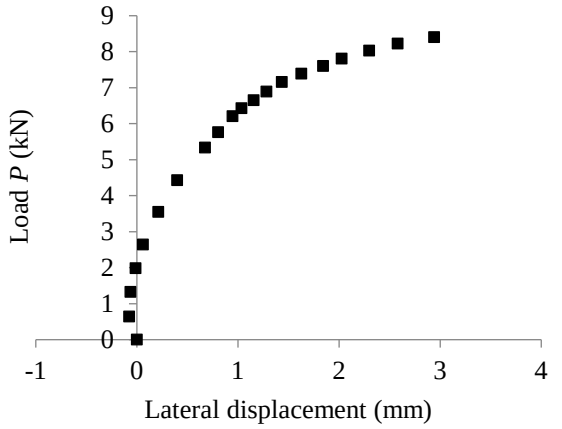	
M_{cr} = 3252 Nm		

Specimen: LTB5	Span: 2896 mm	Date:1/20/2016
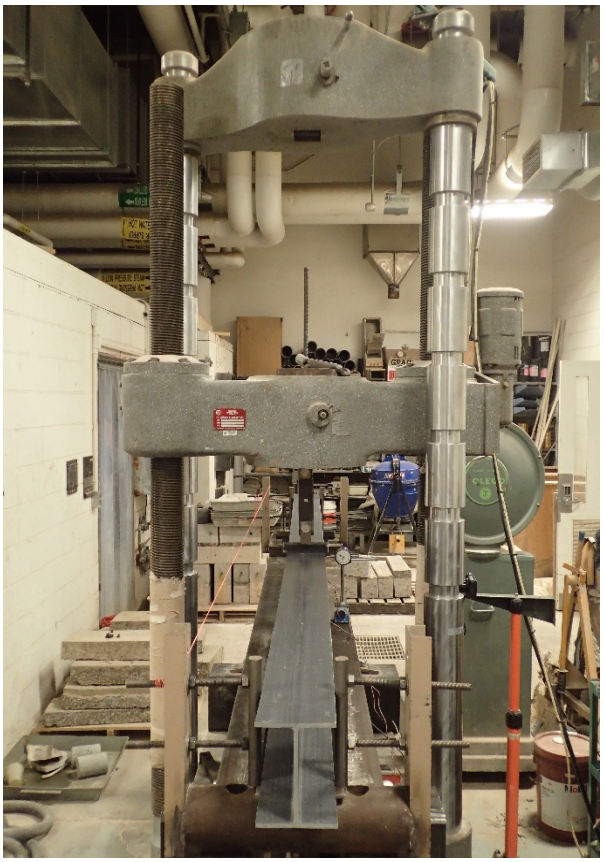	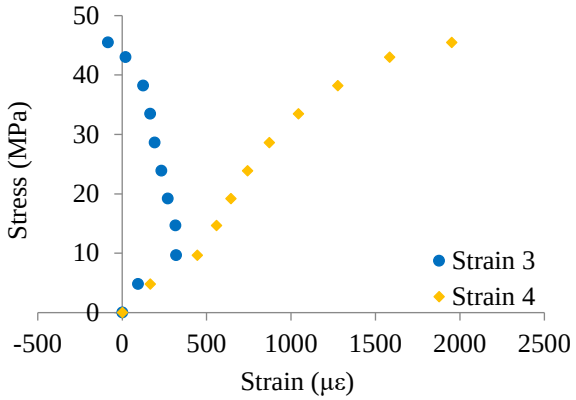 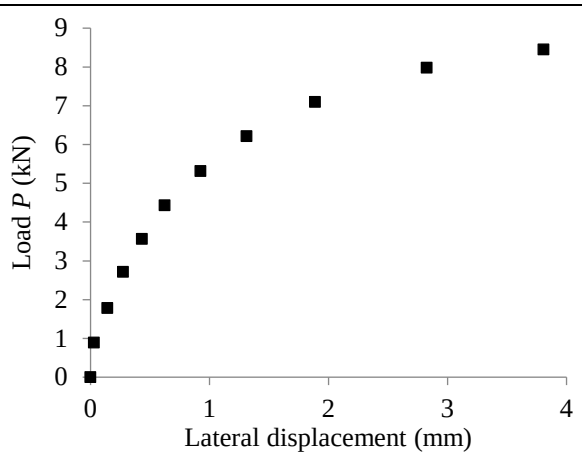	
M_{cr} = 3275 Nm		

Specimen: LTB5	Span: 2896 mm	Date:2/16/2016
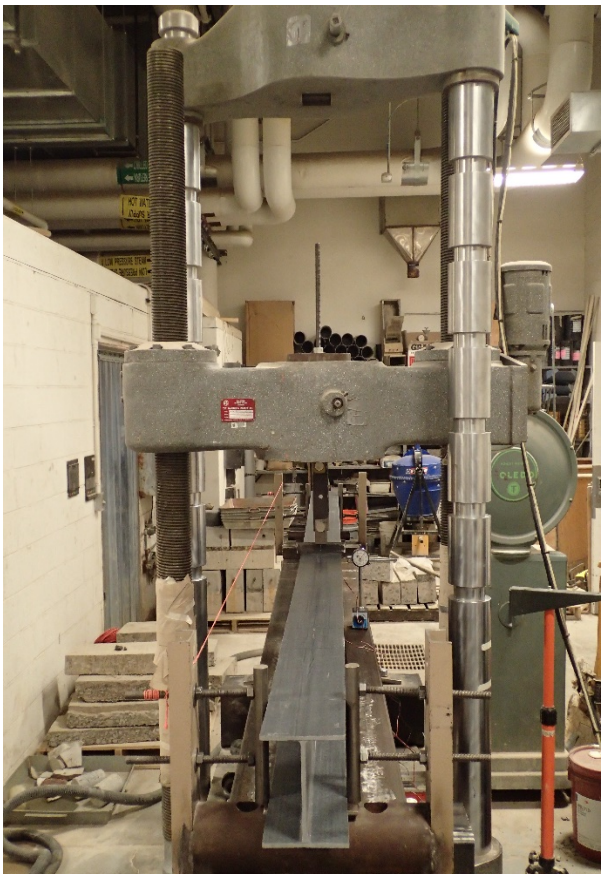	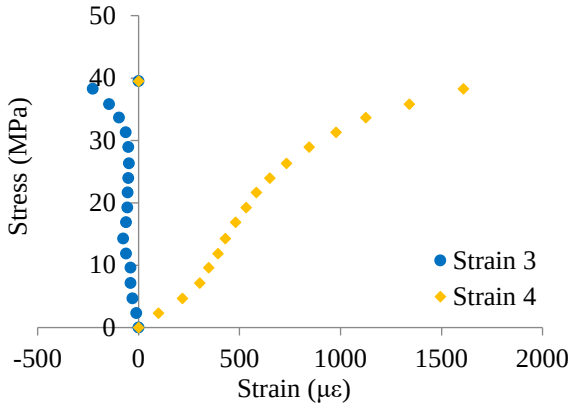 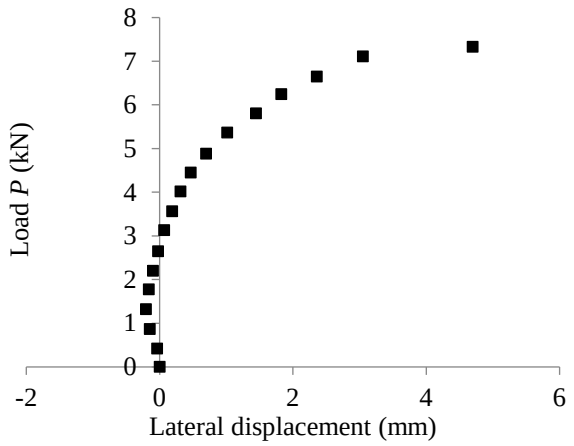	
M_{cr} = 3264 Nm		

Specimen: LTB5	Span: 2896 mm	Date:1/20/2016
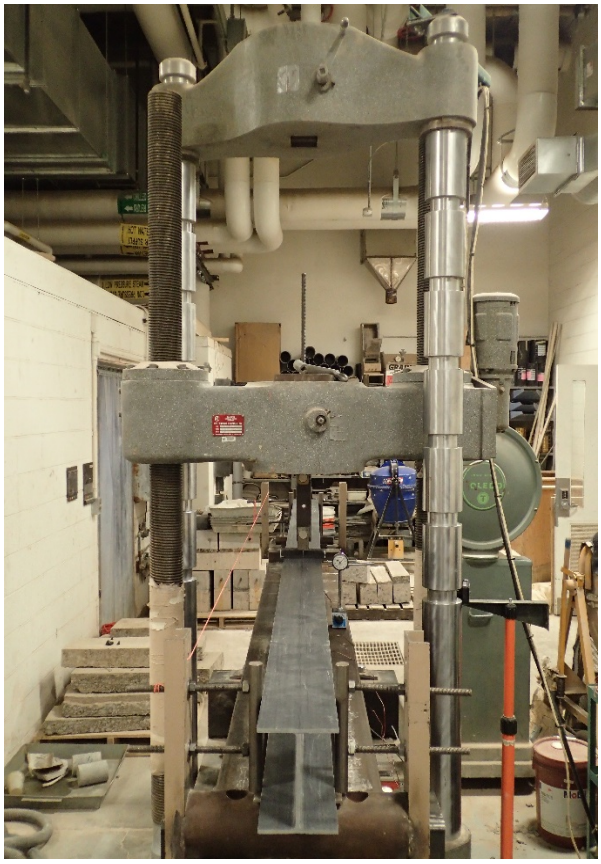	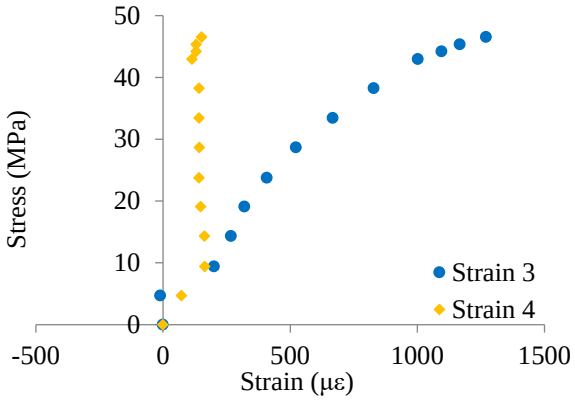 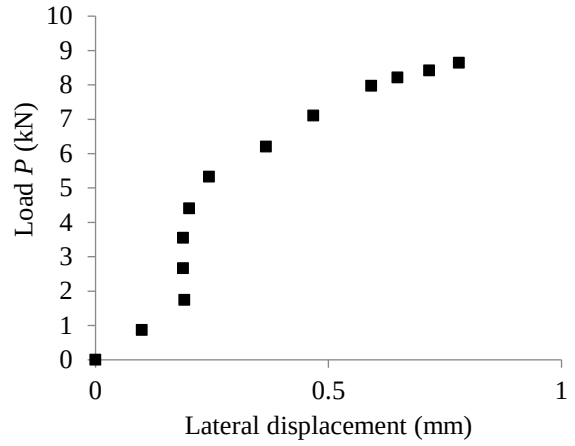	
M_{cr} = 3236 Nm		

Specimen: LTB5	Span: 2438 mm	Date:2/18/2016
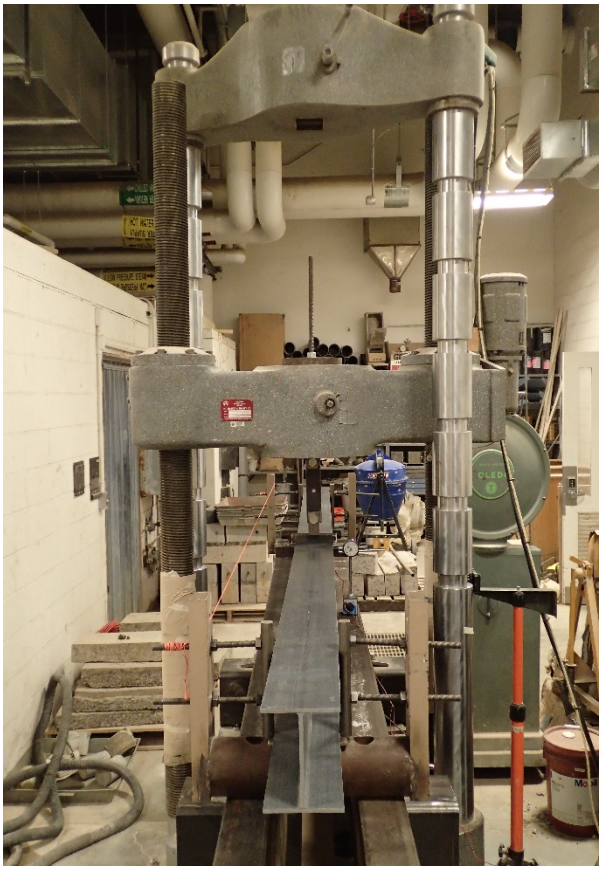	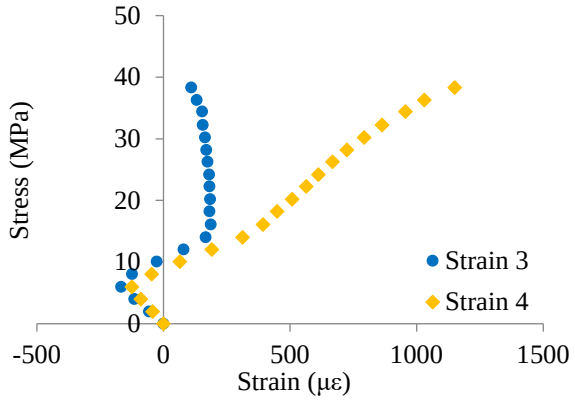 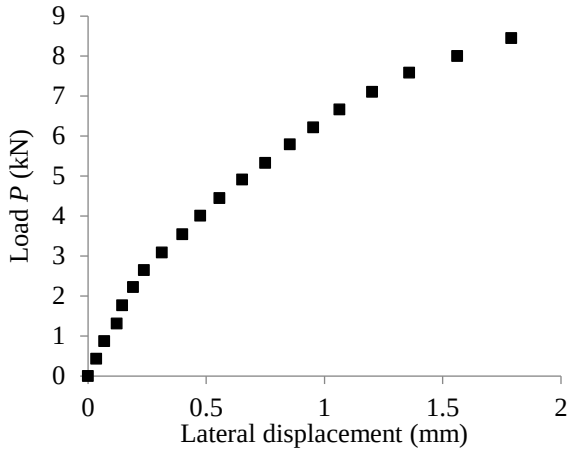	
M_{cr} = 4093 Nm		

Specimen: LTB5	Span: 2438 mm	Date:2/18/2016
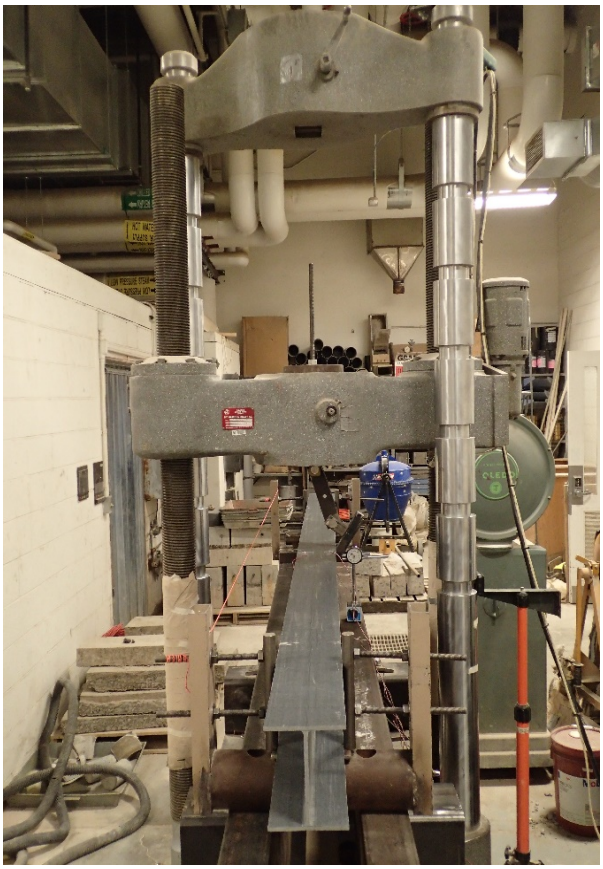	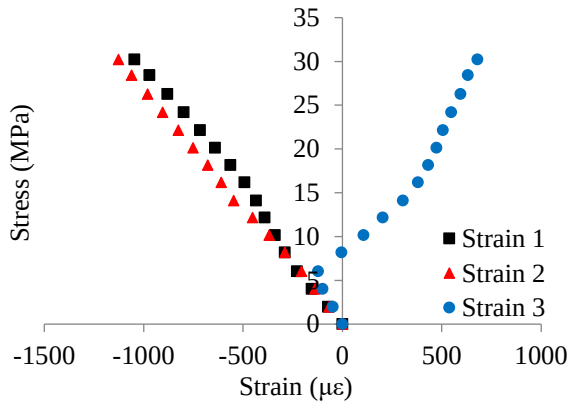 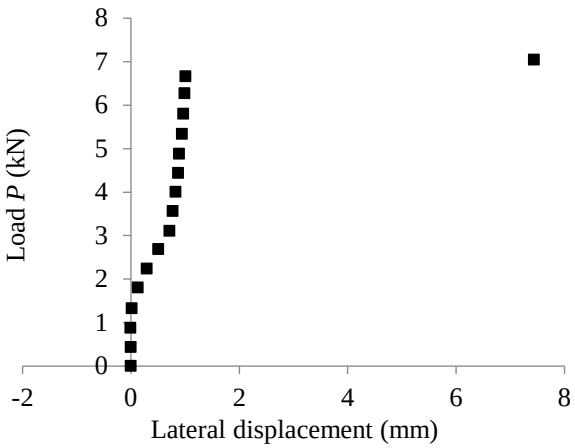	
M_{cr} = 4093 Nm		

Specimen: LTB5	Span: 2134 mm	Date:2/19/2016
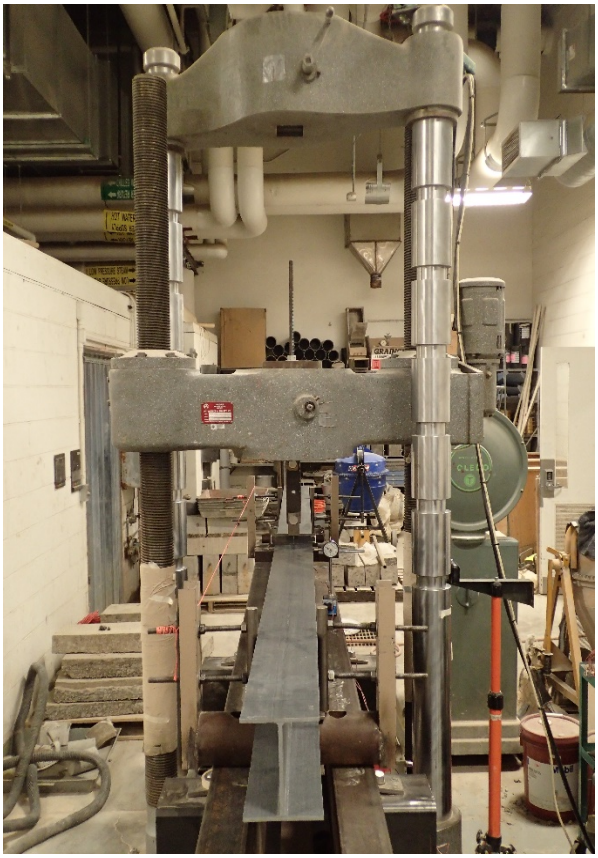	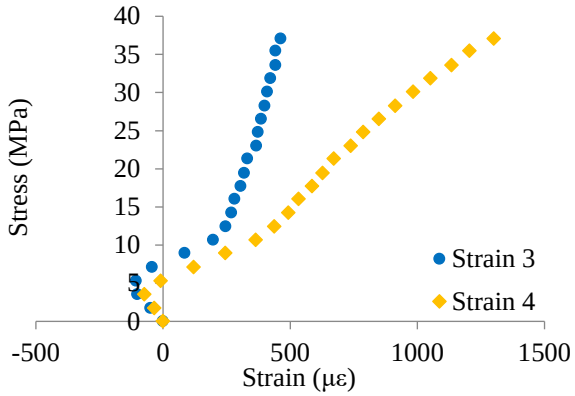 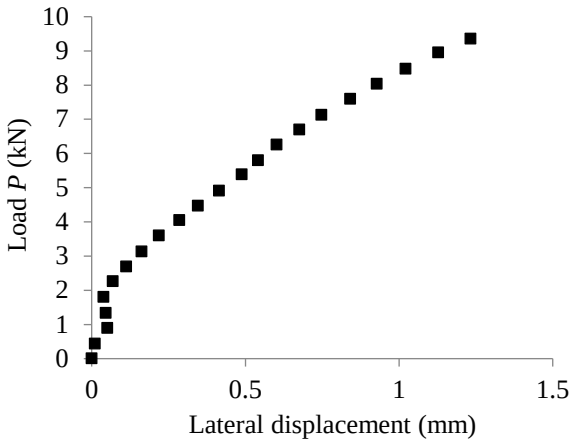	
M_{cr} = 3825 Nm		

Specimen: LTB5	Span: 2134 mm	Date:2/19/2016
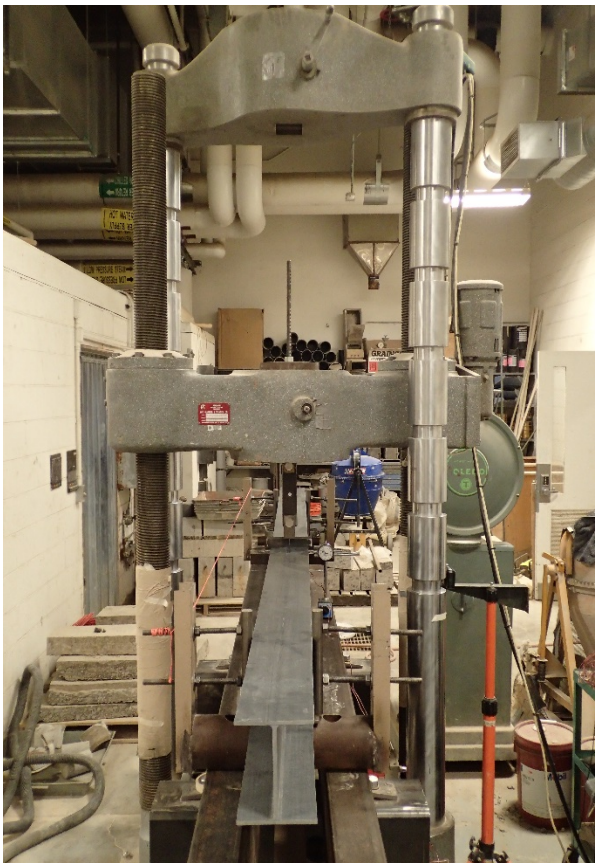	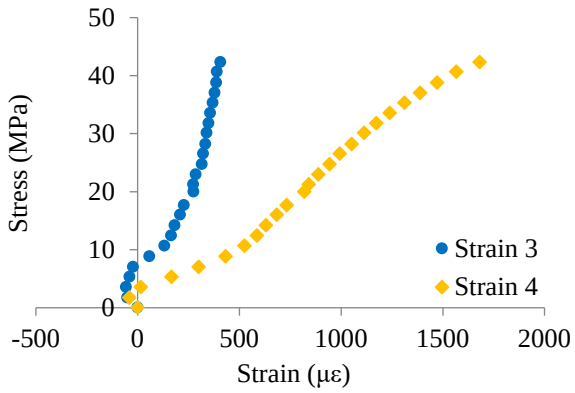 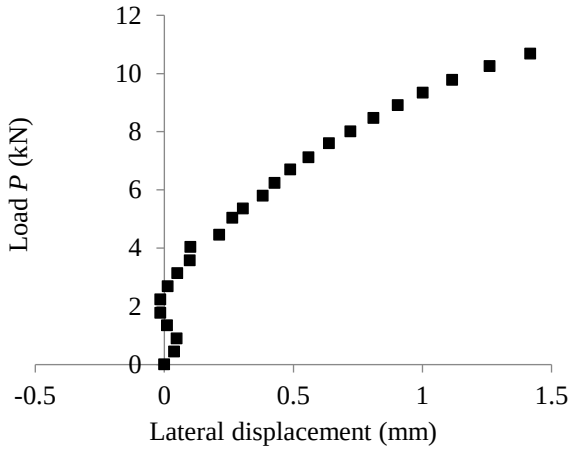	
M_{cr} = 3821 Nm		

Specimen: LTB5	Span: 2134 mm	Date:2/19/2016
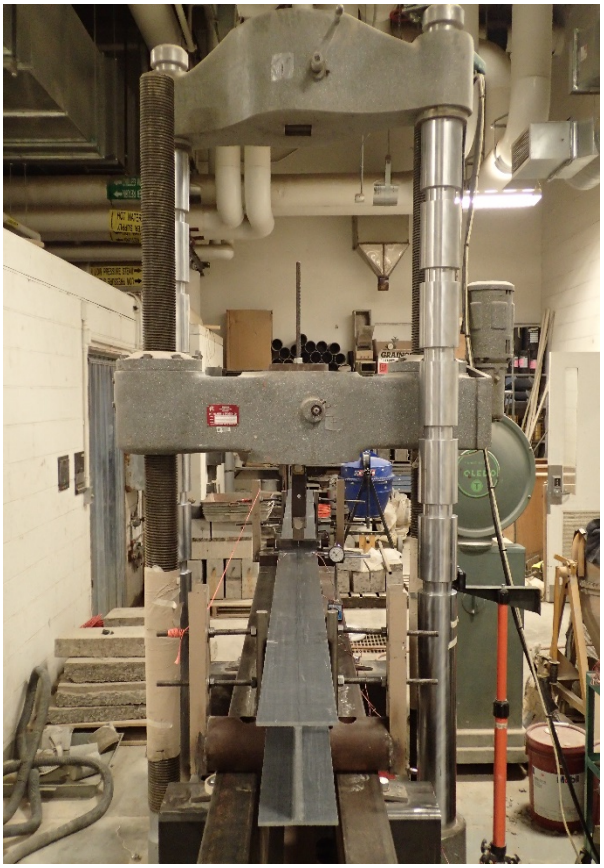	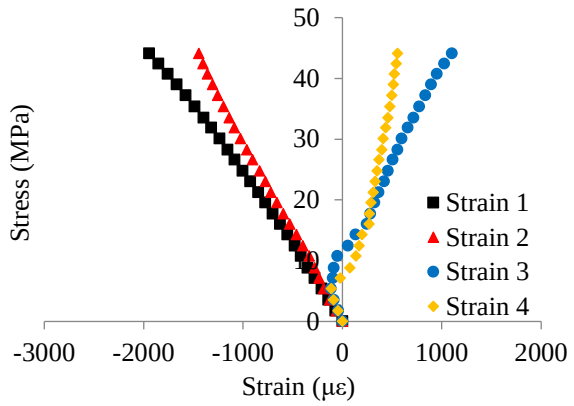	
	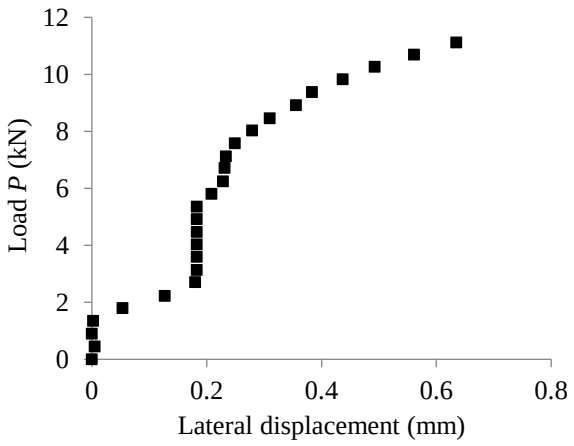	
M_{cr} = 3821 Nm		

Specimen: LTB5	Span: 1829 mm	Date:2/22/2016
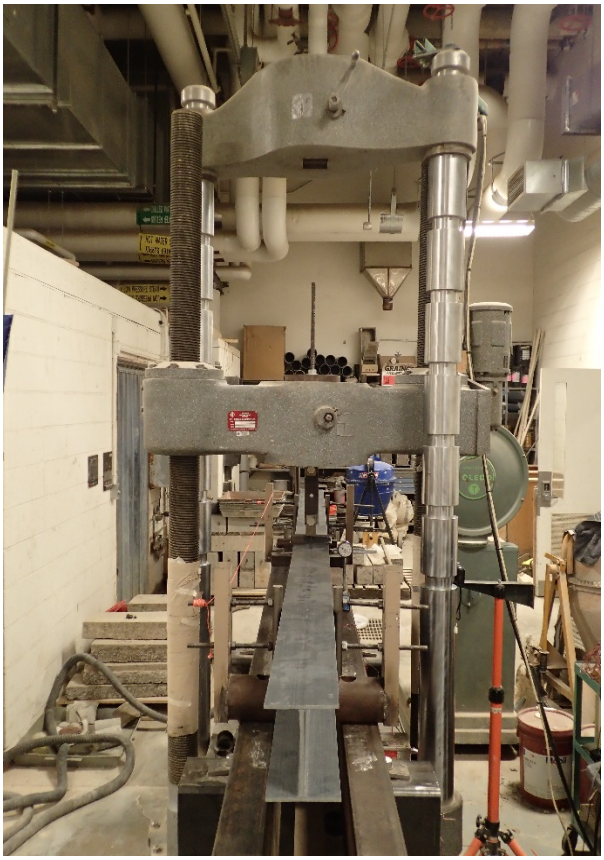	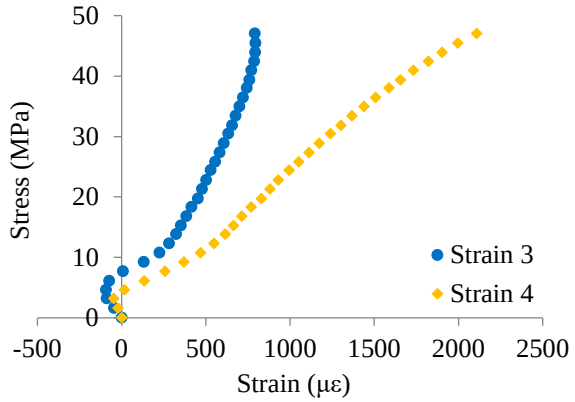 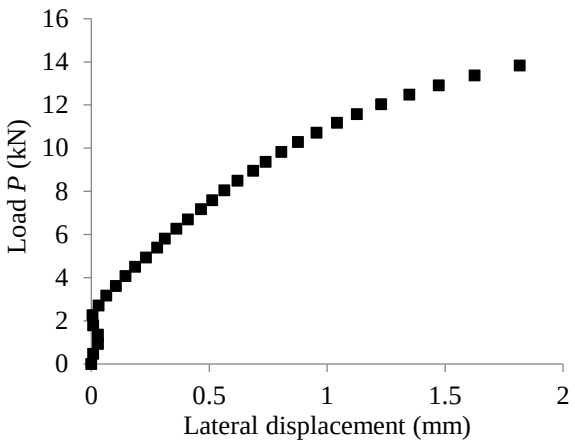	
M_{cr} = 5313 Nm		

Specimen: LTB5	Span: 1829 mm	Date:2/22/2016
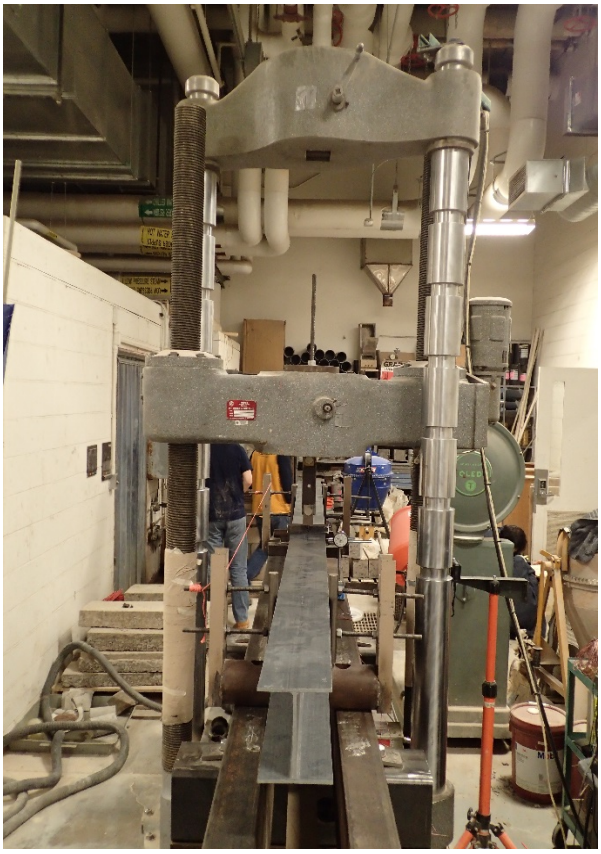	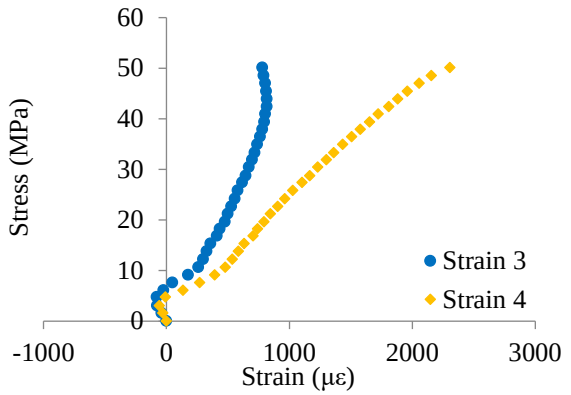 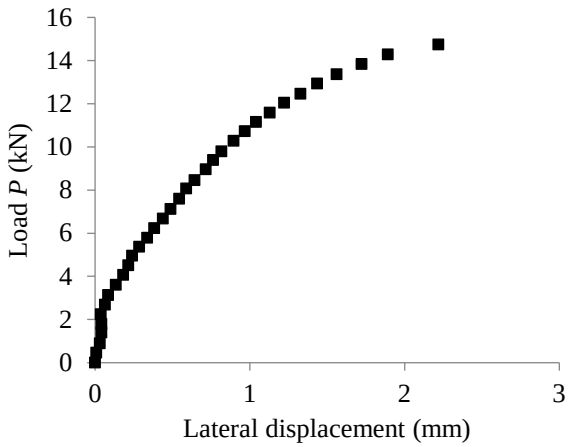	
M_{cr} = 5312 Nm		

Specimen: LTB5	Span: 1829 mm	Date:2/22/2016
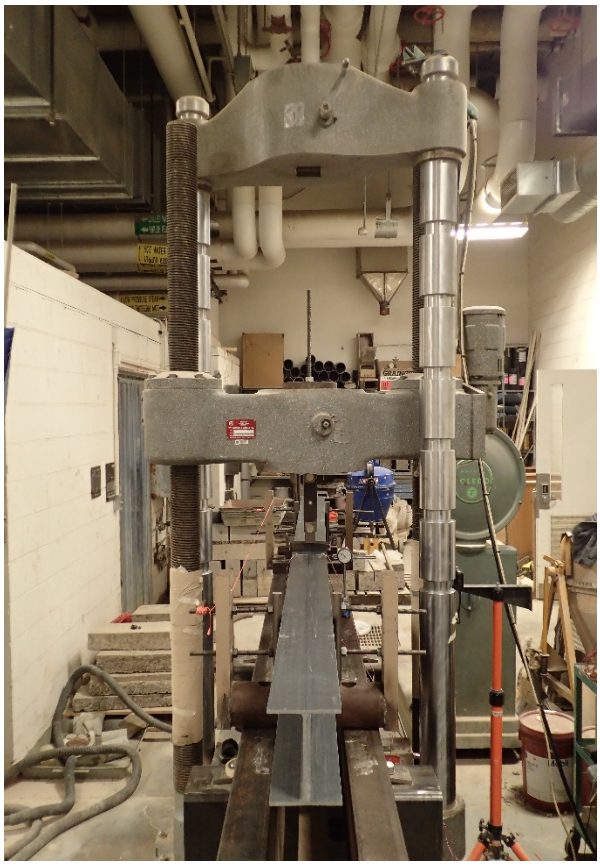	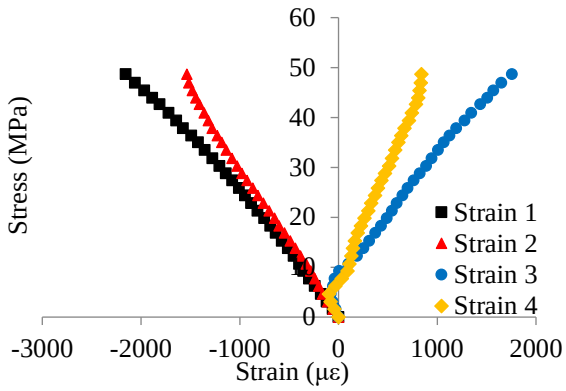 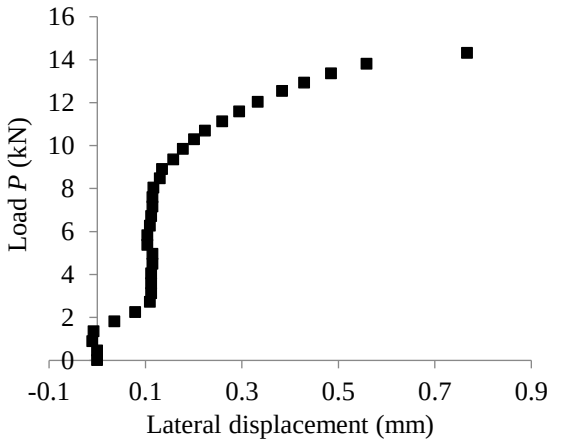	
M_{cr} = 5518 Nm		

Specimen: LTB5	Span: 1829 mm	Date:3/17/2016
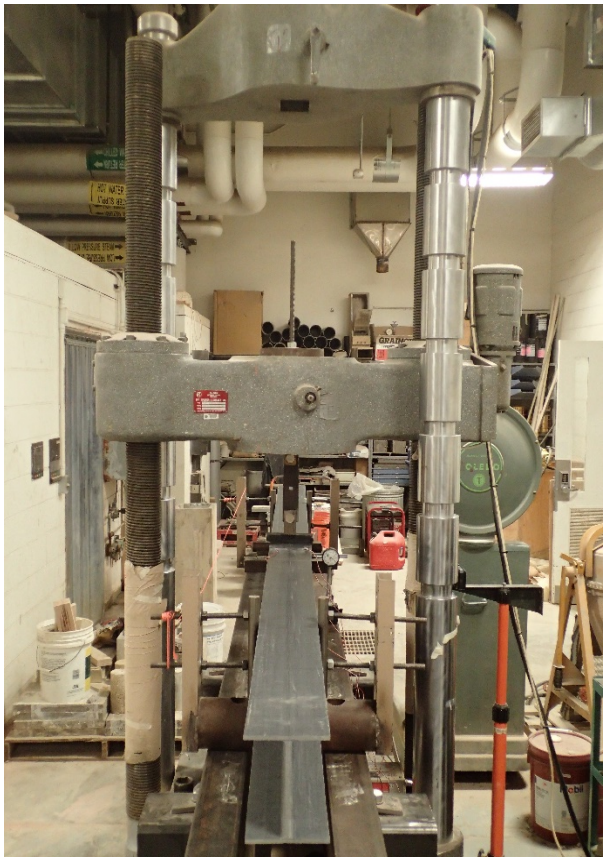	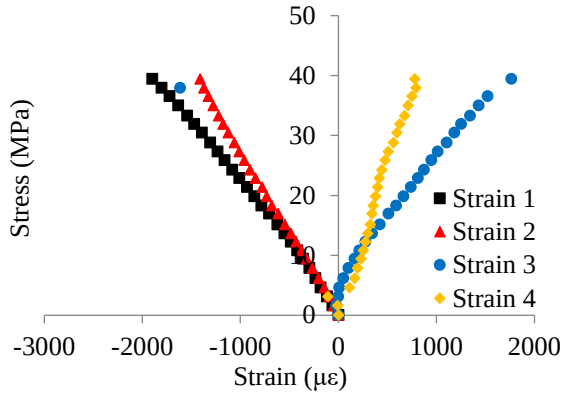 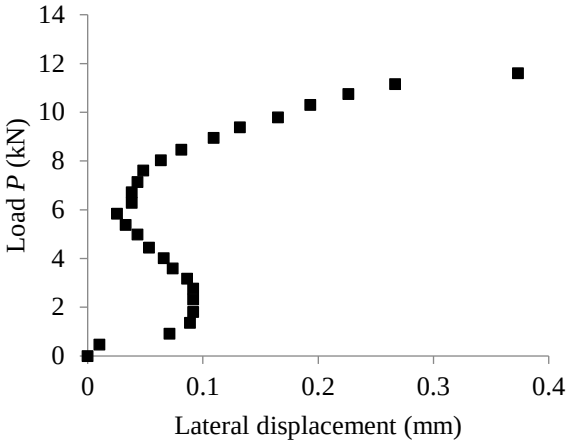	
M_{cr} = 5115 Nm		

Specimen: LTB5	Span: 1524 mm	Date:2/24/2016
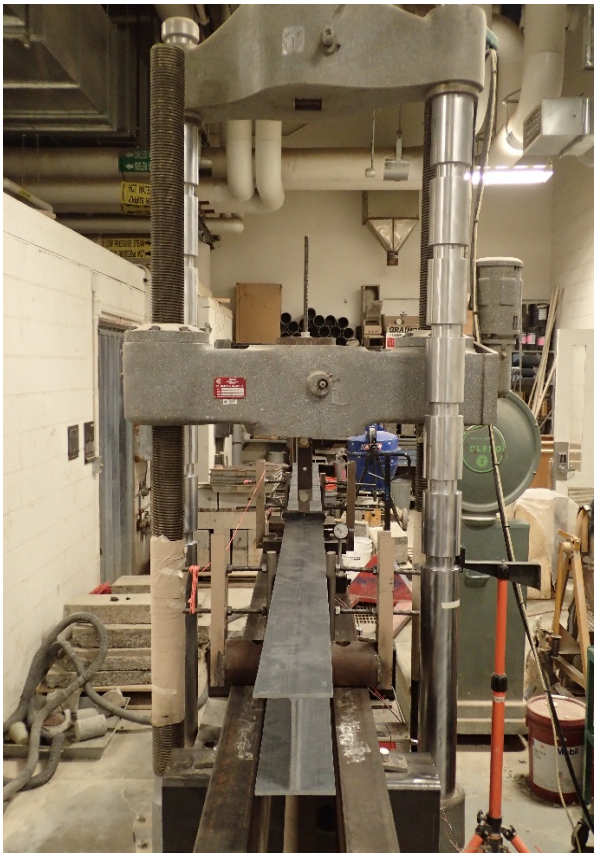	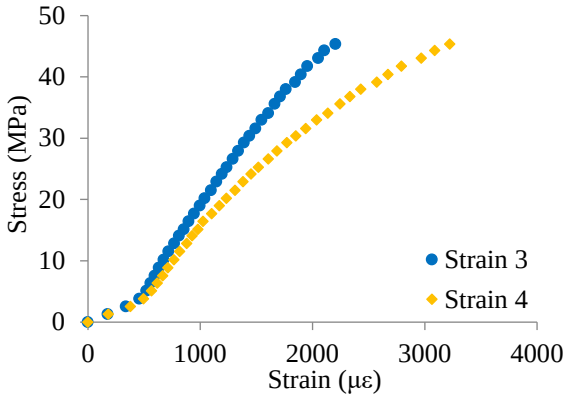	
	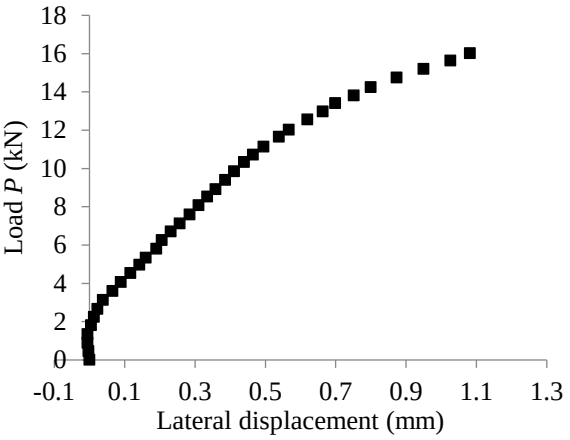	
M_{cr} = 5118 Nm		

Specimen: LTB5	Span: 1524 mm	Date:2/24/2016
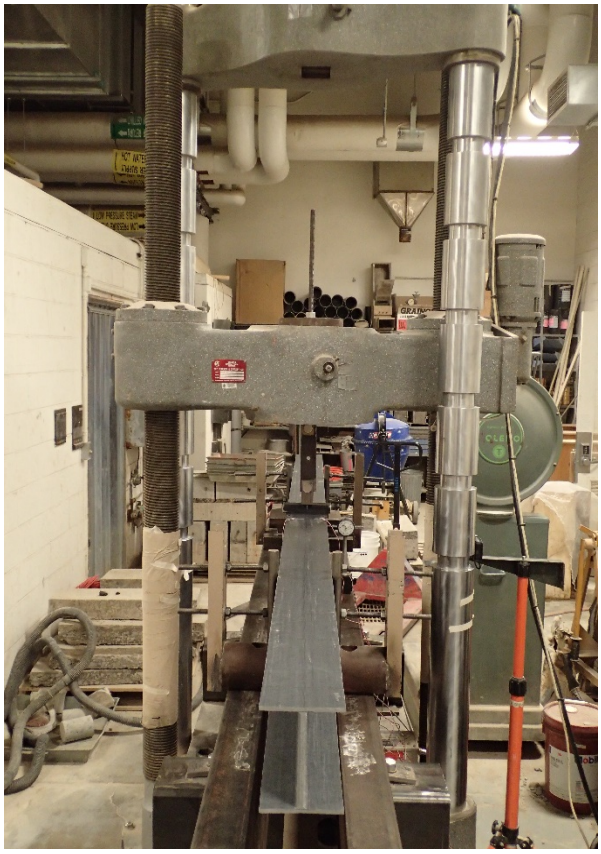	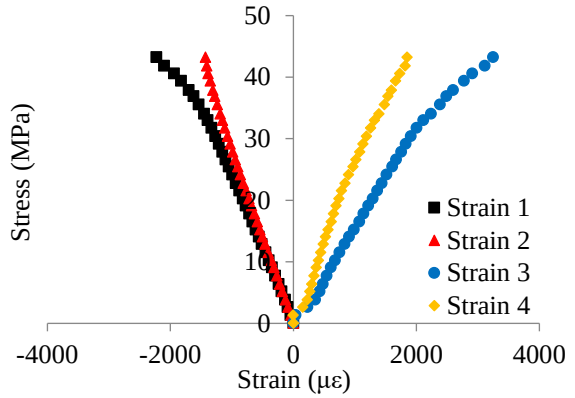 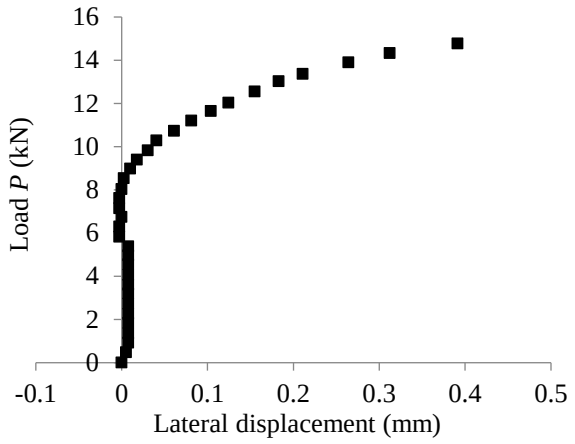	
M_{cr} = 5106 Nm		

Specimen: LTB4	Span: 2896 mm	Date:3/7/2016
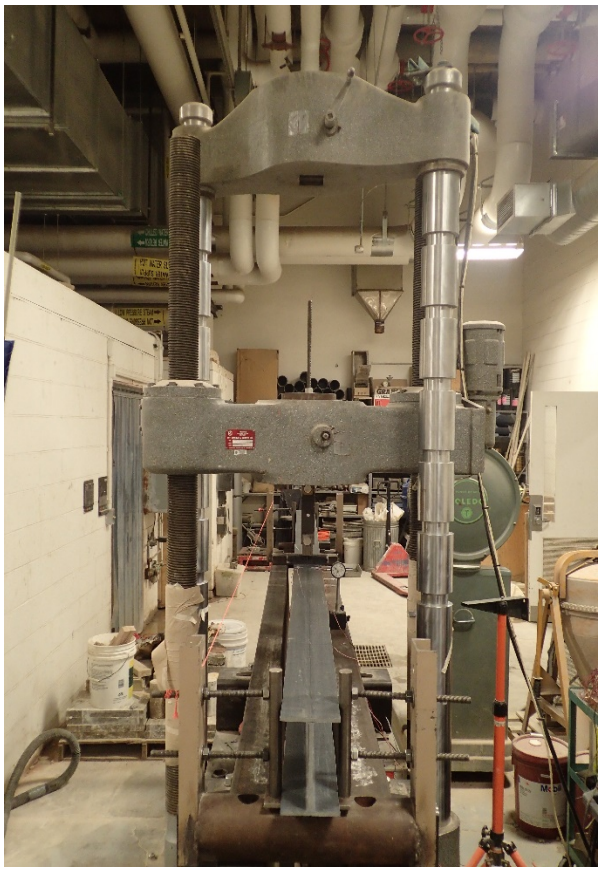	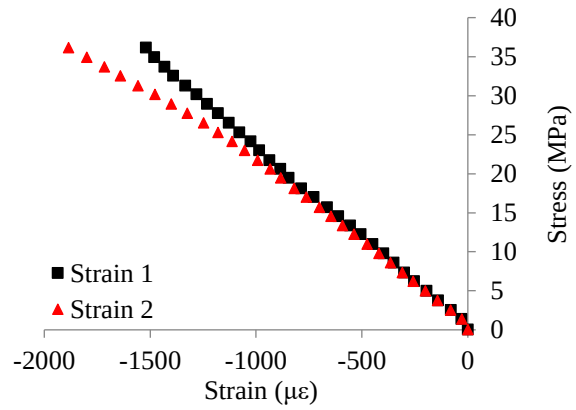	
	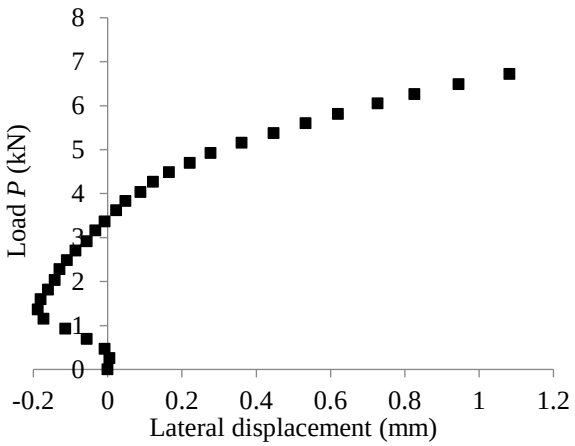	
M_{cr} = 3598 Nm		

Specimen: LTB4	Span: 2896 mm	Date:3/7/2016
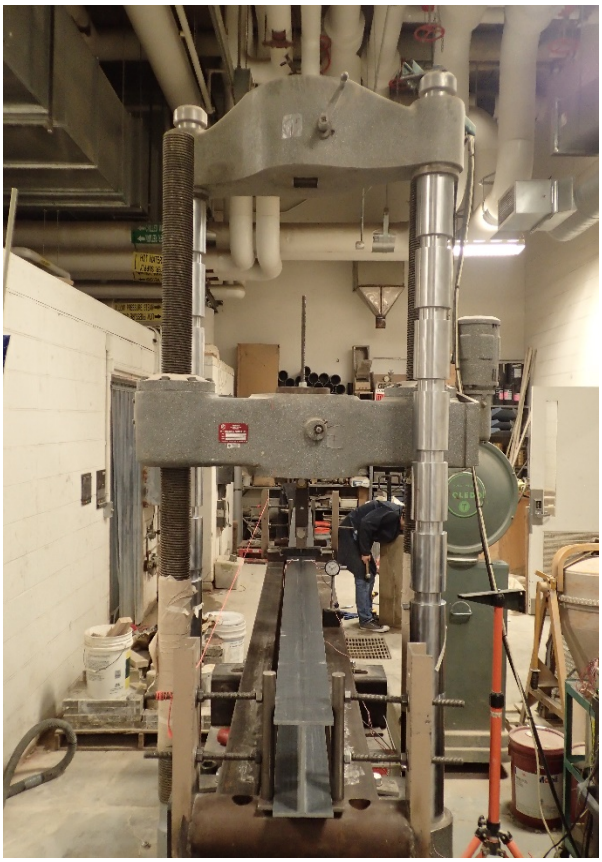	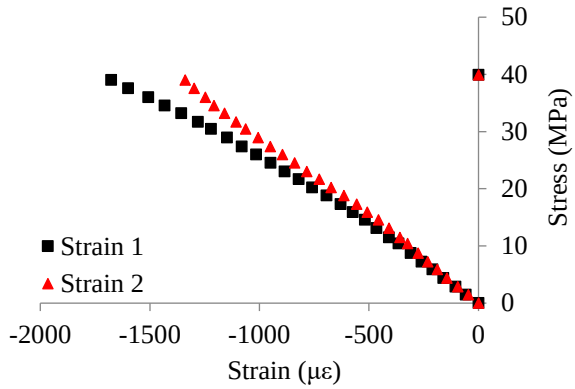	
	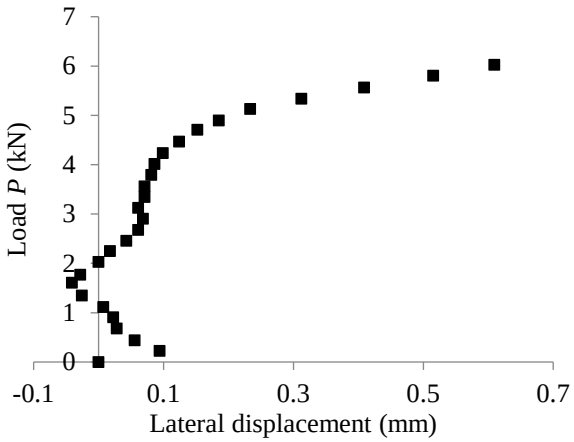	
M_{cr} = 3581 Nm		

Specimen: LTB4	Span: 2438 mm	Date:3/8/2016
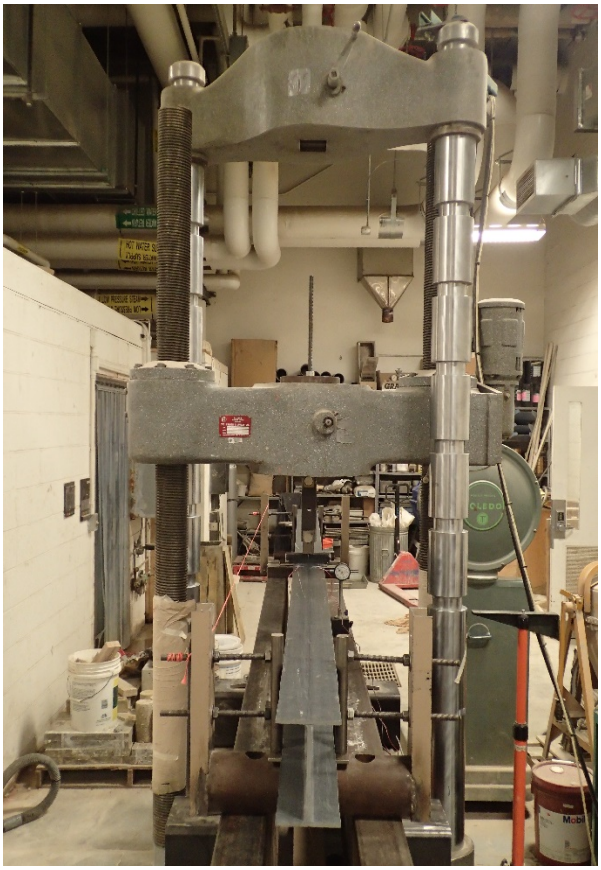	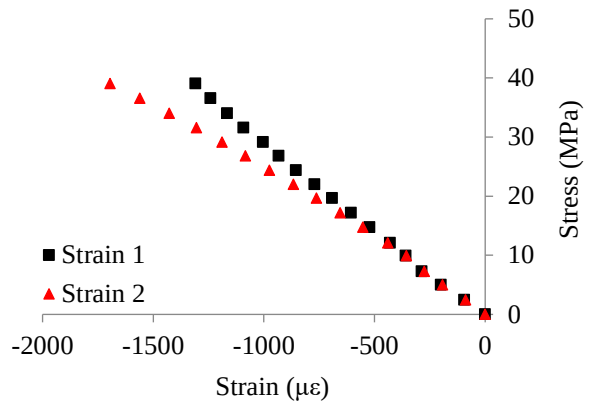	
	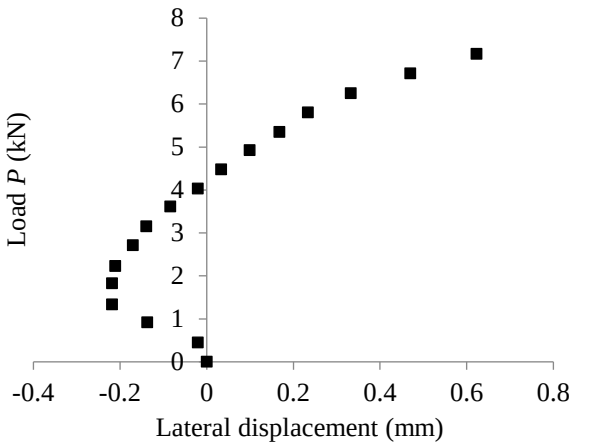	
M_{cr} = 3560 Nm		

Specimen: LTB4	Span: 2438 mm	Date:3/8/2016
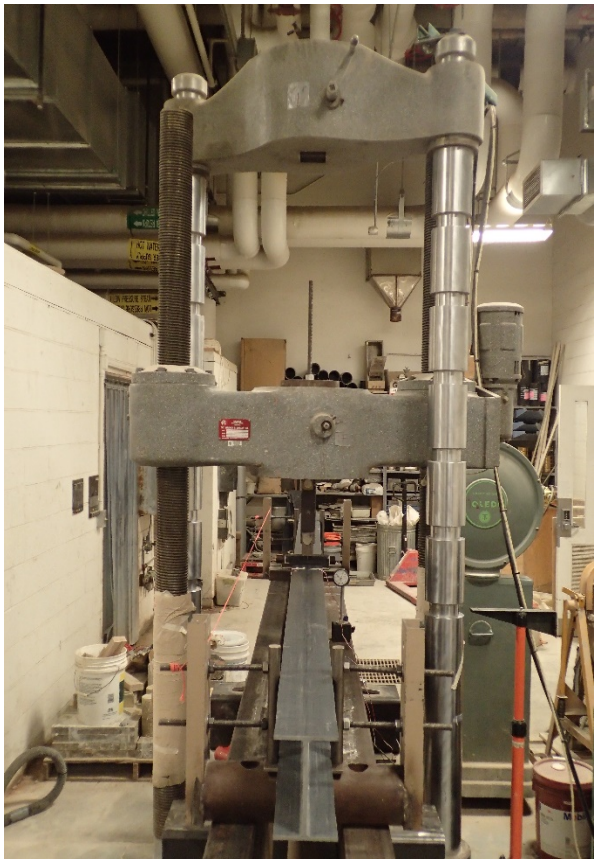	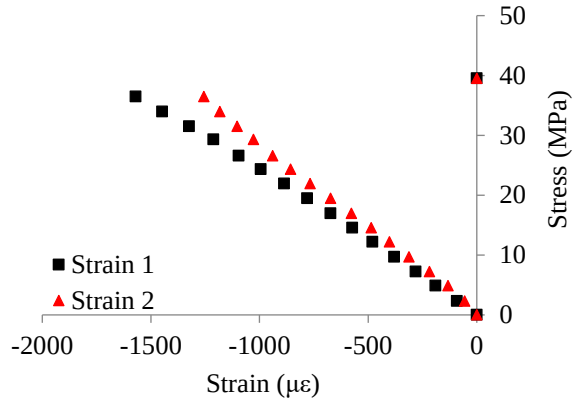 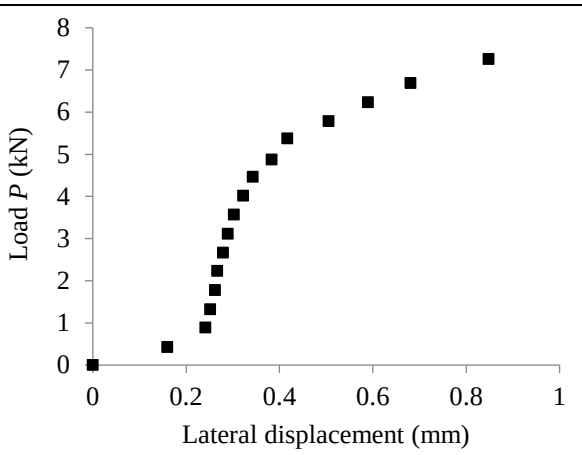	
M_{cr} = 3302 Nm		

Specimen: LTB4	Span: 2134 mm	Date:3/8/2016
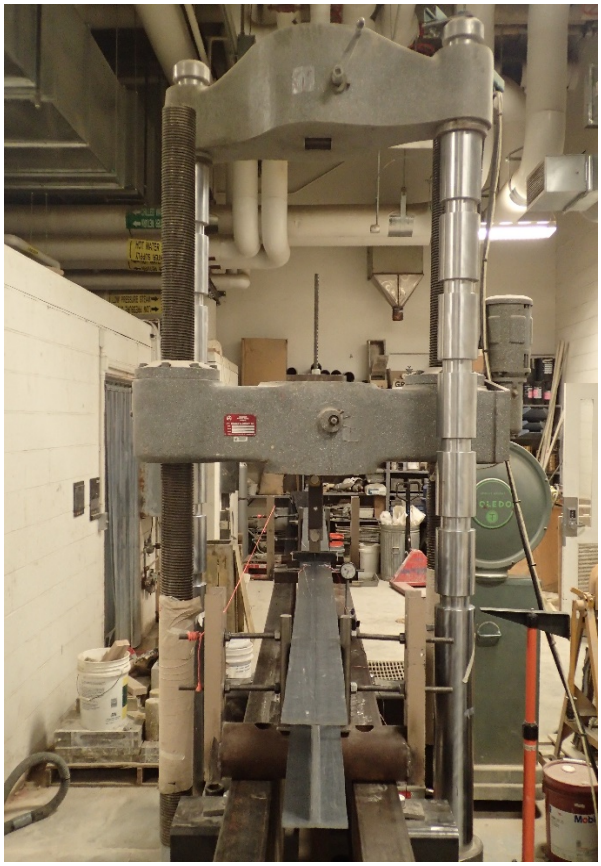	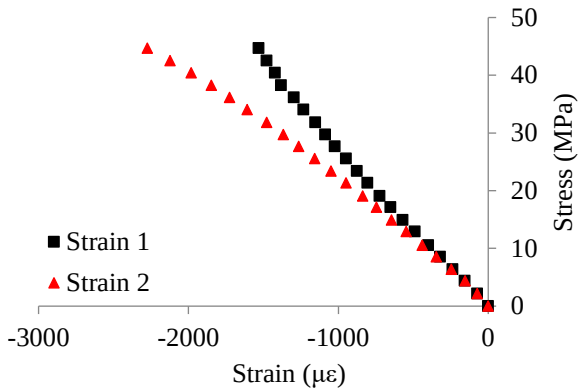	
	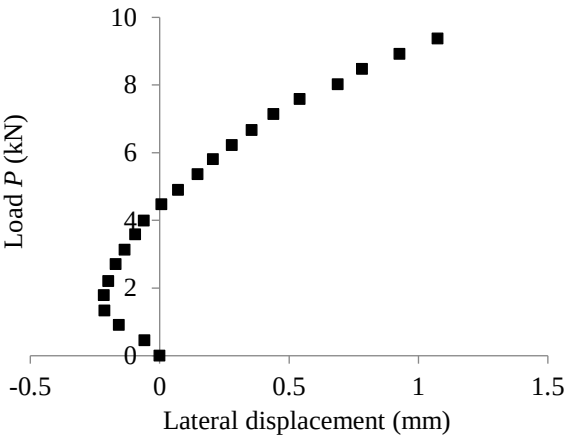	
M_{cr} = 4065 Nm		

Specimen: LTB4	Span: 2134 mm	Date:3/8/2016
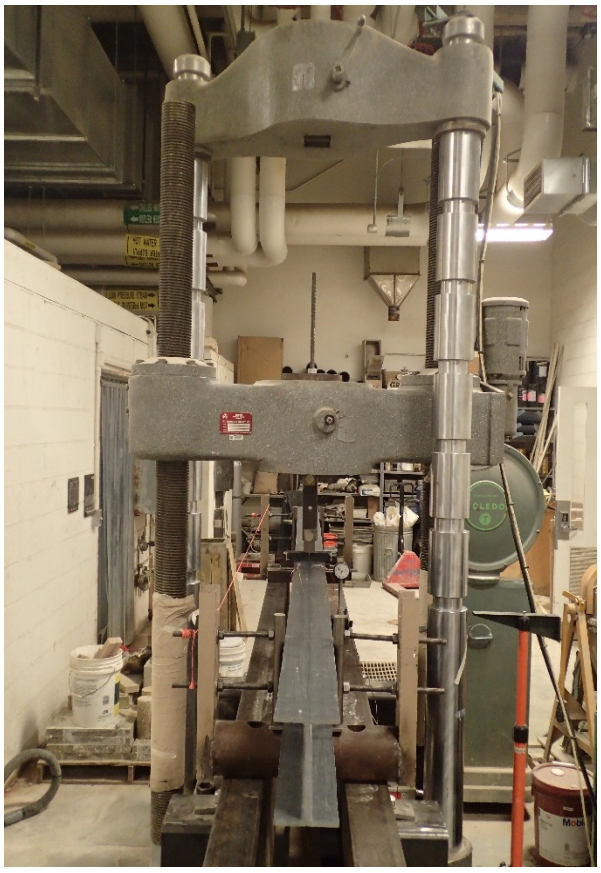	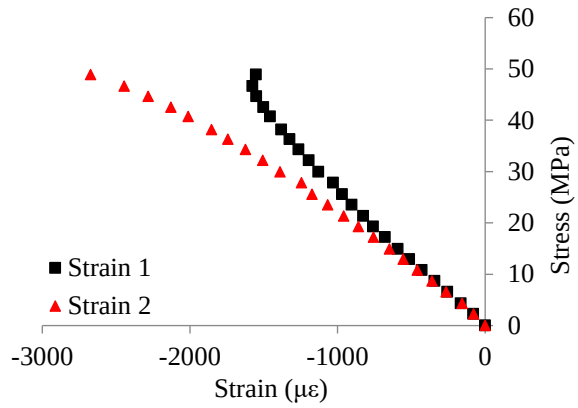	
	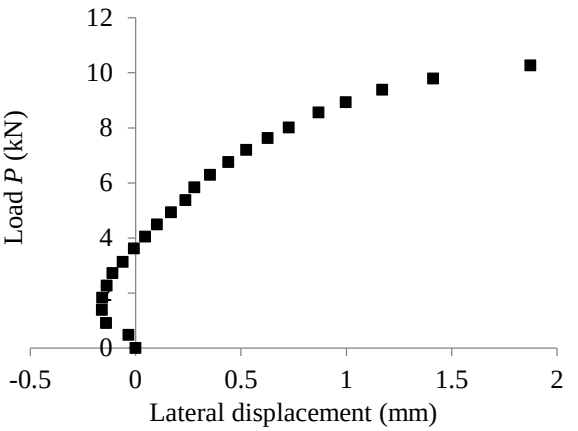	
M_{cr} = 4292 Nm		

Specimen: LTB4	Span: 2134 mm	Date:3/8/2016
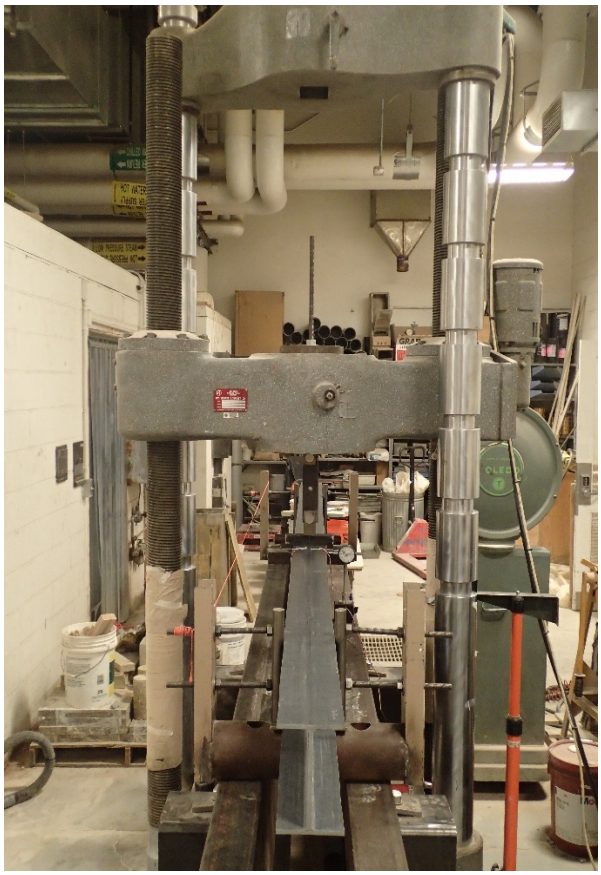	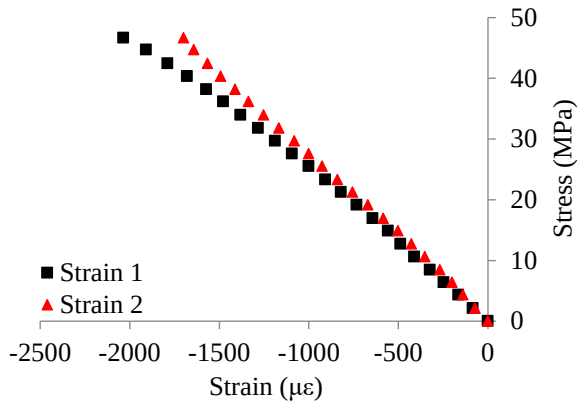	
	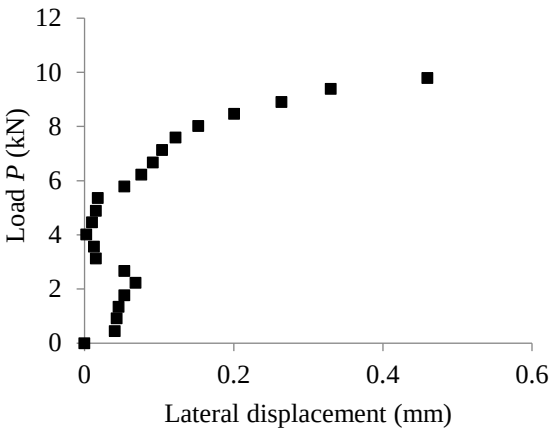	
M_{cr} = 4070 Nm		

Specimen: LTB4	Span: 1829 mm	Date:3/9/2016
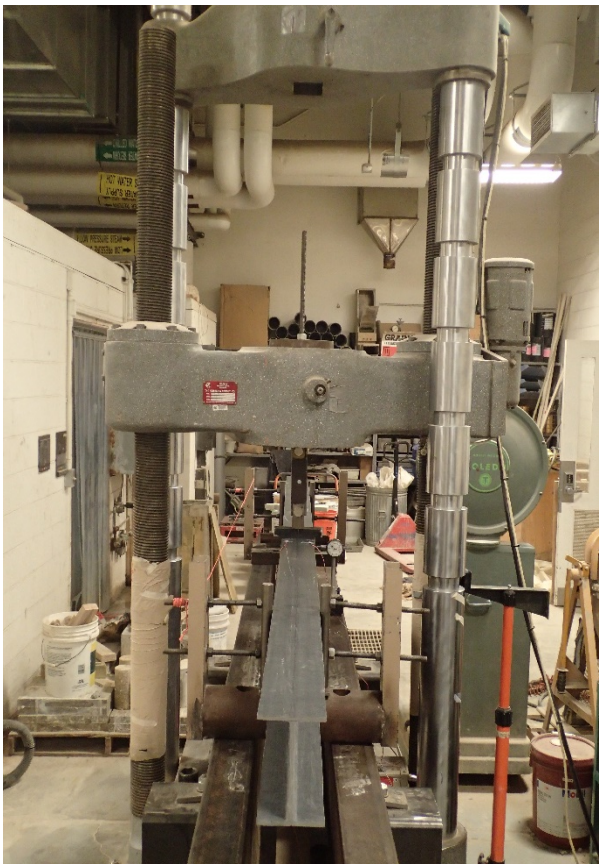	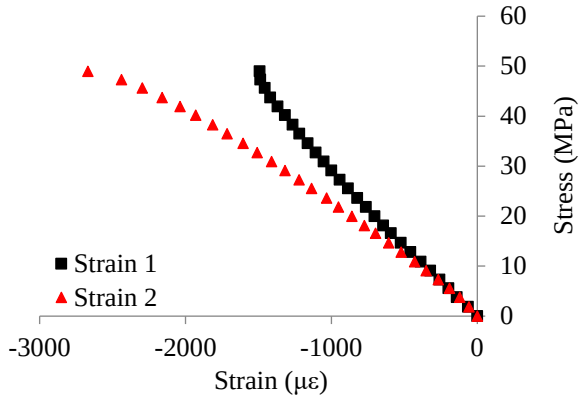	
	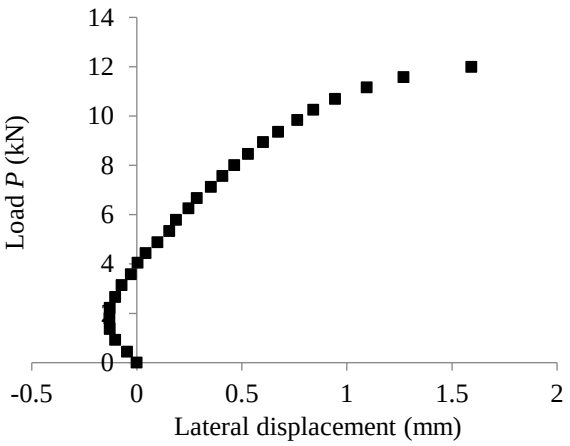	
M_{cr} = 4293 Nm		

Specimen: LTB4	Span: 1829 mm	Date:3/9/2016
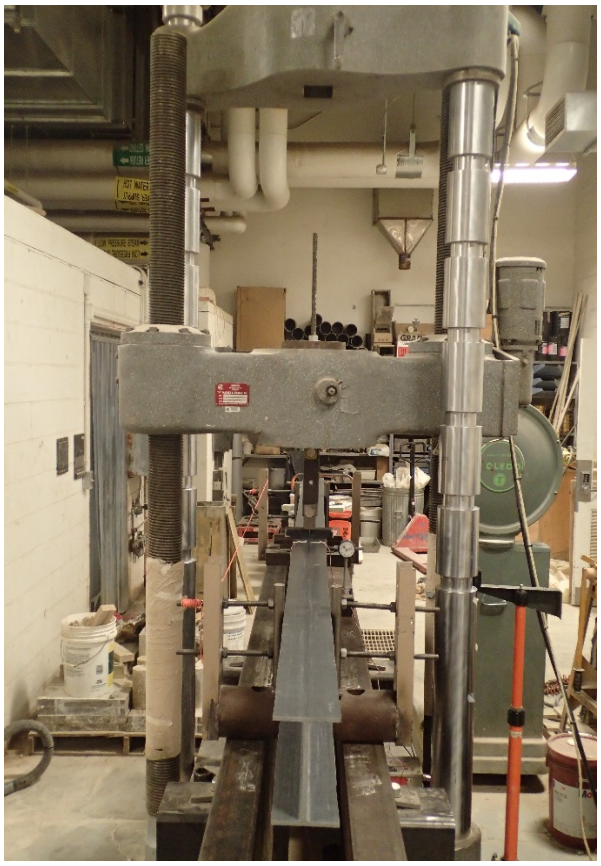	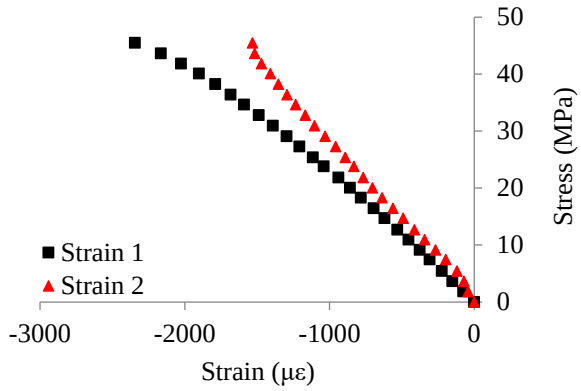	
	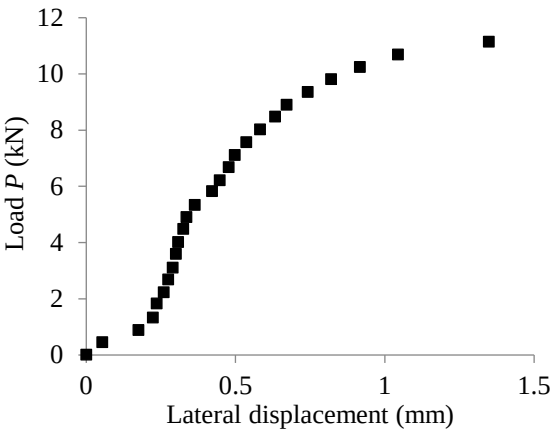	
M_{cr} = 4082 Nm		

Specimen: LTB4	Span: 1524 mm	Date:3/10/2016
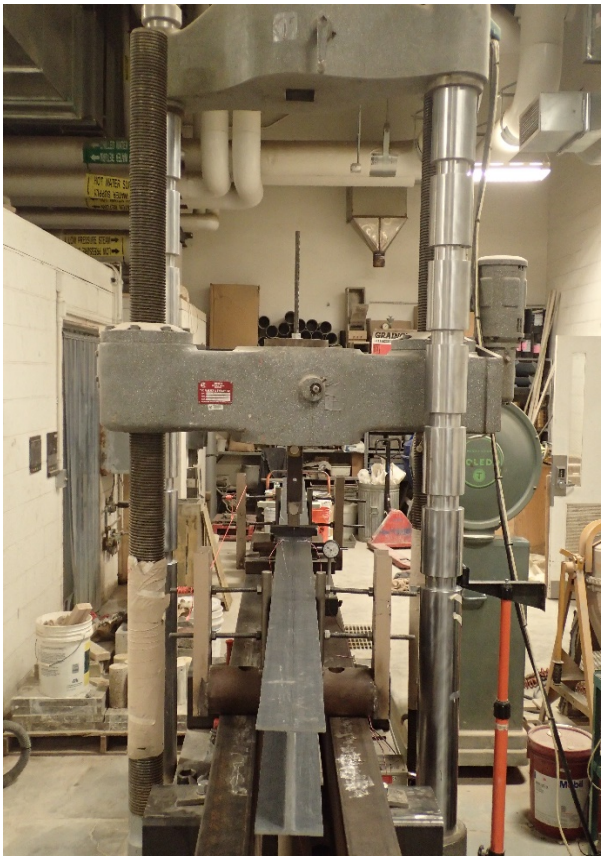	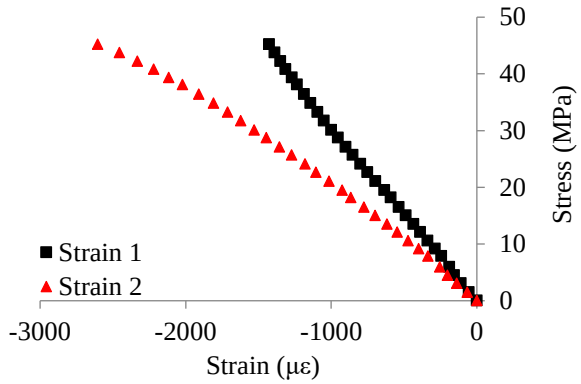	
	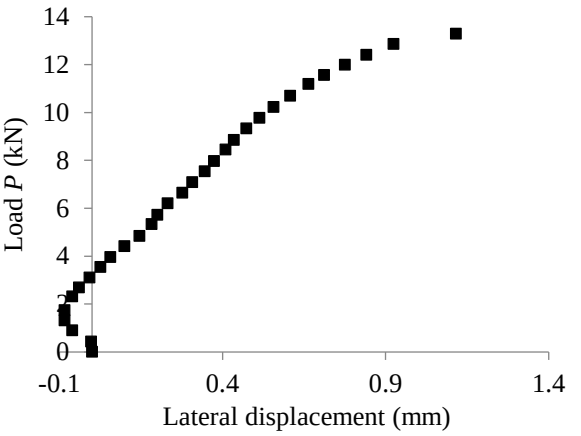	
M_{cr} = 4733 Nm		

Specimen: LTB4	Span: 1524 mm	Date:3/10/2016
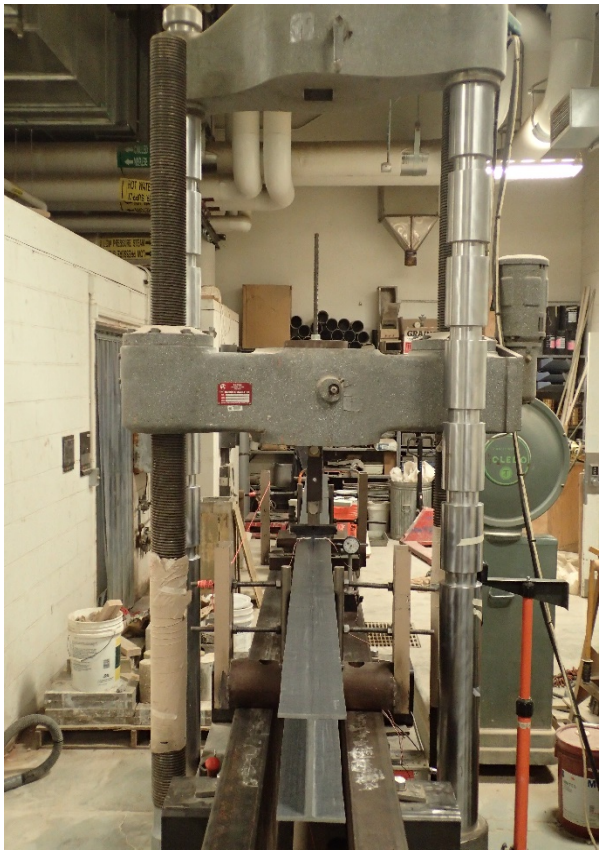	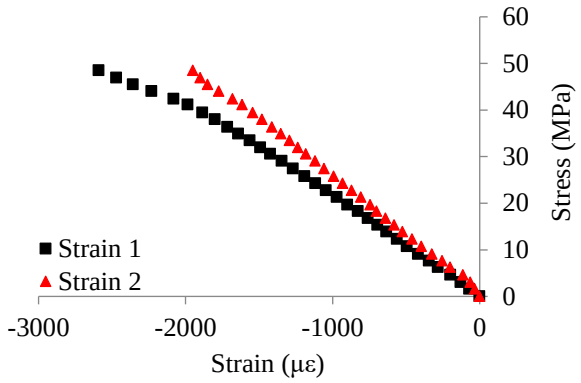 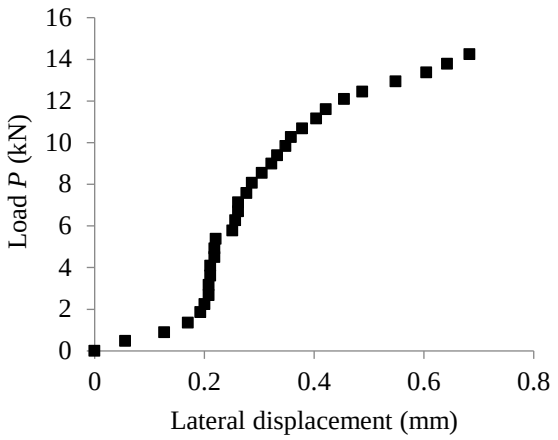	
M_{cr} = 4752 Nm		

Specimen: LTB3	Span: 2896 mm	Date:1/28/2016
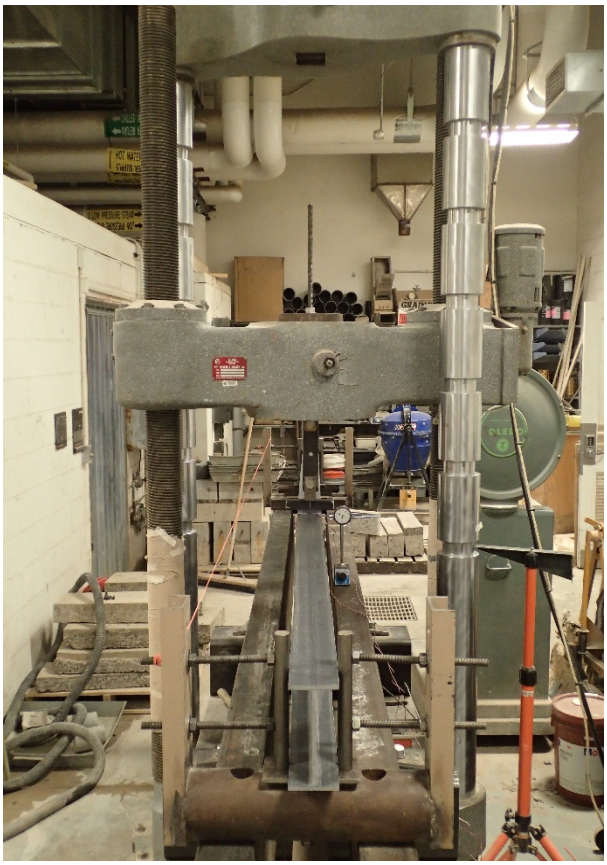	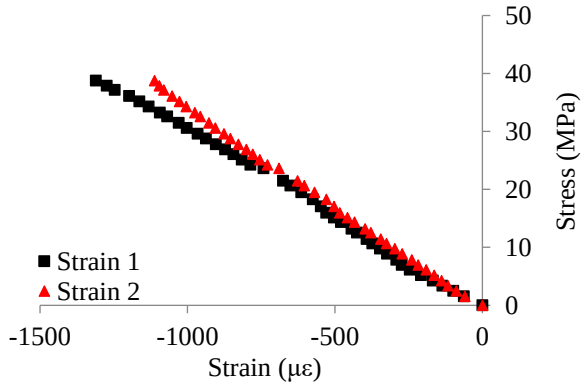 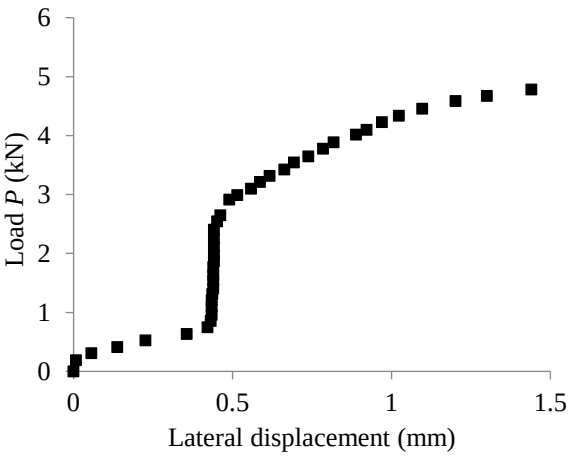	
M_{cr} = 1943 Nm		

Specimen: LTB3	Span: 2896 mm	Date:1/28/2016
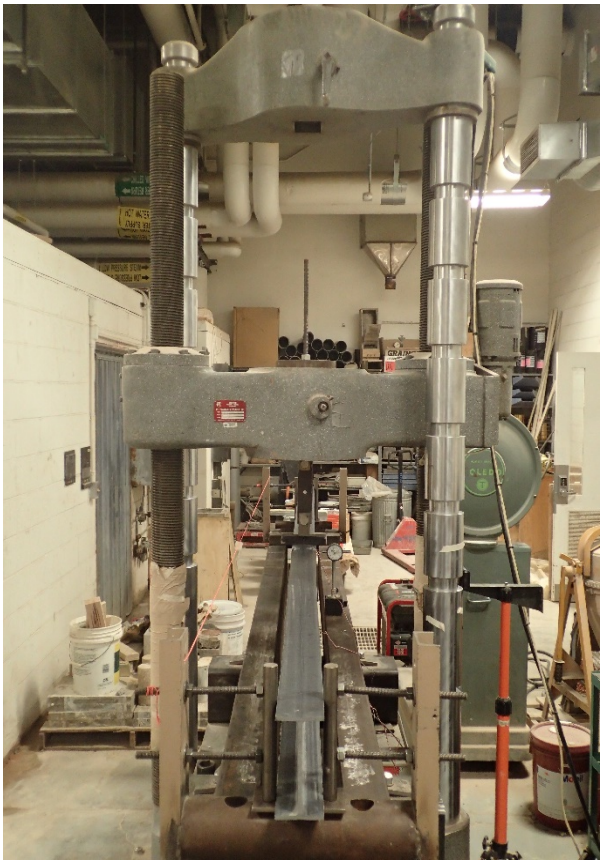	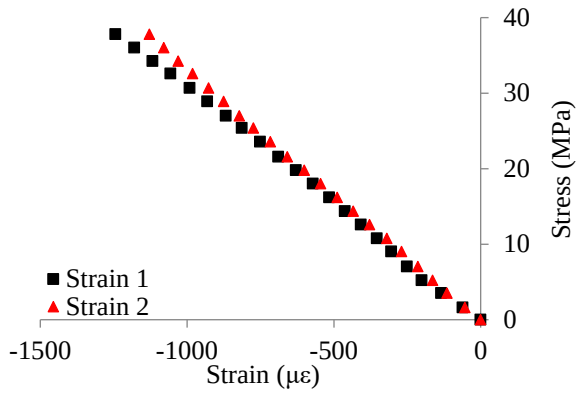 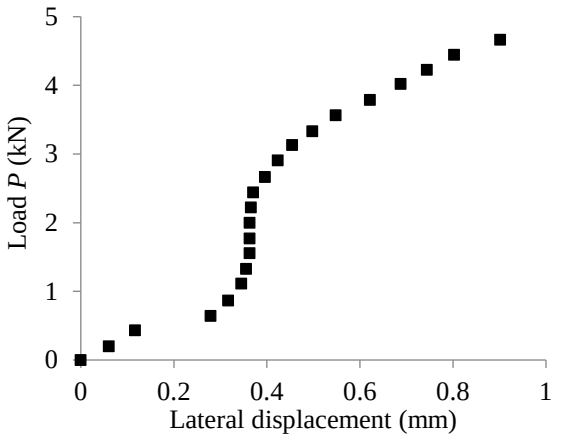	
M_{cr} = 1793 Nm		

Specimen: LTB3	Span: 2896 mm	Date:3/16/2016
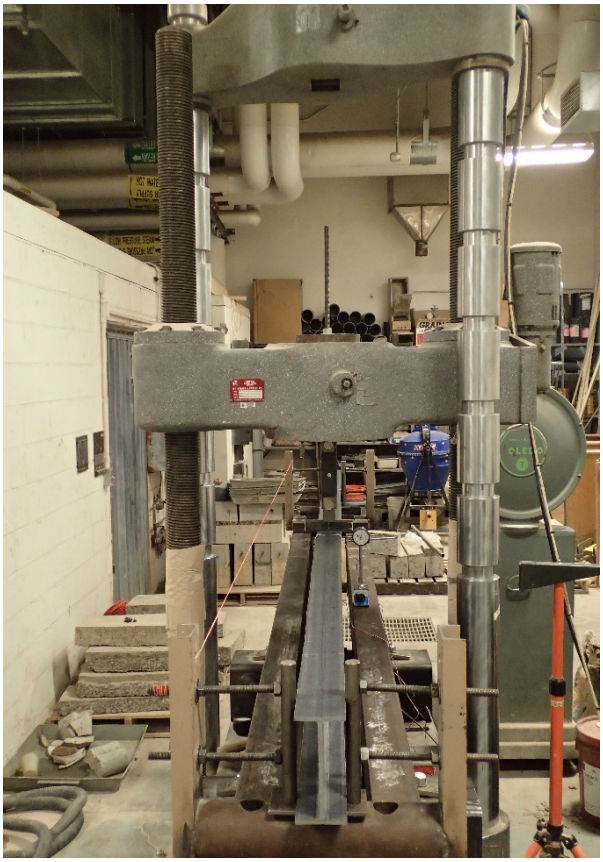	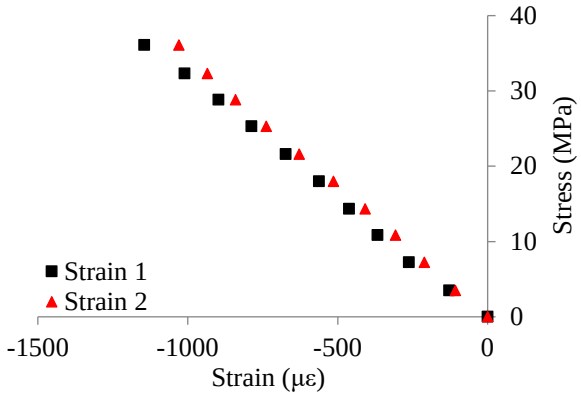 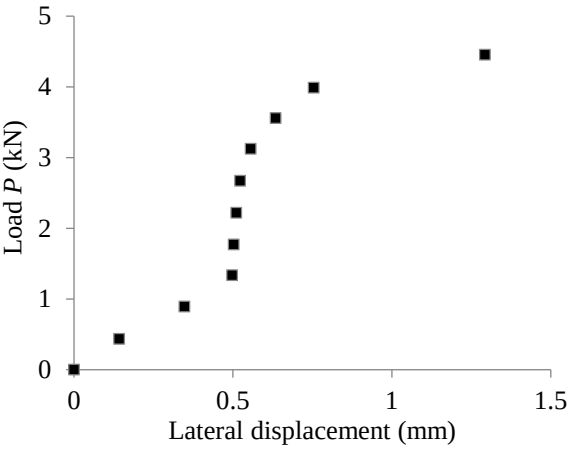	
M_{cr} = 1957 Nm		

Specimen: LTB3	Span: 2896 mm	Date:2/4/2016
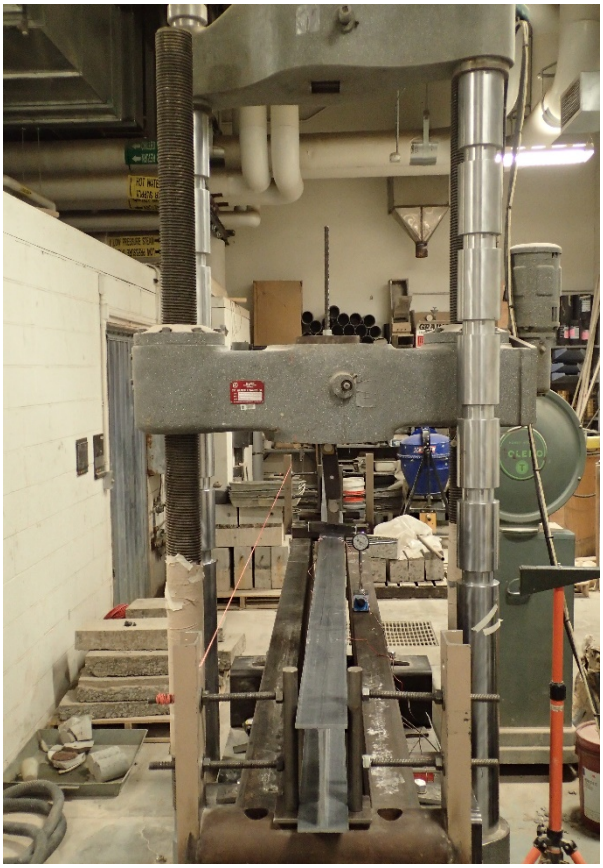	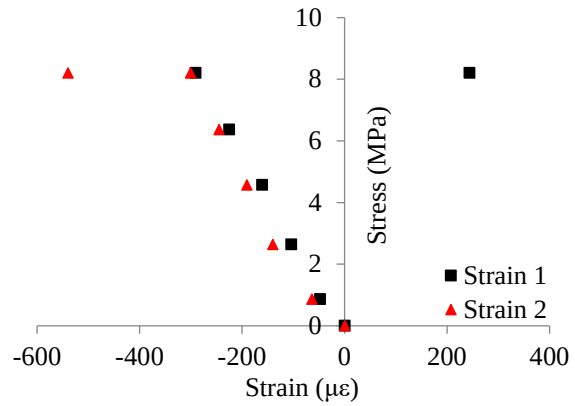	
	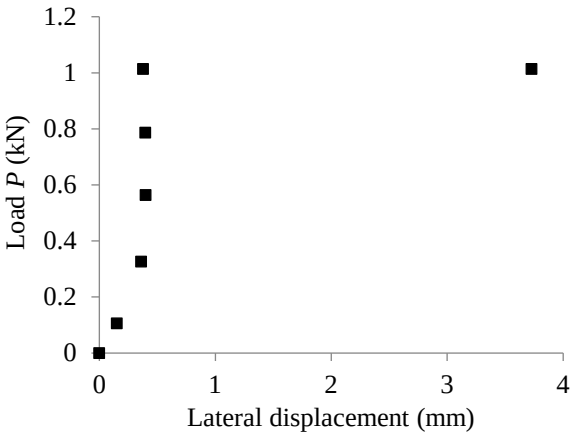	
M_{cr} = 759 Nm		

Specimen: LTB3	Span: 2896 mm	Date:1/28/2016
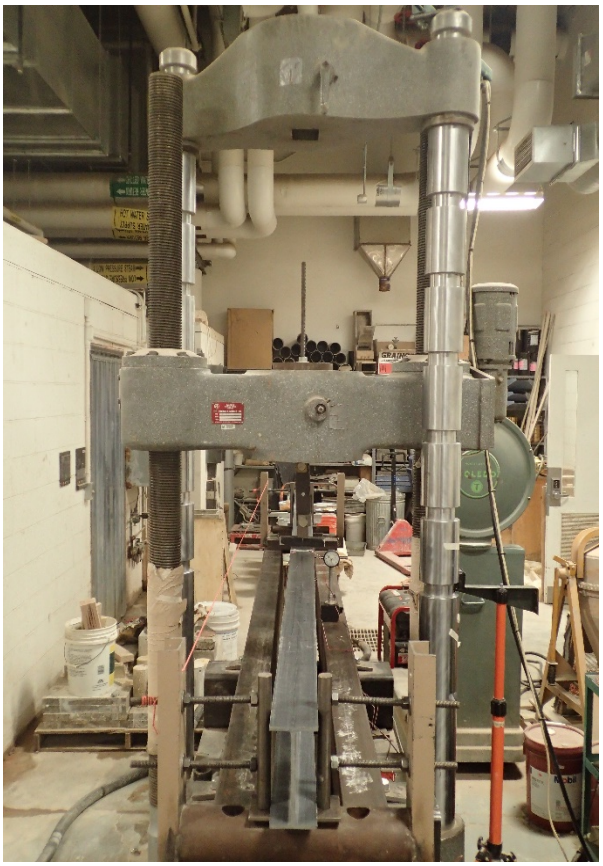	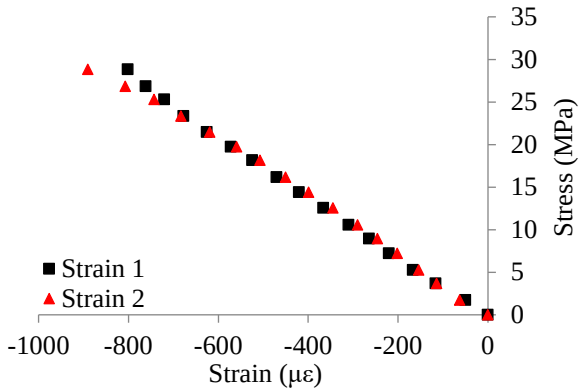	
	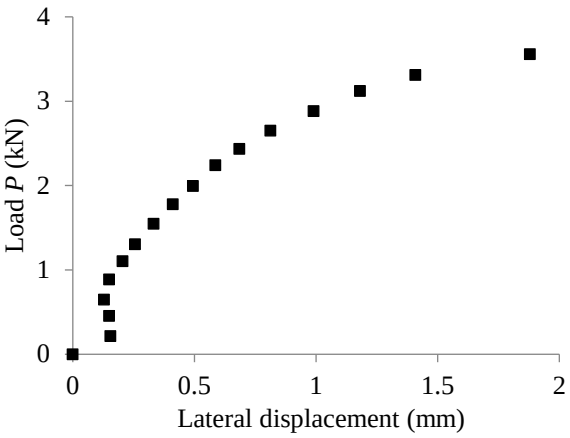	
M_{cr} = 669 Nm		

Specimen: LTB3	Span: 2438 mm	Date:2/8/2016
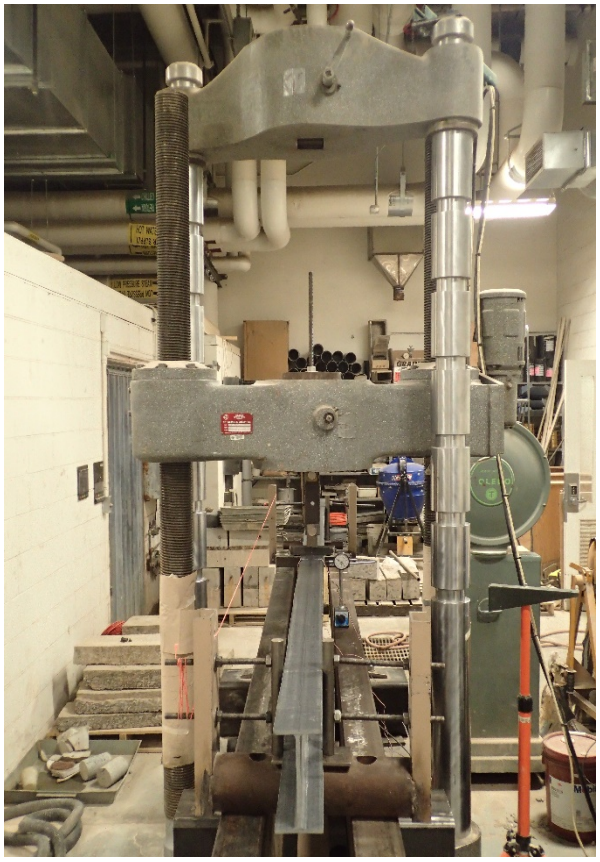	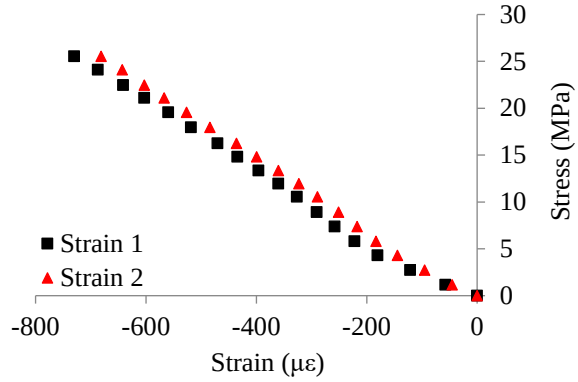 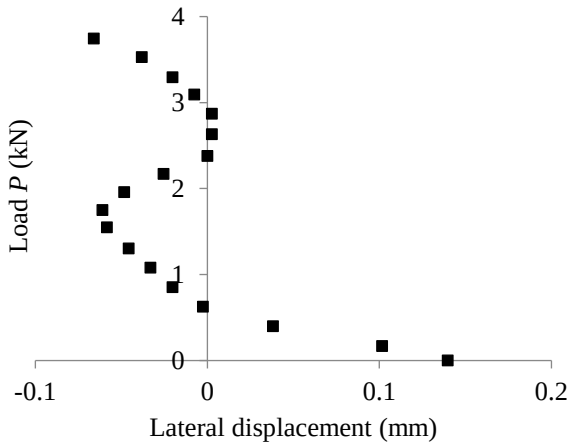	
M_{cr} = 1767 Nm		

Specimen: LTB3	Span: 2438 mm	Date:2/8/2016
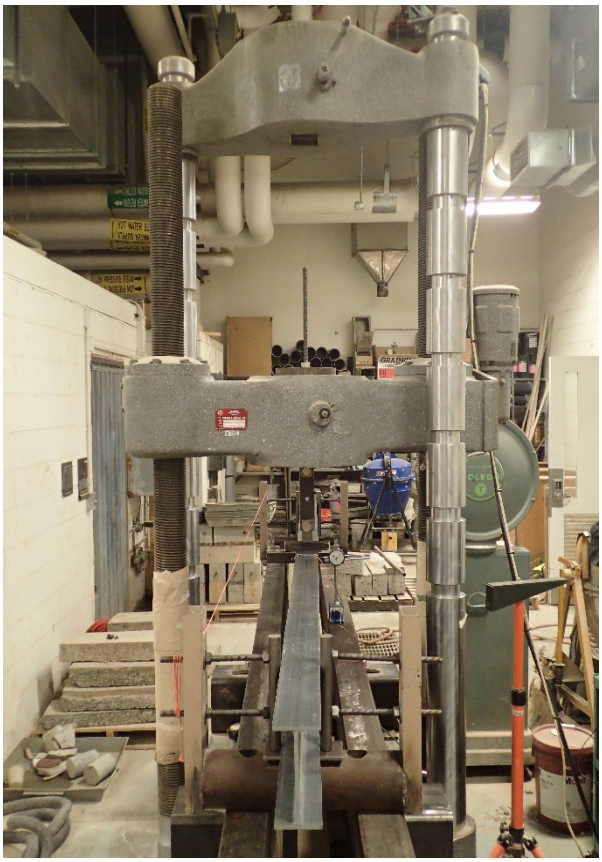	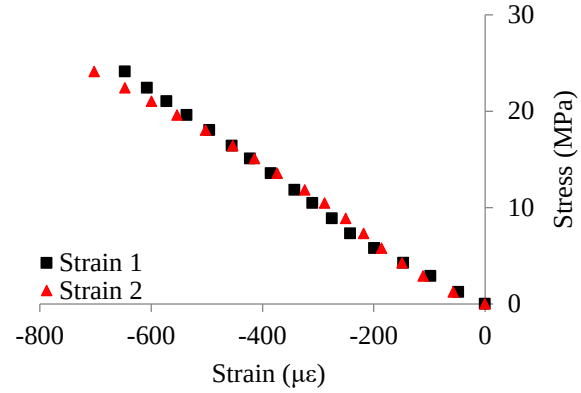 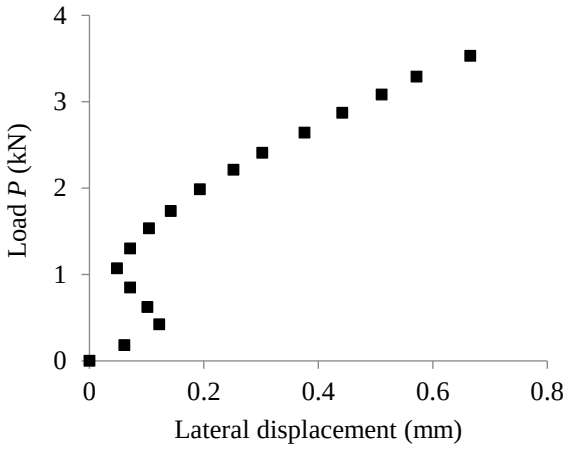	
M_{cr} = 1075 Nm		

Specimen: LTB3	Span: 2438 mm	Date:2/8/2016
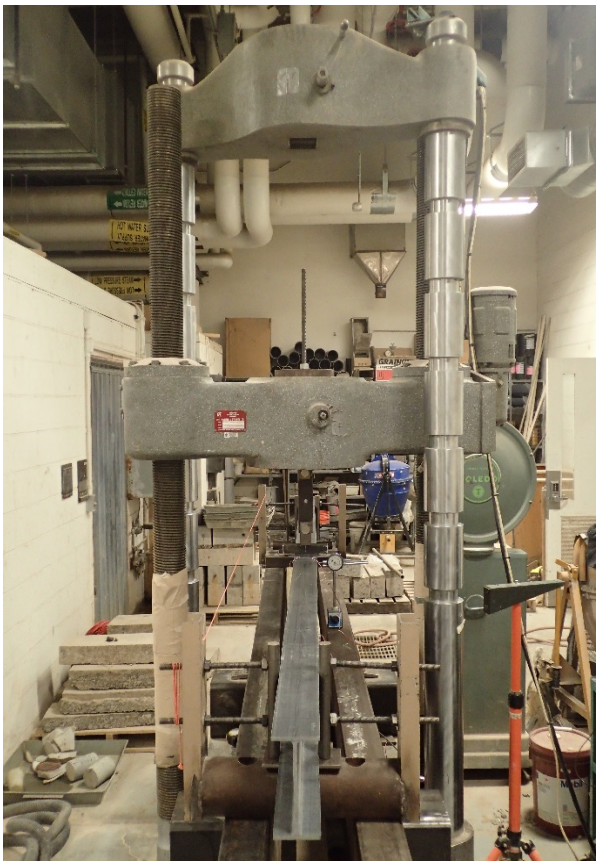	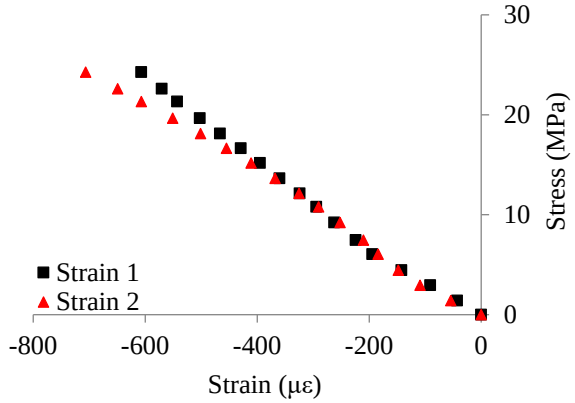 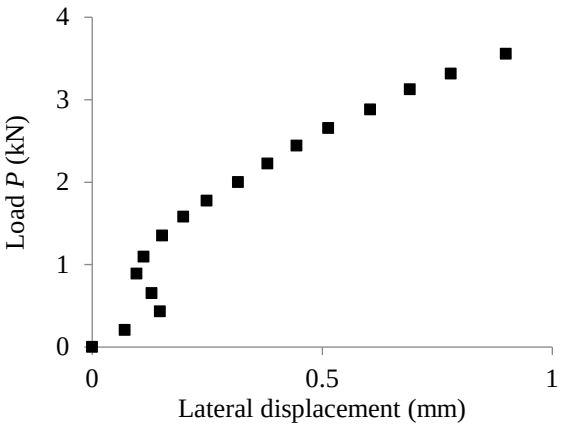	
M_{cr} = 1101 Nm		

Specimen: LTB3	Span: 2438 mm	Date:3/21/2016
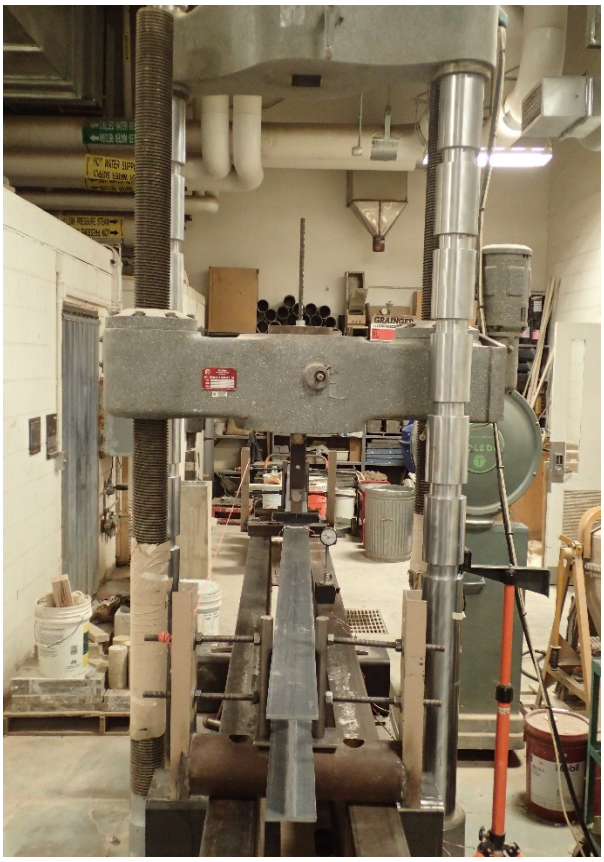	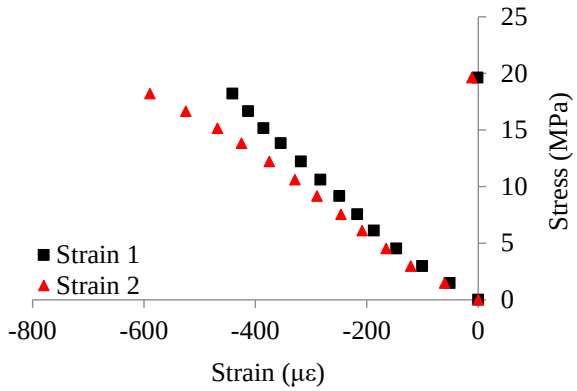 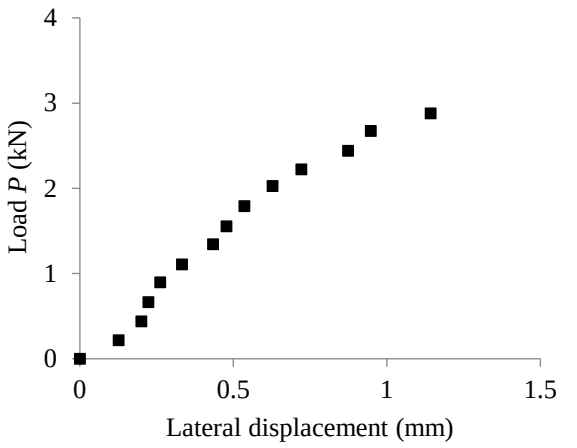	
M_{cr} = 1109 Nm		

Specimen: LTB3	Span: 2134 mm	Date:2/9/2016
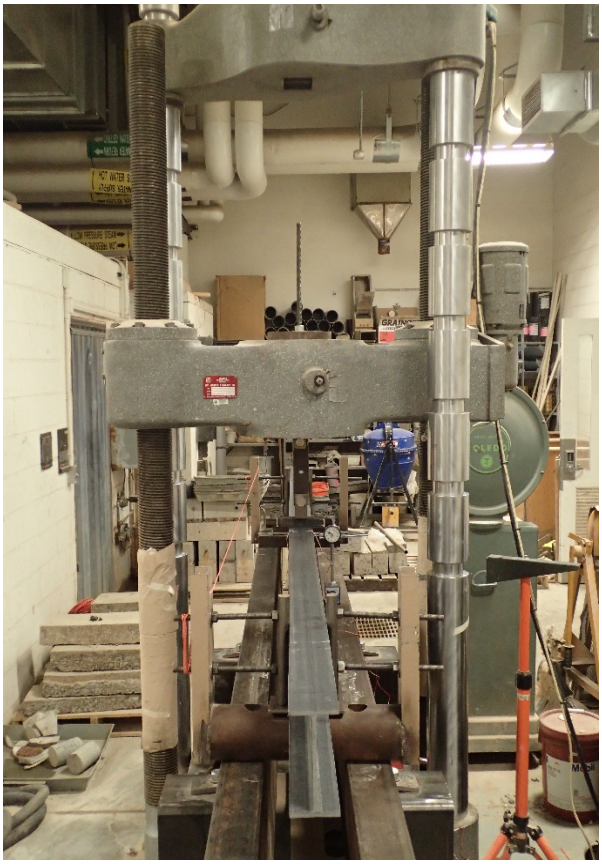	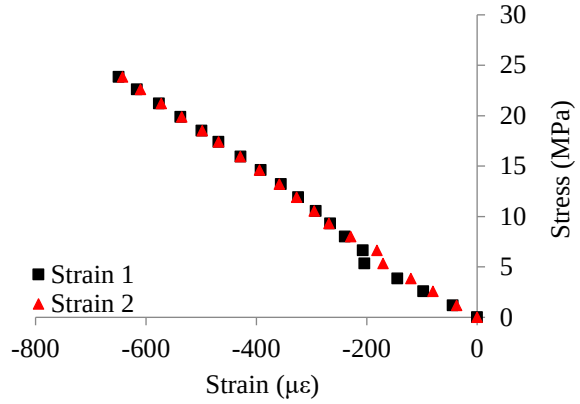	
	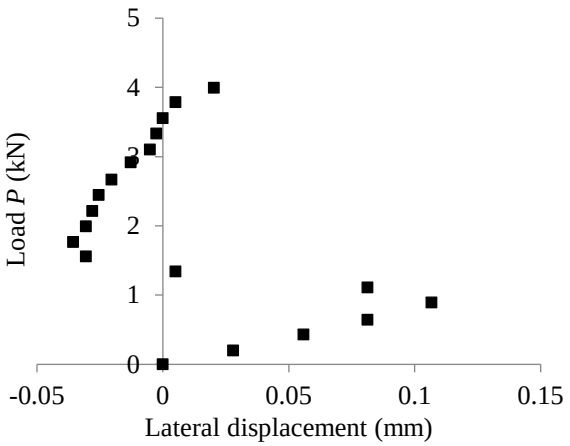	
M_{cr} = 1909 Nm		

Specimen: LTB3	Span: 2134 mm	Date:2/11/2016
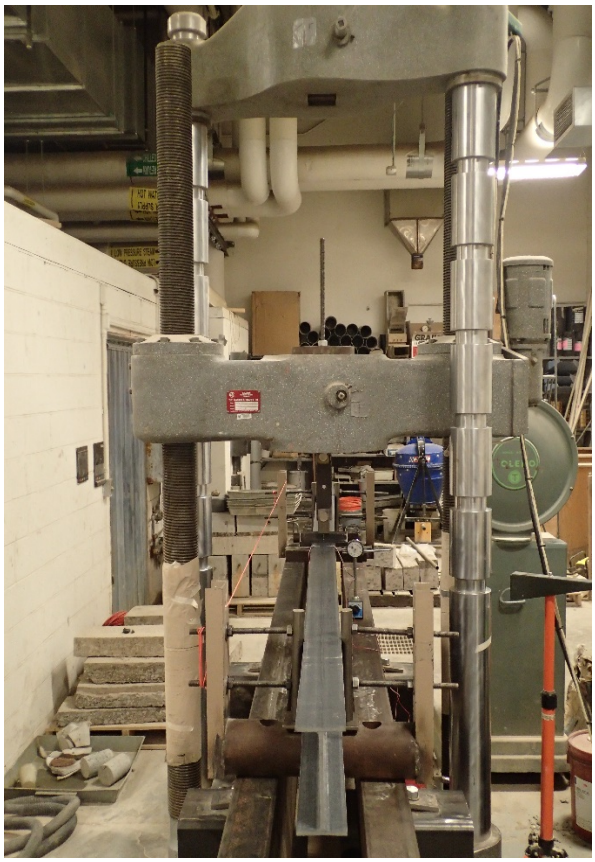	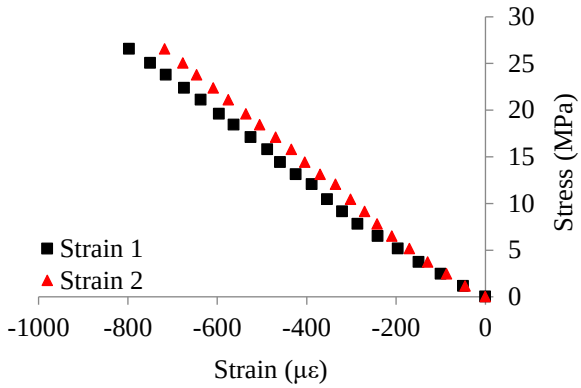	
	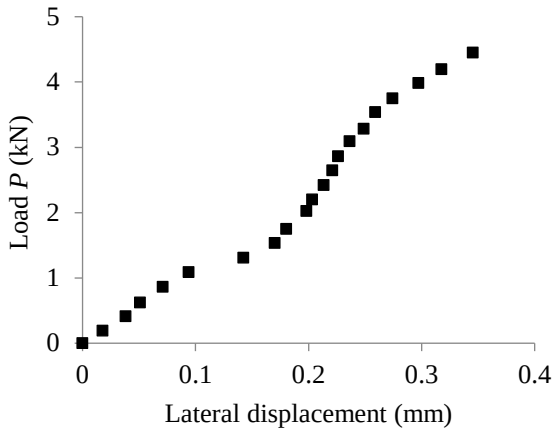	
M_{cr} = 1901 Nm		

Specimen: LTB3	Span: 2134 mm	Date:2/9/2016
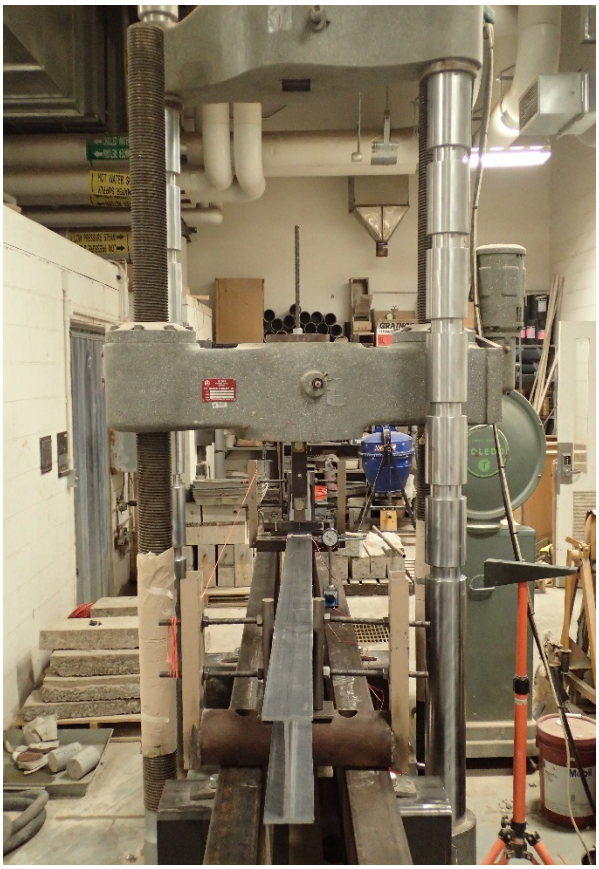	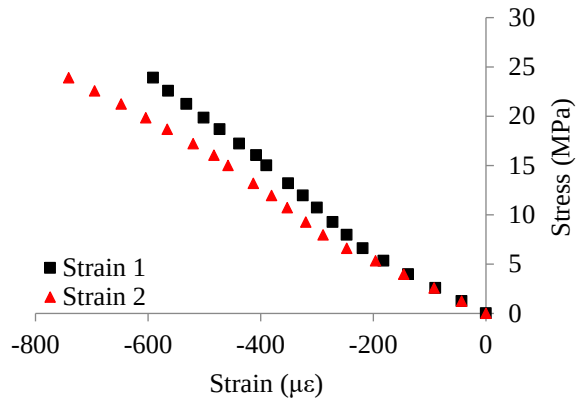 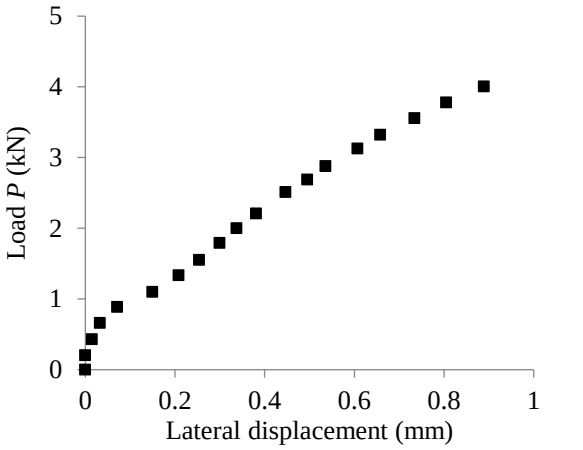	
M_{cr} = 1786 Nm		

Specimen: LTB3	Span: 1829 mm	Date:2/11/2016
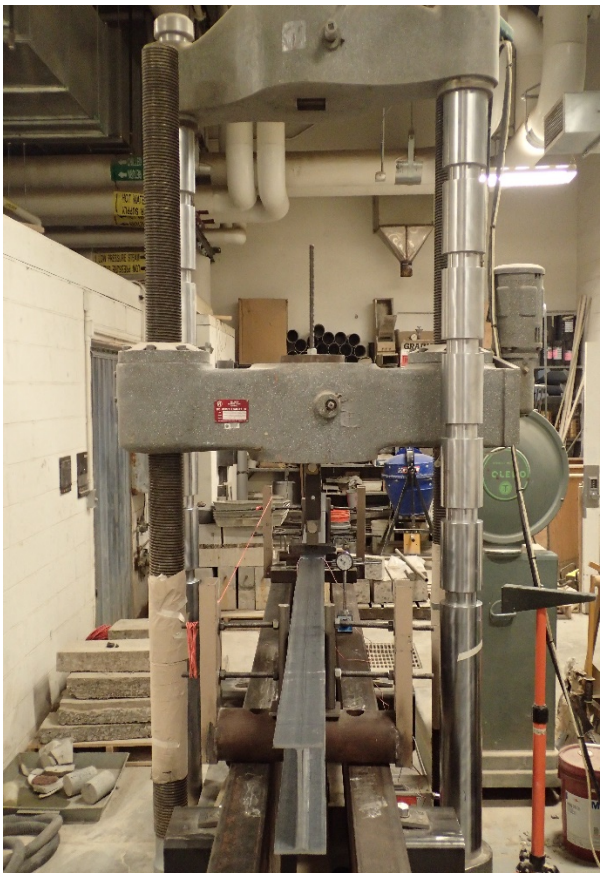	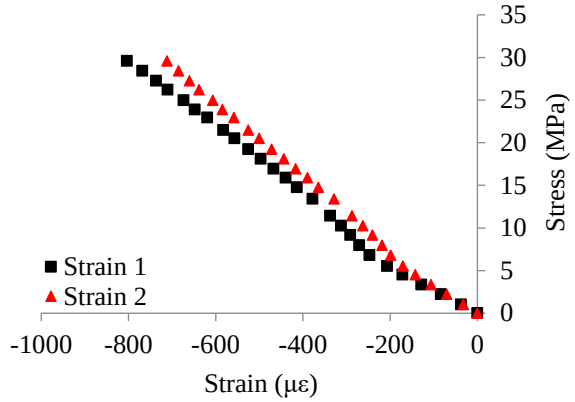	
	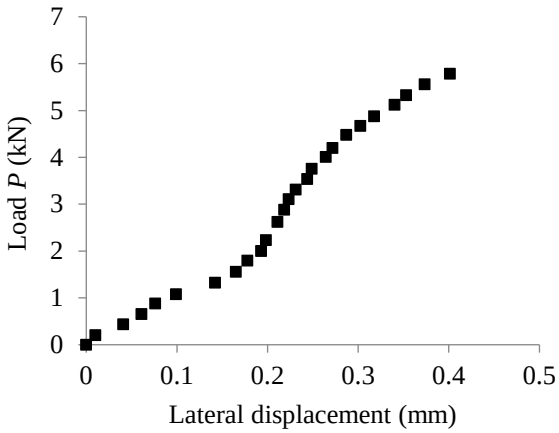	
M_{cr} = 1727 Nm		

Specimen: LTB3	Span: 1829 mm	Date:3/17/2016
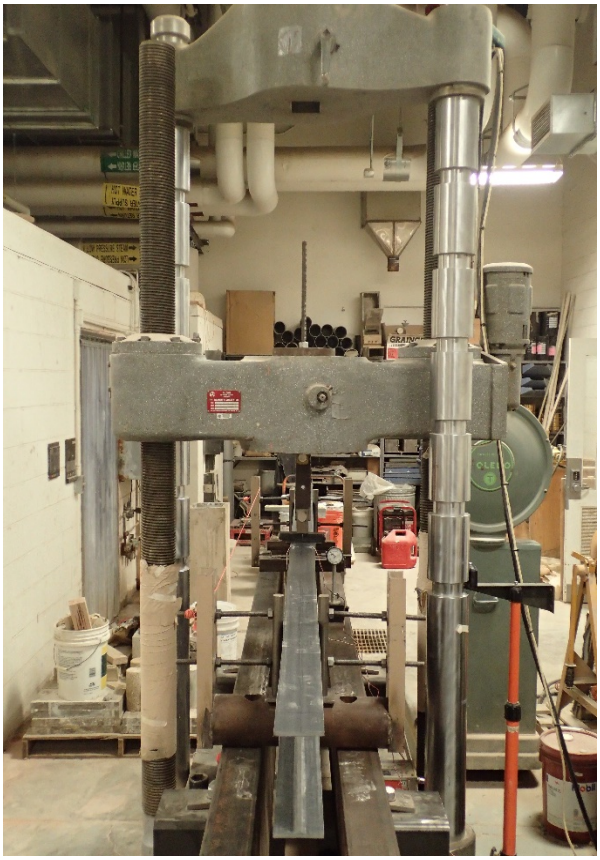	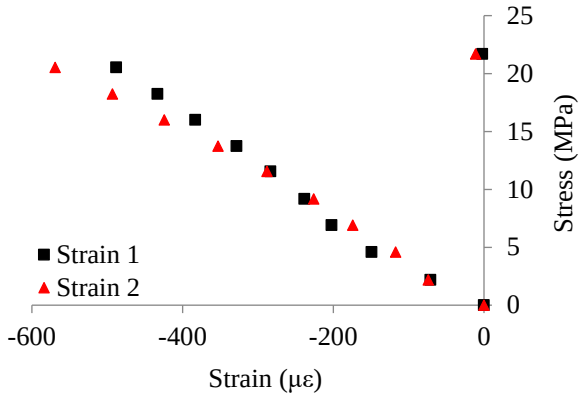 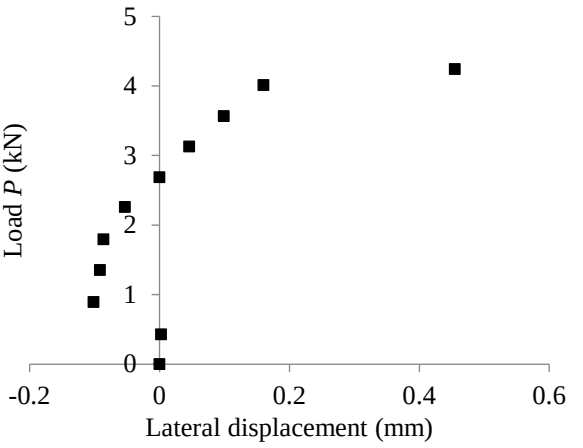	
M_{cr} = 1843 Nm		

Specimen: LTB3	Span: 1829 mm	Date:2/11/2016
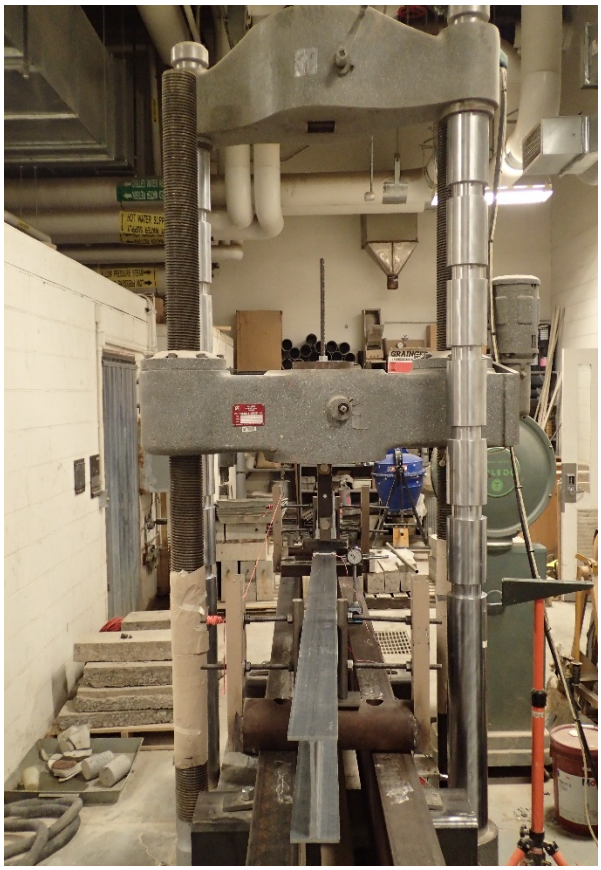	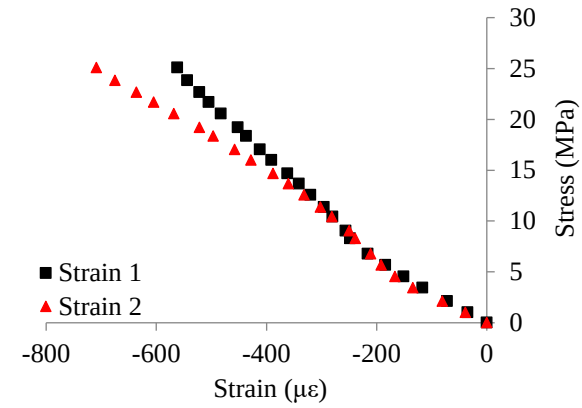 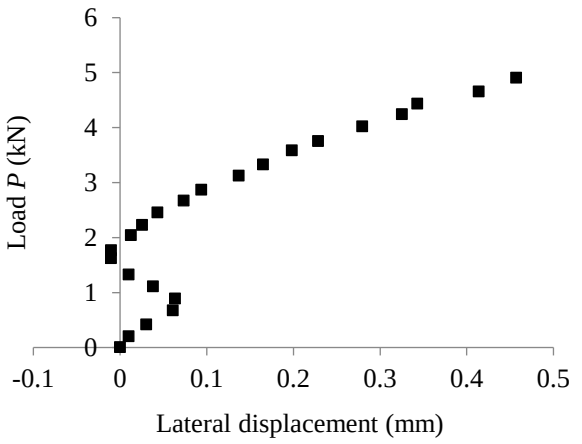	
M_{cr} = 1725 Nm		

Specimen: LTB3	Span: 1829 mm	Date:3/17/2016
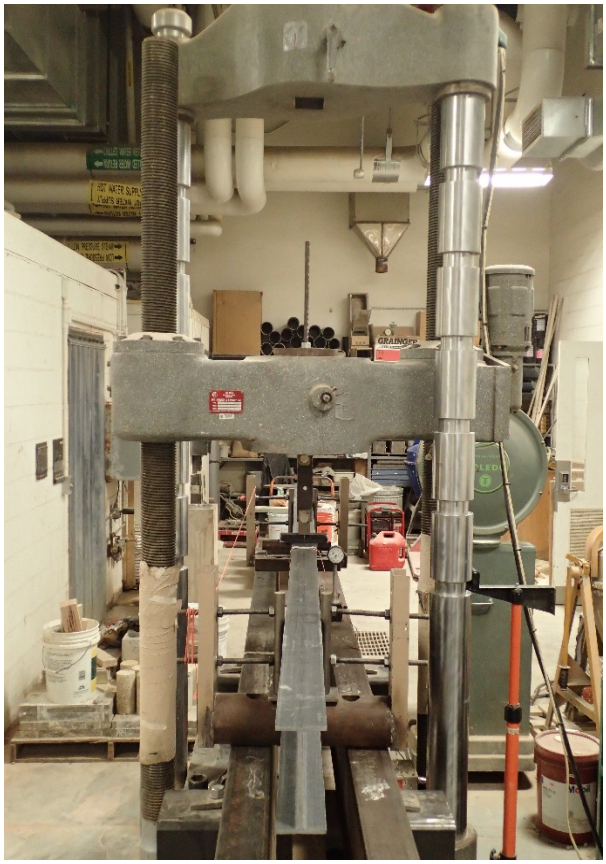	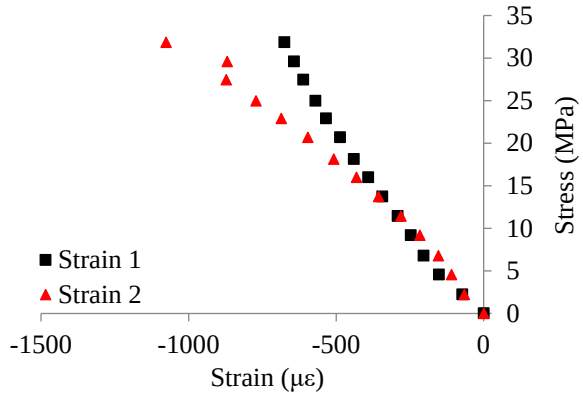	
	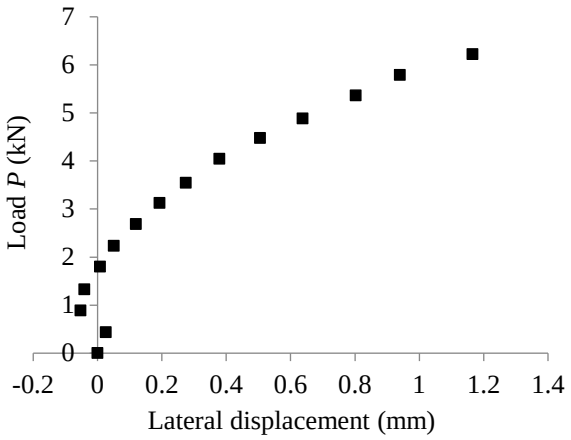	
M_{cr} = 1857 Nm		

Specimen: LTB3	Span: 1524 mm	Date:3/21/2016
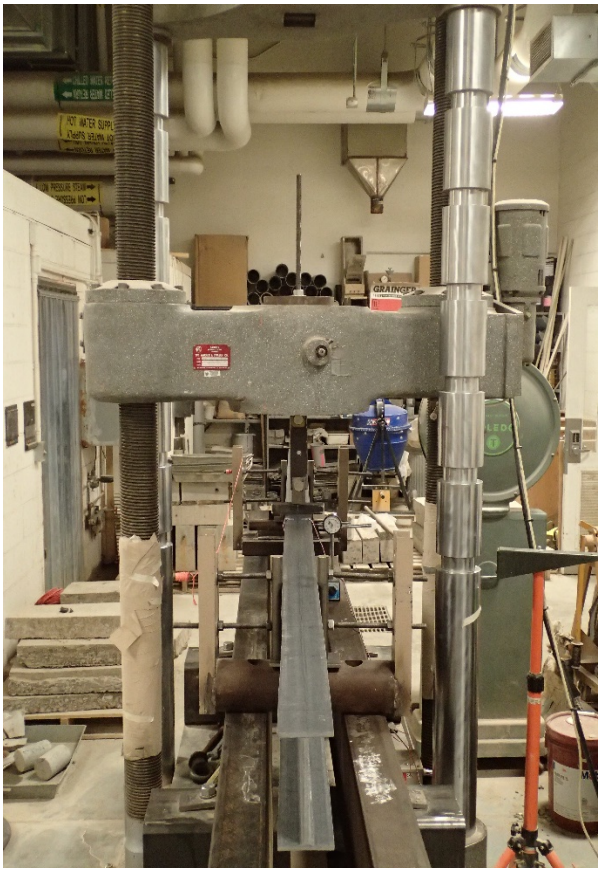	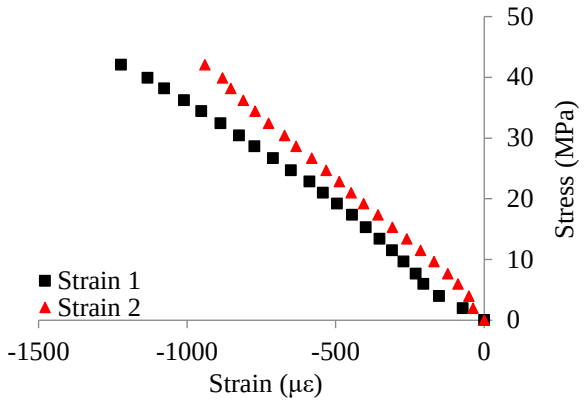	
	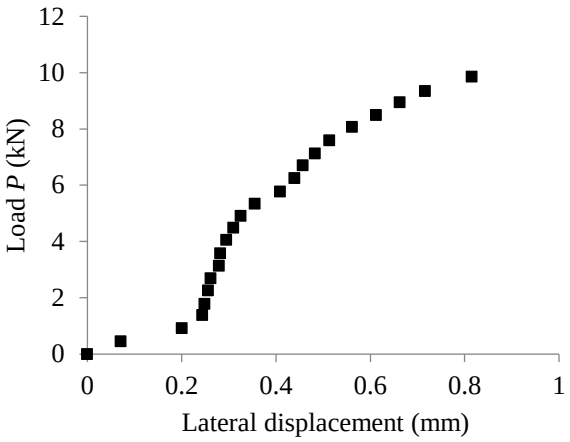	
M_{cr} = 2044 Nm		

Specimen: LTB3	Span: 1524 mm	Date:2/12/2016
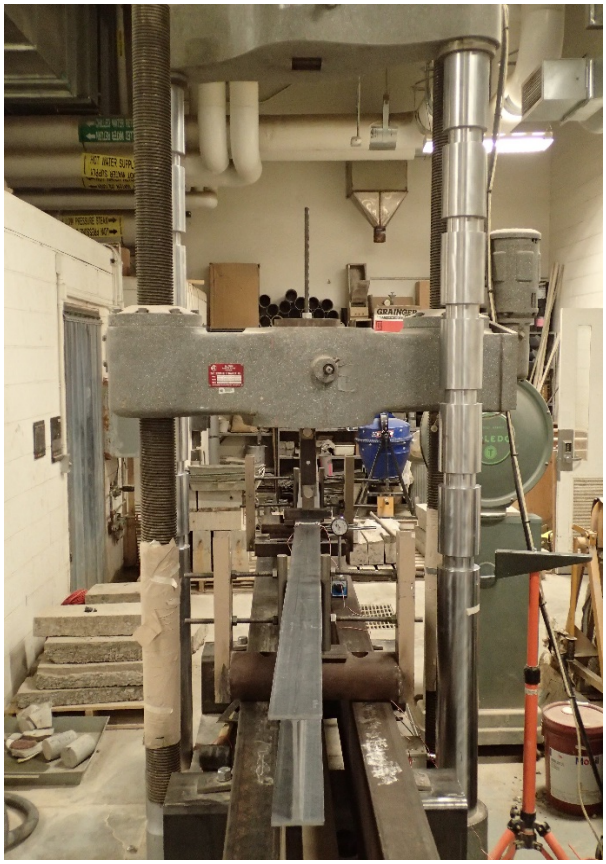	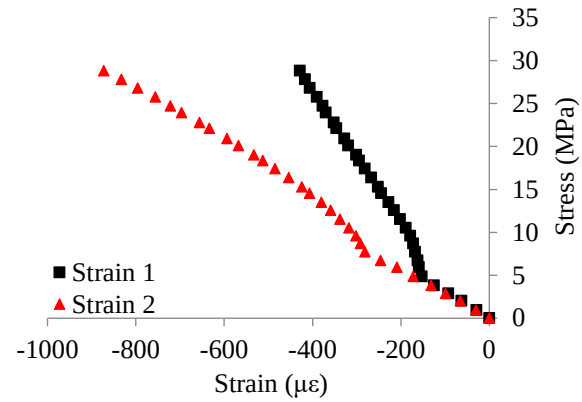 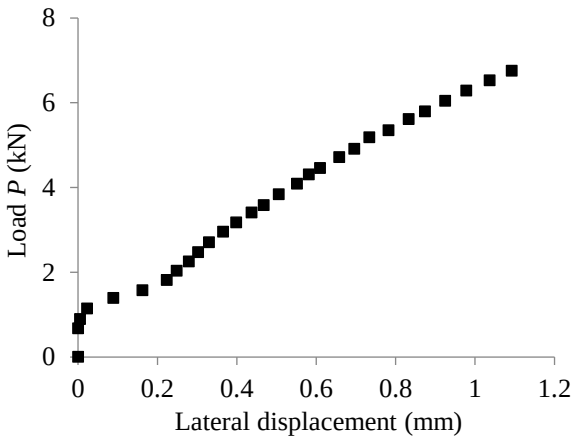	
M_{cr} = 2043 Nm		

Specimen: LTB3	Span: 1524 mm	Date:2/12/2016
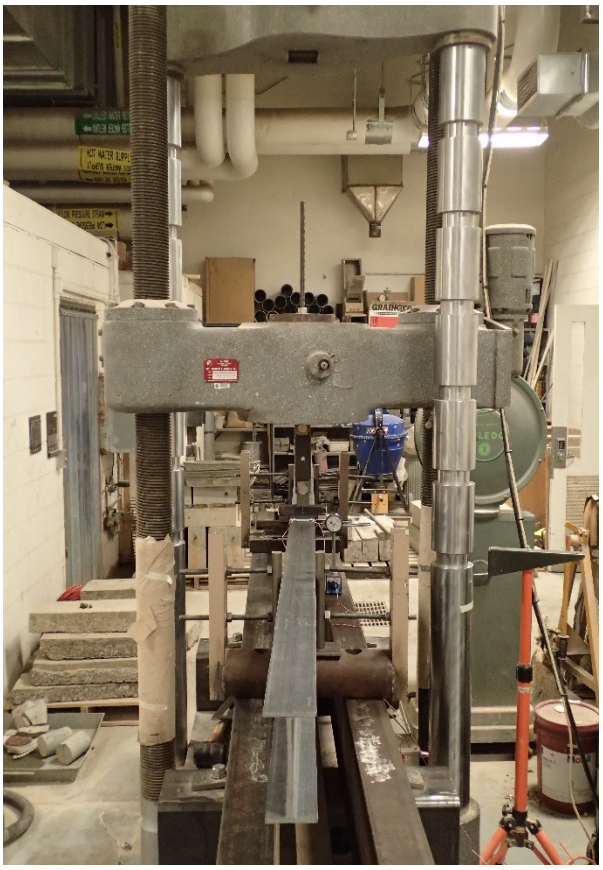	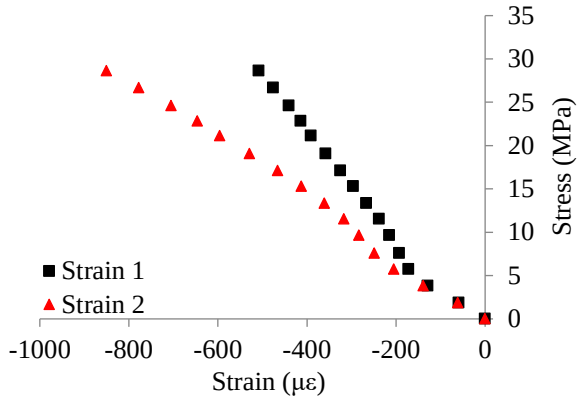 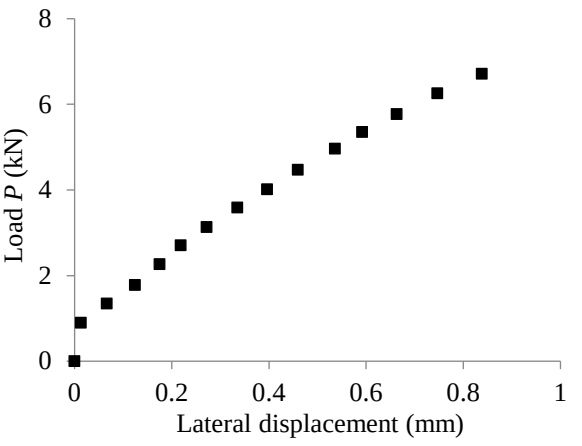	
M_{cr} = 2048 Nm		

Specimen: LTB2	Span: 2896 mm	Date:2/2/2016
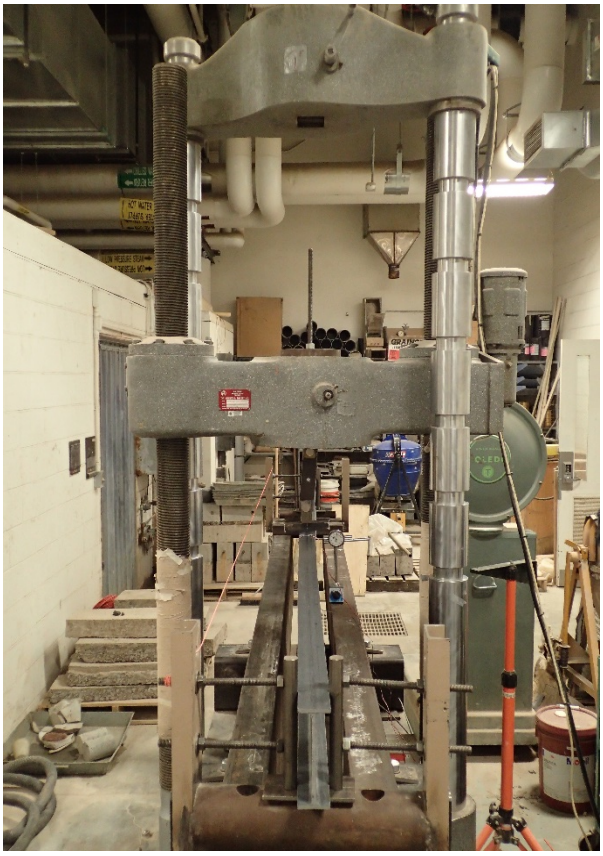	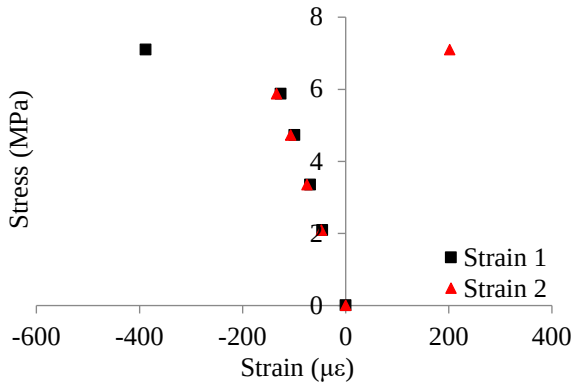 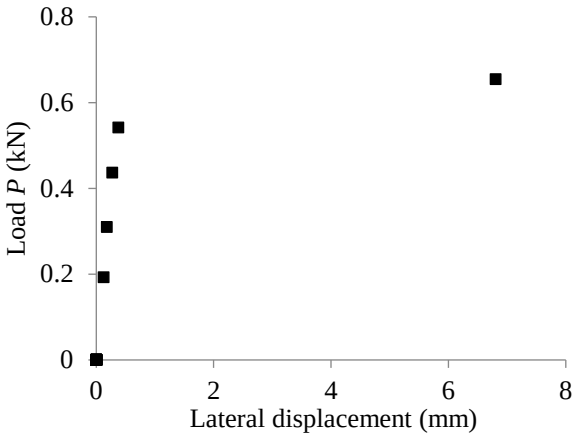	
M_{cr} = 409 Nm		

Specimen: LTB2	Span: 2896 mm	Date:2/2/2016
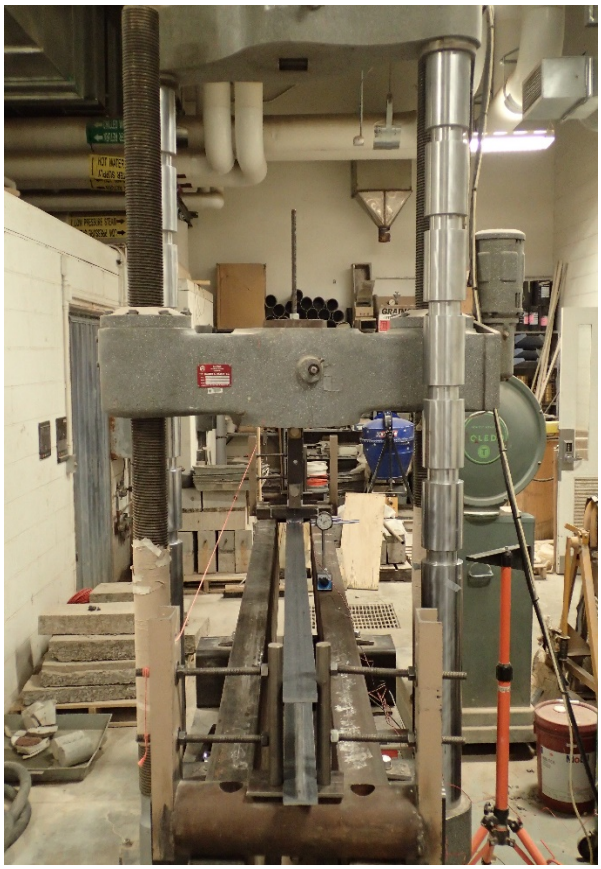	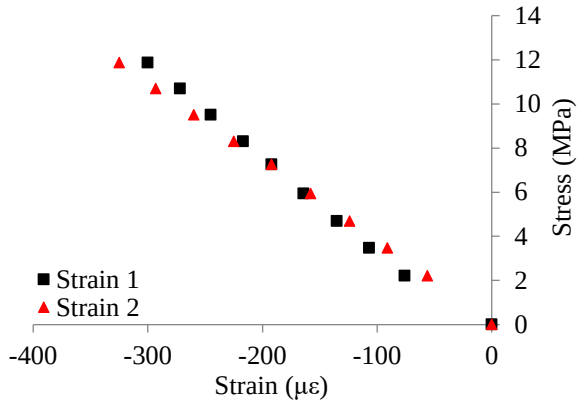 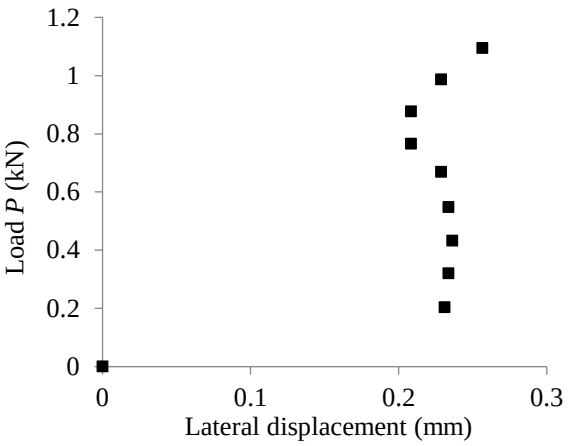	
M_{cr} = 501 Nm		

Specimen: LTB2	Span: 2896 mm	Date:3/16/2016
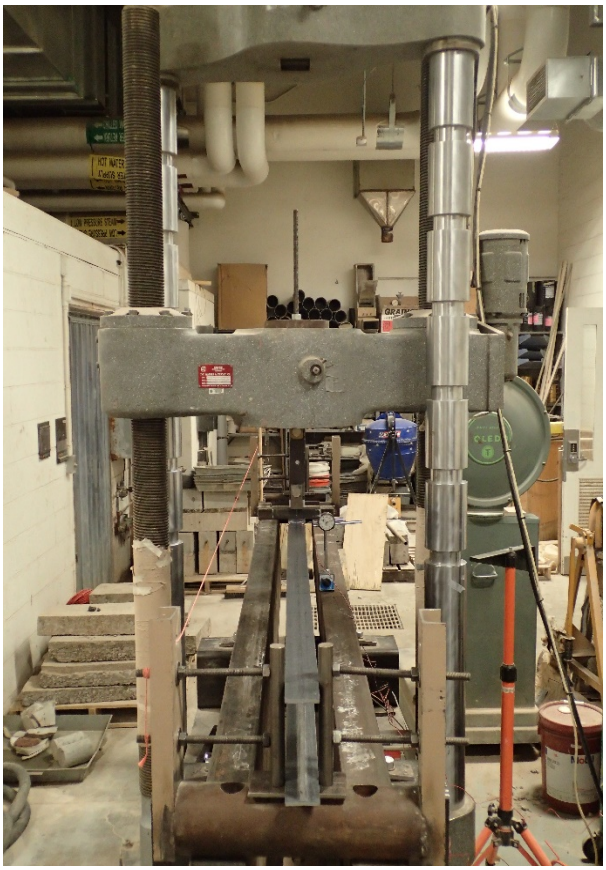	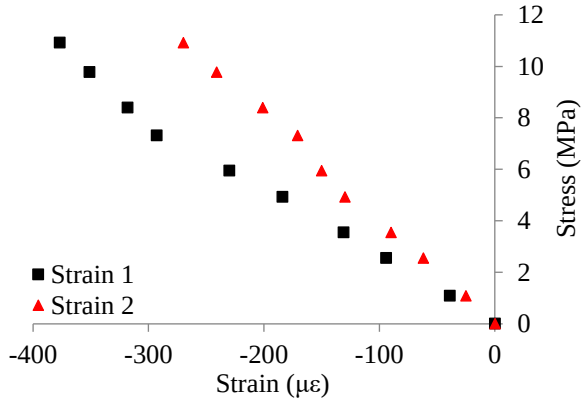	
	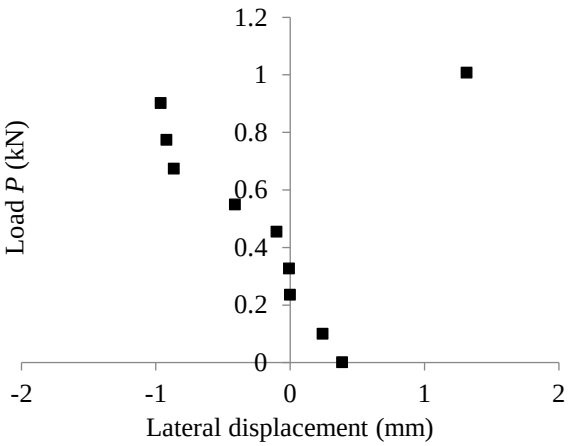	
M_{cr} = 346 Nm		

Specimen: LTB2	Span: 2438 mm	Date:2/8/2016
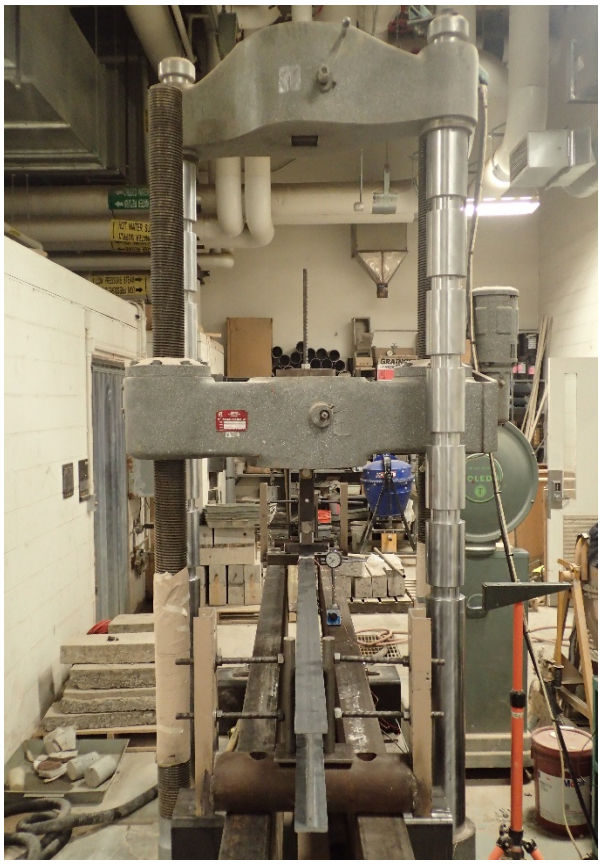	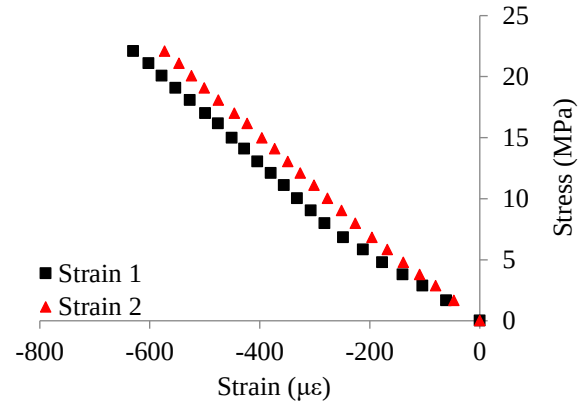	
	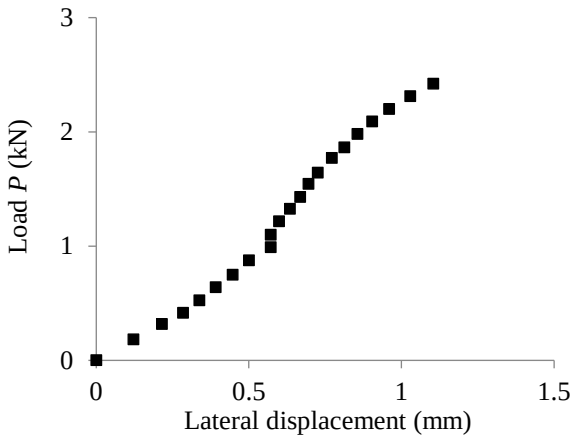	
M_{cr} = 681 Nm		

Specimen: LTB2	Span: 2438 mm	Date:2/8/2016
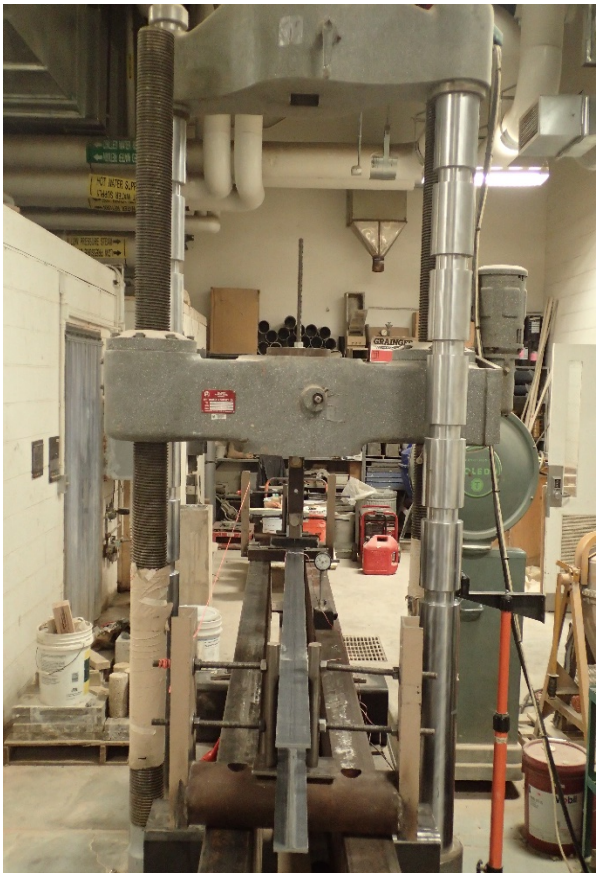	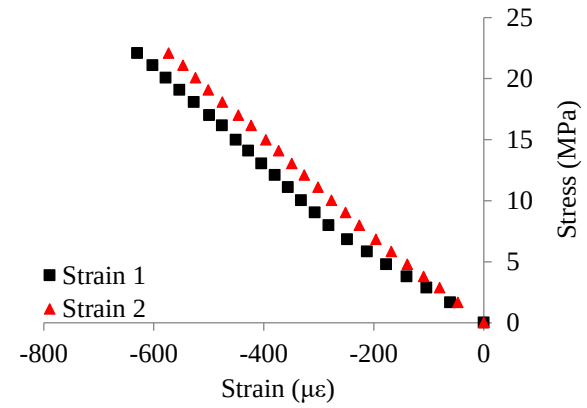 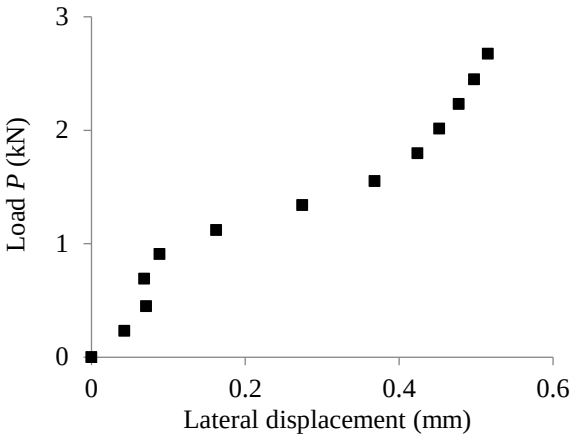	
M_{cr} = 565 Nm		

Specimen: LTB2	Span: 2438 mm	Date:3/18/2016
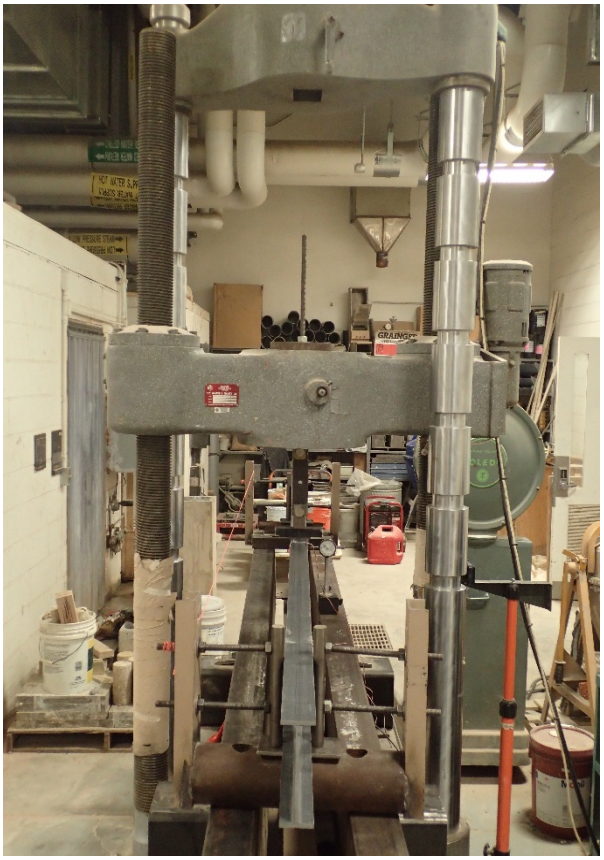	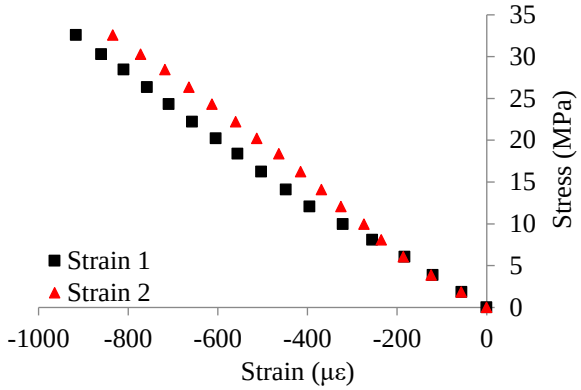	
	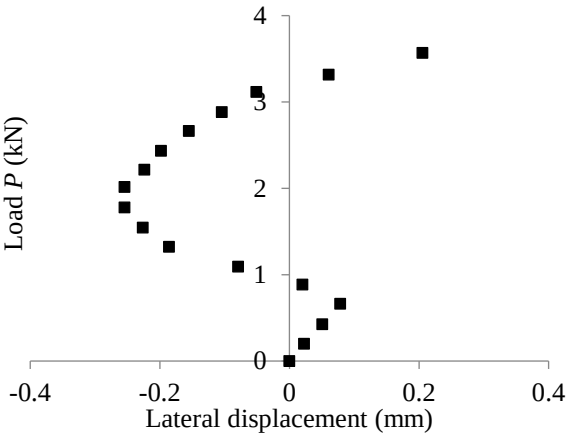	
M_{cr} = 550 Nm		

Specimen: LTB2	Span: 2438 mm	Date:3/18/2016
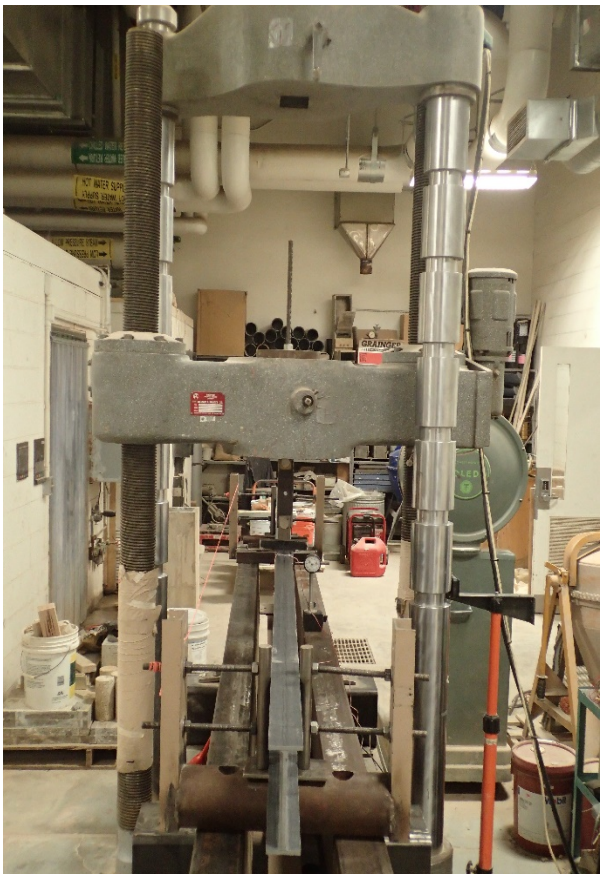	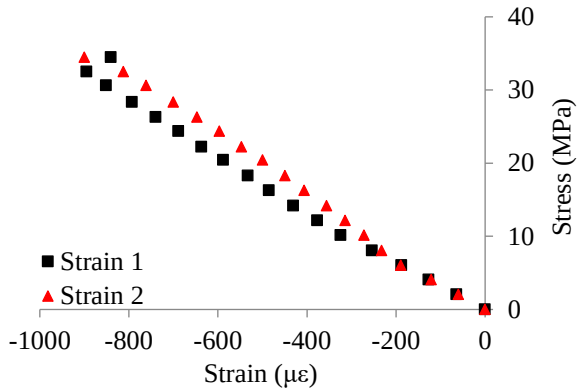 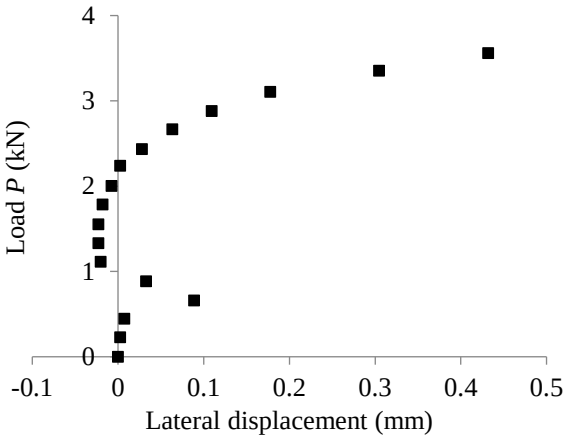	
M_{cr} = 550 Nm		

Specimen: LTB2	Span: 2438 mm	Date:2/9/2016
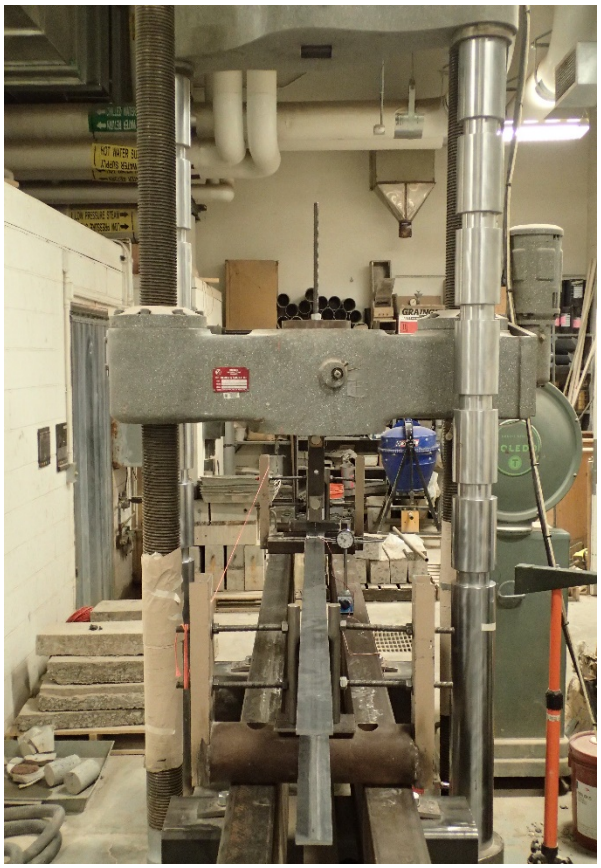	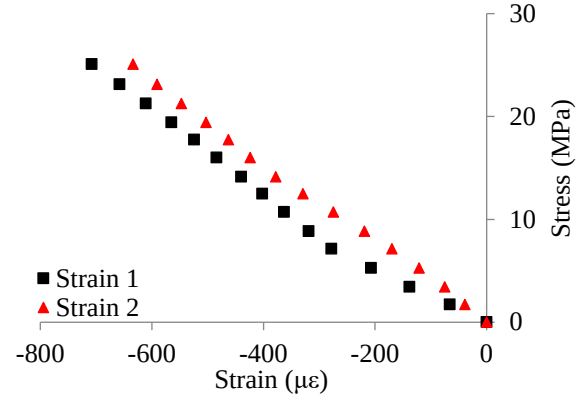 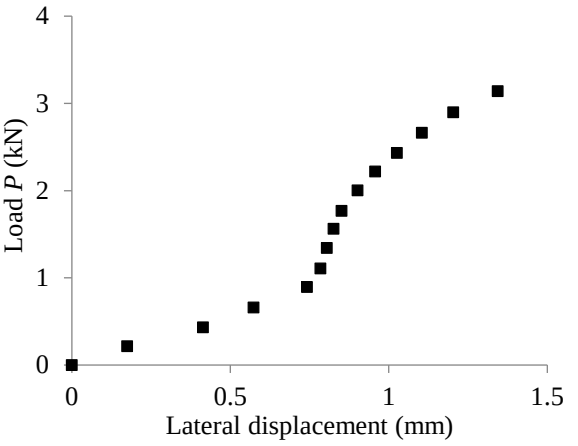	
M_{cr} = 952 Nm		

Specimen: LTB2	Span: 2438 mm	Date:2/9/2016
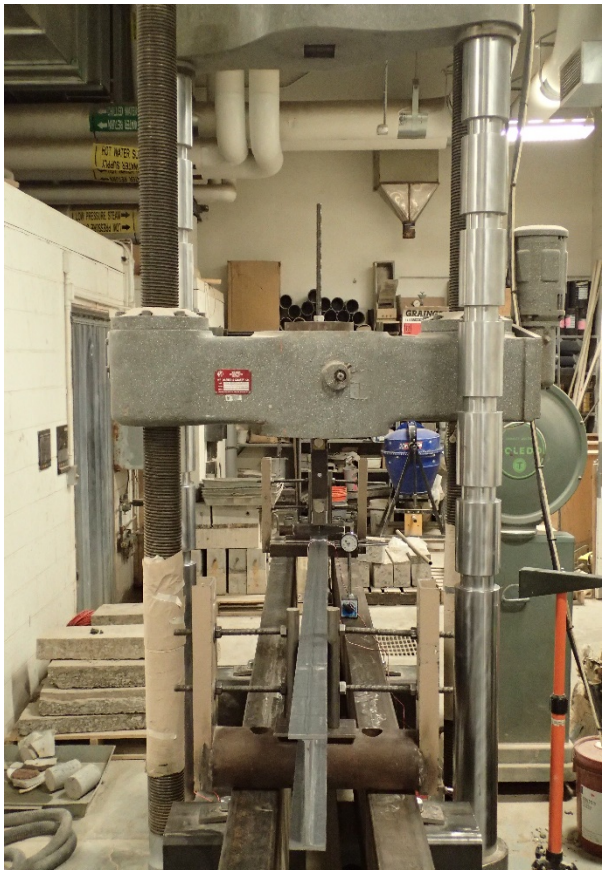	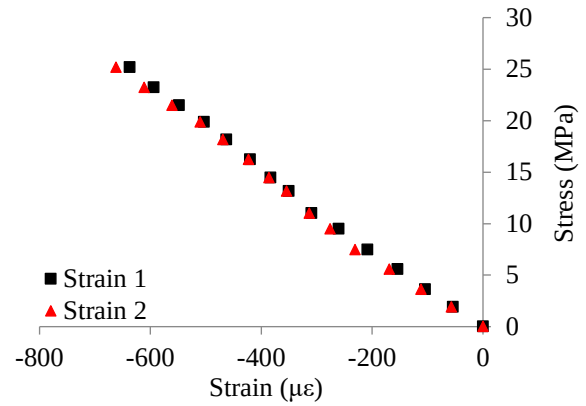	
	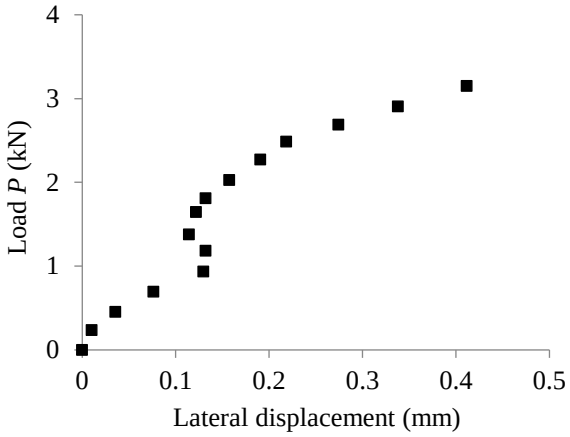	
M_{cr} = 976 Nm		

Specimen: LTB2	Span: 1829 mm	Date:2/11/2016
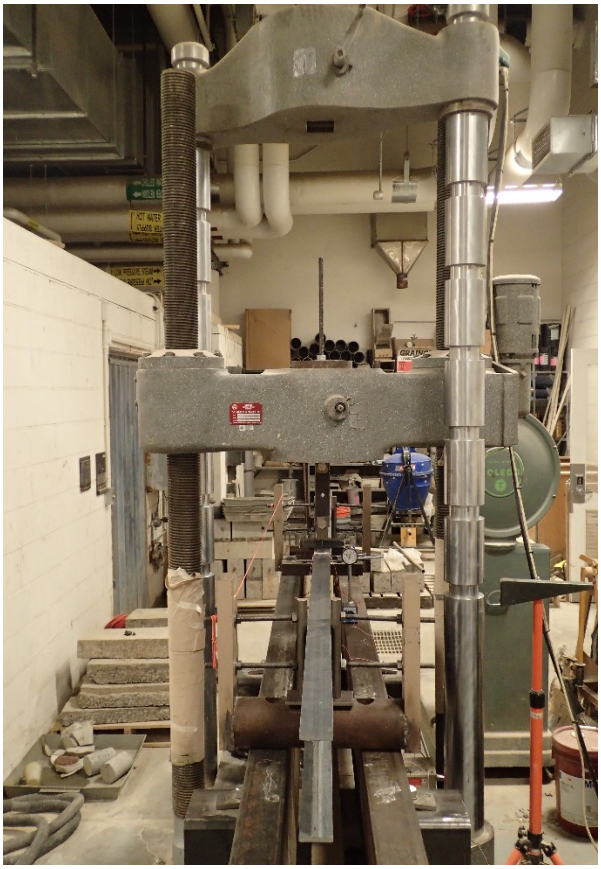	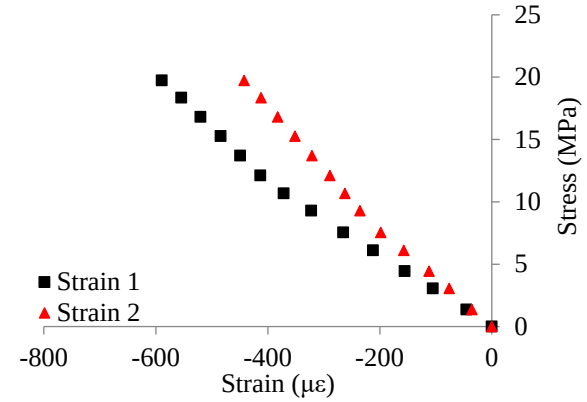 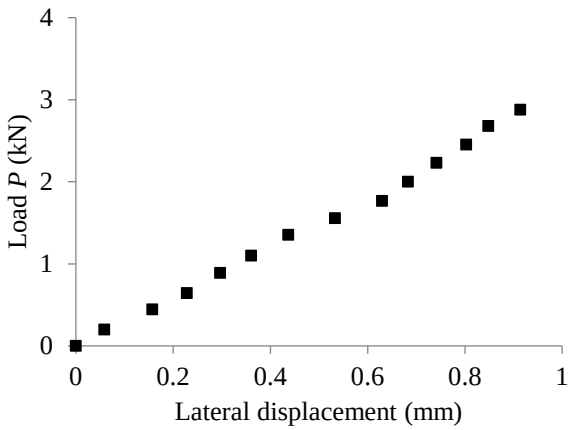	
M_{cr} = 815 Nm		

Specimen: LTB2	Span: 1829 mm	Date:2/11/2016
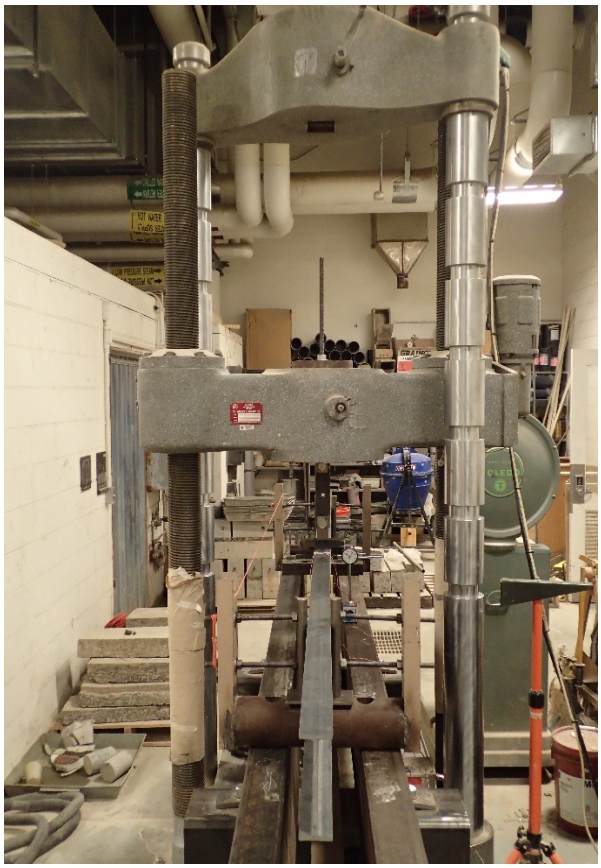	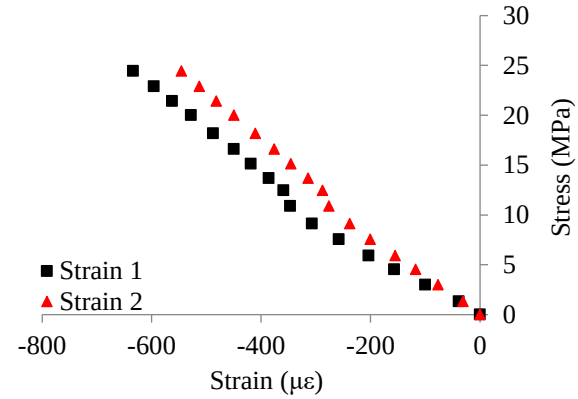	
	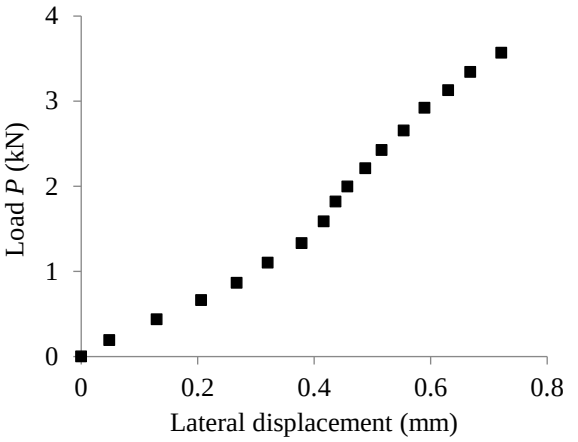	
M_{cr} = 919 Nm		

Specimen: LTB2	Span: 1829 mm	Date:2/11/2016
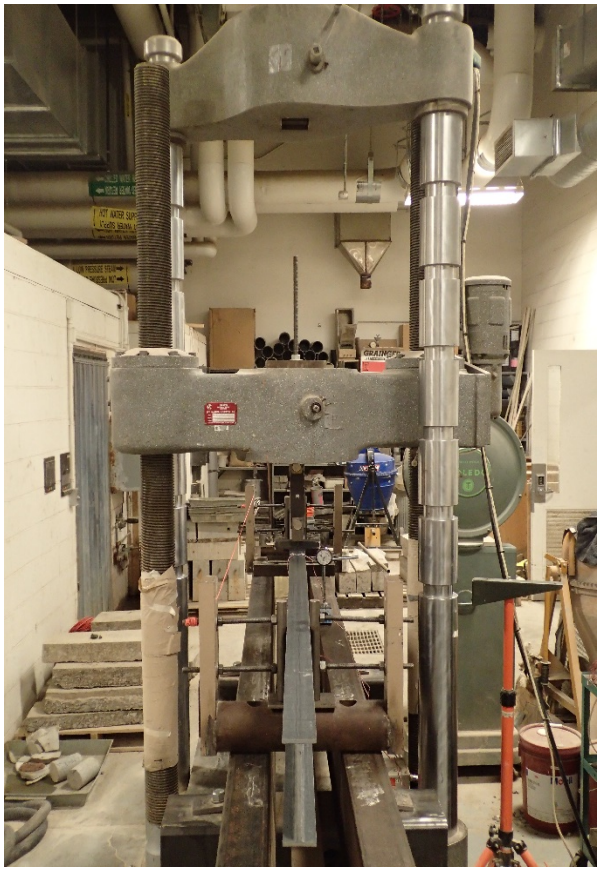	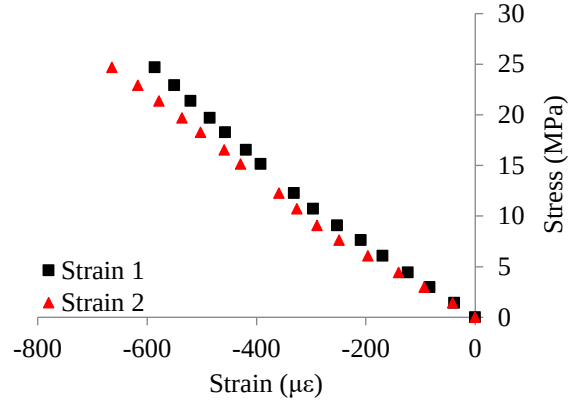	
	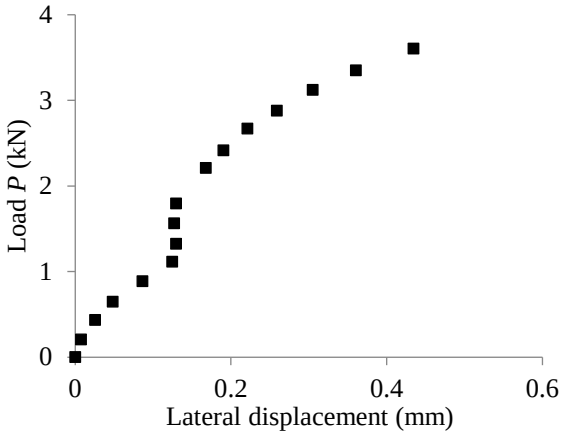	
M_{cr} = 826 Nm		

Specimen: LTB2	Span: 1829 mm	Date:3/17/2016
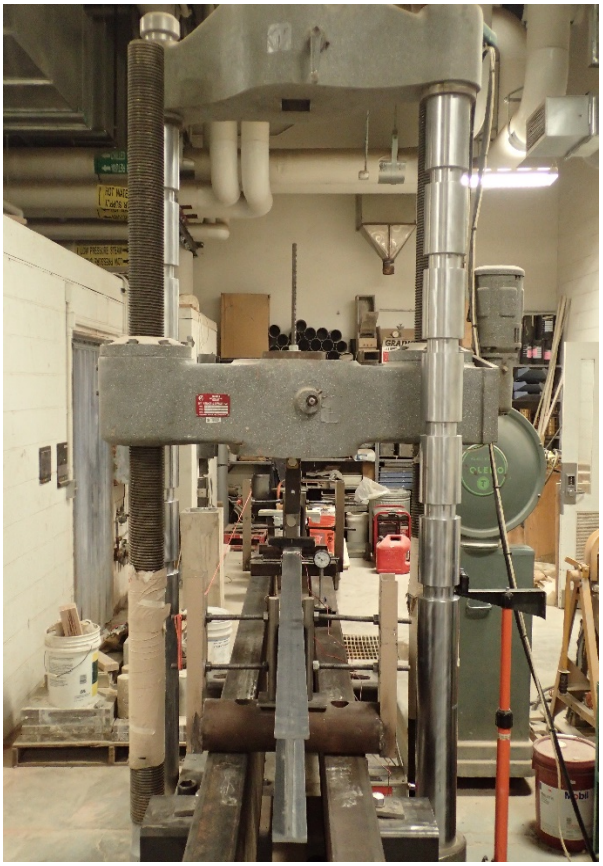	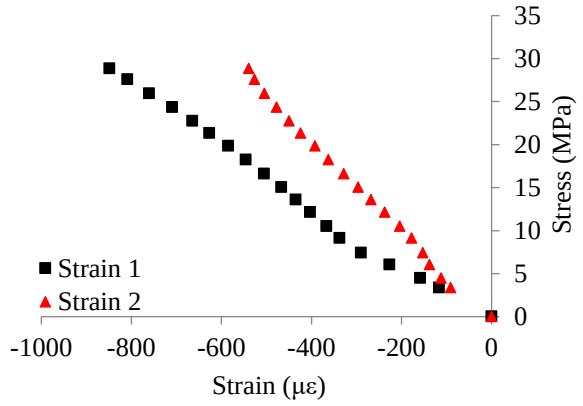	
	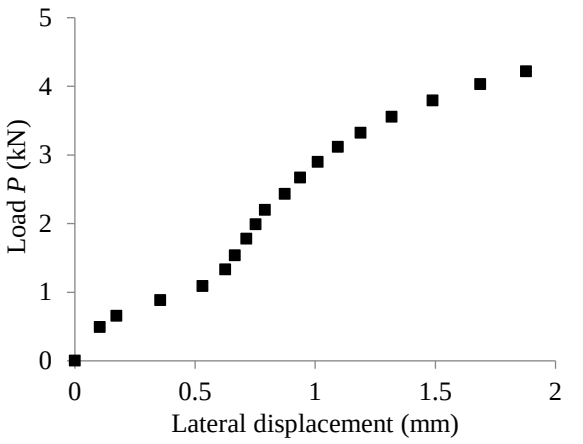	
M_{cr} = 1011 Nm		

Specimen: LTB2	Span: 1524 mm	Date:2/12/2016
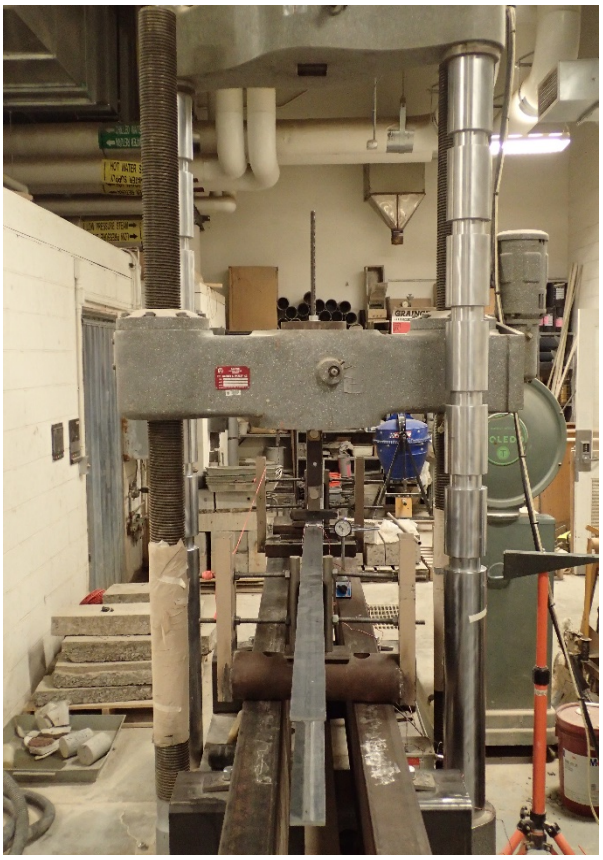	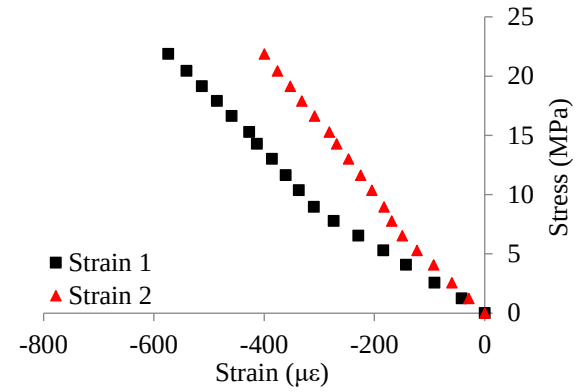 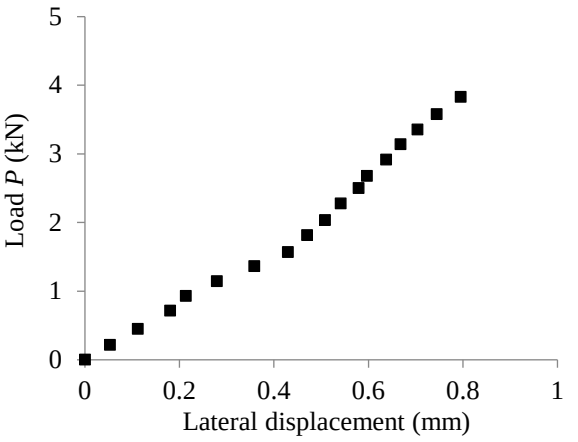	
M_{cr} = 1368 Nm		

Specimen: LTB2	Span: 1524 mm	Date:2/12/2016
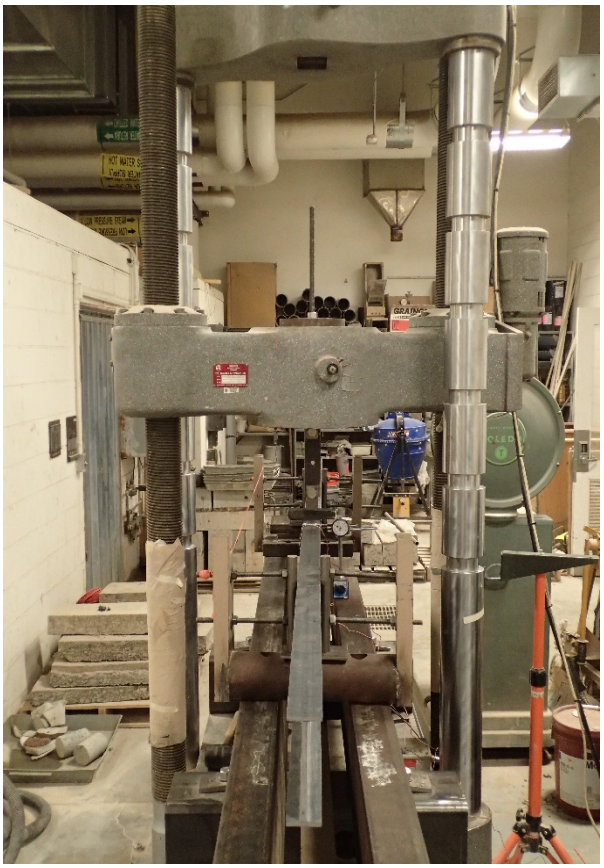	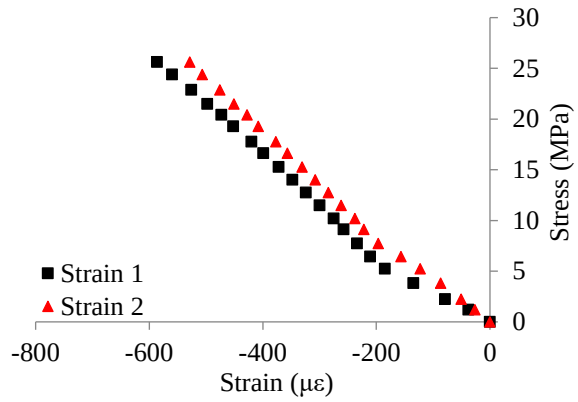 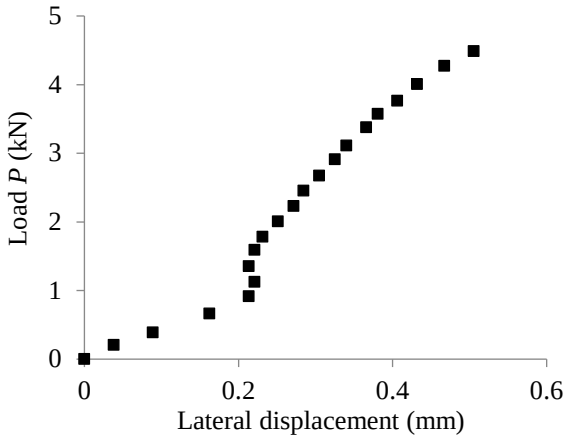	
M_{cr} = 1367 Nm		

Specimen: LTB2	Span: 1524 mm	Date:2/12/2016
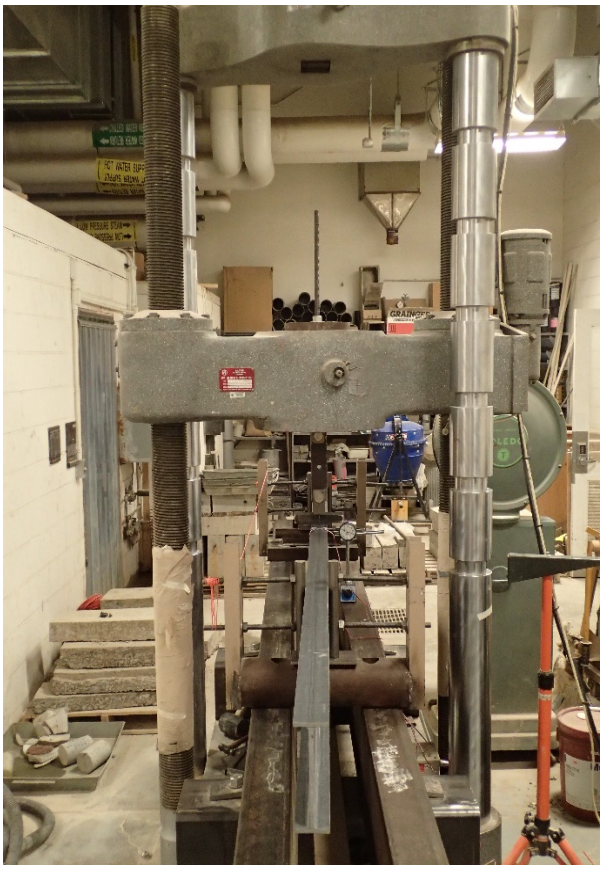	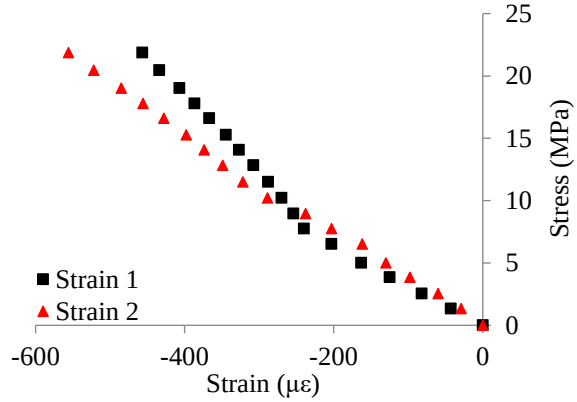 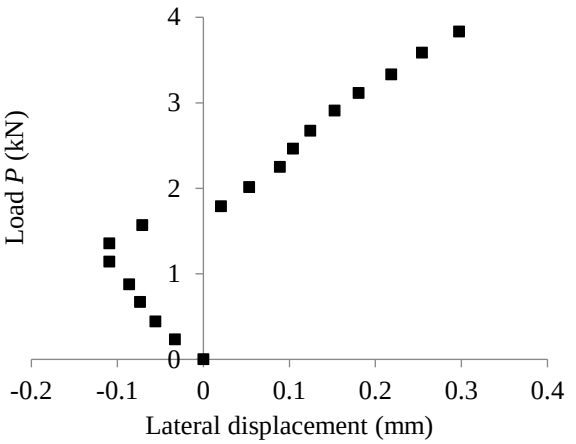	
M_{cr} = 1192 Nm		

Specimen: LTB2	Span: 1524 mm	Date:2/12/2016
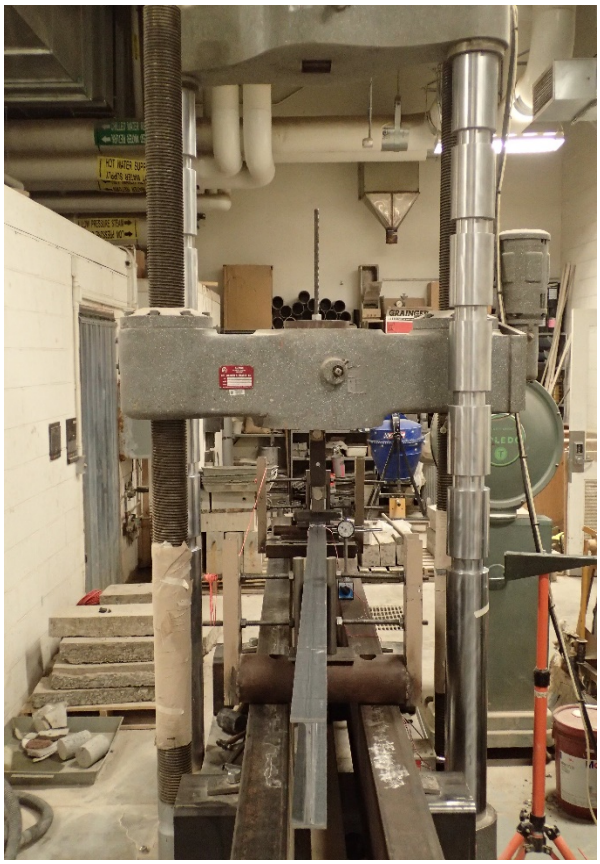	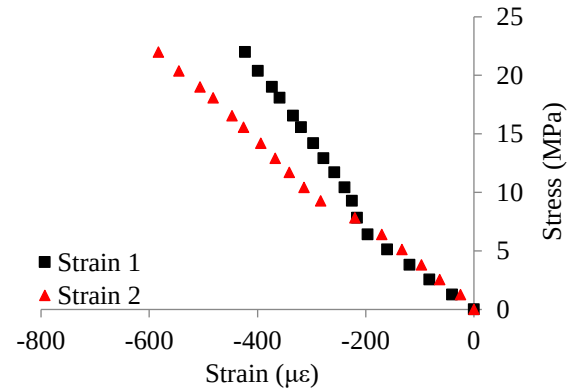 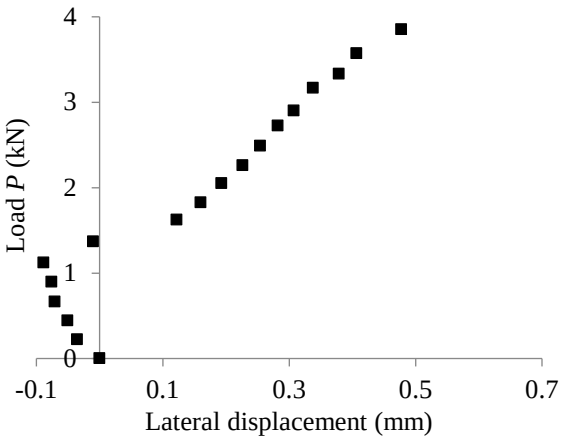	
M_{cr} = 1365 Nm		

APPENDIX B

FLEXURAL STIFFNESS PARAMETERS

The flexural stiffness parameters for a homogenous orthotropic plate are given as (Barbero 2011):

$$D_{11} = \frac{E_L t^3}{12(1 - v_{LT} v_{TL})} \tag{B.1}$$

$$D_{22} = \frac{E_T t^3}{12(1 - v_{LT} v_{TL})} \tag{B.2}$$

$$D_{12} = v_{LT} D_{22} \tag{B.3}$$

$$D_{66} = \frac{G_{LT} t^3}{12} \tag{B.4}$$

The minor Poisson's ratio, v_{TL}, can be calculated as (Barbero 2011):

$$v_{TL} = \frac{E_T}{E_L} v_{LT} \tag{B.5}$$

Axis notation is defined in Figure 1.6. Axis 1 is the longitudinal axis of the plate; that is the direction of pultrusion. Axis 2 is the transverse axis, perpendicular to the direction of pultrusion. Axis 6 is the plate through thickness direction.

APPENDIX C

KOLLÁR'S EQUATIONS

Kollár's equations provide "exact" solutions for the critical buckling stress of orthotropic plates subject to uniaxial compression; they are presented in Table C.1. Although Kollár (2003) presents more cases, only three cases are of interest in this study pertaining to flange local buckling (FLB). The outer edge of the flange is free while the flange-web interface is either: 1) simply-supported (SS); 2) fixed; and 3) rotationally restrained by springs (k is the spring constant).

Table C.1 Kollár's Equations for uniaxially compressed orthotropic plates with various boundary conditions (Kollár 2003)

Boundary conditions	Critical buckling stress, f_{cr}
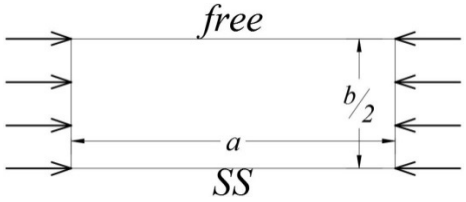	$\frac{12D_{66}}{t\left(\frac{b}{2}\right)^2}+\frac{\pi^2 D_{11}}{ta^2}$
	$\frac{\sqrt{D_{11}D_{22}}}{t\left(\frac{b}{2}\right)^2}\left[15.1K\sqrt{1-v}+7(1-K)\right] \quad when\ K\le 1$
	$\frac{\sqrt{D_{11}D_{22}}}{t\left(\frac{b}{2}\right)^2}\left[15.1\sqrt{1-v}+(K-1)6(1-v)\right]\ when\ K>1$
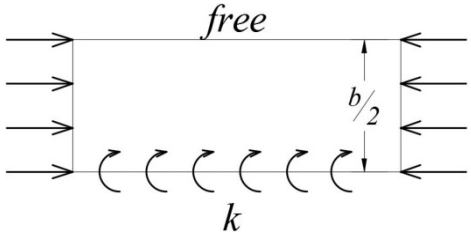	$\frac{\sqrt{D_{11}D_{22}}}{t\left(\frac{b}{2}\right)^2}\left\{K\left[15.1\eta\sqrt{1-v}+6(1-\eta)(1-v)\right]+\frac{7(1-K)}{\sqrt{1+4.12\zeta}}\right\}\ when\ K\le 1$
	$\frac{\sqrt{D_{11}D_{22}}}{t\left(\frac{b}{2}\right)^2}\left[15.1\eta\sqrt{1-v}+6(K-\eta)(1-v)\right]$ $when\ K>1$
Flexural stiffness parameters D_{ij} are given in Appendix B, and: $K=(2D_{66}+D_{12})/\sqrt{D_{11}D_{22}}$ $v=D_{12}/(2D_{66}+D_{12})$ $\zeta=D_{22}/(kb/2)$ $\zeta'=D_{22}(\frac{b}{2})/(GI_t)$ $\eta=1/\sqrt{1+(7.22-3.55v)\zeta}$	

APPENDIX D

FLB FORMULA SIMPLIFICATIONS

As described in Chapter 5, the critical FLB buckling stress is found by substituting Eq. 5.14 into Eq. 5.4. The complete expression for critical FLB buckling stress, f_{cr}, is given as:

$$f_{cr} = \frac{60L_{cr}^4\left(\frac{b}{2}\right)k^2D_{22}}{L_{cr}^2\left(\frac{b}{2}\right)^3\pi^2t\left(20D_{22}^2 + 15D_{22}\left(\frac{b}{2}\right)k + 3\left(\frac{b}{2}\right)^2k^2\right)} + \frac{80L_{cr}^2D_{66}\left(\frac{b}{2}\right)\pi^2\left(3D_{22}^2 + 3D_{22}\left(\frac{b}{2}\right)k + \left(\frac{b}{2}\right)^2k^2\right)}{L_{cr}^2\left(\frac{b}{2}\right)^3\pi^2t\left(20D_{22}^2 + 15D_{22}\left(\frac{b}{2}\right)k + 3\left(\frac{b}{2}\right)^2k^2\right)} + \frac{D_{11}\left(\frac{b}{2}\right)^3\pi^4\left(20D_{22}^2 + 15D_{22}\left(\frac{b}{2}\right)k + 3\left(\frac{b}{2}\right)^2k^2\right)}{L_{cr}^2\left(\frac{b}{2}\right)^3\pi^2t\left(20D_{22}^2 + 15D_{22}\left(\frac{b}{2}\right)k + 3\left(\frac{b}{2}\right)^2k^2\right)} - \frac{20L_{cr}^2D_{12}\left(\frac{b}{2}\right)^2\pi^2k\left(3D_{22} + \left(\frac{b}{2}\right)k\right)}{L_{cr}^2\left(\frac{b}{2}\right)^3\pi^2t\left(20D_{22}^2 + 15D_{22}\left(\frac{b}{2}\right)k + 3\left(\frac{b}{2}\right)^2k^2\right)} \quad (D.1)$$

Where L_{cr} is the critical half wave length for FLB given by Eq. 5.14; b is the width of flange; k is the elastic spring constant; t is the thickness of flange and web; and D_{ij} are the flexural stiffness

parameters of flange plate. The second term in Eq. D.1 can be simplified through a numerical study:

$$\frac{80L_{cr}^2 D_{66}\left(\frac{b}{2}\right)\pi^2\left(3D_{22}^2 + 3D_{22}\left(\frac{b}{2}\right)k + \left(\frac{b}{2}\right)^2 k^2\right)}{L_{cr}^2\left(\frac{b}{2}\right)^3\pi^2 t\left(20D_{22}^2 + 15D_{22}\left(\frac{b}{2}\right)k + 3\left(\frac{b}{2}\right)^2 k^2\right)}$$

$$= \frac{80D_{66}\left(3D_{22}^2 + 3D_{22}\left(\frac{b}{2}\right)k + \left(\frac{b}{2}\right)^2 k^2\right)}{t\left(\frac{b}{2}\right)^2\left(20D_{22}^2 + 15D_{22}\left(\frac{b}{2}\right)k + 3\left(\frac{b}{2}\right)^2 k^2\right)} \approx \frac{80D_{66}}{t\left(\frac{b}{2}\right)^2}\left(\frac{1}{5}\right) = \frac{16D_{66}}{t\left(\frac{b}{2}\right)^2} \quad (D.2)$$

Moreover, the third term can be simplified as:

$$\frac{D_{11}\left(\frac{b}{2}\right)^3\pi^4\left(20D_{22}^2 + 15D_{22}\left(\frac{b}{2}\right)k + 3\left(\frac{b}{2}\right)^2 k^2\right)}{L_{cr}^2\left(\frac{b}{2}\right)^3\pi^2 t\left(20D_{22}^2 + 15D_{22}\left(\frac{b}{2}\right)k + 3\left(\frac{b}{2}\right)^2 k^2\right)}$$

$$= \frac{D_{11}\pi^2\left(20D_{22}^2 + 15D_{22}\left(\frac{b}{2}\right)k + 3\left(\frac{b}{2}\right)^2 k^2\right)}{L_{cr}^2 t\left(20D_{22}^2 + 15D_{22}\left(\frac{b}{2}\right)k + 3\left(\frac{b}{2}\right)^2 k^2\right)} = \frac{D_{11}\pi^2}{tL_{cr}^2} \quad (D.3)$$

Additionally, the fourth term can be simplified through a numerical study:

$$-\frac{20L_{cr}^2 D_{12}\left(\frac{b}{2}\right)^2\pi^2 k\left(3D_{22} + \left(\frac{b}{2}\right)k\right)}{L_{cr}^2\left(\frac{b}{2}\right)^3\pi^2 t\left(20D_{22}^2 + 15D_{22}\left(\frac{b}{2}\right)k + 3\left(\frac{b}{2}\right)^2 k^2\right)}$$

$$= -\frac{20D_{12}k\left(3D_{22} + \left(\frac{b}{2}\right)k\right)}{\left(\frac{b}{2}\right)t\left(20D_{22}^2 + 15D_{22}\left(\frac{b}{2}\right)k + 3\left(\frac{b}{2}\right)^2 k^2\right)}$$

$$= -\frac{20D_{12}k}{t\left(\frac{b}{2}\right)}\frac{\left(3D_{22}^2 + \left(\frac{b}{2}\right)kD_{22}\right)}{D_{22}\left(20D_{22}^2 + 15D_{22}\left(\frac{b}{2}\right)k + 3\left(\frac{b}{2}\right)^2 k^2\right)}$$

$$= -\frac{20D_{12}k}{t\left(\frac{b}{2}\right)} \frac{\left(\left(\frac{3}{\left(\frac{b}{2}\right)^2 k^2}\right) D_{22}^2 + \frac{D_{22}}{\left(\frac{b}{2}\right)k}\right)}{3D_{22}\left(\left(\frac{6.67}{\left(\frac{b}{2}\right)^2 k^2}\right) D_{22}^2 + \frac{5D_{22}}{\left(\frac{b}{2}\right)k} + 1\right)}$$

$$= -\frac{20D_{12}k}{t\left(\frac{b}{2}\right)} \frac{\left(\left(\frac{3}{\left(\frac{b}{2}\right)^2 k^2}\right) D_{22}^2 + \frac{D_{22}}{\left(\frac{b}{2}\right)k}\right)}{3D_{22}\left(\left(\frac{6.67}{\left(\frac{b}{2}\right)^2 k^2}\right) D_{22}^2 + \frac{5D_{22}}{\left(\frac{b}{2}\right)k}\right)}$$

$$\approx -\frac{20D_{12}k}{t\left(\frac{b}{2}\right)}\left(\frac{1}{3D_{22}}\right)\left(\frac{1}{3}\right) = -\frac{20D_{22}v_{LT}k}{t\left(\frac{b}{2}\right)}\left(\frac{1}{3D_{22}}\right)\left(\frac{1}{3}\right)$$

$$= -\frac{2(10v_{LT})k}{3(3)t\left(\frac{b}{2}\right)} \qquad (D.4)$$

According to the material properties reported in the available literature as well as the material properties reported in this work, v_{LT} falls into the range of 0.23 — 0.37. Thus, ($10v_{LT}/3$) can be estimated as 0.77 – 1.23. Taking ($10v_{LT}/3$) as 1.00 (i.e., v_{LT} = 0.3), Eq. D.4 can be further simplified as:

$$-\frac{2(10v_{LT})k}{3(3)t\left(\frac{b}{2}\right)} = -\frac{2k}{3t\left(\frac{b}{2}\right)} \qquad (D.5)$$

In conclusion, the critical FLB stress, f_{cr}, can be simplified as Eq. D.6 and Eq. 5.15:

$$f_{cr} = \frac{60L_{cr}^2 k^2 D_{22}}{t\left(\frac{b}{2}\right)^2 \pi^2 \left(20D_{22}^2 + 15D_{22}\left(\frac{b}{2}\right)k + 3\left(\frac{b}{2}\right)^2 k^2\right)} + \frac{16D_{66}}{t\left(\frac{b}{2}\right)^2} + \frac{D_{11}\pi^2}{tL_{cr}^2} - \frac{2k}{3t\left(\frac{b}{2}\right)} \quad (D.6)$$

In order to compare the simplified (Eq. D.6) and nonsimplified (Eq. D.1) critical FLB stresses, a numerical study was conducted. 38 section geometries having *b/d* and *b/2t* ranging from 0.3 to 1.0 and 2.7 to 16.0, respectively, were used. Material properties were taken as those measured in the present study (Table 3.3). The simplified and nonsimplified critical FLB moments were calculated, as presented in Figure D.1. It can be seen that for sections having *b/d* ranging from 0.7 to 1.0, the simplified M_{cr} is marginally conservative when compared with nonsimplified M_{cr}; and for sections having *b/d* in the ranges of 0.6 – 0.7, 0.5 – 0.6 and 0.3 – 0.5, simplified M_{cr} (Eq. D.6) is marginally unconservative, overestimating Eq. D.1 by 3%, 7% and 15%. These results are considered acceptable since for most pultruded I-shapes *d/b* = 1 and no presently manufactured sections are known for which *d/b* < 0.5.

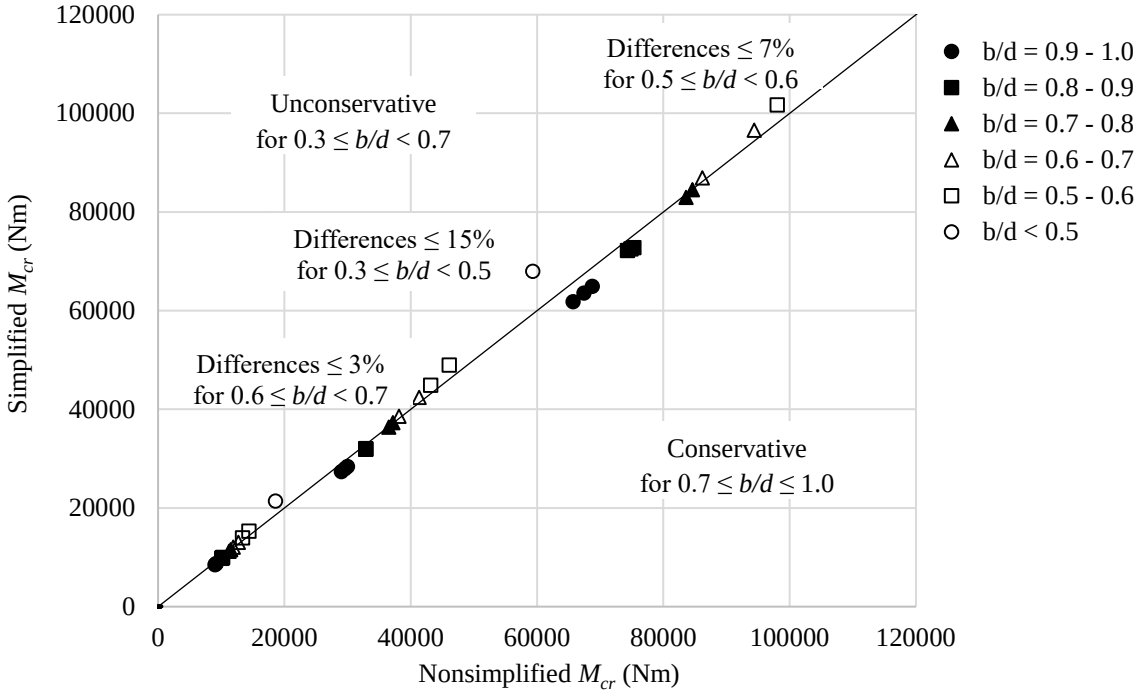

Figure D.1 Simplified- versus nonsimplified-critical FLB moments

BIBLIOGRAPHY

[1] Adams, D. F. (2005). A comparison of shear test methods. *High-Perform. Compos*, 9-10.

[2] Adams, D. F., Carlsson, L. A., & Pipes, R. B. (2003). *Experimental characterization of advanced composite materials (third edition)*. CRC press.

[3] Adams, D. F. (2002). Tabbed Versus Untabbed Fiber-Reinforced Composite Compression Specimens. In *Composite Materials: Testing, Design, and Acceptance Criteria*. ASTM International.

[4] Adams, D. F., & Lewis, E. Q. (1997). Experimental assessment of four composite material shear test methods. *Journal of Testing and Evaluation*, 25(2), 174-181.

[5] Adams, D. F., & Welsh, J. S. (1997). The Wyoming combined loading compression (CLC) test method. *Journal of Composites, Technology and Research*, 19(3), 123-133.

[6] Adams, D. F., & Xie, M. (1995). Effect of specimen tab configuration on compression testing of composite materials. Journal of Composites, Technology and Research, 17(2), 77-83.

[7] Adams, D. F., & Walrath, D. E. (1987). Further development of the losipescu shear test method. *Experimental Mechanics*, 27(2), 113-119.

[8] Adams, D. F., & Walrath, D. E. (1982). Iosipescu shear properties of SMC composite materials. *Composite Materials: Testing and Design (6th Conference)*. ASTM STP 787, 19-33.

[9] Ádány, S., & Schafer, B. W. (2008). A full modal decomposition of thin-walled, single-branched open cross-section members via the constrained finite strip method. *Journal of Constructional Steel Research*, 64(1), 12-29.

[10] American Institute of Steel Construction. (AISC). (2011). *Steel construction manual*. 14th edition, American Institute of Steel Construction.

[11] American Society of Civil Engineers. (ASCE). (2017). *Design Standard for Load & Resistance Factor Design (LRFD) of Pultruded Fiber Reinforced Polymer (FRP) Structures*. draft version available to Prof. Harries

[12] American Society of Civil Engineers. (ASCE). (2010). *Pre-Standard for Load and Resistance Factor Design (LRFD) of Pultruded Fiber Reinforced Polymer (FRP) Structures*.

[13] American Society of Civil Engineers. (ASCE). (1984). *Structural Plastics Design Manual*. American Society of Civil Engineers manuals and reports on engineering practice, No.63, ASCE, New York.

[14] Ascione L, Caron J F, Godonou P, van IJselmuijden K, Knippers J, Mottram T, Oppe M, Gantriis Sorensen M, Taby J, Tromp, L. (2016). *Prospect for new guidance in the design of FRP*; EUR 27666.

[15] Ascione, L., Berardi, V. P., Giordano, A., & Spadea, S. (2013). Local buckling behavior of FRP thin-walled beams: a mechanical model. *Composite Structures*, 98, 111-120.

[16] Ascione, L., Giordano, A., & Spadea, S. (2011). Lateral buckling of pultruded FRP beams. *Composites Part B: Engineering*, 42(4), 819-824.

[17] ASTM Standard D3171-15 (2015). *Standard Test Methods for Constituent Content of Composite Materials*, ASTM International, West Conshohocken, PA.

[18] ASTM Standard D4255/D4255M-15a (2015). *Standard Test Method for In-Plane Shear Properties of Polymer Matrix Composite Materials by the Rail Shear Method*, ASTM International, West Conshohocken, PA.

[19] ASTM Standard D695-15 (2015). *Standard Test Method for Compressive Properties of Rigid Plastics*, ASTM International, West Conshohocken, PA.

[20] ASTM Standard D3039/D3039M-14 (2014). *Standard Test Method for Tensile Properties of Polymer Matrix Composite Materials*. ASTM International, West Conshohocken, PA.

[21] ASTM Standard D638-14 (2014). *Standard Test Method for Tensile Properties of Plastics*, ASTM International, West Conshohocken, PA.

[22] ASTM Standard D6641/D6641M-14 (2014). *Standard Test Method for Compressive Properties of Polymer Matrix Composite Materials Using a Combined Loading Compression (CLC) Test Fixture*, ASTM International, West Conshohocken, PA.

[23] ASTM Standard D2344/D2344M-13 (2013). *Standard Test Method for Short-Beam Strength of Polymer Matrix Composite Materials and Their Laminates*, ASTM International, West Conshohocken, PA.

[24] ASTM Standard D3518/D3518M-13 (2013). *Standard Test Method for In-Plane Shear Response of Polymer Matrix Composite Materials by Tensile Test of a±45° Laminate*. ASTM International, West Conshohocken, PA.

[25] ASTM Standard D7078/D7078M-12 (2012). *Standard Test Method for Shear Properties of Composite Materials by V-Notched Rail Shear Method, ASTM International*, West Conshohocken, PA.

[26] ASTM Standard D5379/D5379M-12 (2012). *Standard Test Method for Shear Properties of Composite Materials by the V-Notched Beam Method*, ASTM International, West Conshohocken, PA.

[27] ASTM Standard D2584-11 (2011). *Standard Test Method for Ignition Loss of Cured Reinforced Resins*, ASTM International, West Conshohocken, PA.

[28] ASTM Standard D3044-94 (2011). *Standard Test Method for Shear Modulus of Wood-Based Structural Panels*, ASTM International, West Conshohocken, PA.

[29] ASTM Standard D5467/D5467M-97(2010). *Standard Test Method for Compressive Properties of Unidirectional Polymer Matrix Composites Using a Sandwich Beam*, ASTM International, West Conshohocken, PA.

[30] ASTM Standard D3410/D3410M-03 (Reapproved 2008). *Standard Test Method for Compressive Properties of Polymer Matrix Composite Materials with Unsupported Gage Section by Shear Loading*. ASTM International, West Conshohocken, PA.

[31] Azizian, Z. G., & Dawe, D. J. (1985). Geometrically nonlinear analysis of rectangular Mindlin plates using the finite strip method. *Computers & structures*, 21(3), 423-436.

[32] Bakis, C., Bank, L. C., Brown, V., Cosenza, E., Davalos, J. F., Lesko, J. J., ... & Triantafillou, T. C. (2002). Fiber-reinforced polymer composites for construction-state-of-the-art review. *ASCE Journal of Composites for Construction*, 6(2), 73-87.

[33] Bank, L. C. (2006). Application of FRP Composites to Bridges in the USA. In Japan Society of Civil Engineers (JSCE), *Proceedings of the International Colloquium on Application of FRP to Bridges*, 9-16.

[34] Bank, L. C., Gentry, T. R., & Nadipelli, M. (1996). Local buckling of pultruded FRP beams-analysis and design. *Journal of reinforced plastics and composites*, 15(3), 283-294.

[35] Bank, L. C., Yin, J., & Nadipelli, M. (1995). Local buckling of pultruded beams—nonlinearity, anisotropy and inhomogeneity. *Construction and Building Materials*, 9(6), 325-331.

[36] Bank, L. C. (1990). Shear properties of pultruded glass FRP materials. *Journal of Materials in Civil Engineering*, 2(2), 118-122.

[37] Bank, L. C. (1989). Flexural and shear moduli of full-section fiber reinforced plastic (FRP) pultruded beams. *Journal of Testing and Evaluation*, 17(1), 40-45.

[38] Barbero, E. J. (2011). *Introduction to composite materials design* (second edition). CRC press.

[39] Barbero, E. J., & DeVivo, L. (1999). Beam-column design equations for wide-flange pultruded structural shapes. *ASCE Journal of Composites for Construction*, 3(4), 185-191.

[40] Barbero, E. J., Makkapati, S., & Tomblin, J. S. (1999). Experimental determination of the compressive strength of pultruded structural shapes. *Composites Science and Technology*, 59(13), 2047-2054.

[41] Barbero, E. J., & Raftoyiannis, I. G. (1994). Lateral and distortional buckling of pultruded I-beams. *Composite Structures*, 27(3), 261-268.

[42] Barbero, E., & Tomblin, J. (1994). A phenomenological design equation for FRP columns with interaction between local and global buckling. *Thin-Walled Structures*, 18(2), 117-131.

[43] Barbero, E. J., & Raftoyiannis, I. G. (1993). Local buckling of FRP beams and columns. *ASCE Journal of Materials in Civil Engineering*, 5(3), 339-355.

[44] Barbero, E. J., Tomblin, J., & Ritchey, R. (1992). Local buckling of FRP structural shapes. *In Proceedings of the forty-seventh Annual Conference, Composites Institute*. London: The Society of Plastic Industry, 1992:1-7 Session 15-E.

[45] Barbero, E. J., Fu, S. H., & Raftoyiannis, I. (1991). Ultimate bending strength of composite beams. *ASCE Journal of Materials in Civil Engineering*, 3(4), 292-306.

[46] Bažant, Z. P., & Cedolin, L. (2010). *Stability of structures: elastic, inelastic, fracture and damage theories*. World Scientific.

[47] Bedford Reinforced Plastics. (2015). *FRP Farm Buildings*. Retrieved from: http://bedfordreinforced.com/markets/agriculture/ (Sep 30, 2015)

[48] Bedford Reinforced Plastics. (2012). *Bedford Reinforced Plastics Inc. Design Guide*. Retrieved from: http://bedfordreinforced.com/resources/?box=design (Sep 13, 2015)

[49] Bleich, F. (1952). *Buckling strength of metal structures*. McGraw-Hill.

[50] Bogetti, T. A., Gillespie, J. W., & Pipes, R. B. (1988). Evaluation of the IITRI compression test method for stiffness and strength determination. *Composites Science and Technology*, 32(1), 57-76.

[51] Bradford, M. A., & Waters, S. W. (1988). Distortional instability of fabricated monosymmetric I-beams. *Computers & Structures*, 29(4), 715-724.

[52] Brooks, R. J., & Turvey, G. J. (1995). Lateral buckling of pultruded GRP I-section cantilevers. *Composite Structures*, 32(1), 203-215.

[53] Butz, T. M. (1997). *Tests on pultruded square tubes under eccentric axial load*. Master Thesis, Georgia Institute of Technology, Atlanta, GA.

[54] Cardoso, D. (2014) *Compressive Strength of Pultruded Glass-Fiber Reinforced Polymer (GFRP) Columns*, PhD Dissertation, Federal University of Rio De Janeiro.

[55] Cardoso, D. C., Harries, K. A., & Batista, E. D. M. (2014a). Compressive local buckling of pultruded GFRP I-sections: development and numerical/experimental evaluation of an explicit equation. *Journal of Composites for Construction*, 19(2), 04014042.

[56] Cardoso, D., Harries, K., & Batista, E. (2014b). On the Determination of Mechanical Properties for Pultruded GFRP Sections. In *Proceedings of the 7th International Conference on FRP composites in Civil Engineering*. Vancouver, Canada: International Institute for FRP in Construction.

[57] Chaterjee, S., Adams, D., & Oplinger, D. W. (1993). *Test Methods for Composites, a Status Report. Volume III: Shear Test Methods*, US Department of Transport, Federal Aviation Administration, Report DOT/FAA/CT-93/17, III, National Technical Information Service, Springfield, VA 22161, USA.

[58] Cheung, M. S., Akhras, G., & Li, W. (1993). Stability analysis of anisotropic laminated composite plates by finite strip method. *Computers & structures*, 49(6), 963-967.

[59] Cheung, M. S., & Chan, M. Y. T. (1981). Static and dynamic analysis of thin and thick sectorial plates by the finite strip method. *Computers & Structures*, 14(1), 79-88.

[60] Cheung, Y. K. (1976). *Finite Strip Method in Structural Analysis*. Pergamon Press, New York, NY.

[61] Composite Advantage (CA 2015). *FiberSPAN pedestrian truss bridges*, Wolf Trap, Virginia. Retrieved from http://www.compositeadvantage.com/gallery/pedestrian-deck-wolf-trap-virginia (Sep 13, 2015)

[62] Correia, J. R., Branco, F. A., Silva, N. M. F., Camotim, D., & Silvestre, N. (2011). First-order, buckling and post-buckling behaviour of GFRP pultruded beams. Part 1: Experimental study. *Computers & Structures*, 89(21), 2052-2064.

[63] Creative Pultrusions. (2015a). *Creative Pultrusions 101*. Retrieved from: http://www.creativepultrusions.com/index.cfm/why-cp/creative-pultrusions-101/ (Sep 30th 2015)

[64] Creative Pultrusions. (2015b). *The new and improved Pultex pultrusion design manual of standard and custom fiber reinforced polymer structural profiles*, 2004 Edition, Vol. 5, Rev. 1. Alum Bank: Creative Pultrusions. Inc., Alum Bank, PA.

[65] Cunningham, D., and Harries, K.A. (2015), Open Hole Tension Capacity of Pultruded GFRP Plate Having Staggered Hole Arrangement, *Proceedings of Advanced Composites in Construction (ACIC2015)*, Cambridge, UK, September 2015

[66] Davalos, J. F., Qiao, P., & Salim, H. A. (1997). Flexural-torsional buckling of pultruded fiber reinforced plastic composite I-beams: experimental and analytical evaluations. *Composite Structures*, 38(1), 241-250.

[67] Davalos, J. F., & Qiao, P. (1997). Analytical and experimental study of lateral and distortional buckling of FRP wide-flange beams. *ASCE Journal of Composites for Construction*, 1(4), 150-159.

[68] Fastec (2015). Retrieved from: http://www.fastecinternational.com/products/pultruded-shapes/ (Sep 30 2015)

[69] Geschwindner, L. F. (2008). *Unified design of steel structures*. Wiley.

[70] Gibson, R. F. (2011). *Principles of Composite Material Mechanics*. CRC press.

[71] Godoy, L. A., Barbero, E. J., & Raftoyiannis, I. (1995). Interactive buckling analysis of fiber-reinforced thin-walled columns. *Journal of Composite Materials*, 29(5), 591-613.

[72] Gurdal, Z., & Starbuck, J. M. (1988). Compressive characterization of unidirectional composite materials. *Analytical and Testing Methodologies for Design with Advanced Materials*, 337-347.

[73] Hai, N. D., Mutsuyoshi, H., Asamoto, S., & Matsui, T. (2010). Structural behavior of hybrid FRP composite I-beam. *Construction and Building Materials*, 24(6), 956-969.

[74] Hancock, G. J., Bradford, M. A., & Trahair, N. S. (1980). Web distortion and flexural torsional buckling. *Journal of the Structural Division*, 106(ST7).

[75] Herakovich, C. T. (1998). *Mechanics of Fibrous Composites* (p. 26). New York: Wiley.

[76] Hodgkinson, J. M. (Ed.). (2000). *Mechanical testing of advanced fibre composites*. Elsevier.

[77] Hofer, K. E., & Rao, P. N. (1977). A new static compression fixture for advanced composite materials. *Journal of Testing and Evaluation*, 5(4), 278-283.

[78] Hull, D., & Clyne, T. W. (1996). *An Introduction to Composite Materials*. Cambridge University Press.

[79] Hyer, M. W. (2009). *Stress Analysis of Fiber-Reinforced Composite Materials*. DEStech Publications, Inc.

[80] Insausti, A., Puente, I., & Azkune, M. (2009). Interaction between local and lateral buckling on pultruded I-beams. *ASCE Journal of Composites for Construction*, 13(4), 315-324.

[81] Iosipescu, N. (1967). New accurate procedure for single shear testing of metals. *J MATER*, 2(3), 537-566.

[82] Johnson, E. T., & Shield, C. K. (1998). Lateral-torsional buckling of composite beams. *Second International Conference on Composites in Infrastructure* (Vol. 2, 275-288).

[83] Kabir, M. Z., & Sherbourne, A. N. (1998). Lateral-torsional buckling of post-local buckled fibrous composite beams. *Journal of Engineering Mechanics*, 124(7), 754-764.

[84] Kang, J. O. (2001). *Fiber reinforced polymeric pultruded members subjected to sustained loads*. Ph.D. Thesis, Georgia Institute of Technology, Atlanta, GA.

[85] Kong, J., & Cheung, Y. K. (1993). Application of the spline finite strip to the analysis of shear-deformable plates. *Computers & structures*, 46(6), 985-988.

[86] Kollár, L. P., Sapkás, Á., & Tarján, G. (2010). Stability analysis of long composite plates with restrained edges subjected to shear and linearly varying loads. *Journal of Reinforced Plastics and Composites*. 29(9), pp 1386-1398.

[87] Kollár, L. P. (2003). Local buckling of fiber reinforced plastic composite structural members with open and closed cross sections. *ASCE Journal of Structural Engineering*, 129(11), 1503-1513.

[88] Lane A., & Mottram J. T. (2002), The influence of modal coupling upon the buckling of concentrically PFRP columns, Institute of Mechanical Engineers Part L: *Journal of Material and Design Application*, 216(12), pp. 133–144.

[89] Lee, J., Kim, S. E., & Hong, K. (2002). Lateral buckling of I-section composite beams. *Engineering Structures*, 24(7), 955-964.

[90] Lee, S., & Munro, M. (1984). *In-Plane Shear Properties of Graphite Fiber/Epoxy Composites for Aerospace Applications: Evaluation of Test Methods by the Decision Analysis Technique*. Aeronautical Note NAE-AS22, NRC No.23778, Mechanical Engineering Department, University of Ottawa, Ottawa, Canada.

[91] Leissa, A. W. (1985). *Buckling of laminated composite plates and shell panels* (No. OSURF-762513/713464). Ohio State University Research Foundation Columbus.

[92] Li, Z., & Schafer, B.W. (2010) "Buckling analysis of cold-formed steel members with general boundary conditions using CUFSM: conventional and constrained finite strip methods." *Proceedings of the 20th Int;l. Spec. Conf. on Cold-Formed Steel Structures*, St. Louis, MO. November, 2010.

[93] Li, W. Y., Cheung, Y. K., & Tham, L. G. (1986). Spline finite strip analysis of general plates. *Journal of Engineering Mechanics*, 112(1), 43-54.

[94] Liu, T. Q., Cardoso, D., Vieira, J. and Harries, K.A. (2017) Convenient and Inexpensive Test Methods for Pultruded GFRP Composite Material, *Proceedings of Advanced Composites in Construction* (ACIC2017), Sheffield, September 2017

[95] Lin, Z. M., Polyzois, D., & Shah, A. (1996). Stability of thin-walled pultruded structural members by the finite element method. *Thin-Walled Structures*, 24(1), 1-18.

[96] Mallick, P. K. (2008). *Fiber-reinforced composites: materials, manufacturing, and design* (third edition). CRC press.

[97] Maji, A. K., Acree, R., Satpathi, D., & Donnelly, K. (1997). Evaluation of pultruded FRP composites for structural applications. *ASCE Journal of materials in civil engineering*, 9(3), 154-158.

[98] Midwest Cooling Towers (2015). Retrieved from: http://midwesttowers.com/cooling-towers/ (Sep 29 2015)

[99] Mockry, E. F. (2001). *Pultruded FRP structural assembly for water cooling towers*. U.S. Patent No. 6,189,285. Washington, DC: U.S. Patent and Trademark Office.

[100] Mottram, J. T. (1992). Lateral-torsional buckling of a pultruded I-beam. *Composites*, 23(2), 81-92.

[101] Mottram, J. T. (2002). Calculation of the critical buckling load in PFRP shapes. In *Proceedings of the First International ACIC Conference on Advanced Polymer Composites for Structural Applications in Construction (ACIC)*, Southampton, 15-17.

[102] Nagaraj, V., & GangaRao, H. V. (1997). Static behavior of pultruded GFRP beams. *ASCE Journal of Composites for Construction*, 1(3), 120-129.

[103] Nethercot, D. A., & Rockey, K. C. (1973). Lateral buckling of beams with mixed end conditions. *The Structural Engineer*, 51(4).

[104] Nethercot, D. A. & Rockey, K. C. (1971). A unified approach to the elastic lateral buckling of beams. *The Structural Engineer*, 49 321-30.

[105] Nguyen, T. T., Chan, T. M., & Mottram, J. T. (2015). Lateral–Torsional Buckling design for pultruded FRP beams. *Composite Structures*, 133, 782-793.

[106] Nguyen, T.T., Chan, T.M. and Mottram, J.T. (2014) Lateral-torsional buckling resistance by testing for pultruded FRP beams under different loading and displacement boundary conditions, *Composite: Part B*, 60 306 – 318.

[107] Nguyen, T. T., Chan, T. M., & Mottram, J. T. (2013). Influence of boundary conditions and geometric imperfections on lateral–torsional buckling resistance of a pultruded FRP I-beam by FEA. *Composite Structures*, 100, 233-242.

[108] Pandey, M. D., Kabir, M. Z., & Sherbourne, A. N. (1995). Flexural-torsional stability of thin-walled composite I-section beams. *Composites Engineering* 5(3), 321-342.

[109] Pecce, M., & Cosenza, E. (2000). Local buckling curves for the design of FRP profiles. *Thin-walled structures*, 37(3), 207-222.

[110] Petit, P. H., (1969). A simplified method of determining the inplane shear stress-strain response of unidirectional composites. *Composite Materials: Testing and Design*. ASTM STP 460, American Society for Testing and Materials, pp83-93.

[111] Qiao, P., & Zou, G. (2003). Local buckling of composite fiber-reinforced plastic wide-flange sections. *ASCE Journal of Structural Engineering*, 129(1), 125-129.

[112] Qiao, P., Zou, G., & Davalos, J. F. (2003). Flexural–torsional buckling of fiber-reinforced plastic composite cantilever I-beams. *Composite Structures*, 60(2), 205-217.

[113] Qiao, P., Davalos, J. F., & Wang, J. (2001). Local buckling of composite FRP shapes by discrete plate analysis. *ASCE Journal of Structural Engineering*, 127(3), 245-255.

[114] Roberts, T. M. (2002). Influence of shear deformation on buckling of pultruded fiber reinforced plastic profiles. *ASCE Journal of Composites for Construction*, 6(4), 241-248.

[115] Roberts, T. M., & Jhita, P. S. (1983). Lateral, local and distortional buckling of I-beams. *Thin-Walled Structures*, 1(4), 289-308.

[116] Rosen, B. W. (1972). A simple procedure for experimental determination of the longitudinal shear modulus of unidirectional composites. *Journal of Composite Materials*, 6(4), 552-554.

[117] Sapkás, Á., & Kollár, L. P. (2002). Lateral-torsional buckling of composite beams. International *Journal of Solids and Structures*, 39(11), 2939-2963.

[118] Schniepp, T. J. (2002). *Design manual development for a hybrid, FRP double-web beam and characterization of shear stiffness in FRP composite beams* (Doctoral dissertation, Virginia Polytechnic and State University).

[119] Scott, D. W. (1997). *Short-and long-term behavior of axially compressed slender doubly symmetric fiber-reinforced polymeric composite members*. Ph.D. Thesis, Georgia Institute of Technology, Atlanta, GA.

[120] Strongwell. (2003). *EXTREN DWB Design Guide*.

[121] Swanson, S. R. (1997). *Introduction to design and analysis with advanced composite materials*. Prentice Hall.

[122] Sonti, S. S., & Barbero, E. J. (1996). Material characterization of pultruded laminates and shapes. *Journal of reinforced plastics and composites*, 15(7), 701-717.

[123] Sonti, S. S., Barbero, E. J., & Winegardner, T. (1995). Determination of shear properties for RP pultruded composites. *Journal of reinforced plastics and composites*, 14(4), 390-401.

[124] Spigel, B. S., Prabhakaran, R., & Sawyer, J. W., (1987). An investigation of the Iosipescu and asymmetrical four-point bend tests. *Experimental Mechanics*, 27(1): 57-63.

[125] Tan, S. C., & Knight, M. (1994). An extrapolation method for the evaluation of compression strength of laminated composites. In *Compression response of composite structures*. ASTM International.

[126] Tham, L. G., & Szeto, H. Y. (1990). Buckling analysis of arbitrarily shaped plates by spline finite strip method. *Computers & structures*, 36(4), 729-735.

[127] Timoshenko, S. P., & Gere, J. M. (1961). *Theory of Elastic Stability*. 1961. McGrawHill-Kogakusha Ltd, Tokyo.

[128] Turvey, G. J. (1996a). Lateral buckling tests on rectangular cross-section pultruded GRP cantilever beams. *Composites Part B: Engineering*, 27(1), 35-42.

[129] Turvey, G. J. (1996b). Effects of load position on the lateral buckling response of pultruded GRP cantilevers—comparisons between theory and experiment. *Composite Structures*, 35(1), 33-47.

[130] Van Den Einde, L., Zhao, L., & Seible, F. (2003). Use of FRP composites in civil structural applications. *Construction and Building Materials*, 17(6), 389-403.

[131] Wang, Y., & Zureick, A. H. (1994). Characterization of the longitudinal tensile behavior of pultruded I-shape structural members using coupon specimens. *Composite structures*, 29(4), 463-472.

[132] Weinberg, M. (1987). Shear testing of neat thermoplastic resins and their unidirectional graphite composites. *Composites*, 18(5), 386-392.

[133] Walrath, D. E., & Adams, D. F. (1983). The losipescu shear test as applied to composite materials. *Experimental mechanics*, 23(1), 105-110.

[134] Zureick, A., & Steffen, R. (2000). Behavior and design of concentrically loaded pultruded angle struts. *Journal of Structural Engineering*, 126(3), 406-416.

[135] Zureick, A. (1998). FRP pultruded structural shapes. *Progress in Structural Engineering and Materials*, 1(2), 143-149.

[136] Zureick, A., & Scott, D. (1997). Short-term behavior and design of fiber-reinforced polymeric slender members under axial compression. *Journal of Composites for Construction*, 1(4), 140-149.

[137] Zureick, A., Kahn, L. F., & Bandy, B. J. (1995). Tests on deep I-shape pultruded beams. *Journal of Reinforced Plastics and Composites*, 14(4), 378-389.